WAVELET MODULATED DC-AC POWER INVERTERS

SALEH A.M. SALEH

WAVELET MODULATED DC-AC POWER INVERTERS

By

© Saleh A. M. Saleh, B.Eng., M.Eng.

A thesis submitted to the School of Graduate
Studies in partial fulfillment of the
Requirements for the degree of
doctor of philosophy

Faculty of Engineering and Applied Science
Memorial University of Newfoundland
April 2007

St.John's Newfoundland Canada

Your file Votre référence
ISBN: 978-0-494-31328-2
Our file Notre référence
ISBN: 978-0-494-31328-2

To My Parents Abed Al-Aziz and Sobhia

To My Brothers and Sisters

To all my Friends

This thesis would be incomplete without a mention of the great and unlimited support by my mother, my brother Omar and my sister Lubna to whom this thesis is dedicated.

Abstract

Modern industrial applications of dc-ac inverters have increasing demands for high quality output voltages and currents. Such demands are met through operating inverters so that output harmonic components are either reduced or eliminated. Developing and testing switching strategies capable of achieving such outputs have been topics for intensive research for the last 4 decades. Several switching strategies realized by modulation techniques have been proposed and tested. As a result, significant contributions on the performance of inverters have been achieved. However, the problem of output harmonic components is still a challenge. One of the most critical limitations of existing modulation techniques is the lack of correlation between these techniques and any inverter models.

An inverter can be modeled as a non-uniform recurrent sampling-reconstruction process, in which instantaneous switching actions are considered as the reconstruction inverter outputs. This modeling approach can also be employed to verify the effects on inverter outputs due to any changes in the switching strategy. Using the concepts of the sampling theorem, a sampling-reconstruction process is represented as a multiresolution analysis (MRA). Effective and accurate MRAs can be constructed using basis functions generated by scaling and wavelet functions. A modulation technique that incorporates the proposed sampling-based inverter model and a wavelet-based MRA can enable the operation of inverters for high quality outputs. The development, implementation and testing of such a modulation technique is the primary objective of this research.

A novel approach to construct a non-dyadic type MRA that is capable of supporting non-uniform recurrent sampling has been developed. The non-dyadic type MRA is developed based on new scale-based linearly-combined scaling and

wavelet functions. The reference-modulating signal is sampled using the new scaling function such that a number of sample groups are formed over each cycle of the reference-modulating signal. Each group has two samples that are created by a dilated and translated version of the scaling function. Reconstructing the reference-modulating signal is carried out by stages of interpolating functions, where each stage is defined over one sample group. This structure of interpolating functions creates one ON switching pulse over each sample group. The approach of operating the inverter aims to concentrate the energy of the output signal in the frequency of the reference-modulating signal. As a result, negligible energy is distributed in the rest of frequency components.

The proposed wavelet modulation technique is implemented using an algorithm for both simulation and experimental testing. The results of both simulations and on-line tests show high quality output voltages and currents indicated by the low values of total harmonic distortion factors. These tests are conducted for different load types under several output frequencies. Also, a new control strategy is developed for adjusting magnitudes and frequencies of wavelet-modulated inverter outputs. This control strategy is called resolution-level control, and is based on changing the scale of the successive reconstruction functions. Simulation and experimental test results of a dc-ac inverter under this control approach demonstrate stable, robust and fast responses for different load changes. The developed non-dyadic type MRA is extended to operate three-phase inverters. An algorithm is developed for simulation and experimental tests of the three-phase wavelet modulated inverter to supply a $R - L$ load. Results obtained from these tests have demonstrated high quality outputs with negligible harmonic contents.

Acknowledgments

I would like to express my gratitude and thanks to my supervisor Dr. M. A. Rahman who provided me with complete freedom to try ideas and be essentially self-directed, and to Dr. Moloney for her continuous support and help throughout all steps of my work. Also, I would like to thank Dr. Masek for his suggestions and help in preparing this thesis. The financial support from the Natural Sciences and Engineering Research Council of Canada (NSERC) through the PGS scholarship is greatly appreciated. I also wish to thank the Faculty of Engineering and Applied Science and Memorial University of Newfoundland, for providing much needed laboratory space, equipment and technical services to take this project from idea to implementation.

Special thanks and appreciations are expressed to my brother Omar and sister Lubna for their great encouragement and support. I would like to thank my colleagues Jahangir Khan, Martin, Casey, Abedel Shafi Khan and late Dr. Tawfiq Radwan for their help and suggestions in the experimental part of this work. Finally, deep appreciations to my roommate Kasem and my special friends Said, Rosemary and Heather for their help in correcting my thesis.

Contents

List of Tables

List of Figures

List of Symbols

α_i	The i^{th} switching angle with respect to an arbitrary reference
$\bigoplus$	The direct sum of two disjoint linear subspaces
$\chi_{[a,b]}$	A rectangular box function extending from a to b
$\delta(t)$	The Dirac delta function
γ_a	The scale-time interval factor for phase A
γ_b	The scale-time interval factor for phase B
γ_c	The scale-time interval factor for phase C
γ_d	The scale-time interval factor for the sample group d
$\hat{ac}(\omega)$	The DTFT of the autocorrelation sequence $ac[k]$
$\lambda_{ad}(t)$	An interpolating function over the sample group d of phase A
$\lambda_{bd}(t)$	An interpolating function over the sample group d of phase B
$\lambda_{cd}(t)$	An interpolating function over the sample group d of phase C
$\lambda_d(t)$	The interpolating function over the sample group d

$\left(\tilde{\psi}_{\varphi}\right)_j(t)$	The dual scale-based linearly-combined wavelet function at scale j
$(\tilde{\varphi}_a(t))$	The synthesis scale-based linearly-combined scaling function to reconstruct $S_{Ma}(t)$ (the reference-modulating signal for phase A)
$(\tilde{\varphi}_b(t))$	The synthesis scale-based linearly-combined scaling function to reconstruct $S_{Mb}(t)$ (the reference-modulating signal for phase B)
$(\tilde{\varphi}_c(t))$	The synthesis scale-based linearly-combined scaling function to reconstruct $S_{Mc}(t)$ (the reference-modulating signal for phase C)
$(\varphi_a(t))$	The scale-based linearly-combined scaling function to sample $S_{Ma}(t)$
$(\varphi_b(t))$	The scale-based linearly-combined scaling function to sample $S_{Mb}(t)$
$(\varphi_c(t))$	The scale-based linearly-combined scaling function to sample $S_{Mc}(t)$
$(L_a x_c)(t)$	The orthogonal projection mapping operator on $x_c(t)$
$(O_a x_c)(t)$	The sampling operator on $x_c(t)$
$\langle , \rangle$	The inner product operation
$\{(t_{dp})_a\}$	The set of time locations for the non-uniform samples over one cycle of $S_{Ma}(t)$
$\{(t_{dp})_b\}$	The set of time locations for the non-uniform samples over one cycle of $S_{Mb}(t)$

$\{(t_{dp})_c\}$	The set of time locations for the non-uniform samples over one cycle of $S_{Mc}(t)$
$\mathbb{R}$	The set of real numbers
$\mathbb{Z}$	The set of integer numbers
ω_c	The frequency of the carrier signal in $rad/sec.$
ω_m	The frequency of the reference-modulating signal $rad/sec.$
$\phi_H(t)$	The Haar scaling function
$\phi_{j,k}(t)$	A scaling function at scale j and translation k
$\psi_\varphi(t)_j$	The scale-based linearly-combined wavelet function at scale j
$\psi_H(t)$	The Haar wavelet function
$\psi_{j,k}(t)$	A wavelet function at scale j and translation k
θ_c	An arbitrary phase shift of the carrier signal
θ_m	An arbitrary phase shift of the reference-modulating signal
$\tilde{\phi}_{j,k}(t)$	The dual scaling function at scale j and translation k
$\tilde{\psi}_{j,k}(t)$	The dual wavelet function at scale j and translation k
$\tilde{\varphi}_j(t)$	The dual scale-based linearly-combined scaling function at scale j
$\varphi_j(t)$	The scale-based linearly-combined scaling function at scale j
$\Delta\vec{V}$	The change in the voltage vector in a $d-q$ frame
$\vec{I}$	The current vector in a $d-q$ frame

A_M	The peak value of $S'_M(t)$ (the first derivative of the reference-modulating signal $S_M(t)$)
$a_n,\ b_n$	Coefficients of the n^{th} term of Fourier series
a_o	The magnitude of the dc component present in a signal
$ac[k]$	An autocorrelation sequence
C_{mn}	Complex coefficients of Fourier series
D_s	The steady-state value of the ON time of the switch-cell
$D_s(t)$	The instantaneous value of the ON time of the switch-cell
f_c	The carrier signal frequency in Hz
f_m	The reference-modulating signal frequency in Hz
$G_d(t)$	The Lagrange interpolating function over the sample group d
H	The Hilbert space
$h_\varphi[k]$	The refinement filter associated with $\varphi(t)$
$H_{sn}(f)$	The frequency response of a synthesis filter
I_L	The load current
$I_L(f)$	The spectrum of the load current
I_m	The motor current
J	The maximum value the scale j can have
j	The scale (dilation)

L^2	Space of square-integrable functions
M	The normalized output voltage magnitude
m_a	The amplitude modulation index
$ON_{\tilde{\varphi}}$	The duration of the ON switching pulse created by $\tilde{\varphi}_j(t)$
$P_a(t)$	The train of impulses to sample the reference-modulating signal for phase A
$P_b(t)$	The train of impulses to sample the reference-modulating signal for phase B
$P_c(t)$	The train of impulses to sample the reference-modulating signal for phase C
$S_{dM}[n]$	The non-uniform recurrent sampled version of $S_M(t)$ (the reference-modulating signal)
$S_{dM}[n]_a$	The non-uniform recurrent sampled version of $S_{Ma}(t)$ (the reference-modulating signal for phase A)
$S_{dM}[n]_b$	The non-uniform recurrent sampled version of $S_{Mb}(t)$ (the reference-modulating signal for phase B)
$S_{dM}[n]_c$	The non-uniform recurrent sampled version of $S_{Mc}(t)$ (the reference-modulating signal for phase C)
$S_{Ma}(t)$	The reference-modulating signal for phase A
$S_{Mb}(t)$	The reference-modulating signal for phase B

$S_{Mc}(t)$	The reference-modulating signal for phase C
$S_M(t)$	The reference-modulating signal
$S_{SCF}[n]$	The discrete signal created by falling portions of $S_{SC}(t)$
$S_{SCR}[n]$	The discrete signal created by rising portions of $S_{SC}(t)$
$S_{SC}(t)$	The carrier signal
$Sa_{s;a}(t)$	The Shannon sampling function
t_{1j}	Time location of the first sample in the sample group d
t_{2j}	Time location of the second sample in the sample group d
T_c	The period of the carrier signal
T_m	The period of the sampled continuous-time (CT) signal
T_Q	The Nyquist period
t_{sp}	The time interval separating time intervals of two successive sample groups
T_s	The uniform sampling period
V_{AB}	The line-to-line voltage of phase A
V_{AN}	The line-to-neutral voltage of phase A
V_{DC}	The DC supply voltage to the inverter
V_j	A space spanned by scaling basis functions at scale j
V_o	The inverter output voltage

$V_o(f)$	The spectrum of the output voltage
W_j	A space spanned by wavelet basis functions at scale j
$X(\omega)$	The discrete-time Fourier transform of $x[n]$
$X_c(\Omega)$	The continuous time Fourier transform of $x_c(t)$
z_b	The shift in the scaling function $(\varphi_b(t))_j$
z_c	The shift in the scaling function $(\varphi_c(t))_j$
$\mathcal{B}^2_{2\Omega_o}(\mathbb{R})$	The space of all signals band limited to Ω_o
$\mathcal{C}_b[0, T_s]$	The space of continuous and bounded functions on $[0, T_s]$
$\mathcal{C}_n$	The space of complex functions
$\mathcal{D}$	The number of sample groups created by $S_{SC}(t)$ over one cycle of $S_M(t)$
$\mathcal{D}_\varphi$	The number of sample groups created by $\varphi_{j,k}(t)$ over one period of $x_c(t)$
$\mathbb{C}$	The set of complex numbers

List of Abbreviations

1ϕ	Single-phase
3ϕ	Three-phase
clos	The closure operation
CS	Current-source
CT	Continuous-time
CTFT	Continuous-time Fourier transform
DM	Delta modulation
DO/P	Digital output port of the ds1102 board
DPWM	Direct Pulse-width modulation
DSP	Digital signal processing
DT	Discrete-time
DTFT	Discrete-time Fourier transform
FT	The Fourier Transform
hp	Horse power; $1hp$=746 watts
HPF	High-pass filter
I_1	The fundamental component of the current
IGBT	Insulated gate bipolar transistor
inf	The infimum: the greatest lower bound of a set S
LPF	Low-pass filter
MRA	Multiresolution analysis
NSPWM	Naturally sampled Pulse-width modulation
PWM	Pulse-width modulation
Q_i	The i^{th} switching element of an inverter

RMS	Root-mean square
RPM	Revolution per minute
RPWM	Random PWM
RSPWM	Regularly sampled PWM
SBM	Sampling-based model
SHE	Specific harmonic elimination
SPWM	Sinusoidal pulse-width modulation
sup	The supremum: the least upper bound of a set S
SVM	Space-Vector Modulation
THD	Total harmonic distortion
UPS	Uninterruptible power supplies
V_1	The fundamental component of the voltage
VS	Voltage-source
WKS	Whittaker-Kotel$\acute{n}$ikov-Shannon
WM	Wavelet modulated
Z_L	Load impedance

Chapter 1

Introduction

1.1 General

Dc-ac inverters have become key components in a wide range of industrial applications. Such applications include ac motor drives, control systems, uninterruptible power supply (UPS) systems, power quality, power systems, renewable energy utilization, etc. Most of these applications have critical conditions for high quality power supplies. Such conditions on the quality of power supplies are being translated into standards for allowable harmonic content in supply voltages and currents. These standards have pushed toward operating dc-ac inverters to produce very low harmonic contents in their outputs [1].

A dc-ac inverter is an electronic device composed of groups of switching elements that are operated in a certain sequential manner to produce outputs with predefined specifications. The operation of these groups of switching elements is established so that they are switched ON and OFF in a sequential periodic manner. The dc-ac inverter is usually called, simply, an inverter. Hence, the term dc-ac will be dropped in the text of this thesis. There are two popular types of invert-

ers, single-phase inverters and three-phase inverters. It is to be noted that the term "power inverter" is related to inverters with high power ratings. Figure 1.1 shows the schematic diagrams of conventional 1ϕ and 3ϕ inverters along with obtained output voltages using the square-wave operation and the multi-switching one [1, 2].

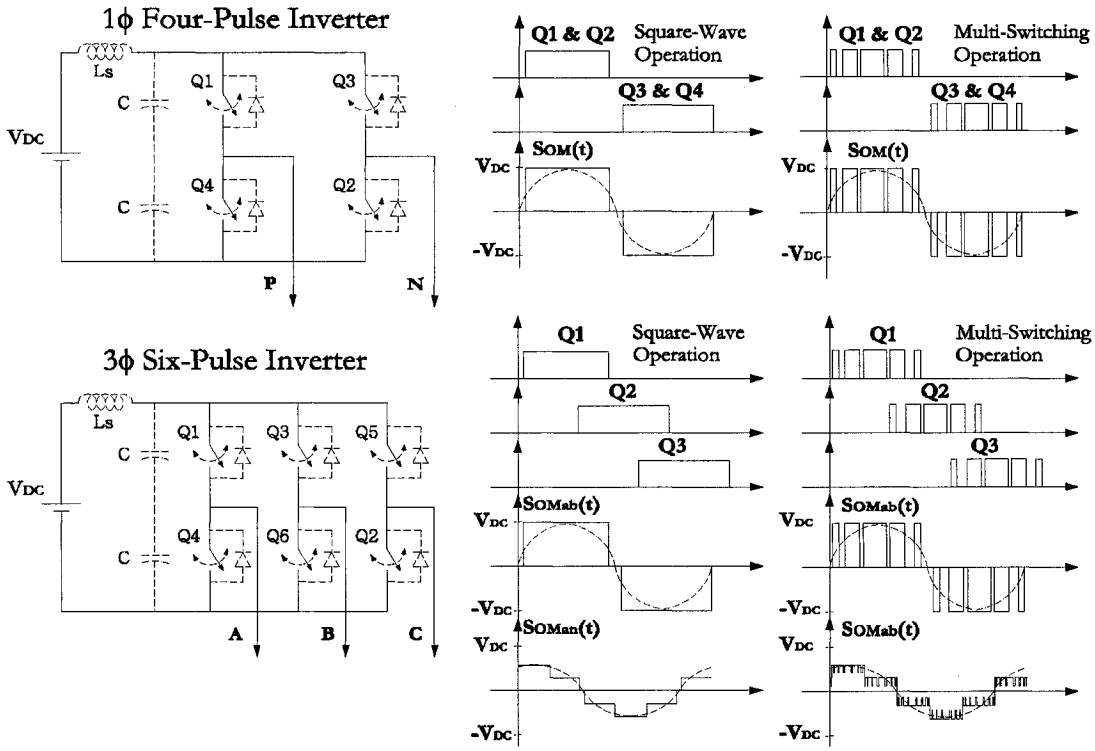

Figure 1.1: Schematic diagrams of single-phase and three-phase inverters along with output voltages ($S_{OM}(t)$) obtained using the square-wave operation and the multi-switching one.

The problem of harmonic content in inverter outputs has been a challenging consideration as early as the first application of inverters as power conditioners. Since then, operating inverters employing switching strategies to reduce the output harmonic content has been a topic for intensive research. Various switching

strategies have been developed and tested to operate inverters so that the output harmonic content is reduced or eliminated. Among these strategies are the square-wave and multi-switching strategies. The multi-switching strategy has been found effective in reducing the output harmonic content, and as a result is capable of improving the quality of inverter outputs. The multi-switching strategy is based on activating a group of switching elements ON and OFF with a rate higher than the desired output frequency. The process of changing the status of a switching element from ON to OFF or OFF to ON is known as a modulation process [1, 2]. Modern inverters employ different modulation techniques to generate outputs with harmonic contents as low as possible. Pulse-width modulation (PWM) and delta modulation (DM) are the most popular modulation techniques employed to switch inverters. However, PWM inverters are more popular, and are extensively used in various industrial applications [1, 2].

The continuous advancements in both solid-state technology and digital systems have provided inverters with new modulation techniques. The main improvement has been the ability to switch inverters with higher frequencies in a stable and reliable manner. Also, with these advancements and the developments in micro-processor technology, modulation techniques that require complex computations have become implementable [1, 2]. As a result, new modulation techniques have been developed and tested to improve the performance of power inverter outputs. These new modulation techniques include: the specific harmonic elimination (SHE), space-vector modulation, hysteresis-band current control and random PWM. On the other hand, the application of inverters in high power applications have made switching losses, switching capabilities and inverter efficiency critical issues that have to be taken into account [3].

In modern inverter operation and control, there are several modulation techniques with different improvements to meet practical requirements. However, these techniques produce very similar harmonic distribution patterns in the outputs of modulated inverters. One of the main reasons for such behavior is the lack of rigorously valid models for inverter functions that can provide the basis for any modulation technique. Furthermore, the lack of such models has limited the integration of inverter functions with developing modulation techniques [4]. There are few available models of inverter functions that are mainly based on circuit theory, where time-averaged quantities are considered only. Other models are based on numerical approximations of the relations between currents and voltages on both input and output sides of a power inverter. In all these models, switching actions are not explicitly represented in the model of inverter functions, and the inverter is lumped into a supply-to-load entity. These approaches have limited capabilities of providing effective mathematical description of inverter functions [4]. The performance limitations due to the lack of correlation between modulation techniques and any inverter models and their effects on inverter performance are the main motivation of this work.

1.2 Thesis Motivations and Objectives

With extensive research conducted on modulation techniques [1, 4], there exists a need for a rigorous model for justifying any modification or improvement of inverter operation. Existing representations of modulating techniques can not provide a very accurate verification for several aspects of modulated inverters performance. These aspects include: selecting the carrier signal, using non-sinusoidal reference-modulating signals, existence of harmonics in sidebands around the car-

rier frequency and its multiples, appearance of the jitter when using rectangular pulses as a carrier signal, etc. [4]. On the other hand, the application of signal processing concepts was helpful in developing the Fourier double integral criteria to evaluate the performance of modulation techniques. Other concepts of signal processing can be helpful both in modeling and modulating inverters.

The spectra of modulated inverter outputs have almost identical harmonic distributions as those of reconstructed continuous band limited signals from their samples. Such a similarity can lead to viewing the modulating process as a process of reconstructing a sinusoidal signal from its samples. A modulated inverter operation can be modeled as a non-uniform recurrent sampling-reconstruction process. Modeling an inverter using this approach considers instantaneous switching actions as a main part of the model. This modeling approach can also provide an opportunity for developing and testing new modulation techniques. In general, any sampling-reconstruction process can be represented as a multi-resolution analysis-synthesis (MRA) process. One of the most accurate approaches to construct MRAs is using wavelet functions. Using wavelet-based MRAs makes it possible to sample the reference-modulating signal and reconstruct it through switching actions.

There is a need for a modulation technique that meets the increasing demands for power inverters with negligible output harmonic contents. If a modulation technique can operate power inverters to meet such demands, then this modulation technique will be useful in wide range of industrial applications. The motivation for this research arises from the need to develop and test a modulation technique that is capable of eliminating harmonics regardless of load characteristics, output frequency requirements and switching elements properties. The desired modulation technique will be very advantageous for a wide range of industrial

applications including speed control in AC motor drives, UPS, power quality applications and renewable energy utilization. The development and testing of a new modulation technique that can be correlated with a valid inverter model are the main focus of this thesis whose objectives are described in the following subsection.

1.2.1 Thesis Objectives

There are several modulation techniques with different approaches to implement for different inverter topologies. However, none of these techniques has been developed in correlation with any modeling approach of inverters. On the other hand, there are a few models of inverter based on averaging inverter switched outputs over time. This averaged modeling cannot properly consider instantaneous switching actions as a key part of the desired inverter model. This discontinuity between modeling and modulating inverters has limited the performance of existing inverter modulation techniques. As a consequence, harmonic components present in the outputs of inverters is still a critical issue when considering inverter applications in high performance drives and systems. As electrical loads become more sensitive to the quality of power supplies, optimal inverter modulation becomes more demanding. On the other hand, utilizing renewable energy sources and integrating such sources with existing power grids require additional care for harmonic levels.

The first objective of this work is to develop an inverter model that ensures instantaneous switching actions as a main part of the model. This desired model must be able to account for the effects on inverter outputs due to any change in the switching strategy. Also, this model must be capable of correlating with differ-

ent existing modulation techniques. It will be shown that the desired model is a dedicated non-uniform recurrent sampling-reconstruction process, where switching actions are modeled as interpolating functions for reconstructing a sinusoidal signal.

The second objective of this work is to design sets of basis functions that are capable of constructing a multiresolution analysis (MRA) to support a non-uniform recurrent sampling structure. The required basis functions are generated by a single scaling function that has a dual synthesis scaling function. These two functions will carry out a non-uniform recurrent sampling-reconstruction process that can be correlated with the sampling-based inverter model.

The third objective of this work is to realize the MRA and to generate switching signals with which to operate inverters. This objective includes building procedures to realize the proposed MRA for both simulating and experimental testing of single-phase and three-phase inverters. These simulation and experimental tests will be conducted for different load types under different operating conditions. Furthermore, part of this objective is to compare the performance of the proposed wavelet modulation technique with other techniques under the same operating conditions.

The final objective of this work is to develop and test a control strategy that can be used to adjust the outputs of wavelet modulated (WM) inverters. Also, this objective includes conducting simulation and experimental tests to investigate the performance of WM inverters under this control strategy. Such tests will include changing the WM inverter output magnitudes as well as frequencies.

It is to noted that different types of loads will be used to test the performance of the proposed wavelet modulation technique including static loads $(R - L)$ as well

as dynamic ones (induction motors). The following section provides a review of different modulation techniques that have been used in switching inverters.

1.3 Literature Review of Inverter Modulation Techniques

In mid 1950's, Royer and Uchrin [5] and Taylor [6] have presented the earliest two-transistor saturable-core parallel-inverter configurations. Their introduction of the square wave magnetically-coupled multi-vibrators has paved the way for developing a large family of power processing devices. Lee and Willson [7] developed mathematical models that verified the inverter function presented by Royer, Uchrin and Taylor. These models were the first reported square wave switched inverters. However, in these inverters the problems of harmonics and switching losses were not discussed. McMurray has presented a new silicon-controlled rectifier (SCR)-based inverter topology with resonant switching to improve the ON-OFF switching times. This approach has provided the first practical consideration of multi-switching techniques [8]. Later, McMurray extended this switching approach for power electronic converters including the dc-dc switched converters [8, 9].

1.3.1 Traditional Pulse-Width Modulation (PWM)

The early developed square wave inverters have several inherent disadvantages including harmonic distortion, switching losses, low efficiency, complex models and complicated circuitry for implementation. The increasing demands for high power quality by sensitive loads have led to the development of other switching

strategies based on modulation techniques. The earliest modulation schemes using single and multiple pulse modulations were introduced by Kirnnick and Heinrick [10]. These schemes were capable of producing inverter output voltages and currents with lower harmonic contents. Mokrytzki [11] modified single and multiple pulse width modulations through defining a reference-modulating sinusoidal waveform. This modification on generating switching pulses with variable width was achieved by comparing the reference-modulating sinusoidal waveform to a high frequency sawtooth signal and was later defined as the pulse-width modulation (PWM) technique. The introduction of the general sine-triangle voltage PWM and the definition of the fundamental concepts of sinusoidal pulse-width modulation (SPWM) were carried out by Schonubg and Stemmler [12].

The application of both analog and digital electronic technologies made switching with higher frequencies more feasible. Moreover, it became possible to use triangular carrier signals instead of sawtooth ones that improved the inverter performance in terms of harmonic contents as well as switching losses. At the beginning, two different switching strategies, namely the asynchronous and the synchronous SPWM, were used for generating switching pulses to operate power inverters. However, rapid developments in digital electronics and microprocessor technology created modulation techniques that are based on predefined parameters. Such techniques were divided into three major schemes of PWM as [13]:

- Naturally Sampled PWM
- Regularly Sampled PWM
- Direct PWM

Earlier research in developing and testing modulation techniques aimed to [14]:

- Minimize output harmonic contents
- Maximize dc-bus utilization
- Increase inverter efficiency through minimizing switching losses
- Produce inverter outputs with controllable magnitudes and frequencies

The first reported research to consider the phenomenon of harmonics and develop an optimal switching strategy to minimize them was done by Bowes in 1975 [15]. Bowes derived a double Fourier integral formula that is the most well known analytical method to identify harmonic existence resulting from inverter switching actions. This analytical approach was originally developed for communication applications. The double Fourier integral formula approach assumes the existence of two independent linear time variables defined as [16]:

$$x(t) = \omega_c t + \theta_c \tag{1.1}$$

$$y(t) = \omega_m t + \theta_m \tag{1.2}$$

where ω_c is the carrier signal frequency, θ_c is an arbitrary phase shift of the carrier signal, ω_m is the reference-modulating signal frequency and θ_m is an arbitrary phase shift of the reference-modulating signal. A multi-variable function $f(t)$ can be defined as:

$$f(t) = f\left(x(t), y(t)\right) \tag{1.3}$$

Using Fourier analysis theory, complex coefficients of Fourier series for the function $f(t)$ can be determined as [1, 16]:

$$C_{mn} = \frac{1}{2\pi^2} \int_{-\pi}^{\pi} \int_{-\pi}^{\pi} f\left(x(t), y(t)\right) e^{j(mx+ny)} dxdy \tag{1.4}$$

The complex coefficients C_{mn} can determine the magnitude and the phase of each harmonic component present in the function $f(t)$ [1]. This analysis was used as a performance criterion for testing effective switching strategies that resulted in implementing the naturally sampled PWM scheme. In the beginning of 1980's, Bowes and Mount [17] used the same approach to successfully implement the regularly sampled PWM using a microprocessor technology.

The direct pulse-width modulation technique (DPWM) has capabilities of producing inverter outputs with very small amount of harmonics. The basic idea of DPWM is to create ON pulses that exactly produce the same volt-second average as the reference-modulating signal over each cycle of the carrier signal. There are two methods to determine the widths of ON switching pulses created by the DPWM technique. These methods are [1]:

- Symmetrical pulse duration, where the widths of ON pulses are determined using the following relation:

$$D_{ON} = t_2 - t_1 = 2W = 2\int_{t_i}^{t_i+T_c} M\sin(\omega_m t)\,dt \tag{1.5}$$

- Asymmetrical pulse duration, where the widths of ON pulses are determined using the following relation:

$$D_{ON} = t_1 = W = \int_{t_i}^{t_i+T_c/2} M\sin(\omega_m t)\,dt \tag{1.6}$$

where M is the normalized output voltage magnitude, T_c is the period of the carrier signal and ω_m is the fundamental frequency (the frequency of the reference-modulating signal). The two methods of DPWM are shown in Figure 1.2.

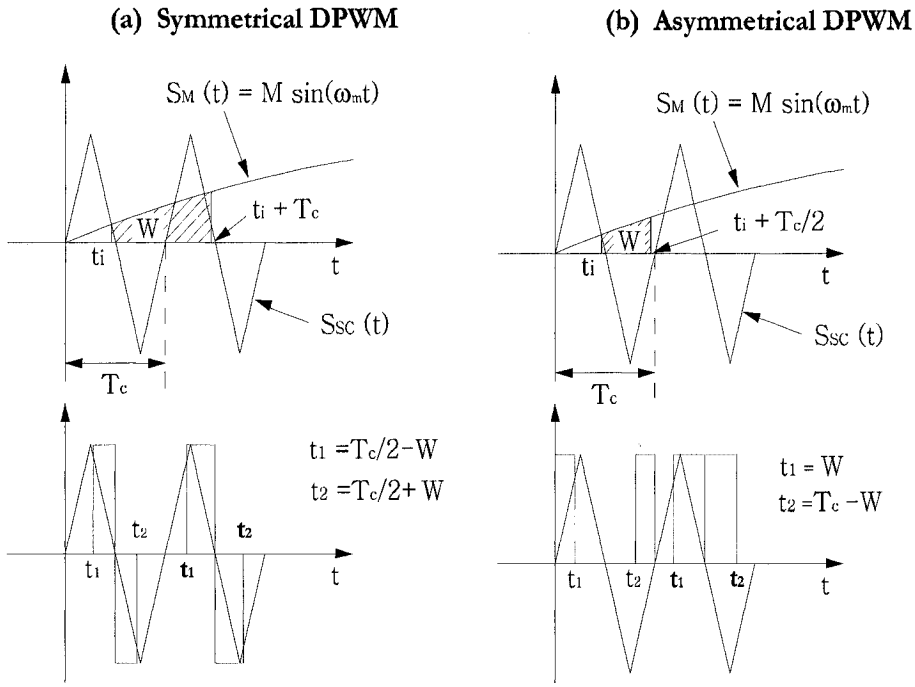

Figure 1.2: The DPWM technique for generating ON switching pulses: (a) the symmetrical DPWM and (b) the asymmetrical DPWM.

The major disadvantage of DPWM is that it requires pre-knowledge of the reference-modulating signal. Moreover, the determination of each ON pulse width and position may involve complex mathematical operations. Such disadvantage has made carrier-based modulation techniques more popular for industrial applications [1, 15].

The employment of advanced digital technology has made implementing new switching strategies realistic and practical. Regularly sampled pulse-width modulation (RSPWM) and naturally sampled pulse-width modulation (NSPWM) are new carrier-based strategies that were developed as a result of employing digital computer systems. The NSPWM strategy generates switching pulses that have

edges determined by the intersection points of the carrier signal and the reference-modulating signal. The carrier signal used in this strategy (mostly a triangular signal) has a higher frequency than a reference-modulating signal (mostly a sinusoid). This PWM strategy was developed to replace the square wave switching used in early inverters. NSPWM has only two implementation types, one uses a sawtooth carrier signal and the other uses a triangular carrier signal [1, 2, 6, 7]. Figure 1.3 shows NSPWM implemented using a sawtooth carrier signal. Figure 1.4

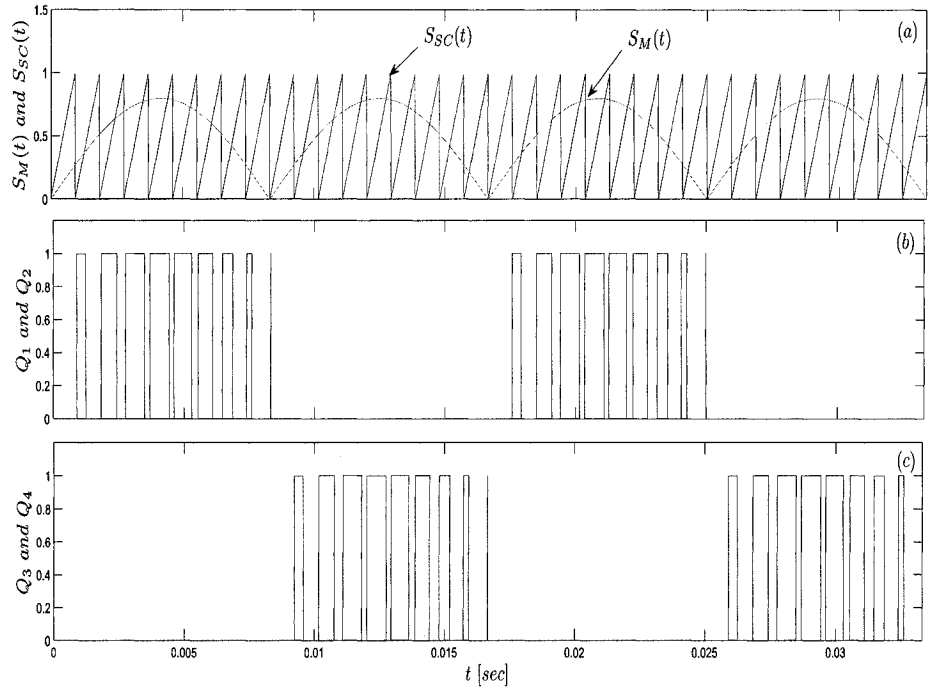

Figure 1.3: The NSPWM technique using a sawtooth carrier signal $S_{SC}(t)$ with a frequency of 1.8 kHz: (a) a rectified version of a sinusoidal reference-modulating signal $S_M(t)$ along with the sawtooth carrier signal $S_{SC}(t)$, (b) switching pulses for Q_1 and Q_2 switching elements of a 1ϕ four-pulse inverter and (c) switching pulses for Q_3 and Q_4 of the same 1ϕ four-pulse inverter shown in Figure 1.

shows NSPWM implemented using a triangular carrier signal.

In the RSPWM strategy, a sinusoidal reference-modulating signal is regularly

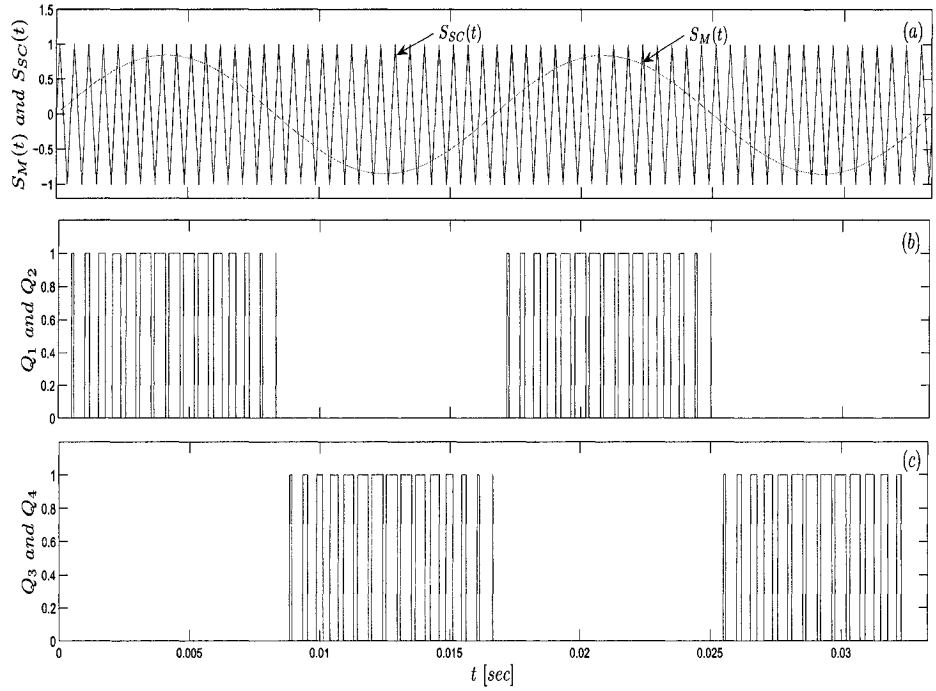

Figure 1.4: The NSPWM technique using a triangular carrier signal $S_{SC}(t)$ with a frequency of 1.8 kHz: (a) a sinusoidal reference-modulating signal $S_M(t)$ along with the triangular carrier signal $S_{SC}(t)$, (b) switching pulses for Q_1 and Q_2 switching elements of a 1ϕ four-pulse inverter and (c) switching pulses for Q_3 and Q_4 of the same 1ϕ four-pulse inverter shown in Figure 1.

sampled and held constant at the beginning of each switch cycle before being compared with a triangular carrier signal. Two forms of the RSPWM strategy became popular such that [14–16]:

1. The symmetrical RSPWM that is based on sampling the reference-modulating signal at either positive or negative peaks of the carrier signal and holding that value over a complete cycle of the carrier signal.

2. The asymmetrical RSPWM that is based on sampling the reference-modulating signal at both positive and negative peaks of the carrier signal and holding that value over a half cycle of the carrier signal.

These new strategies were developed to achieve optimal switch-mode inverter operation to meet the increasing demand for accurate and high quality output voltages and/or currents. Figure 1.5 shows both forms of the RSPWM technique.

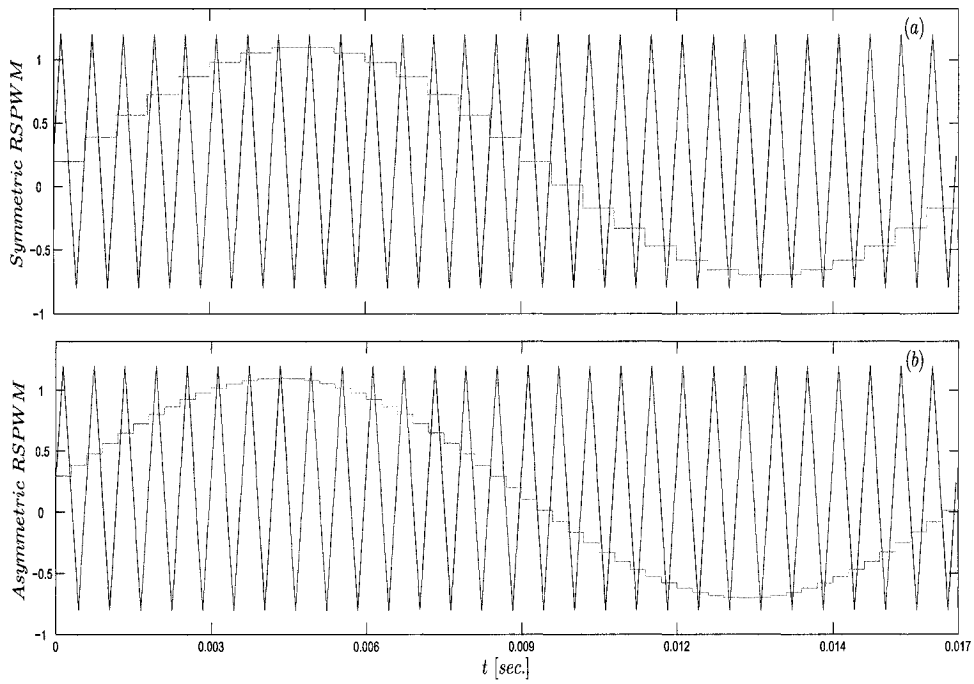

Figure 1.5: The regularly sampled pulse-width modulation (RSPWM) technique: (a) the symmetrical RSPWM and (b) the asymmetrical RSPWM

1.3.2 Pulse-Width Modulation (PWM) Schemes

The advances of power electronics and computer technologies have made operating inverters on high power levels with acceptable quality input/output performance realistic and feasible. However, such requirements are self-contradictory due to the conflicting relation between power handling capacity and switching capabilities of semiconductor switching elements. These additional constraints on

operating inverters have made it necessary to develop new modulation schemes. Among many developed modulation schemes, few have been successfully implemented for industrial applications. These include [1–3]:

1. Specific Harmonic Elimination
2. Non-Sinusoidal Reference-Modulation Signals
3. Hysteresis-Band Current Control
4. Space-Vector Modulation
5. Random PWM

Specific Harmonic Elimination (SHE)

Specific Harmonic Elimination (SHE) is an on-line (pre-calculated) non-carrier based PWM scheme. This scheme is based on the fact that conditions of quarter and half wave symmetry are capable of eliminating even-indexed harmonics. Extending this fact has led to considering angles of switching pulses in the first quarter cycle as variables for optimization in order to eliminate more harmonics from the inverter output. Each angle of switching pulses is considered as one degree of freedom. For each degree of freedom, one harmonic may be set to zero or any other reasonable desired value. Using Fourier transforms, simultaneous equations in these angles are solved given desired values for the fundamental and the targeted harmonics. Examples of switching angles are shown in Figure 1.6.

The output of an inverter can be expressed in the Fourier series form as [1]:

$$V_o(t) = \frac{a_o}{2} + \sum_{n=1}^{\infty} (a_n \cos(n\omega_m t) + b_n \sin(n\omega_m t)) \tag{1.7}$$

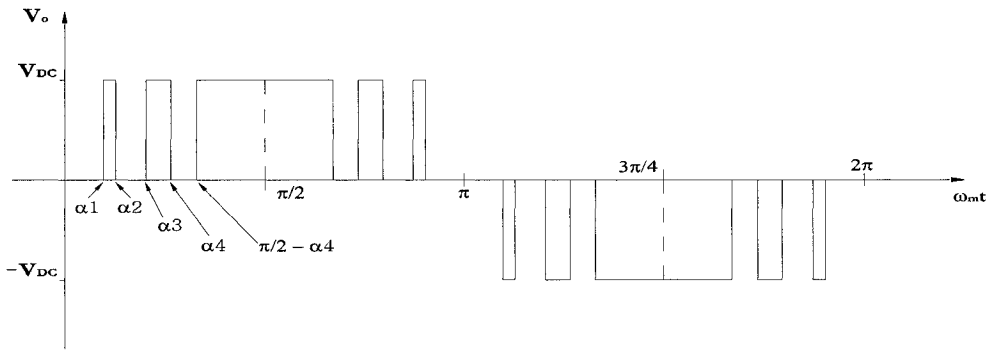

Figure 1.6: An examples of defined switching angles α_1, α_2, α_3 and α_4 for eliminating certain harmonic components.

where $a_o/2$ is the dc component present in $V_o(t)$ and ω_m is the frequency of the fundamental component. The coefficient sets $\{a_n\}$ and $\{b_n\}$ are coefficients of Fourier series [1–3]. The Fourier series form of an inverter output voltage has non-zero odd harmonic coefficients. As a result, equation (1.7) can be reduced to:

$$V_o(t) = \sum_{n=1,3,5,..}^{\infty} b_n \sin(n\omega_m t) \tag{1.8}$$

The coefficient of the n^{th} harmonic can be evaluated for switching angles $\{\alpha_1, \alpha_2, \alpha_3, \alpha_4\}$ as in the following equation [1, 2]:

$$b_n = \frac{2V_{DC}}{\pi}\left(\int_{\alpha_1}^{\alpha_2} \sin(n\omega_m t)d\omega_m t + \int_{\alpha_3}^{\alpha_4} \sin(n\omega_m t)d\omega_m t + \int_{\pi/2-\alpha_4}^{\pi/2} \sin(n\omega_m t)d\omega_m t\right) \tag{1.9}$$

$$b_n = \frac{4V_{DC}}{\pi n}\left[-\cos(n\alpha_1) + \cos(n\alpha_2) - \cos(n\alpha_3) + \cos(n\alpha_4) - \cos(n\pi/2 - n\alpha_4)\right] \tag{1.10}$$

where V_{DC} is the input dc voltage to the inverter. Substituting equation (1.10) into

equation (1.8) produces the inverter output voltage $V_o(t)$ as:

$$V_o(t) = \sum_{n=1,3,5,..} \frac{4V_{DC}}{\pi n} [-\cos(n\alpha_1) + \cos(n\alpha_2) - \cos(n\alpha_3)] \sin(n\omega_m t) + \sum_{n=1,3,5,..} \frac{4V_{DC}}{\pi n} [\cos(n\alpha_4) - \cos(n\pi/2 - n\alpha_4)] \sin(n\omega_m t) \quad (1.11)$$

For the case of selecting four switching angles $\{\alpha_1, \alpha_2, \alpha_3, \alpha_4\}$, four harmonic components (the k^{th}, l^{th}, m^{th} and w^{th}) can be eliminated. Using Fourier series coefficients, four different nonlinear equations are created as [1–6]:

$$b_k = [-\cos(k\alpha_1) + \cos(k\alpha_2) - \cos(k\alpha_3) + \cos(k\alpha_4) - \sin(k\alpha_4)] = 0 \quad (1.12)$$

$$b_l = [-\cos(l\alpha_1) + \cos(l\alpha_2) - \cos(l\alpha_3) + \cos(l\alpha_4) - \sin(l\alpha_4)] = 0 \quad (1.13)$$

$$b_m = [-\cos(m\alpha_1) + \cos(m\alpha_2) - \cos(m\alpha_3) + \cos(m\alpha_4) - \sin(m\alpha_4)] = 0 \quad (1.14)$$

$$b_w = [-\cos(w\alpha_1) + \cos(w\alpha_2) - \cos(w\alpha_3) + \cos(w\alpha_4) - \sin(w\alpha_4)] = 0 \quad (1.15)$$

where $k, l, m, w \in (1, \infty)$. Solving these equations provides the required values of α_1, α_2, α_3 and α_4.

The first research to consider SHE as switching scheme was conducted by Patel and Hoft in 1973-74 [19, 20]. This switching scheme can provide significant improvement of inverter outputs in terms of harmonics presence. However, calculating switching angles needs solving systems of non-linear equations that can complicate its implementation [3, 4].

Early trails to minimize the required computations were made by Enjeti and Lindsay [21]. They proposed a mathematical solution that was based on solving a set of nonlinear transcendental equations to eliminate the undesired harmonics of the inverter output voltage. The proposed solution achieved limited success

due to the slow speed in solving systems of non-linear equations. In 1990, Enjeti, Ziogas and Lindsay developed a PWM technique programmed to eliminate harmonics based on optimizing several predefined quality factors [22]. This approach has reduced the computational burden. However, these predefined quality factors were non-linear functions of load currents and/or inverter output voltages. Maswood, Shen and Rahman [18] have developed a genetic algorithm-based method for determining the optimal switching angles so as to eliminate specific harmonics. The simplicity of on-line implementation of this method has made it advantageous over other previous methods. Liang, OConnell and Hoft [23] developed a Walsh transform-based method for determining the switching angles for selected harmonics elimination. Their method was easy to implement and had smaller computational complexities. Nevertheless, the Walsh transform-based method lacked significant accuracy due to approximating and linearizing transcendental non-linear equations to obtain the required switching angles.

Non-Sinusoidal Reference-Modulation Signals

In general, the fundamental concept of PWM is to compare a sinusoidal reference-modulating signal with a triangular high frequency carrier signal. This process suffers from a major limitation that is the reduced magnitude of the fundamental component of the inverter output voltage [1, 24]. Trzynadlowski [25] classified the PWM switching methods into two basic types, which are:

- The optimal harmonic spectrum, which is oriented to optimizing the harmonics on the output of the inverter
- The application of a certain reference-modulating signal that is a pivotal element of the switching schemes, which is known also as the carrier-based

PWM schemes

In carrier-based PWM, the main function of comparing a carrier signal (either a sawtooth or a triangular) with a reference-modulating signal is to determine the duration and location of each ON switching pulse within one cycle of the carrier signal. The duration of each ON switching pulse contributes to the fundamental component $(V_o)_1$ volt-second average as the reference-modulating signal over that cycle of the carrier signal. On the other hand, the location of each ON switching pulse does not affect the fundamental component volt-second average over any cycle of the carrier signal. This can be interpreted as the effect of the switching scheme on output harmonic components. An index relating the magnitude of the carrier signal to the magnitude of the reference-modulating signal can be defined as a magnitude modulation index m_a as [2–4]:

$$m_a = \frac{\text{Peak of } S_M(t)}{\text{Peak of } S_{SC}(t)} \tag{1.16}$$

The magnitude modulation index m_a can be considered as a gain of the inverter so that the relation between $S_M(t)$ and $V_o(t)$ is linear for $m_a < 1$. However, increasing the modulation index m_a ($m_a \geq 1$) can cause an over-modulation mode of operation, which is known to generate low-frequency base-band distortion [1, 10]. Holmes [26] proposed adding a proper amount of the third harmonic component to the original sinusoidal reference-modulating signal $S_M(t)$ such that any change in widths of the switching pulses will not affect their symmetry around the center of the carrier signal interval. Figure 1.7 shows two reference-modulating signals with and without the addition of the third harmonic component. This switching scheme can improve the output voltage and/or current in terms of harmonic con-

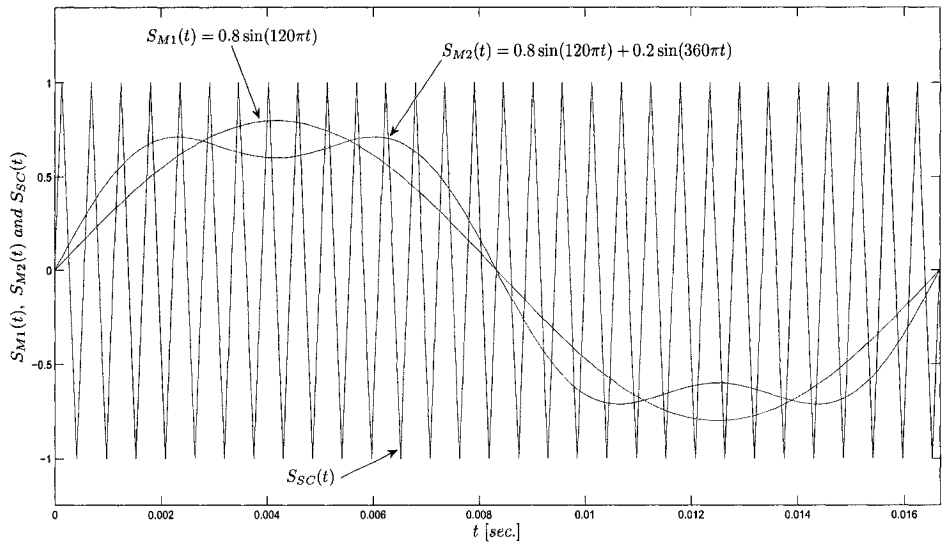

Figure 1.7: The triangular carrier signal (S_{SC}) and two reference-modulating signals (S_{M1} and S_{M2}), S_{M2} has a third harmonic component.

tents. However, there is no defined procedure for determining the proper amount of the added third harmonic component.

Hysteresis-Band Current Control

A hysteresis band switching scheme is based on calculating the error between a reference output and the measured output. States of switching elements are changed when the instantaneous calculated error falls outside a pre-defined hysteresis band so as to drive the error back within that band. Plunckett [27] proposed this switching scheme, where the targeted output was the inverter output current. The early implementations of hysteresis-band current control switching scheme were based on a fixed hysteresis band. Bose [28] developed an adaptive current controller that used a variable hysteresis band. This controller suffered from the stability problems as the load changes.

Rahman *et al.* [29] developed a sinusoidal hysteresis band for current control switching scheme. The sinusoidal hysteresis band was able to limit the maximum switching frequency and improved both output current and voltage of the operated inverter. However, this method requires that the controlled output quantity of the inverter be integrated either by the load or as a part of the controller. Furthermore, the switching instants are not necessarily synchronous or cyclic. Thus, sub-harmonics may be present in inverter outputs. These reasons made the hysteresis band current control switching scheme not very accurate for industrial applications with low switching frequencies. Figure 1.8 shows the two popular types of hysteresis bands.

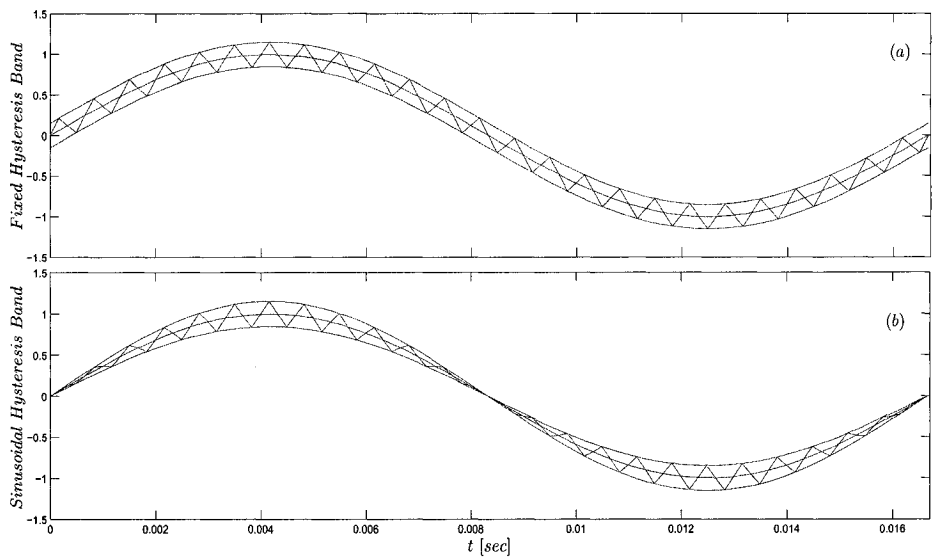

Figure 1.8: Hysteresis bands for current controlled PWM: (a) the fixed hysteresis band and (b) the sinusoidal hysteresis band.

Space-Vector Modulation (SVM)

The previous PWM switching schemes were based on either considering a reference-modulating signal or optimizing switching instants. Another successful approach is to center switching pulses for each leg of three-phase power inverters within each half carrier signal cycle. This approach not only ensures that the maximum possible modulation of an inverter can be achieved, but also it results in significant elimination of harmonics from the output of a three-phase inverter [1, 2]. In mid 1980's Holtz and Stadtfeld [30] introduced a new scheme of PWM, which is based on considering all possible combinations of a three-phase inverter switching elements states known as the space vector modulation (SVM). SVM-PWM scheme has been a subject of extensive research, where all possible switching combinations are converted to stationary vectors in the $d-q$ complex plane. Eight different switching combinations were introduced; only two of them represented short circuit on the output, hence they were dropped from effective switching combinations. Figure 1.9 shows the switching combinations of a three-phase SVM-PWM inverter.

These SVM switching schemes have shown significant advantages over other PWM switching schemes in terms of implementation, harmonic contents and output voltage fundamental component [1, 2]. Figure 1.10 shows a sample pulse pattern of SVM-PWM in the first sextant [1].

There are some researchers who claim that the SVM-PWM scheme is an independent switching scheme. However, Lipo and Holmes [1] as well as Bowes and Lai [2] have proved that the SVM is simply a variation of regular sampled PWM

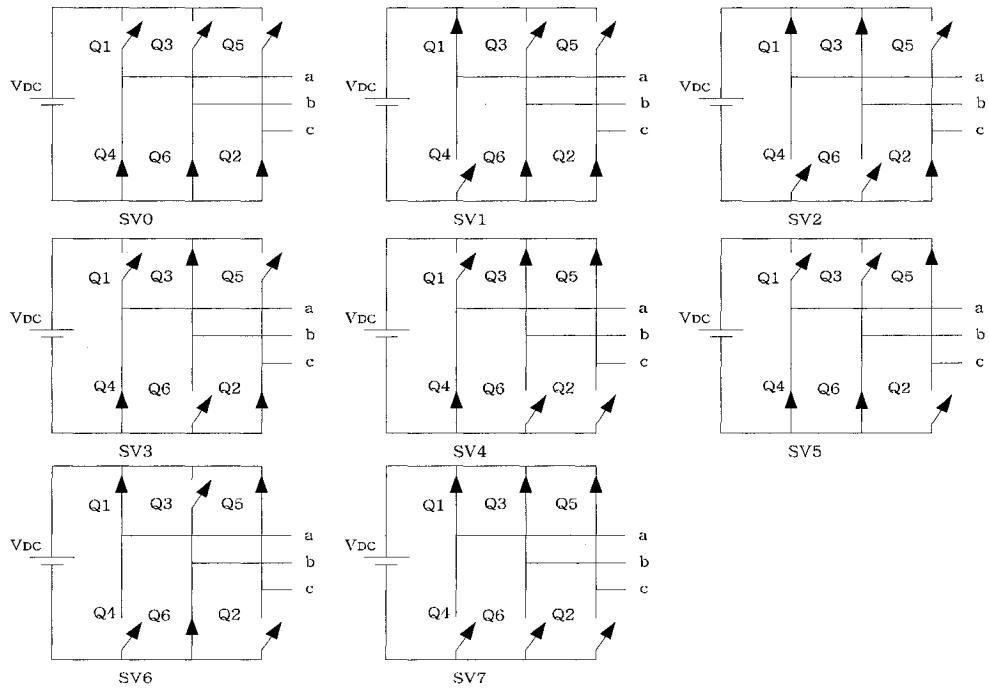

Figure 1.9: The eight different possible switching combinations of a three-phase six-pulse inverter.

with switching pulses placed in a different way over each carrier interval.

Random PWM (RPWM)

The random PWM is a new PWM switching scheme introduced by Trzynadlowski *et al.* [31] to spread the energy concentrated in output harmonic components over a wide range of frequencies to minimize their effects. The RPWM switching scheme is based on adding a random noise to the carrier signal such that the energy concentrated in the switching noise is spread over a wide frequency band. It is carried out in such a way that the impact of output harmonic components is decreased. Hui *et al.* categorized the RPWM switching scheme as one of the following forms [32]:

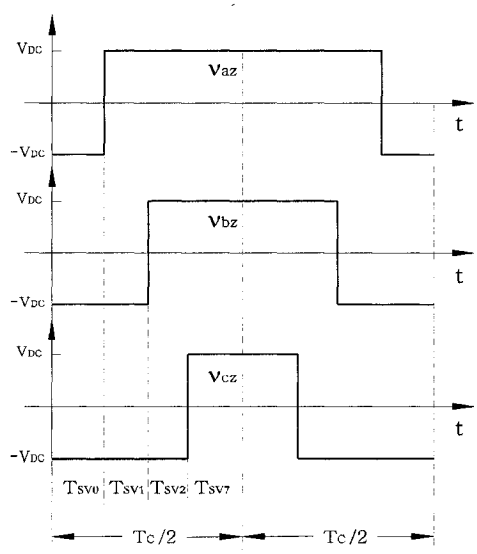

Figure 1.10: Pulse pattern of space-vector modulation (SVM) in the first sextant, $0 \leq \theta_m \leq \pi/3$ with centered active space vectors [1]. T_{SV0} is the time interval of the switching combination $SV0$, T_{SV1} is the time interval of the switching combination $SV1$, T_{SV2} is the time interval of the switching combination $SV2$ and T_{SV7} is the time interval of the switching combination $SV7$,

1. Randomized switching frequency

2. Randomized pulse position

3. Random switching

4. Combinations of previous three methods

RPWM switching scheme is capable of limiting effects of some of the output harmonics. Nevertheless, the nature of the required random signals can cause reduction of the energy concentrated in the desired output frequency. Furthermore, there is no systematic description of the required random signal magnitude, frequency or phase.

Different modulation techniques have been developed and tested to operate power inverters. Moreover, several improvements and modifications have been applied on such techniques to further enhance their performance. In general, these techniques aimed to operate power inverters to achieve the following:

- AC voltages and currents obtained on the output side;
- The produced voltage and current to be as close to sinusoidal waveforms as possible;
- Minimum energy transfered to the load through harmonic components;
- Minimum energy losses through switching elements;
- Stable operation regardless of operating power, nominal voltage, load type, desired output frequency variation or switching frequency.

Theoretical analysis and numerical simulations along with close experimental results can provide the basis for evaluating the performance of modulation techniques reviewed in this section. Although, some of the reviewed techniques have made significant contributions, others are still under investigation to improve and optimize their performances. Moreover, achieved contributions by various switching schemes have been validated under assumptions of load types and/or specific inverter topology.

1.3.3 Delta Modulation

The delta modulation (DM) technique is based on approximating the reference-modulating signal by sinusoid piece-wise linear segments. Each one of such segments is compared to the reference-modulating signal to determine the increase

or decrease in its relative amplitude. Only the change in amplitude is considered for changing the state of the modulated signal [12]. In DM modulation technique, pulse widths are not modulated rather they have constant widths. The correct terminology for such a modulation technique is pulse density modulation (PDM) or pulse frequency modulation (PFM). The DM technique is known as the simplest method for quantizing analog signals into digital sequences of data with significant accuracy. This accuracy can be achieved by using switching frequencies much higher than the frequency of the reference-modulating signal [33]. Figure 1.11 shows simple DM multi-switching signals generated through quantizing a sinusoidal reference-modulating with a sampling interval of 0.00001 second, while the quantizer period is around 0.0375 second.

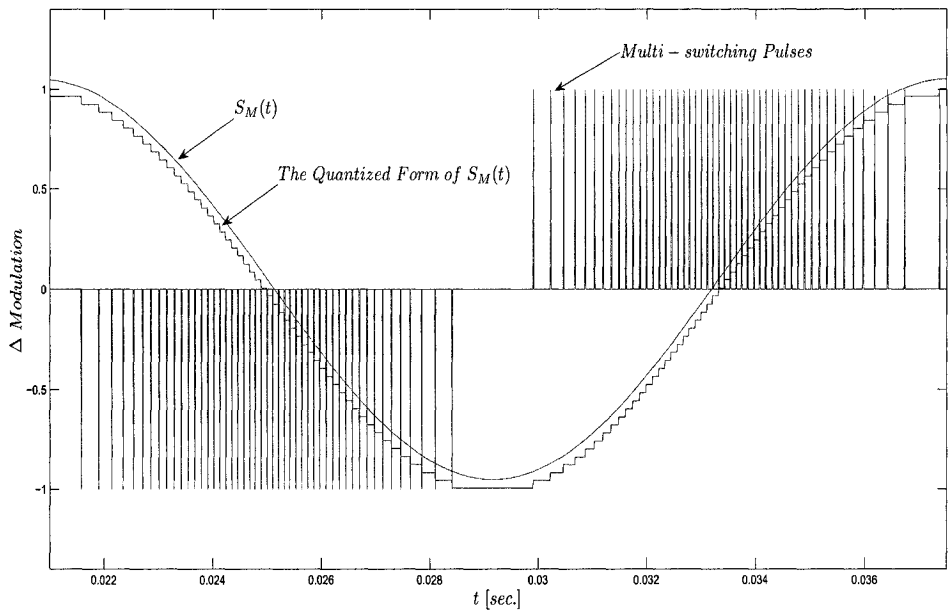

Figure 1.11: The quantization of the reference-modulating signal and the generated pulses as segment heights change.

The harmonic spectra of outputs obtained using different implementations of

both pulse-width and delta modulated inverters show that certain harmonics form side-bands around multiples of the carrier signal frequency f_c. An almost identical pattern of such frequency sidebands is formed when a band limited signal is sampled with a sampling frequency f_c. Such close spectra of the inverter output and the sampled band limited signals can help in developing a new model for inverters.

The earlier research being conducted about power inverters has been mainly elaborating a basic modeling approach that considers a power inverter as a supply-to-load entity. This approach has led to the common assumption of load dominant models where instantaneous switching actions are averaged over pre-defined time intervals. Another approach to model inverters is based on logic-type switching actions, which expresses states of switching elements as ON $\rightarrow$ 1 and OFF $\rightarrow$ 0 [1]. These modeling approaches can not help in anticipating impacts on the inverter outputs under changing switching process. Also, these models are based on considering only the fundamental frequency components of the inverter outputs, while ignoring other harmonic components. The aforementioned modeling approaches have been found very difficult to correlate with any modulation technique that caused extra limitations on the inverter performance. Thus, there exists a need to develop a new inverter model that can provide a new and better modulation technique.

This section has provided a review of the different techniques used in operating inverters. Furthermore, it highlighted the performance limitations of these techniques, in particular, the harmonic contents of the inverter outputs. There is a need for a modulation technique capable of operating inverters to meet increasing demands for high quality outputs. The key for developing such a modulation technique lies in the successful correlation with an accurate and a valid inverter model,

which considers the inverter instantaneous switching actions as a main part. A modulating technique incorporating this unique correlation is unreported in literature and developing and testing such a modulation technique would be a major contribution to the fields of power electronics and signal processing.

1.4 Thesis Outline

Chapter 2 provides a review of the sampling theorem, different sampling forms and mathematical relations between discrete and continuous domains. The classical sampling theorem and the latter extensions along with relation between sampling-reconstruction concept and the approximation theory are presented. In addition, the sampling theorem in the context of multiresolution analysis and wavelet theory is reviewed.

The non-uniform recurrent sampling-based model of 1ϕ inverters is developed in chapter 3. This model will be tested for the conventional SPWM inverter to investigate its validity and accuracy for different operating conditions. Also, the inverter sampling-based model will be extended to model three-phase inverters. Some simulation results will be presented for demonstration and comparison purposes.

Chapter 4 introduces a non-dyadic MRAs for supporting a recurrent non-uniform sampling-reconstruction process. Also, this chapter presents a novel method of designing wavelet basis function for constructing non-dyadic MRAs. This method is used to define a scale-based linearly-combined wavelet basis function for inverter modulation. In addition, chapter 4 describes the proposed wavelet modulation technique and develops an algorithm for implementing it.

Simulating the proposed wavelet modulation techniques using MATLAB is

presented in chapter 5. These simulations include both static and dynamic loads for different output frequencies. Also, chapter 5 presents comparison results for the WM inverters with a conventional SPWM ones under same loading conditions.

Chapter 6 develops a real-time implementation of the wavelet modulation technique for experimental testing. The wavelet modulation technique algorithm is realized using a $Turbo - C$ code for the $dSPACE\ ds1102$ controller board. Experimental tests are carried out on a single-phase voltage-source four-pulse $IGBT$ inverter for different loads and output frequencies.

A new control strategy for adjusting the outputs of WM inverters is introduced in chapter 7. This control strategy is called the resolution-level control, and is based on changing the scale of the generated switching pulses. Moreover, chapter 7 develops an algorithm for implementing the resolution-level control strategy for simulation and experimental tests. Results for several simulation and experimental tests representing different load types with different operating conditions are provided.

Chapter 8 introduces an extension of the wavelet modulation technique to operate three-phase inverters. A procedure for implementing the three-phase wavelet modulation is developed for both simulation and experimental tests. Furthermore, chapter 8 provides simulation and experimental test results for a $3\phi\ R - L$ load.

The last chapter, chapter 9, summarizes and concludes the research work. Also, it provides a description of the main contributions and future scopes of this work in various avenues.

Chapter 2

Sampling Theorem, Multiresolution Analysis and Wavelet Sampling

2.1 General

There has been extensive research devoted to the sampling theorem, with the most important piece of work being the classical sampling theorem. The classical sampling theorem, also known as Whittaker-Kotelńikov-Shannon (WKS) theorem [34], states that a low pass signal continuous-time (CT) band-limited to a frequency band of $(-f_0, f_0)$ can be reconstructed perfectly from its samples taken uniformly at no less than the Nyquist rate of $2f_0$ samples/sec. Another alternative condition for successful sampling and reconstruction of CT band-limited signals was introduced in terms of constraining the lower bound on the sampling density for perfect reconstruction [35]. According to the classical WKS sampling theorem, a CT signal $x_c(t)$ band-limited to $(-\Omega_0, \Omega_0)$, such that $X_c(\Omega) = 0, |\Omega| > \Omega_0$ $(\Omega_0 = 2\pi f_0)$, can be perfectly recovered from samples spaced by T_s $(T_s \leq \pi/\Omega_0)$

[34, 35]. It is to be noted that $X_c(\Omega)$ is the continuous time Fourier transform (CTFT) of $x_c(t)$ as:

$$X_c(\Omega) = \int_{-\infty}^{\infty} x_c(t) e^{-j\Omega t} dt \tag{2.1}$$

The ideal sampled version of $x_c(t)$ is a sequence of discrete points located at multiples of the sampling period T_s, and can be defined as:

$$x[n] = \sum_n x_c(t)\delta(t - nT_s) \tag{2.2}$$

Ideal Reconstruction of the CT signal from its samples ($x[n]$) can be done as:

$$x_c(t) = \sum_n x[n] \operatorname{sinc}(t - nT_s) \tag{2.3}$$

where $\operatorname{sinc}(t) = \sin(\pi t)/\pi t$. This form of sampling is known as the uniform (periodic) sampling. It should be noted that there are other forms of sampling that employ a non-uniform sampling approach. Such sampling forms have been employed in many areas of signal and image processing applications [36].

2.2 Sampling Theorem- A Brief History

There have been several interpretations of the classical sampling theorem. One of these interpretations was developed by Whittaker, which was based on the idea that a sequence of points does not uniquely define a signal or a function. Whittaker called all functions that might be defined by the same sequence of points a co-tabular set of functions. Among these co-tabular functions, the function of the lowest harmonic constituents was called a cardinal function. This cardinal

function can be defined as follows [37]:

Let $f : \mathbb{R} \rightarrow \mathbb{R}$ be a function, and $T_s > 0$, then a cardinal series of f with respect to T_s can be defined as:

$$C(f, t, T_s) = \sum_{n=-\infty}^{\infty} f(nT_s) \frac{\sin \pi \frac{(t-nT_s)}{T_s}}{\pi \frac{(t-nT_s)}{T_s}} \tag{2.4}$$

If this series converges, it is known as the cardinal function of $f(t)$. Also, when $C(f, t, T_s)$ converges to $f(t)$ it is named the Whittaker cardinal function of $f(t)$. The cardinal series interpolates between equidistant values of $f(t)$ that can be interpreted as one form of approximating the continuous version of $f(t)$, provided that $f(t)$ is band limited to π/T_s. Hence, sampling-reconstruction process can be seen as an approximation case: given a sequence of data (samples of a CT band-limited signal $x_c(t)$), approximate this signal using these data points as accurately as possible.

In 1977, Papoulis proposed an extension of WKS classical sampling theorem, showing that a band-limited signal $x_c(t)$ could be reconstructed accurately from samples taken from responses of m ideal linear shift-invariant systems at a rate of $1/m$ of the Nyquist rate. This generalization was the first introduction to non-uniform sampling and reconstruction. Also, this generalization indicated that there are many possible ways of extracting data from a signal for a complete characterization other than the conventional uniform sampling [37].

If the Fourier transform is applied to equation (2.2), and using the fact that the Fourier transform of $\mathrm{sinc}(t)$ is the characteristics function $\chi_{[-1/2,1/2]}$ (a rectangular box function extending from -1/2 to 1/2), then for any $\lambda \in [-1/2, 1/2]$ [35]

$$X(\lambda) = \sum_n x[n]e^{-j2\pi n\lambda} = \sum_n \left\langle X, e^{-j2\pi n\lambda} \right\rangle_{L^2(-1/2,1/2)} e^{-j2\pi n\lambda} \tag{2.5}$$

where $\left\langle X, e^{-j2\pi n\lambda} \right\rangle$ is the inner product operation and is defined by:

$$\langle p_1[n], p_2[n] \rangle = \sum_n p_1[n]p_2^*[n] \tag{2.6}$$

If the frequency variable ω is related to the variable λ by $\lambda = \frac{\omega}{2\pi}$, then equation (2.5) becomes the discrete-time Fourier transform (DTFT) of $x[n]$. The DTFT of a band limited discrete signal $d[n]$ can be defined as:

$$D(\omega) = \sum_{n=-\infty}^{\infty} d[n]e^{-jn\omega} \tag{2.7}$$

where $D(\omega)$ is the DTFT of $d[n]$. It is to be noted that the frequency variable ω represents radian frequencies present in a discrete signal, while the frequency variable Ω represents radian frequencies present in continuous signals. These two frequency variables are related to each other through the sampling time T_s as:

$$\Omega = \frac{\omega}{T_s}, \quad \Omega \in \left[\frac{-\pi}{T_s}, \frac{\pi}{T_s}\right] \tag{2.8}$$

Reconstructing the signal $x_c(t)$ using equation (2.3) is equivalent to the fact that the set $\left\{e^{j2\pi k\lambda}, k \in \mathbb{Z}\right\}$ forms an orthonormal basis of $L^2(-1/2, 1/2)$, where L^2 here is the space of absolutely summable DT functions. This set of orthonormal basis functions is called harmonic Fourier basis functions. This equivalence between reconstructing signals from their uniform samples and the harmonic Fourier basis has been extended by Paley and Wiener to process certain cases of non-uniform

sampling-reconstruction of band-limited signals [38, 39]. The next section presents some common forms of sampling that include uniform as well as non-uniform sampling forms.

2.3 Sampling Forms

Discrete-time signals can arise in different ways, but the most common way is the representation of continuous-time signals. It is remarkable that under reasonable conditions and constraints, a continuous-time signal is accurately represented by its values at discrete points in time. These points in time are selected so that the sampled continuous-time signal can be recovered perfectly without any distortion or loss of information. Two forms for selecting time instants are commonly used in signal processing applications, uniform sampling and non-uniform sampling. In the uniform sampling, time instants are selected with equidistant spacings. On the other hand, non-uniform sampling involves selecting time instants with variable spacings [37]. Figure 2.1 shows a signal $x_c(t)$ sampled both uniformly and non-uniformly.

The following subsections provide more insight about these sampling forms.

2.3.1 Uniform Sampling

Uniform sampling, also known as periodic sampling, is the most common form of sampling that is used in a wide range of signal and image processing applications. Moreover, all mathematical approaches of the sampling theorem were initially developed considering the uniform sampling. In this sampling form, samples are taken at a constant rate resulting in a constant spacing between successive samples

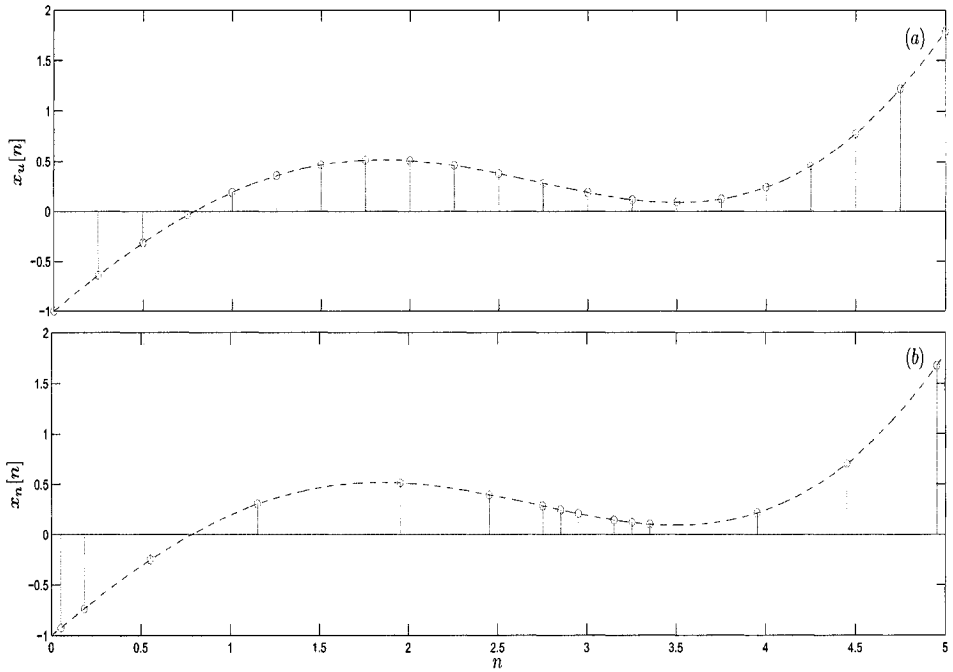

Figure 2.1: Sampling a continuous signal $x_c(t)$: (a) in a uniform sampling manner $x_u[n]$ and (b) in a non-uniform sampling manner $x_n[n]$.

[34–37, 39].

Let $x_d[n]$ be the sampled form of a band limited signal $x_c(t)$, where $x_c(t) \in \mathcal{B}^2_{2\Omega_o}(\mathbb{R})$. The space $\mathcal{B}^2_{2\Omega_o}(\mathbb{R})$ is the space of all signals band limited to Ω_o, and is defined as:

$$\mathcal{B}^2_{2\Omega_o}(\mathbb{R}) = \left\{x_c(t) \in L^2(\mathbb{R}) : \sup(X_c(\Omega)) \subseteq [-\Omega_o, \Omega_o]\right\} \tag{2.9}$$

A discrete signal $x_d[n]$ is defined by samples taken with an equidistant spacing of T_s such that.

$$\forall n, n \in \mathbb{Z}, x_d[n] = x_c\left(nT_s\right) \tag{2.10}$$

The equidistant samples can be created by using a train of impulses located at

integer multiples of T_s. Such a train of impulses can be defined as:

$$p(t) = \sum_{n=-\infty}^{\infty} \delta\left(t - nT_s\right) \tag{2.11}$$

where $\delta(t)$ is the Dirac delta function, defined by the following properties:

- Unit area:

$$\int_{-\infty}^{\infty} \delta(t)dt = 1 \tag{2.12}$$

- Sifting property: for a function $f(t)$ continuous at $t = \tau$

$$\int_{-\infty}^{\infty} f(t)\delta(t - \tau)dt = f(\tau) \tag{2.13}$$

Let $x_s(t)$ be defined as: for $x_c(t)$ continuous at all $t = nT_s$

$$x_s(t) = x_c(t).p(t) = x_c(t) \sum_{n=-\infty}^{\infty} \delta\left(t - nT_s\right) \tag{2.14}$$

using the sifting property of $\delta(t)$, $x_s(t)$ becomes:

$$x_s(t) = \sum_{n=-\infty}^{\infty} x_c\left(nT_s\right)\delta\left(t - nT_s\right) \tag{2.15}$$

The discrete signal $x_d[n]$ can be defined as:

$$x_d[n] = \int_{nT_s-\epsilon}^{nT_s+\epsilon} x_s(t)dt, \quad \epsilon \in [0, T_s] \tag{2.16}$$

Figure 2.2 shows $x_c(t)$, $p(t)$, and $x_d[n]$, while Figure 2.3 shows $|X_c(\Omega)|$ and $|X_d(\omega)|$.

From Figure 2.2 and Figure 2.3, it can be shown that if the spacing between

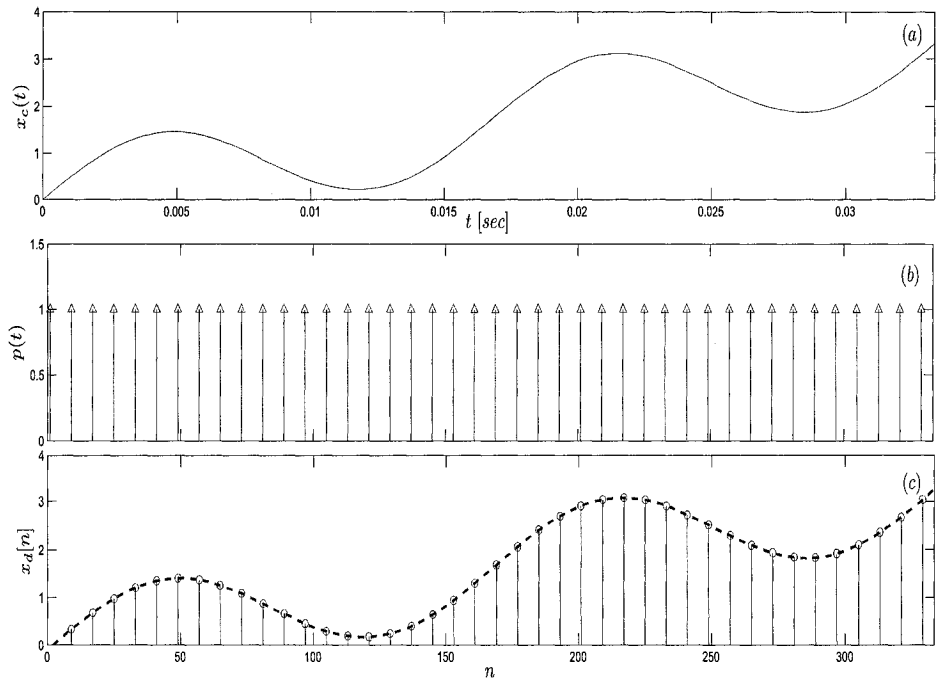

Figure 2.2: Sampling a continuous-time signal $x_c(t)$: (a) the continuous time signal $x_c(t)$, (b) the train of impulses $p(t)$ and (c) the discrete signal $x_d[n]$.

cent samples is large (so that the sampling rate is low), then replicas of the sampled signal spectrum (as shown in Figure 2.4) will overlap. Such an overlap is known as the aliasing, and it prevents recovering the continuous-time signal $x_c(t)$ perfectly from its samples. The aliasing can be avoided if the spacing between the adjacent samples is less than a value known as the Nyquist rate T_Q. In general, the Nyquist rate is related to the highest frequency component present in the continuous-time signal such that:

$$T_Q \leq \frac{1}{2f_{hst}} \implies f_Q \geq 2f_{hst} \tag{2.17}$$

where f_{hst} is the highest frequency component present in $x_c(t)$ in cycles/sec. and f_Q is the Nyquist frequency. If the Nyquist condition is met, then the continuous-

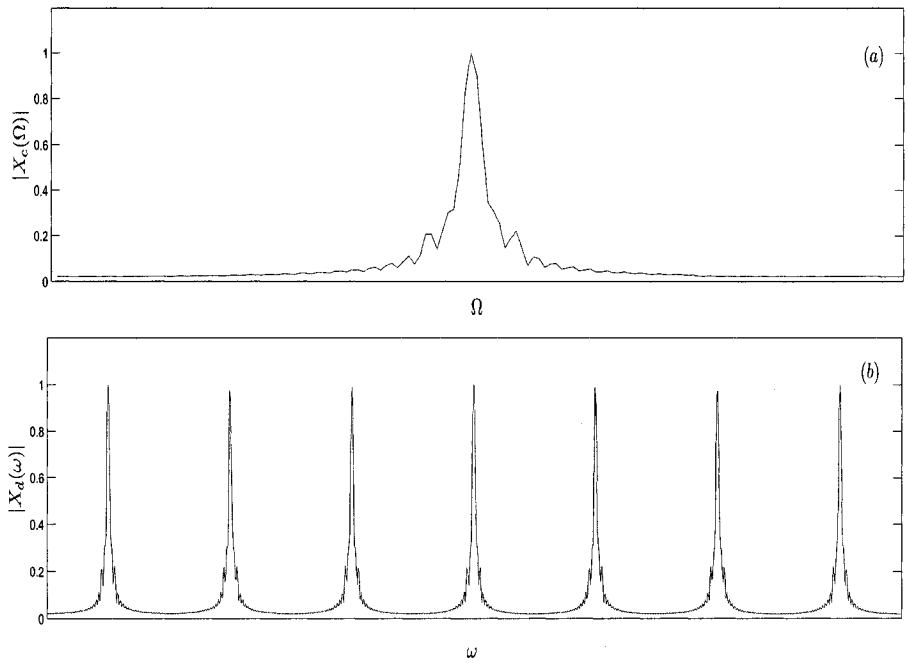

Figure 2.3: Sampling a continuous-time signal $x_c(t)$: (a) the magnitude of the CTFT of the signal $x_c(t)$: $X_c(\Omega)$ and (b) the magnitude of the DTFT of the sampled signal $x_d[n]$: $X_d(\omega)$.

time signal $x_c(t)$ can be recovered perfectly from its samples. This perfect recovery is represented using a low-pass filter with a cut-off frequency of $\Omega_{CF} = \frac{\Omega_s}{2}$. Figure 2.4 shows a typical low pass filter ($H_{rec}(\Omega)$) to recover $x_c(t)$ and an aliasing case.

2.3.2 Non-uniform Sampling

A uniform sampling case turns into a non-uniform sampling one if T_s fails to remain constant. This condition implies that the spacing between adjacent samples will no longer be constant. This non-uniform sampling form can be found in some engineering and geophysics data acquisition applications [40, 41]. Although, non-uniform sampling is the norm rather than the exception, it has not received the same attention as the uniform sampling in signal and image processing applica-

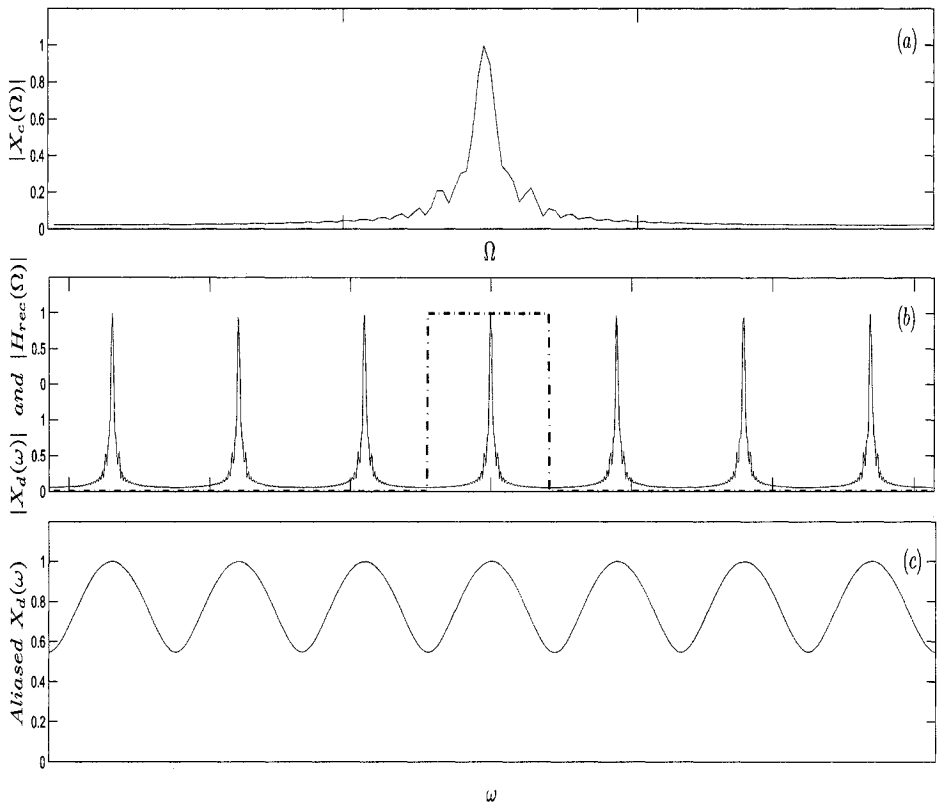

Figure 2.4: Recovering $x_c(t)$: (a) $|X_c(\Omega)|$ (the CTFT of the signal $x_c(t)$), (b) $|X_d(\omega)|$ (the DTFT of the discrete signal $x_d[n]$) and a low pass filter and $H_{rec}(\Omega)$ and (c) an aliased version of $|X_d(\omega)|$.

tions. One of the main reasons for the lack of attention to the non-uniform sampling is the difficulty encountered when performing the Fourier analysis. For example, sequences with non-equidistant samples affect the convergence of the infinite series required for applying Fourier analysis [40, 42]. From a theoretical point of view, the non-uniform sampling problem has inspired many deep but mostly not constructive theorems. However, there exist some algorithms for approximating or reconstructing one-dimensional and two-dimensional band limited signals from their non-uniform samples. These algorithms include polynomial and spline

methods [39–41].

The first theoretical approach to processing signals with non-uniform samples based on the theory of non-harmonic Fourier series was developed by Paley and Wiener [38] and Levinson [43]. Later in 1952, Duffin and Schaeffer presented the frame theory, which gave rise to further theoretical statements and some powerful algorithms for non-uniform sampling [44]. The most popular work in this aspect was the theory developed by Levinson that is based on *Lagrange interpolation functions* such that [39, 43]:

Let $h(t)$ be an entire function with zeros only at $\{t_n : n \in \mathbb{Z}\}$ defined as [40]:

$$h(t) = (t - t_o) \prod_n \left(1 - \frac{t}{t_n}\right) \left(1 - \frac{t}{t_{-n}}\right) \tag{2.18}$$

where t_o is an arbitrary reference point. Using the defined Lagrange interpolation function $h(t)$, a band limited signal can be expanded using these functions. In other words, a band limited signal can be recovered from its non-uniform samples using this type of interpolation functions such that [40, 43]:

$$x_c(t) = \sum_{n \in \mathbb{Z}} x_c(t_n)\, h(t_n) \tag{2.19}$$

There are two main disadvantages of this interpolation type [40, 44]:

1. The numerical computations required by this method are sometimes complex and cannot be easily implemented.

2. If one sample is lost, the whole recovered signal may be affected.

The focus in this thesis will be on band limited signals, where more efficient algorithms are developed. One of the popular approaches is the lower uniform

Beurling density condition [37, 40, 41, 43, 44]. In this approach, if a set of non-uniform samples $\{x_n\}_{n\in\mathbb{Z}}$ generates a frame $\{T_{x_n}\,\mathrm{sinc}_{\Omega_o}\}_{n\in\mathbb{Z}}$ for $\mathcal{B}^2_{\Omega_o}(\mathbb{R})$, then [40, 41]:

$$\Delta\left(\{x_n\}\right) > 2\Omega_o \tag{2.20}$$

where $\{T_{x_n}\,\mathrm{sinc}_{\Omega_o}\}$ is given by:

$$\{T_{x_n}\,\mathrm{sinc}_{\Omega_o}\} = \delta\left(x - x_n\right) * \mathrm{sinc}(x),\ \text{with}\ \mathrm{sinc}(x) \overset{CTFT}{\longleftrightarrow} \chi_{[-\Omega_o,\Omega_o]} \tag{2.21}$$

Also, $\Delta\left(\{x_n\}\right)$ is defined as [40]:

$$\Delta\left(\{x_n\}\right) = \lim_{r\to\infty} \frac{\beta(r)}{r} \tag{2.22}$$

where r is an interval and $\beta(r)$ is given by:

$$\beta(r) = \inf_r \beta_r \tag{2.23}$$

where β_r is the minimal number of samples in the interval r.

The above approach simply describes non-uniform samples with spacings between them such that the minimum spacing between them satisfies the Nyquist condition [43]. As a result, if a set of non-uniform samples satisfies the above condition, then recovering a signal from that set of samples is possible [39, 41, 43]. One of the most pertinent cases of non-uniform sampling is the case when a set of non-uniform samples can be divided into subsets with a condition that the number of these subsets is finite such that [36, 40]:

$$|t_n - t_m|_k > \alpha_k, \quad m \neq n, \quad m,\ n \in \mathbb{Z},\ k < \infty \tag{2.24}$$

where $\{\alpha_k\}_{k\in\mathbb{Z}} > 0$. This condition is known as the relative separation principle [39, 49], which defines the condition over the spacing between samples in each subset k. If there are sets of separable non-uniform samples, then there exists a lower uniform Beurling density condition [37, 40, 41, 43, 44]. Moreover, if such sets have a repetitive nature (periodicity), then this type of non-uniform sampling becomes the non-uniform recurrent sampling. The next section presents this type of non-uniform sampling.

2.4 Non-uniform Recurrent Sampling

In some practical applications, aliasing can cause problems in recovering periodic signals from their uniform samples. One of the possible methods to avoid such problems is using the non-uniform sampling, in particular, the non-uniform recurrent sampling. In this form of sampling, non-uniform samples are divided into groups (subsets) of N samples each. These sample groups have a recurrent period of T, which can be related to N by [36]:

$$T = NT_Q \tag{2.25}$$

where T_Q satisfies:

$$T_Q \leq \frac{T_m}{2} \tag{2.26}$$

The case when non-uniform samples have a minimum spacing that satisfies the Nyquist condition, the recovery of the signal from such samples is possible. This case has been described by the lower uniform Beurling density approach that has been mentioned in section 2.3. Also, the case when non-uniform samples can be

divided into a finite number of subsets as in equation (2.24) can be employed for recovering signals from their non-uniform recurrent samples. The locations of non-uniform recurrent samples in the sample group (subset) d can be stated as $\{t_p\}_{p=0,1,2,\cdots,N-1}$ relative to a start time for that group [36].

If the non-uniform recurrent samples of the signal $x_c(t)$ satisfy the lower uniform Beurling density condition, then it can be recovered from these samples provided the average sampling period is smaller than the Nyquist rate. The average sampling period for the case of non-uniform recurrent sampling can be defined as [36]:

$$T_{avg} = \lim_{n\to\infty} \frac{t_n - t_{n-1}}{n} \tag{2.27}$$

Figure 2.5 shows a band limited signal sampled in a non-uniform recurrent manner.

Recovering the signal $x_c(t)$ from its non-uniform samples located at $\{t_p\}$ can be done using Lagrange interpolation functions as [36, 40]:

$$x_c(t) = \sum_{n=-\infty}^{\infty} x_c(t_n) \frac{G(t)}{G'(t_n)(t - t_n)} \tag{2.28}$$

where

$$G(t) = (t - t_o) \prod_p \left(1 - \frac{t}{t_p}\right) \tag{2.29}$$

and

$$G'(t_n) = \frac{dG(t)}{dt}|_{t=t_n} \tag{2.30}$$

The recovery of a signal from its samples (uniform or non-uniform) can be carried out using interpolation processes implemented using filter banks. One of the most efficient structures of filter banks is the quadrature-mirror filter banks, which

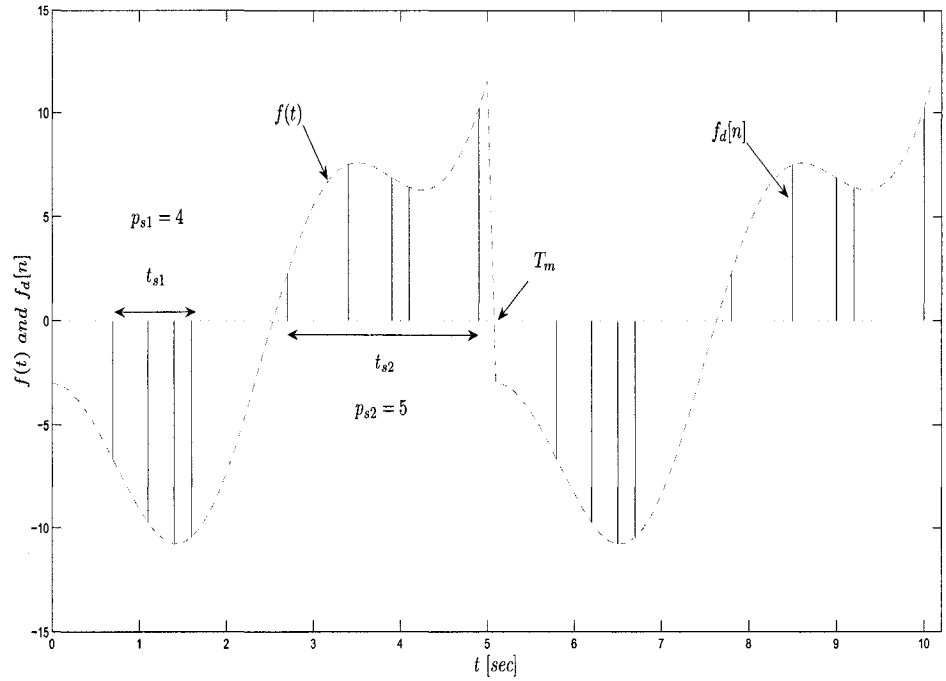

Figure 2.5: Sampling a continuous-time signal $f(t)$ in a non uniform recurrent manner using two sample groups at each period.

can define a multiresolution analysis-synthesis structure. The next section introduces the relation between sampling a band-limited signal and a multiresolution analysis carried out on the same signal.

2.5 Sampling Process as a Multiresolution Analysis (MRA)

The classical WSK sampling theorem and its application have been the subject of extensive research by mathematicians and signal processing engineers during the last 5 decades. This section reviews the research that led to the multiresolution analysis representation of the sampling-reconstruction process.

An important extension to the basic sampling theorem was contributed by Kramer who proposed the use of generalized integral transforms rather than using the Fourier transform only. This proposed integral transform takes the following mathematical form [40–42]:

$$X(\Omega) = \int_I \rho(t) K^*(\Omega, t) x_c(t) dt \tag{2.31}$$

where $X(\Omega)$ is a square-integrable function and $K(\Omega, t)$ is a complete orthogonal set on the integration interval I, $\rho(t)$ is a function such that $\rho(t) \in L^2(I)$ and the (*) denotes a complex conjugate. It can be shown that the Fourier transform is a special case by setting $\rho(t) = 1$ and $K(\Omega, t) = e^{j\Omega t}$ or $K^*(\Omega, t) = e^{-j\Omega t}$ [40–44]. This extension generalized the sampling theorem so that the sampling expansion of a band limited signal $x_c(t)$ can be expressed as [45]:

$$x_c(t) = \lim_{N \to \infty} \sum_{|n| \leq N} x(t_n) S_n(t) \tag{2.32}$$

where $S_n(t)$ is an interpolating function given by [39]:

$$S_n(t) = S(t, t_n) = \frac{\int_I \rho(\Omega) K^*(\Omega, t_n) K(\Omega, t) d\Omega}{\int_I \rho(\Omega) |K(\Omega, t_n)|^2 d\Omega} \tag{2.33}$$

Kramer's extension provided a general representation of a CT signal by its samples at $t = t_n$ regardless of these time instants being equidistant or not.

Kramer's extension has led to an important interpretation of the sampling process that can be stated as: sampling a CT signal $x_c(t)$ $(x_c(t) \in \mathcal{C}_b[0, T_s])$ is equivalent to extracting a set of N real-valued parameters from that signal $x_c(t)$. The space $\mathcal{C}_b[0, T_s]$ is a space of continuous and bounded functions on $[0, T_s]$. The span

of a collection of N linearly independent basis vectors $\{\nu_1, \nu_2..., \nu_N\}$ $(\nu_k \in \mathcal{C}_b[0, T_s])$ will create an N-dimensional subspace of $\mathcal{C}_b[0, T_s]$ [40–43]. Furthermore, if the real-valued parameters are considered weights to these basis vectors, any vector in this subspace can be expressed as: [38–44].

$$\hat{x} = \sum_{k=1}^{N} c_k \nu_k, \quad c_k \in \mathbb{R} \tag{2.34}$$

where the set $\{c_k\}$ represents the projection of $\hat{x}$ on individual subspaces spanned by the basis vectors.

The vector $\hat{x}$ can be considered a reconstruction of the signal $x_c(t)$. Such an interpretation is basically an approximation of $x_c(t)$ in the N-dimensional subspace V of $\mathcal{C}_b[0, T_s]$. Moreover, highly accurate reconstruction can be achieved if the signal $x_c(t)$ lies in the subspace V [38–41]. Walter [47] generalized the idea of reconstructing a signal as a form of an approximation problem and developed this type of N-dimensional approximation problem in a multiresolution approximation layout.

The classical sampling theorem can be interpreted in terms of an orthogonal projection of the sampled signal onto a function subspace V. A set of band limited continuous-time signals $\{\mathcal{CT}(t)\}$ can be expressed as [44–46]:

$$\{\mathcal{CT}(t)\} \subseteq \mathcal{B}^2_{2\Omega_o}, \quad \Omega_o > 0 \tag{2.35}$$

If the spacing between samples is a such that $0 < a \leq \frac{\pi}{\Omega_o}$, then any CT signal $x_c(t) \in \{\mathcal{CT}(t)\}$ can be perfectly recovered using [47, 52]:

$$x_c(t) = \sum_{k=-\infty}^{\infty} x_c(ka) Sa_{s;a}(t - ka) \tag{2.36}$$

where $Sa_{s;a}(t)$ is the Shannon sampling function given by

$$Sa_{s;a}(t) = \frac{\sin\left(\pi \frac{t}{a}\right)}{\pi \frac{t}{a}} \tag{2.37}$$

Equation (2.36) has two implications:

1. The spacing between successive samples a has to be $a > 0$.

2. The signal $x_c(t)$ has constant values at $ka,\ k \in \mathbb{Z}$.

These implications indicate that the summation of equation (2.36) is finite and it converges to $x_c(t)$. Also, the function subspace V is an L^2-closure that is [46, 47]:

$$V_{Sa,\{\mathcal{CT}(t)\}} = \text{clos}_{L^2}\left\langle Sa(t-ka) :\ k \in \mathbb{Z}\right\rangle \tag{2.38}$$

This can help in defining a mapping for the function space L^2 into the subspace $V_{Sa,\{\mathcal{CT}(t)\}}$. Such mapping can be defined using a sampling operator $\left(O_a x_c\right)(t)$ as:

$$\left(O_a x_c\right)(t) = \sum_{k=-\infty}^{\infty} x_c(ka) Sa_{s;a}(t-ka) \tag{2.39}$$

This mapping provides a fairly accurate signal representation for $x_c(t) \in \{\mathcal{CT}(t)\}$ due to the conditions imposed on the spacing a between samples. In order to obtain a more accurate representation of the signal $x_c(t)$, an orthogonal projection mapping $\left(L_a x_c\right)(t)$ can be used. This mapping is defined as[41, 43]:

$$\left(L_a x_c\right)(t) = \sum_{k=-\infty}^{\infty} c_k(ka) Sa_{s;a}(t-ka) \tag{2.40}$$

such that:

$$\int_{-\infty}^{\infty} \left(x_c(t) - \left(L_a x_c\right)(t)\right) Sa_{s;a}(t-ka)dt = 0 \tag{2.41}$$

the coefficients $\{c_k\}$ are defined as:

$$c_k = \int_{-\infty}^{\infty} x_c(t) Sa_{s;a}(t - ka)dt,\ k \in \mathbb{Z} \tag{2.42}$$

The relation between the two mappings can be investigated under the following conditions [43]:

- The signal $x_c(t) \in \{\mathcal{CT}(t)\}$.
- The sampling function $Sa(t)$ is capable of generating an orthonormal family on the samples set $\{ka\}$, $k \in \mathbb{Z}$.
- The spacing between samples a has to satisfy $0 < a \leq \frac{\pi}{\Omega_o}$.
- The Fourier transform of the sampling function $Sa(t)$ is such that:

$$\hat{Sa}(\Omega) = \int_{-\infty}^{\infty} Sa(t) e^{-j\Omega t} dt = 1\ for\ |\Omega| \leq \Omega_o \tag{2.43}$$

The orthogonal projection mapping becomes:

$$\left(L_a x_c\right)(t) = \sum_{k=-\infty}^{\infty} \left(\int_{-\infty}^{\infty} x_c(t) Sa_{s;a}(t - ka)dt \right) Sa_{s;a}(t - ka) \tag{2.44}$$

Using the Parseval's identity, equation (2.40) can be written as [44]:

$$\left(L_a x_c\right)(t) = \sum_{k=-\infty}^{\infty} \left(\frac{1}{2\pi} \int_{-\Omega_o}^{\Omega_o} X_c(\Omega) \hat{Sa}^*(\Omega) e^{jka\Omega} d\Omega \right) Sa_{s;a}(t - ka) \tag{2.45}$$

$$\left(L_a x_c\right)(t) = \sum_{k=-\infty}^{\infty} \left(\frac{1}{2\pi} \int_{-\Omega_o}^{\Omega_o} X_c(\Omega) e^{jka\Omega} d\Omega \right) Sa_{s;a}(t - ka) \tag{2.46}$$

The term $\frac{1}{2\pi}\int_{-\Omega_o}^{\Omega_o} X_c(\Omega)e^{jka\Omega}d\Omega$ is an inverse CTFT that is equal to $x_c(ka)$ such as:

$$\frac{1}{2\pi}\int_{-\Omega_o}^{\Omega_o} X_c(\Omega)e^{jka\Omega}d\Omega = x_c(ka) \tag{2.47}$$

The equation of the orthogonal mapping becomes:

$$\left(L_a x_c\right)(t) = \sum_{k=-\infty}^{\infty} x_c(ka)Sa_{s;a}(t-ka) = \left(O_a x_c\right)(t) \tag{2.48}$$

Equation (2.44) shows that the two mappings perform the same decomposition under certain conditions. Among these conditions is the capability of the sampling function to generate an orthonormal family over the sampling set. This condition indicates that the sampling function has to satisfy specific conditions required by a scaling function for generating a set of orthonormal basis functions [43–45, 47, 48].

The sampling mapping and the orthogonal projection mapping are identical if the sampling function $Sa(t)$ can generate orthonormal basis functions over the samples set $\{ka\}$, $k \in \mathbb{Z}$. This condition can be verified using the concept of multi-dimensional approximation [42, 45–48]. Starting with the classical WSK sampling theorem, a signal $x_c(t)$ band-limited to $(-\Omega_o, \Omega_o)$ $(x_c(t) \in CT(t))$ can be reconstructed or approximated from its samples as [45–47]:

$$x_c(t) = \sum_{n=-\infty}^{\infty} x(nT_s)\frac{\sin\Omega_o(t-nT_s)}{\Omega_o(t-nT_s)} \tag{2.49}$$

where $T_s = \pi/\Omega_o = a$ and $t \in \mathbb{R}$. If Ω_o is allowed to vary as $\Omega_o = 2^m\pi, m \in \mathbb{Z}$, then this can be viewed as a setting of a multiresolution analysis (MRA) [5, 43]. The sinc function can be defined then as a scaling function of the MRA such that it can generate a collection of linear independent basis vectors $\{\nu_1, \nu_2..., \nu_N\}$. The scaling

function satisfies the following dilation equation [43, 44, 47]:

$$\phi(t) = \sum_k \frac{\sin \pi k/2}{\pi k/2} \phi(2t - k) \tag{2.50}$$

This setting encompasses the classical WSK sampling theorem in an MRA context. Also, it creates a connection between the WSK classical sampling theorem and the wavelet theory [47, 48]. The relation between wavelet theory and MRA has led to an important conclusion that there exists a sampling function $\phi(t)$, which can provide a sampling expansion of any CT signal $x_c(t) \in V_0$. The conditions required for a function to generate orthonormal bases for an MRA are described as follows [46–49]:

- The function has to be a real and a continuous function with a decaying property such that:

$$\lim_{|t| \to \infty} \phi(t) = 0, \quad t \in \mathbb{R} \tag{2.51}$$

- The integer translations of $\phi(t)$ of the form $\{\phi(t - l)\}$, $l \in \mathbb{Z}$ form an orthonormal basis for a subspace V_0 of $L^2(\mathbb{R})$.

- The MRA generated by $\phi(t)$ of closed subsets $\{V_m^2\}_{m \in \mathbb{Z}}$ of $L^2(\mathbb{R})$ has to satisfy:

$$0... \subset V_{-1} \subset V_0 \subset V_1 \subset V_2... \subset V_m \subset L^2(\mathbb{R}) \tag{2.52}$$

$$x_c(t) \in V_m \Leftrightarrow x(2t) \in V_{m+1} \tag{2.53}$$

$$\bigcap_{m \in \mathbb{Z}} V_m = 0, \quad \overline{\bigcup_{m \in \mathbb{Z}} V_m} = L^2(\mathbb{R}) \tag{2.54}$$

- Since $\phi(t) \in V_1$, there exists a sequence $\{a_k\}$ of length N such that:

$$\phi(t) = \sum_{k=0}^{N-1} a_k \phi(2t - k) \tag{2.55}$$

When the aforementioned conditions are met by a function $\phi(t)$ the wavelet theory defines this function as a scaling function, and ensures the existence of an associated wavelet function $\psi(t)$. The wavelet function can generate a set of orthonormal basis functions for a subspace W_0 that is an orthogonal complement of the subspace V_0. Such a set of orthonormal basis functions is generated by integer translations of the wavelet function $\psi(t)$ as $\{\psi(t-l)\}$, $l \in \mathbb{Z}$. As an example, the WSK function $\phi(t)$ can be defined as [47–51]:

$$\phi(t) = \frac{\sin \pi t}{\pi t} \tag{2.56}$$

Also, the wavelet function can be defined in terms of the scaling function as [42]:

$$\psi(t) = \frac{\sin \pi(t - \frac{1}{2}) - \sin 2\pi(t - \frac{1}{2})}{\pi(t - \frac{1}{2})} \tag{2.57}$$

The previous discussion of the relation between the sampling process and the MRA provided an interesting relation between sampling a function and analyzing the same function. Moreover, the sampling process can be realized accurately using an MRA structure. Also, the discussion indicated that there exists a strong connection between sampling a function and processing the same function using the wavelet analysis. The next section provides additional interpretation of sampling a signal using wavelet basis functions.

2.6 Wavelet Sampling Theory

A continuous-time (CT) signal $x_c(t)$ can be perfectly recovered from its samples created by a scaling function. A scaling function $\phi(t)$ has to be capable of generating basis functions that span a set of closed spaces $\{V_m\}$, $m \in \mathbb{Z}$. Moreover, the density and completeness conditions require an orthogonal complement space W_m for each space V_m. Each orthogonal complement space W_m is spanned by another set of basis functions generated by $\phi_m(t)$. Such a set of basis functions define a wavelet function $\psi(t)$ associated with $\phi(t)$ as [49–52]:

$$\psi(t) = \sum_{k=1}^{N} (-1)^k a_{N-k} \phi(2t - k) \tag{2.58}$$

Basis functions required to span each W_j can be generated at each scale j by integer translations of the wavelet function $\psi(t)$, and are known as wavelet basis functions as [47–51]:

$$\{\psi_{j,k}\} = 2^{j/2} \psi(2^j t - k) \tag{2.59}$$

Each orthogonal complement space W_m can be defined as a linear span of wavelet basis functions as [41, 48–50, 53–56]:

$$W_j = \operatorname*{span}_k \{\psi_{j,k}\} \tag{2.60}$$

The same applies for the space V_m that is a linear span of scaling basis functions as:

$$V_j = \operatorname*{span}_k \{\phi_{j,k}\} \tag{2.61}$$

A collection of scaling spaces $V_m(\phi)$ and wavelet spaces $W_M(\psi)$ constitutes a mul-

tiresolution analysis (MRA). It is to be noted that wavelet and scaling spaces have to be dense and complete in $L^2(\mathbb{R})$ that is:

$$MRA = \left\{ V_m \bigoplus_{m=0}^{J-1} W_m \right\} \tag{2.62}$$

Density and completeness conditions of both spaces can be used to relate them with MRA as the scale j changes. This can be translated in constructing scaling space $V_q(\phi)$ as [53, 54]:

$$V_q(\phi) = V_{q-1}(\phi) \oplus W_{q-1}(\psi) \tag{2.63}$$

One of the interpretations of sampling a signal is an N dimensional approximation case. If a CT signal $x_c(t)$ is contained in a space V_q, then it can be expanded using basis functions generated at scale q as:

$$x_c(t) = \sum_{k\in\mathbb{Z}} (c_\phi)_k \, \phi(t-k) + \sum_{j=0}^{q} \sum_{k\in\mathbb{Z}} (c_\psi)_{k,j} \, \psi_j(t-k) \tag{2.64}$$

where coefficient sets $\{(c_\phi)_k\}$ and $\left\{(c_\psi)_{k,j}\right\}$ represent projecting the signal on scaling and wavelet spaces, respectively. These coefficient sets can be determined using inner product operations as:

$$\{(c_\phi)_k\} = \left\langle x_c(t), \tilde{\phi}(t-k) \right\rangle \tag{2.65}$$

$$\left\{(c_\psi)_{k,j}\right\} = \left\langle x_c(t), \tilde{\psi}_j(t-k) \right\rangle \tag{2.66}$$

where $\tilde{\phi}(t)$ is the dual scaling function and $\tilde{\psi}_j(t)$ is the dual wavelet function.

The previous discussion indicates that the projection of a CT signal $x_c(t)$ can represent a sampling-reconstruction process. This can be generalized to an ap-

proximation case in terms of a wavelet-based MRA as [41, 48, 49]:

$$x_c(t) = \sum_{j=0}^{q-1} \sum_{k \in \mathbb{Z}} \left\langle x_c(t), \tilde{\phi}_j(t-k) \right\rangle \phi_j(t-k) \tag{2.67}$$

The term $\left\langle x_c(t), \tilde{\phi}_j(t-k) \right\rangle$ represents a generalized sampling of the CT signal $x_c(t)$, where the set of basis functions $\{\phi_j(t-k)\}_{k \in \mathbb{Z}}$ span an approximation space at each scale j [40, 42–44, 46, 54].

For the last 50 years, the sampling theorem has been a subject for extensive research due to its wide applications. There have been detailed mathematical derivations for the sampling process using the functional space analysis and the approximation theory. Due to new applications, different forms of sampling emerged and derivations had to be generalized to accommodate the new sampling forms. One of these sampling forms is the non-uniform recurrent sampling form that is applied in periodic signal sampling and reconstruction. Furthermore, the interest of applying wavelet MRA in signal processing areas has led to the wavelet sampling theory. Several important contributions have been achieved in this aspect, in particular the representation of sampling-reconstruction process as a wavelet-based multiresolution analysis-synthesis [42–46].

The wavelet-based MRA representation of a CT signal $x_c(t)$ is carried out such that the signal energy will be small for high frequencies, hence the wavelet coefficients will vanish after a certain scale j. This fact leads to an important conclusion that scaling function coefficients are the sampling expansion of a CT band limited signal $x_c(t)$ at each scale j [45, 46]. As a result, the reconstruction of that signal from its samples is carried out by sets of scaling and wavelet basis functions.

The concepts developed for the sampling theorem can be employed to build

mathematical models for various system functions. Among such functions are the switching functions, in particular, power electronic dc-ac inverters. Power electronic switch-mode inverters carry out switching actions for different time intervals. The main objective of such switching actions is to synthesize a sinusoidal signal on a high power level. Different aspects of operating these systems are still not validated using the conventional interpretation of the inverter operation. The next chapter presents a mathematical modeling of power electronic switch-mode inverter functions based on concepts of the sampling theorem.

Chapter 3

Modeling DC-AC Inverters

3.1 General

Dc-ac inverters are mostly operated using multi-switching techniques to eliminate or reduce as much energy distributed in the output harmonic components as possible. Multi-switching techniques can be realized through a modulation process that determines time instants at which switching element(s) change their status (ON to OFF or OFF to ON). Various approaches with different schemes of implementation have been developed and tested to carry out multi-switching techniques for improving inverter performance. Although extensive research has focused on operating and controlling inverters, little effort has been made to model the inverter. Moreover, existing modulation techniques are optimized to meet load requirements without correlation with any existing inverter model. This approach of operating inverters has caused several limitations of modulated inverters performance. These limitations include the spectral distribution of inverter output harmonic components, the jitter phenomenon when using rectangular pulse carrier signals and impacts on the output due to changing the switching strategy [1–

4, 55, 56]. There exists a need for a rigorous model for justifying and verifying the fundamental function of inverters. Such model is to consider the instantaneous switching element actions as a main part of the inverter function.

This chapter aims to develop a new inverter modeling approach, and test this approach for modeling single-phase (1ϕ) and three-phase (3ϕ) inverters. The desired inverter modeling approach has to have the capability of:

- Providing a mathematical tool for verifying the impact on inverter outputs due to applying a switching strategy.
- Providing a basis for novel modulation techniques that can be correlated with the inverter model.
- Providing new approaches for realizing new control techniques for inverter outputs.

The basis of the desired model will incorporate several concepts of the sampling theorem, in particular, the concept of non-uniform sampling and reconstruction of continuous-time (CT) signals. The next section provides a brief review of the available inverter models.

3.2 Review of Available DC-AC Inverter Models

The common assumption in modeling power electronic converters has been based on time-averaging the switching actions over one cycle of a reference-modulating signal (usually a sinusoidal signal). This assumption has been realized in three main models, which include steady-state models derived using circuit theory, operational models derived from numerical data and models derived from

a unified converter theory [1, 2, 57]. These models are reviewed in the following subsections.

3.2.1 Steady-State Circuit Models

The earliest steady-state circuit modeling approach of switching converters was introduced by Tymerski based on the small-signal analysis concept. In this model, any switching circuit is assumed to be piece-wise linear and its response is determined for any small perturbation of steady-state operating conditions. Also, each switching element is considered as a three-terminal device that is reminiscent of a typical transistor. This basic model of each switching element became known as a switch-cell. The switch-cell terminal voltages and currents are averaged over each switching cycle [59]. This averaging step is performed to validate the assumption of piece-wise linear outputs. However, the assumption of piece-wise input/output relations can reduce the bandwidth of the switch-cell and make it valid over a narrow range of switching frequencies.

The incremental small-signal model of the switch-cell can be constructed using the basic transistor linear model. The instantaneous ON time of the switch-cell is defined as $D_s(t)$, which is composed of a steady-state value and an increment as in the following equation [59]:

$$D_s(t) = D_s + \delta \tag{3.1}$$

where D_s is the steady-state ON time and δ is the increment. Moreover, the steady-state OFF time is defined as $D'_s = 1 - D_s$. The output current of the switch-cell during the ON time is $I_A(t)$, and during OFF time is $I_P(t)$. Also, the switch-cell output voltage during ON time is $V_{AC}(t)$, and during OFF is $V_{PC}(t)$. These voltages

and currents are defined as [60]:

$$I_A(t) = f(D_s + \delta) = I_A + I_{A\delta} \tag{3.2}$$

$$I_P(t) = f(D_s + \delta) = I_C + I_{C\delta} \tag{3.3}$$

$$V_{AC}(t) = f(D_s + \delta) = V_{AC} + V_{AC\delta} \tag{3.4}$$

$$V_{PC}(t) = f(D_s + \delta) = V_{PC} + V_{PC\delta} \tag{3.5}$$

The description of a typical switch-cell can be stated as [58]:

$$I_A(t) = I_A + D_s\delta I_C + D_s I_{C\delta} \tag{3.6}$$

$$I_P(t) = I_P + D'_s\delta I_C - D_s I_{C\delta} \tag{3.7}$$

$$V_{PC}(t) = V_{PC} + D_s\delta V_{AP} + D_s V_{AP\delta} \tag{3.8}$$

$$V_{AC}(t) = V_{AC} + D'_s\delta V_{AP} + D_s V_{AP\delta} \tag{3.9}$$

The model of the switch-cell can be constructed using the above equations, and can be built in a circuit as shown in Figure 3.1.
It is to be noted that the transformer used in the switch-cell circuit model with turns ratio of $1 : D_s$ converts both voltages and currents by the ratio of D_s.

The incremental method sets the operating point depending on steady-state values of the switch-cell parameters: I_C, V_{AP} and D_s. This method of defining the operating point makes this model valid for a nominal value of D_s that is related to a limited range of switching frequencies. Furthermore, conditions on switching frequencies are required to validate modeling the overall converter using the switch-cell basic model.

This circuit model can now be substituted for the switch in a converter topol-

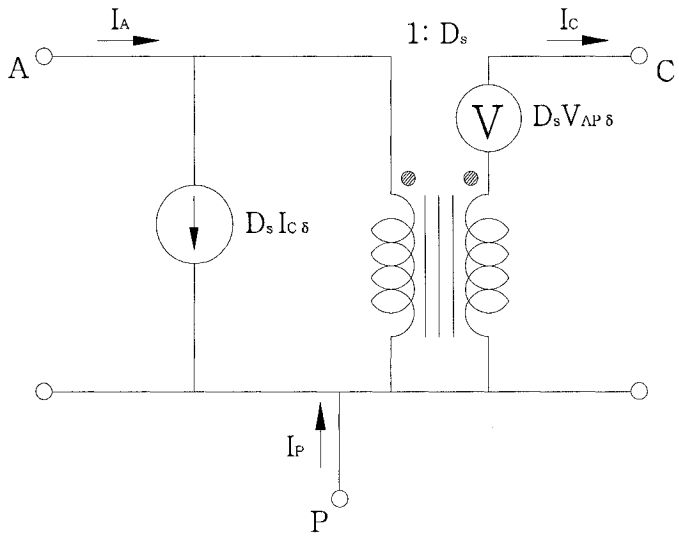

Figure 3.1: The small signal circuit model of the switch-cell [60].

ogy, and the dynamic behavior of the circuit can be derived using the usual linear methods of circuit analysis. It is very critical to connect a series inductor to limit the variations in the current I_A. This condition is necessary since the switch-cell model is validated under the assumption of flux-balance per cycle [57]. These conditions are imposed to ensure the linearization of the switch-cell model around a fixed value of D_s with a small variation δ. This results in a linear circuit under assumptions of passive components, which can be analyzed using linear time-invariant system methods [54, 60].

The switch-cell modeling approach has been used to construct general linear models of switching power electronic converters. The most popular application of the switch-cell model in inverters is a model based on the decoupling principle developed by Milosevic [54]. This model aimed to define a transfer function of a 3ϕ voltage source inverter considering only fundamental components of output

voltage and current. The equivalent circuit is shown in Figure 3.2.

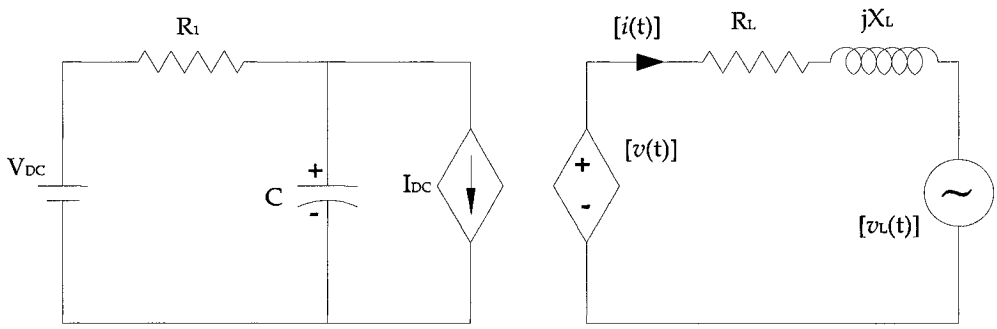

Figure 3.2: The equivalent circuit model of a three-phase inverter based on the switch-cell linearized model approach [54].

where $[v(t)]$, $[i(t)]$ and $[v_L(t)]$ are given by:

$$[v(t)]^T = [v_{ab}(t)\ v_{bc}(t)\ v_{ca}(t)] \tag{3.10}$$

$$[i(t)]^T = [i_a(t)\ i_b(t)\ i_c(t)] \tag{3.11}$$

$$[v_L(t)]^T = [(v_{ab}(t))_L\ (v_{bc}(t))_L\ (v_{ca}(t))_L] \tag{3.12}$$

Using a developed approximate equivalent steady-state circuit-model and the $d-q$ rotating frame, a transfer function can be derived to describe the steady-state inverter operation mathematically as [54]:

$$G(s) = \frac{\vec{I}}{\Delta\vec{V}} = \frac{1}{sL + R_L + j\omega_1 L} \tag{3.13}$$

where $\vec{I} = I_d + jI_q$, $\Delta\vec{V} = \Delta V_d + j\Delta V_q$ and ω_1 is the fundamental frequency. The

developed transfer function of a 3ϕ VS inverter has several limitations that include:

- The assumption of small variations of the ON-time D_s (only by δ).
- The assumption of passive components needed to build the switch-cell model.
- The averaged values of currents and voltages over each switching cycle
- Complicated mathematical formulation when modeling a switching converter with several switching elements

3.2.2 Operational Data Models

The integration of inverters in different industrial applications has made it possible to consider them as parts of such applications. One of the famous examples of such applications is the utilization of renewable energy. In such applications, an inverter is considered as one component of a complete system model. Moreover, the requirements imposed by renewable energy systems define the operating point of the employed inverter. As a result, the inverter is considered as a single element, where input and output powers, voltages and currents are taken as parameters of such an element. A transfer function relating input power with output power is developed based on the modeled system voltage-current relations. Furthermore, a curve-fit approximation is applied on collected inverter powers, voltages and currents data to define a set of mathematical equations describing the final model. One of the popular curves used to obtain good fitting is the empirical efficiency curve [61].

The data based models have several limitations that include:

- High dependence on data that can be affected by the whole system and measuring equipments.
- The model is valid only for pre-defined inverter voltages, currents, power losses and output frequency ratings.
- The model transfer function is derived through curve fitting, which is based on assumptions of pre-defined linear voltage-current relations.

3.2.3 Unified Converter Theory

The unified converter theory was developed by Wood [60], who considered that switching converters are related by their functions and behaviors. Also, the basic characteristics of switching converters depend neither on their applications, nor on their topologies [62]. According to this theory, a typical switching converter is simply a matrix of switching elements that connects its input nodes to its output nodes. These input and output nodes can be ac or dc, capacitive or inductive. Moreover, the direction of the power flow can be from output nodes to input nodes or vice versa. This model is valid under constraints imposed by fundamental concepts of circuit theory, which include [1, 62]:

1. If one set of nodes (input or output) is inductive, the other set must be capacitive to avoid creating any cut-set of voltage or current sources when converter switches are activated.
2. Any combination of open and closed switches should never open circuit an inductor, or short circuit a capacitor.

Conventional inverter models are based on major assumptions of linearity and time averaged switching actions. These assumptions have resulted in approxi-

mated and inaccurate models that can not be generalized for modern modulated inverters. Also, if these models are valid for certain operating conditions, they are not capable of justifying changes in switching technique or switching frequency. The assumption of time-averaged switching actions can be avoided if instantaneous switching actions are considered as part of the inverter model. One of the possible ways to validate this approach is using sampling-reconstruction concepts.

The previous section has provided a brief review of the available inverter models along with their structures, drawbacks and relation with modulation techniques. The next section presents a new approach for modeling single-phase (1ϕ) voltage-source (VS) inverters based on a non-uniform recurrent sampling-reconstruction of continuous-time (CT) signals. Also, section 3.5 extends this approach for modeling 3ϕ inverters.

3.3 Sampling-Based Modeling

Multi-switching techniques are very common in operating and controlling modulated inverters. Such techniques are able to improve the performance of inverters in terms of output quality, efficiency and dc-bus utilization. The fundamental idea of most modulation techniques is to compare a high frequency signal known as the carrier (e.g. a triangular signal with frequency f_c) to a low frequency signal known as the reference-modulating signal (usually a sinusoidal signal with frequency f_m). Also, some modulation techniques pre-define switching instants like SHE and SVM. The reference-modulating signal has the same frequency as the desired output of any modulated dc-ac inverter [1–3]. Pulse-width modulated (PWM) and delta modulated (DM) inverters are very popular in different industrial applications [31]. The harmonic spectra of outputs of PWM and DM inverters

are shown in Figures 3.3 and Figure 3.4, respectively. It is to be noted that the

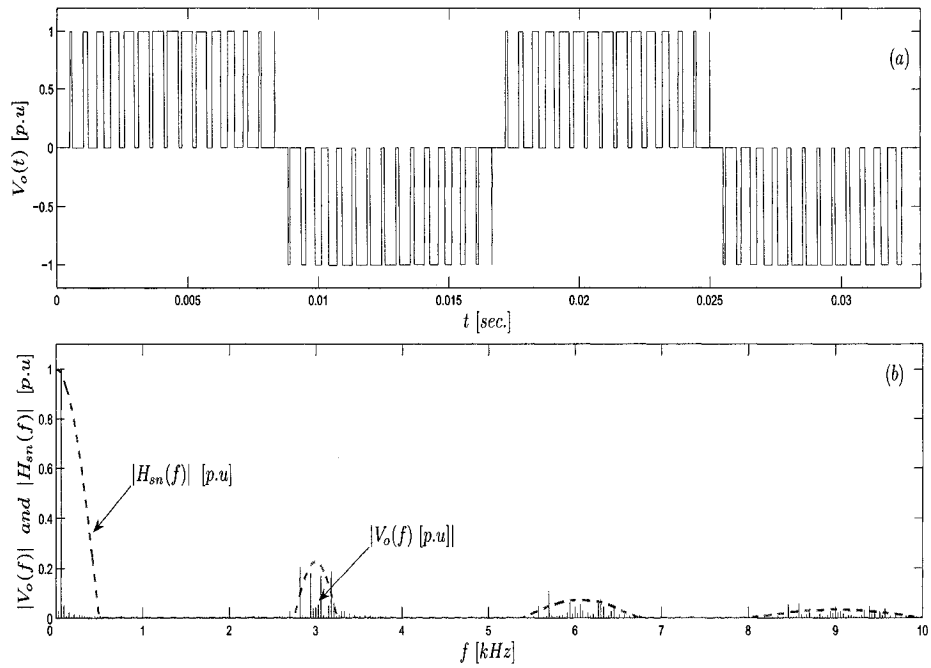

Figure 3.3: The pulse-width modulation (PWM) technique: (a) the per-unit output voltage of a single-phase PWM inverter and (b) the harmonic spectrum of the output voltage.

per-unit ($p.u$) in both figures represents the ratio of the magnitude to a pre-defined value, which in these figures is taken as the maximum value of each quantity.

Figure 3.3 and Figure 3.4 show harmonic components forming frequency side-bands centered at even multiples of the carrier frequency f_c. Similar frequency formations are found in spectra of reconstructed continuous-time (CT) signals from their samples [4].

3.3.1 Non-uniform Sampling-Based Representation

The change in the status of the switching elements occurs at intersection points between the carrier signal and the reference-modulating signal. Unit impulses

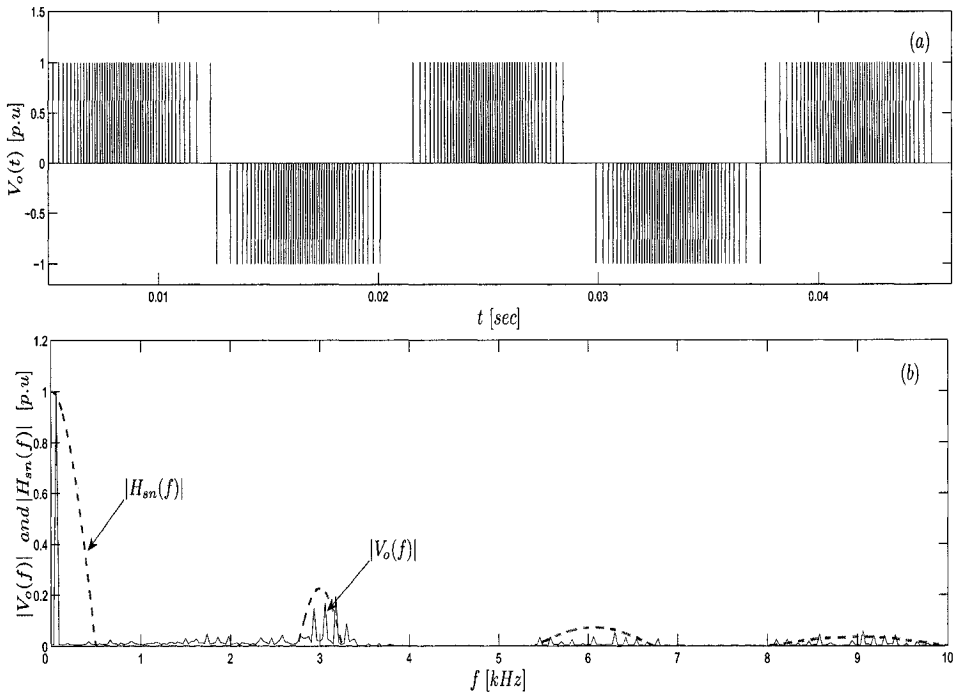

Figure 3.4: The delta modulation (DM) technique: (a) the per-unit output voltage of a single-phase DM inverter and (b) the harmonic spectrum of the output voltage.

created at each intersection point can be viewed as non-uniform samples of the reference-modulating signal. Furthermore, each cycle of the carrier signal produces two samples; the rising portion of the carrier signal produces one sample, while the falling portion produces the other [4]. As a result, these samples appear to be taken at a sampling frequency of $2f_c$.

Samples created at intersection points have a non-uniform repetitive nature due to the periodicity and the symmetry of the carrier and the reference-modulating signals. This type of non-uniform sampling is known as the non-uniform recurrent sampling [36]. The non-uniform recurrent sampling structure is based on arranging non-uniform samples into limited number of repetitive groups, where each group has a finite number of samples. For the case of sampling a sinu-

soidal reference-modulating signal using a triangular carrier signal, each sample group will have two samples. The number of sample groups in one cycle of the sinusoidal reference-modulating signal will depend on the frequency of the reference-modulating signal and the frequency of the carrier signal. If the sinusoidal reference-modulating signal has a frequency of f_m and the carrier signal has a frequency of f_c, the number of sample groups can be defined as:

$$\mathcal{D} = 2\frac{f_c}{f_m} \tag{3.14}$$

The formed groups of non-uniform recurrent samples over one cycle of the reference-modulating signal can be viewed as a set $\mathcal{D} = \{d_1, d_2, ..., d_{\mathcal{D}}\}$. The created non-uniform recurrent sample groups can take a discrete form of the reference-modulating signal $S_M(t)$ that can be expressed as:

$$S_{dM}(t) = \sum_{k=-\infty}^{\infty} \sum_{d=0}^{\mathcal{D}} \sum_{p=1}^{2} S_M(t)\, \delta(t - t_{pd} - kT_m) \tag{3.15}$$

where the variable t_{pd} represents d groups of p samples, which form one of the recurrent periods. The sampled form of the reference-modulating signal can be expressed as a discrete signal as:

$$S_{dM}[n] = S_{dM}(t)|_{t=t_{pd}+kT_m} \tag{3.16}$$

This discrete form provides a basis for viewing the instantaneous switching actions of an inverter as stages of interpolating functions. Such interpolating functions are used to recover $S_M(t)$ from its samples $S_{dM}[n]$.

The popular sinusoidal pulse-width modulation (SPWM) technique uses a triangular carrier signal for creating trains of switching pulses. These pulses are characterized by their widths and locations relative to the beginning of each cycle of $S_M(t)$. In SPWM, non-uniform recurrent samples are created by the carrier signal that can be expressed mathematically as [19]:

$$S_{SC}(t) = \begin{cases} 4f_c t & 0 \leq t \leq \frac{T_c}{4} \\ 2 - 4f_c t & \frac{T_c}{4} \leq t \leq \frac{3T_c}{4} \\ 4f_c t - 4 & \frac{3T_c}{4} \leq t \leq T_c \end{cases} \tag{3.17}$$

Two signals of different functional forms representing the rising and the falling portions of $S_{SC}(t)$ that are responsible for creating two samples for each sample group, can be defined as trains of non-uniform recurrent impulses as:

$$S_{SCR}(t) = \sum_k \sum_{d=1}^{\mathcal{D}} \delta\left(t - t_{Rdr} - dT_c - kT_m\right) \tag{3.18}$$

$$S_{SCF}(t) = \sum_k \sum_{d=1}^{\mathcal{D}} \delta\left(t - t_{Fdr} - dT_c - kT_m\right) \tag{3.19}$$

The discrete form of these two signals can be defined as:

$$S_{SCR}[n] = S_{SCR}(t)|_{t=t_{Rdr}-dT_c-kT_m} \tag{3.20}$$

$$S_{SCF}[n] = S_{SCF}(t)|_{t=t_{Fdr}-dT_c-kT_m} \tag{3.21}$$

where the set $\{t_{Rdr}\}$ represents the intersection points of the rising portion of $S_{SC}(t)$ with $S_M(t)$, while the set $\{t_{Fdr}\}$ represents the intersection points of the falling portion of $S_{SC}(t)$ with $S_M(t)$. These sets of time instants can be determined over a

cycle of $S_{SC}(t)$ as:

$$S_M\left(t_{Rr}\right) - 4f_c t_{Rr} = 0 \tag{3.22}$$

$$S_M\left(t_{Fr}\right) - \left(2 - 4f_c t_{Fr}\right) = 0 \tag{3.23}$$

Figure 3.5 shows the intersection points of both discrete signals $S_{SCR}[n]$ and $S_{SCF}[n]$ with a sinusoidal reference-modulating signal.

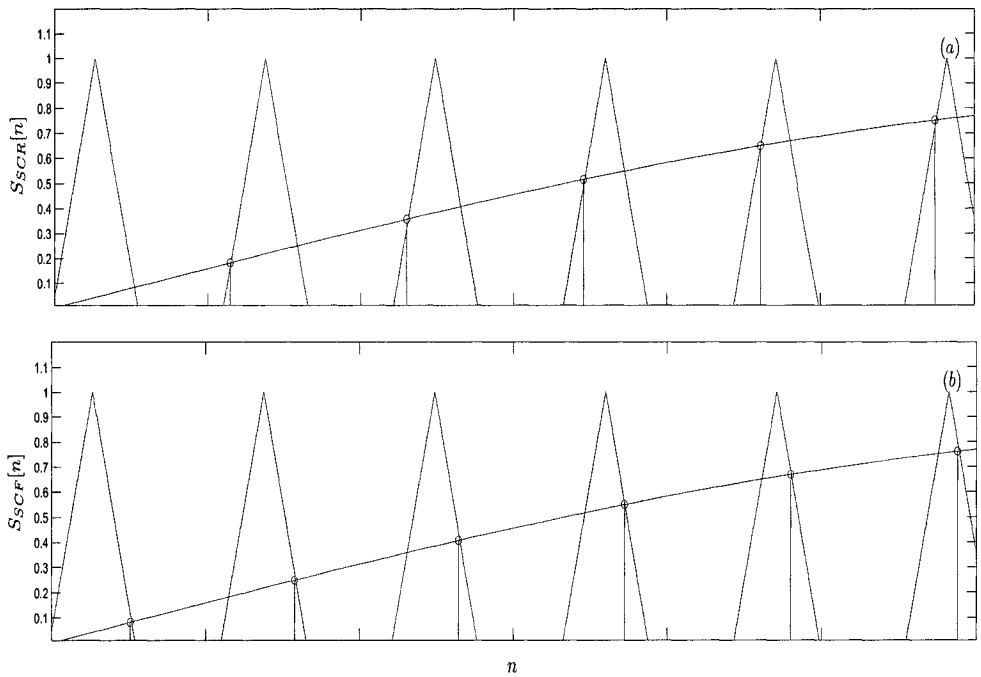

Figure 3.5: Sampling the reference-modulating signal $S_M(t)$ in a non-uniform recurrent manner: (a) $S_{SCR}[n]$; the samples created by the rising portion of $S_{SC}(t)$ and (b) $S_{SCF}[n]$; the samples created by the falling portion of $S_{SC}(t)$.

The period of sample groups T_m is related to the Nyquist interval T_Q and the number of sample groups $\mathcal{D}$ by the following relation [36]:

$$T_m > N\mathcal{D}T_Q \tag{3.24}$$

where N is the number of samples in each sample group, which is $N = 2$ for the SPWM technique case. Figure 3.6 shows the discrete form of the reference-modulating signal $S_M(t)$.

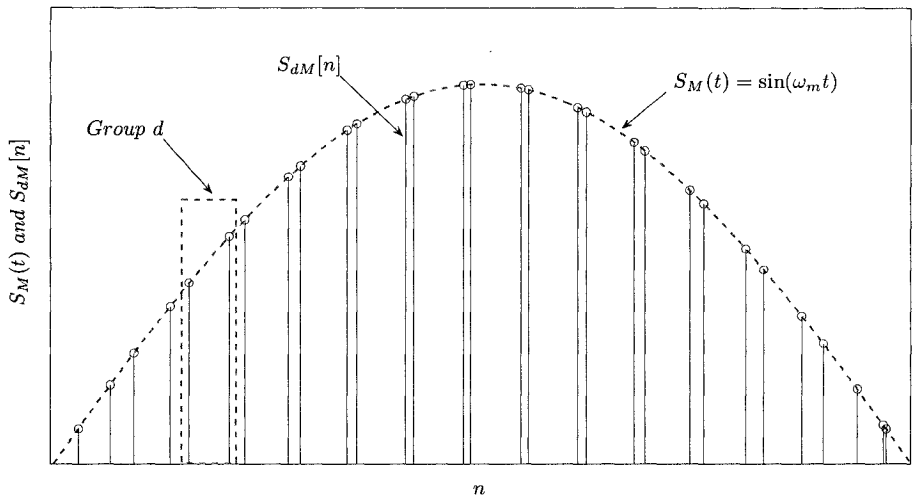

Figure 3.6: Groups of non-uniform recurrent samples of the reference-modulating signal $S_M(t)$ using both discrete signals $S_{SCR}(t)$ and $S_{SCF}(t)$ to form $S_{dM}[n]$.

The discrete signal $S_{SCR}[n]$ is the result of sampling the reference-modulating signal $S_M(t)$ with the rising portion of the carrier signal, while the discrete signal $S_{SCF}[n]$ is the result of sampling $S_M(t)$ with the falling portion. This interpretation of creating samples of the reference-modulating signal $S_M(t)$ can be constructed in a block diagram as shown in Figure 3.7.

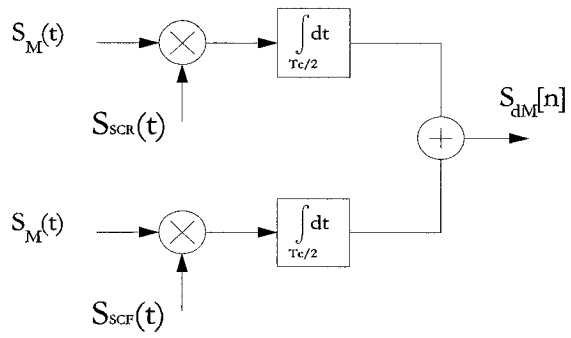

Figure 3.7: A block diagram of non-uniform sampling the reference-modulating signal using the rising portion $S_{SCR}[n]$ and the falling portion $S_{SCF}[n]$ of the triangular carrier signal $S_{SC}(t)$ [4].

3.3.2 Reconstructing the Reference-Modulating Signal from Non-uniform Samples

The reconstruction of a continuous-time (CT) signal from its samples is carried out through a filtering process. The classical sampling theorem states that if a CT signal $s(t)$ has a Fourier transform $F\{s(t)\} = S(\Omega) = 0$ for $|\Omega| > \Omega_o$ (*i.e.* the signal $s(t)$ is band limited to Ω_o), then $s(t)$ can be recovered perfectly from its samples $s_d[n]$ by the following formula [40]:

$$s(t) = \sum_{n=-\infty}^{\infty} s_d[n] \frac{\sin(\pi(t-n))}{\pi(t-n)} \tag{3.25}$$

The reconstruction formula of equation (3.22) represents an interpolating function, which is valid under a strict condition of equi-spaced samples [13]. However, for the case of non-uniform recurrent sampling, reconstructing the CT signal is carried out through stages of interpolating functions. This can be realized using

different stages of filters or a filter bank, where the number of the required filters depends on the number of sample groups $\mathcal{D}$. In general, a CT signal $x_c(t)$ can be reconstructed from its non-uniform recurrent samples $x_d[n]$ using the Lagrange general interpolating formula as [36]:

$$x_c(t) = \sum_{n=-\infty}^{\infty} x_d[n] \frac{G_n(t)}{G'_n(t_n)(t - t_n)} \tag{3.26}$$

where

$$G_n(t) = t \prod_p \left(1 - \frac{t}{t_p}\right) \tag{3.27}$$

and

$$G'_n(t_p) = \frac{dG_n(t)}{dt}|_{t=t_p} \tag{3.28}$$

For the case of $N = 2$, the function $G_n(t)$ can be simplified to:

$$G_n(t) = t \left(1 - \frac{t}{t_1}\right) \left(1 - \frac{t}{t_2}\right) \tag{3.29}$$

The case of $N = 2$ can be employed to express the Lagrange interpolating function for the SPWM technique so that $t_1 = t_{Rdr}$ and $t_2 = t_{Fdr}$. Hence, the Lagrange interpolation formula can be expressed for the case of SPWM technique ($N = 2$) as:

$$S_{MS}(t) = \sum_r \sum_{d=1}^{\mathcal{D}} \sum_{p=1}^{2} S_{dM}[pd] \frac{G_d(t)}{G'_d(t_p)(t - t_p)} \tag{3.30}$$

One group of non-uniform recurrent samples is created each cycle of the triangular carrier signal $S_{SC}(t)$. Also, one stage of Lagrange interpolating functions is

defined over that group of samples. This representation can be stated as:

$$\{S_M(t_{d1}), S_M(t_{d2})\},\ t \in [t_{d1}, t_{d2}] \tag{3.31}$$

where $\{S_M(t_{d1}), S_M(t_{d2})\}$ is the sample group d. The interpolating function for non-uniform recurrent sample group d can be defined as:

$$\lambda_d(t) = \frac{S_M(t_{d1})\, G_d(t)}{G'_d(t_{d1})\,(t - t_{d1})} + \frac{S_M(t_{d2})\, G_d(t)}{G'_d(t_{d2})\,(t - t_{d2})} \tag{3.32}$$

where the function $G_d(t)$ is defined for the sample group d as:

$$G_d(t) = t\left(1 - \frac{t}{t_{d1}}\right)\left(1 - \frac{t}{t_{d2}}\right),\ t \in [t_{d1}, t_{d2}] \tag{3.33}$$

The time interval $[t_{d1}, t_{d2}]$ is known as the interval of support of the interpolating function $\lambda_d(t)$ over the sample group d. Due to the periodicity of the sample groups, the function $\lambda_d(t)$ is periodic with a period of T_m so that [4]:

$$\lambda_d(t) = \begin{cases} \lambda_d(t - rT_m) & t_{d1} \le t \le t_{d2} \\ 0 & \text{otherwise} \end{cases} \tag{3.34}$$

where $r = 0, 1, 2, ...$ Figure 3.8 shows two successive interpolating functions and their associated inverter output switching actions.

Successive interpolating functions $\{\lambda_d(t)\}_{d=1,2..,\mathcal{D}}$ are defined through simplifying the Lagrange general interpolating formula as given in equation (3.26) for the case of the inverter that is characterized by $N = 2$. Moreover, the interval of support for each interpolating function $\lambda_d(t)$ is stated as $\{[t_{d1}, t_{d2}]\}_{d=1,2,..,\mathcal{D}}$. These interpolation functions can produce a reconstructed CT signal to model the output

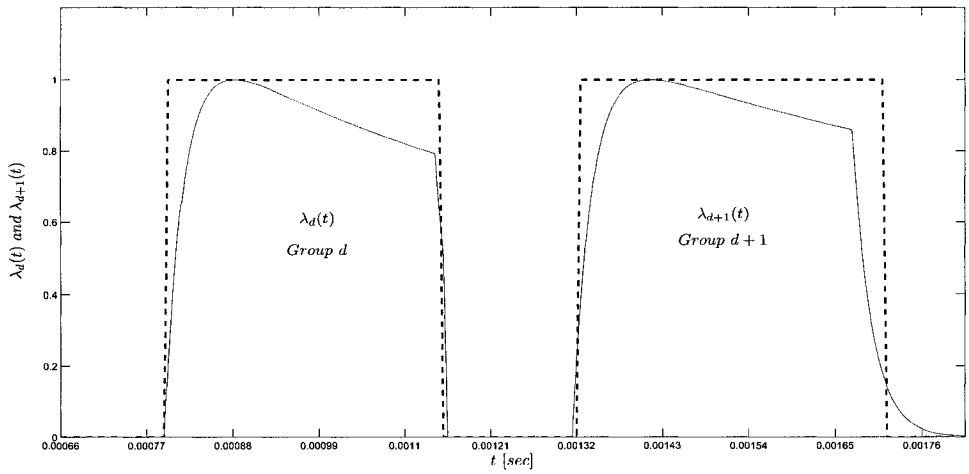

Figure 3.8: Two successive interpolating functions $\lambda_d(t)$ and $\lambda_{d+1}(t)$ and their normalized associated ON-switching inverter output.

of a SPWM inverter $V_o(t)$ as [4]:

$$V_o(t) = V_{DC} \sum_{r=0}^{\infty} \sum_{d=1}^{\mathcal{D}} \lambda_d \left(t - rT_m\right) \tag{3.35}$$

Figure 3.9 shows two cycles of the reconstructed $V_o(t)$ along with its associated inverter output voltage. The two reconstructed signals are analyzed using Fourier analysis, the harmonic distributions for both of them are shown in Figure 3.10.

Instantaneous switching actions are considered a main part of the developed inverter sampling-based model. Such consideration makes this model capable of simulating the performance of modulated inverters. As Figure 3.9 shows, the outputs of the developed model are almost identical to the actual inverter outputs. The non-uniform recurrent sampling-based model is tested for different operating conditions that include changing the switching frequency. The next section provides the simulation test results for these cases.

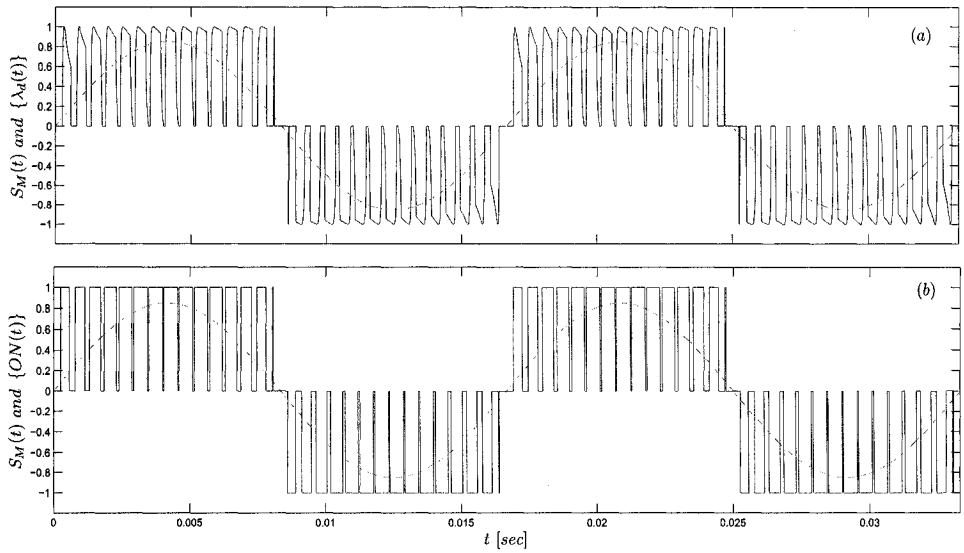

Figure 3.9: Reconstructing sinusoidal signals for the SPWM case: (a) reconstructing a sinusoidal signal using the interpolating functions generated by the sampling-based model ($\{\lambda_d(t)\}_{d=1,2..,\mathcal{D}}$) and (b) the reconstructed sinusoidal signal using switching pulses generated by the SPWM technique.

3.4 Testing the Non-uniform Recurrent Sampling-Based Model of Inverters

The proposed non-uniform recurrent sampling-based model represents the inverter output as a reconstructed CT signal using sets of interpolating functions. The proposed model is tested for producing the output voltage of a SPWM inverter for two carrier frequencies.

3.4.1 SPWM Inverter Output Voltage for Two Carrier Frequencies

In general, the carrier frequency of a SPWM technique determines the rate at which inverter switching elements change their status. If the carrier frequency f_c is changed, locations as well as the number of intersection points of $S_{SC}(t)$ with $S_M(t)$

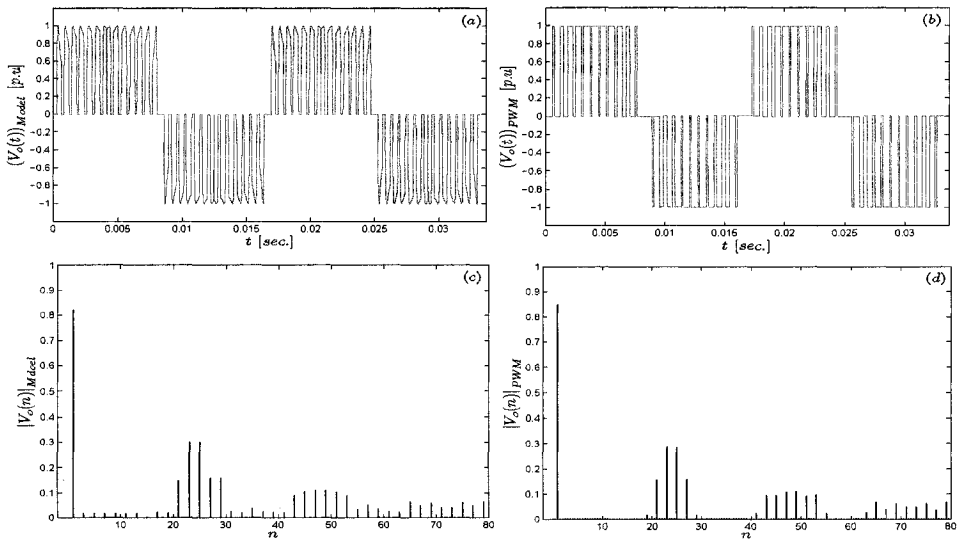

Figure 3.10: Spectra of reconstructed sinusoidal signals for $f_c = 1.08\ kHz$: (a) the reconstructed sinusoidal signal using $\{\lambda_d(t)\}_{d=1,2..,\mathcal{D}}$, (b) the reconstructed sinusoidal signal using switching pulses generated by the SPWM technique, (c) the spectrum of the reconstructed sinusoidal signal using $\{\lambda_d(t)\}_{d=1,2..,\mathcal{D}}$ and (d) the spectrum of the reconstructed sinusoidal signal using switching pulses generated by the SPWM technique. n id the harmonic order

will change. Moreover, changing f_c has a direct impact on the spectral distribution of the SPWM inverter output harmonic components. From the perspective of the proposed model, changing f_c affects locations of samples as well as the number of sample groups created over each cycle of $S_M(t)$. As a result, intervals of support and locations of the proposed model interpolating functions are affected. Figures 3.11(a) and 3.11(b) show successive non-uniform recurrent sample groups of $S_M(t)$ with $f_m = 60\ Hz$ for two common values of switching frequency $f_c = 1.08\ kHz$ and $1.8\ kHz$, respectively.

Figure 3.12 shows the normalized output of a SPWM inverter for a carrier frequency of $f_c = 1.8\ kHz$ and sets of interpolating functions produced by the proposed sampling model for this value of f_c along with their spectra. The recon-

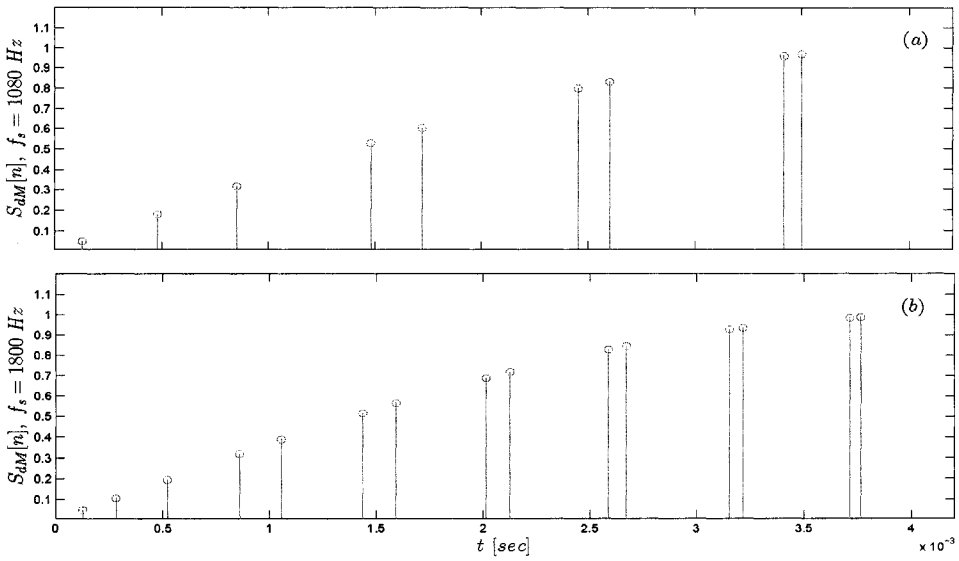

Figure 3.11: Non-uniform recurrent sample groups for different values of f_c: (a) successive sample groups of $S_M(t)$ for $f_c = 1.08\ kHz$ and (b) successive sample groups of $S_M(t)$ for $f_c = 1.8\ kHz$.

structed CT signal using model sets of interpolating functions has a spectrum that is very close to the output voltage of a SPWM inverter, which again confirms its accuracy.

The proposed model is entirely based on considering instantaneous switching actions rather than averaging them over time. This main feature of the proposed model has made it possible to verify the effects on the inverter output due to different modifications of switching strategy, which is clear from results of Figure 3.12. It is worth mentioning that existing inverter models lack the adequate capability to interpret impacts on inverter outputs due to any change in the switching strategies involving non-sinusoidal reference modulating signals and multiple carrier frequencies. The proposed non-uniform recurrent sampling model can easily create the outputs and their harmonic spectra of an inverter. If spacings between samples are selected so that optimal interpolating functions can be used, then a per-

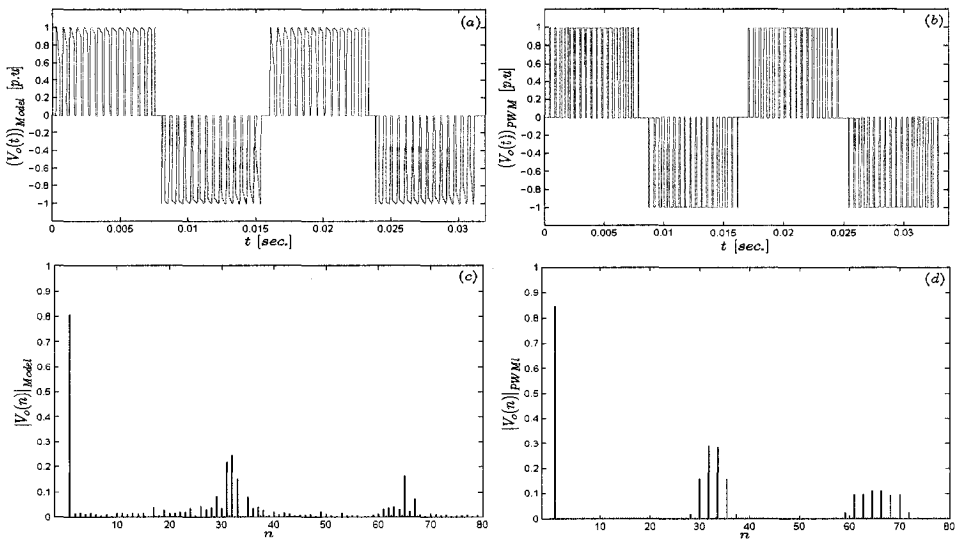

Figure 3.12: Spectra of reconstructed sinusoidal signals for a carrier frequency of $f_c = 1.8\,kHz$: (a) the reconstructed sinusoidal signal using $\{\lambda_d(t)\}_{d=1,2..,\mathcal{D}}$, (b) the reconstructed sinusoidal signal using switching pulses generated by the SPWM technique, (c) the spectrum of the reconstructed sinusoidal signal using $\{\lambda_d(t)\}_{d=1,2..,\mathcal{D}}$ and (d) the spectrum of the reconstructed sinusoidal signal using switching pulses generated by the SPWM technique. n id the harmonic order

fect reconstruction of the sinusoidal reference-modulating signal becomes possible. Such optimization can be achieved using signal processing and wavelets concepts as will be discussed in chapter 4. It is worth mentioning that the proposed non-uniform recurrent sampling-based model has been used to develop new carrier signals and modulation technique that aim to improve the performance of dc-ac inverters and other power electronic converters. The next section presents a detailed extension of the developed sampling-based approach to model three-phase (3ϕ) inverters.

3.5 Sampling-Based Modeling of Three-Phase Inverters

The non-uniform recurrent sampling-based mathematical model of single-phase inverters has shown an encouraging accuracy and significant capabilities of modeling modulated inverters. This approach of modeling single-phase inverters can be extended for three-phase (3ϕ) inverters. In a typical three-phase (3ϕ) inverter, three reference-modulating signals are used to generate the required switching pulses. These three signals are shifted by $\frac{2\pi}{3}$ from each other so that each one of them is associated with one phase on the output side of the 3ϕ inverter. It is to be noted that 3ϕ inverters can have different configurations. However, 3 legs six-pulse configuration is the most common one in industrial applications [1]. Figure 3.13 shows a schematic diagram of the common 3-leg six-pulse topology of 3ϕ inverters.

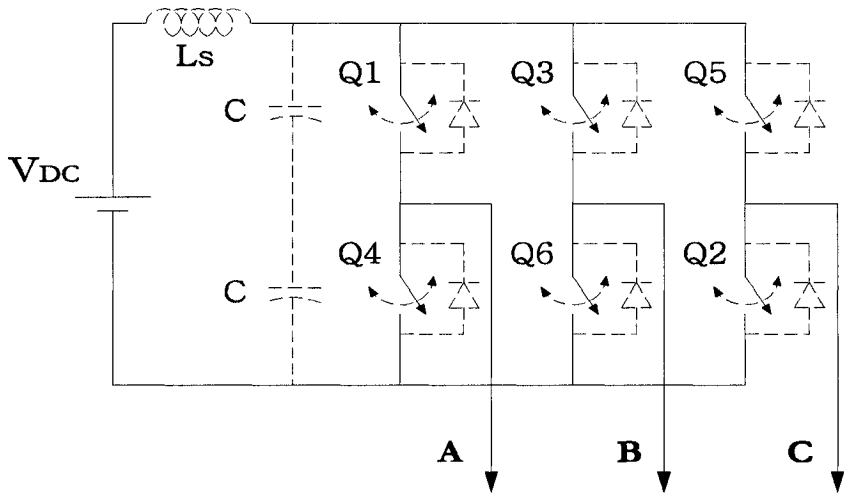

Figure 3.13: A schematic diagram of a typical 3ϕ 3 legs six-pulse inverter.

The required reference-modulating signals for a 3ϕ inverter are given by [1]:

$$S_{Ma}(t) = \sin(\omega_m t) \tag{3.36}$$

$$S_{Mb}(t) = \sin\left(\omega_m t - \frac{2\pi}{3}\right) \tag{3.37}$$

$$S_{Mc}(t) = \sin\left(\omega_m t + \frac{2\pi}{3}\right) \tag{3.38}$$

The carrier-based techniques are the most common techniques used to generate switching pulses for 1ϕ as well as 3ϕ inverters. In theses techniques, switching pulses widths and locations are determined by the locations of intersection points of reference-modulating signals and a carrier signal [1, 4]. Triangular signals are widely used in carrier-based techniques to generate trains of periodic switching pulses. This process can be viewed as multiplying each reference-modulating signal with a train of impulses located at the intersection points. For the case of 3ϕ inverters, three trains of impulses are required to generate switching pulses for each leg of the 3ϕ inverter. These trains of impulses can be expressed as:

$$P_a(t) = \sum_r \sum_{d=1}^{\mathcal{D}} \sum_{pa=1}^{2} \delta\left(t - t_{pa} - dT_c - rT_m\right) \tag{3.39}$$

$$P_b(t) = \sum_r \sum_{d=1}^{\mathcal{D}} \sum_{pb=1}^{2} \delta\left(t - t_{pb} - dT_c - rT_m\right) \tag{3.40}$$

$$P_c(t) = \sum_r \sum_{d=1}^{\mathcal{D}} \sum_{pc=1}^{2} \delta\left(t - t_{pc} - dT_c - rT_m\right) \tag{3.41}$$

where $T_c = \frac{1}{f_c}$ is the period of the carrier signal, $T_m = \frac{1}{f_m}$ is the period of each reference-modulating signal and $\delta(t)$ is the Dirac delta function. Using these trains of impulses, the three reference-modulating signals can be sampled in a non-uniform recurrent manner. The sampled versions of these reference-modulating

signals can be stated as:

$$S_{dM}[n]_a = \int_{\frac{T_c}{2}} S_{Ma}(t)P_a(t)dt \tag{3.42}$$

$$S_{dM}[n]_b = \int_{\frac{T_c}{2}} S_{Mb}(t)P_b(t)dt \tag{3.43}$$

$$S_{dM}[n]_c = \int_{\frac{T_c}{2}} S_{Mc}(t)P_c(t)dt \tag{3.44}$$

Figure 3.14 shows the three reference-modulating signals, the triangular carrier signal and the resultant non-uniform recurrent sampled versions of the three reference-modulating signals.

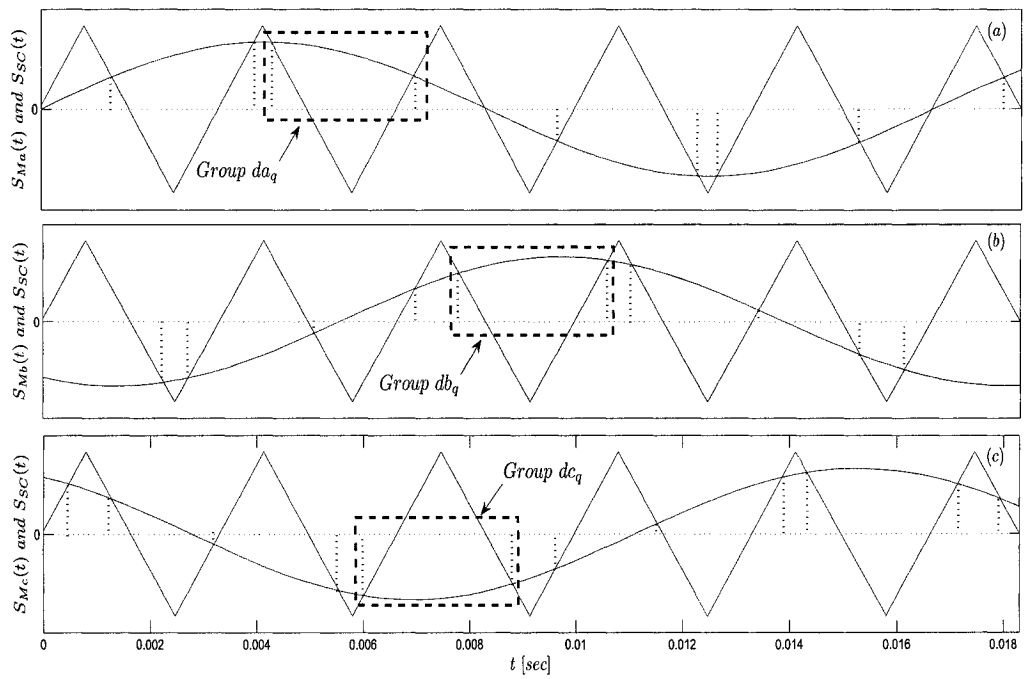

Figure 3.14: Non-uniform sample groups of the three reference-modulating signals $S_{Ma}(t)$, $S_{Mb}(t)$ and $S_{Mc}(t)$ created using the same triangular carrier signal $S_{SC}(t)$.

Each cycle of the carrier signal produces two samples for each sinusoidal

reference-modulating signal. The time intervals $[t_{ad1}, t_{ad2}]$, $[t_{bd1}, t_{bd2}]$ and $[t_{cd1}, t_{cd2}]$ are intervals of the group d of non-uniform recurrent samples of $S_{Ma}(t)$, $S_{Mb}(t)$ and $S_{Mc}(t)$, respectively. This representation is considered a line-to-line one due to the operation of a typical 3ϕ 3-leg six-pulse inverter [1, 2, 6]. In 3ϕ voltage-source (VS) six-pulse inverters, the voltage across each leg is switched from $+V_{DC}$ to $-V_{DC}$ alternately. Such an alternate switching causes each leg to change its connection with the other inverter legs. A leg appears in series with a parallel connection of the other two legs; when switched, it becomes in parallel with one leg and both are in series with third leg. The changes in the connections over a time interval of T_m are illustrated in Figure 3.15 [1].

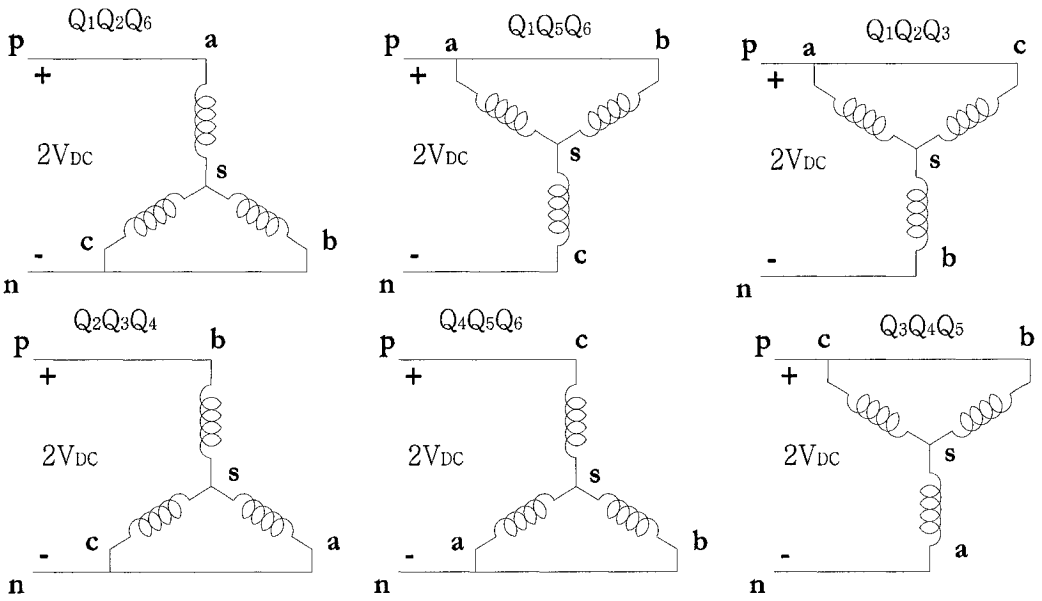

Figure 3.15: Inverter legs connection changes due to alternate switching of the DC supply [1].

A similar alternate switching takes place in 3ϕ current-source (CS) six-pulse inverters. The dc current flowing through each leg is switched alternately causing

inverter legs to undergo similar alternate connections [1].

The alternate switching of a 3ϕ inverter produces outputs that can be measured either as line-to-line or as line-to-neutral quantities. Figure 3.16 shows line-to-line and line-to-neutral quantities for a square wave switching operation [1].

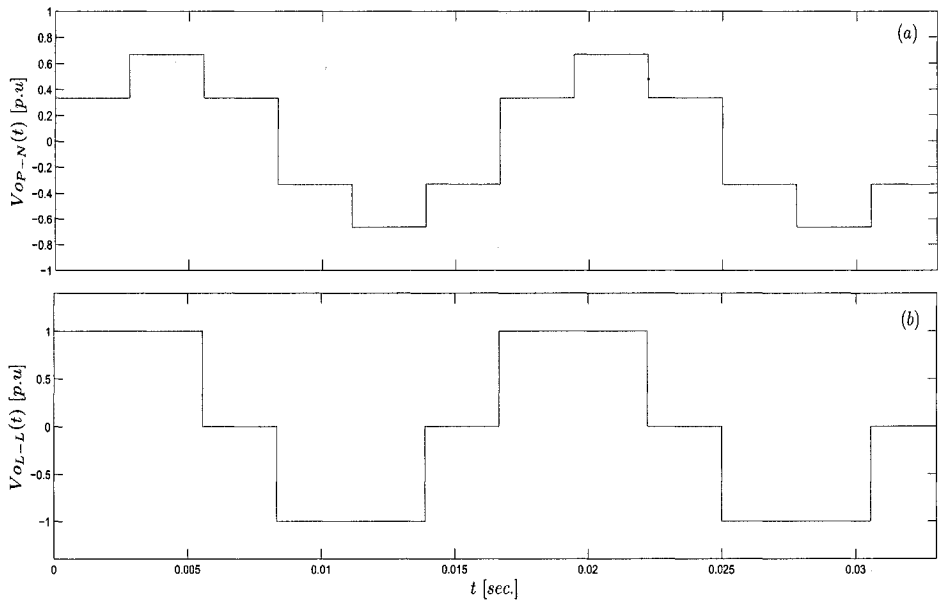

Figure 3.16: 3ϕ six-pulse inverter output voltages: (a) the line-to-neutral voltage (Vo_{P-N}) for one phase leg and (b) the output line-to-line voltage (Vo_{L-L}) for the same phase leg. The base value is Vo_{L-L}.

When a 3ϕ six-pulse inverter is switched through a modulation process, both line-to-line and line-to-neutral quantities appear as trains of ON switching pulses. Such outputs are shown in Figure 3.17 [1, 2, 4].

The previous description of a 3ϕ inverter operation indicates that switching signals are generated based on a line-to-line quantity for each leg. This result can be utilized in developing a sampling-based model of a 3ϕ inverter. As the three reference-modulating signals are sampled in a non-uniform recurrent manner, the reconstruction can be carried out as three independent reconstruction processes.

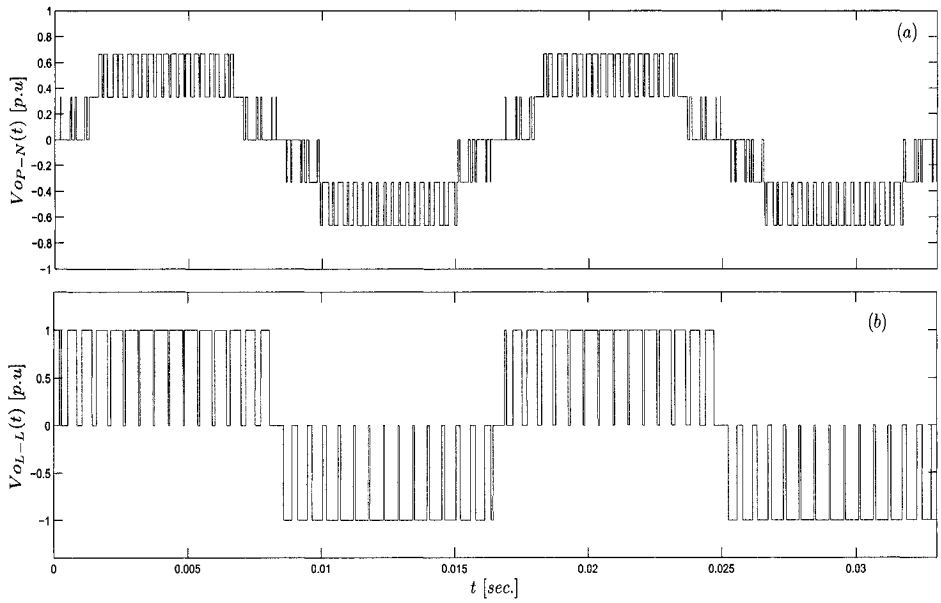

Figure 3.17: 3ϕ PWM six-pulse inverter output voltages: (a) per unit line-to-neutral voltage (Vo_{P-N}) and (b) per unit line-to-line voltage (Vo_{L-L}). The base value is Vo_{L-L}.

As a consequence, three switches located in different legs of the inverter are activated at any given time. One of these switches is replaced by another switch each α_μ, where α_μ is expressed as [1, 2]:

$$\alpha_\mu = \mu\omega_m \frac{T_m}{12};\ \mu = 1, 2, ..., 12 \tag{3.45}$$

where $\omega_m = 2\pi f_m$. Each switching element is activated for a period of $\frac{T_m}{2}$ $sec.$. This is necessary to avoid creating any short circuits in parallel with any inverter leg [1, 3]. The reconstruction of the three reference-modulating signals from their non-uniform recurrent samples is carried out using Lagrange interpolation functions,

which can be defined for sample group d as:

$$\lambda_{ad}(t) = \frac{S_{Ma}(t_{ad1})\,G_{ad}(t)}{G'_{ad}(t_{ad1})\,(t - t_{ad1})} + \frac{S_{Ma}(t_{ad2})\,G_{ad}(t)}{G'_{ad}(t_{ad2})\,(t - t_{ad2})} \tag{3.46}$$

$$\lambda_{bd}(t) = \frac{S_{Mb}(t_{bd1})\,G_{bd}(t)}{G'_{bd}(t_{bd1})\,(t - t_{bd1})} + \frac{S_{Mb}(t_{bd2})\,G_{bd}(t)}{G'_{bd}(t_{bd2})\,(t - t_{bd2})} \tag{3.47}$$

$$\lambda_{cd}(t) = \frac{S_{Mc}(t_{cd1})\,G_{cd}(t)}{G'_{cd}(t_{cd1})\,(t - t_{cd1})} + \frac{S_{Mc}(t_{cd2})\,G_{cd}(t)}{G'_{cd}(t_{cd2})\,(t - t_{cd2})} \tag{3.48}$$

where $G_{ad}(t)$, $G_{bd}(t)$ and $G_{cd}(t)$ are Lagrangian interpolating functions over the group d of non-uniform recurrent samples, and are given by:

$$G_{ad}(t) = t \prod_{p} \left(1 - \frac{t}{t_{adp}}\right) \tag{3.49}$$

$$G_{bd}(t) = t \prod_{p} \left(1 - \frac{t}{t_{bdp}}\right) \tag{3.50}$$

$$G_{cd}(t) = t \prod_{p} \left(1 - \frac{t}{t_{cdp}}\right) \tag{3.51}$$

Also, $G'_{ad}(t)$, $G'_{bd}(t)$ and $G'_{cd}(t)$ are the first derivatives of the Lagrangian interpolating functions over the sample group d that can be defined as:

$$G'_{ad}(t_{adp}) = \frac{dG_{ad}(t)}{dt}|_{t=t_{adp}} \tag{3.52}$$

$$G'_{bd}(t_{bdp}) = \frac{dG_{bd}(t)}{dt}|_{t=t_{bdp}} \tag{3.53}$$

$$G'_{cd}(t_{cdp}) = \frac{dG_{cd}(t)}{dt}|_{t=t_{cdp}} \tag{3.54}$$

where $p = 1, 2$. Time intervals $[t_{ad1}, t_{ad2}]$, $[t_{bd1}, t_{bd2}]$ and $[t_{cd1}, t_{cd2}]$ are time intervals for the three interpolating functions $\lambda_{ad}(t)$, $\lambda_{bd}(t)$ and $\lambda_{cd}(t)$ for the samples groups ad, bd and cd, respectively. Due to the periodicity of sample groups, these three interpolating functions are periodic with a period of T_m, and can be defined for

sample groups ad, bd and cd as follows:

$$\lambda_{ad}(t) = \begin{cases} \lambda_{ad}(t - rT_m) & t_{ad1} \leq t \leq t_{ad2},\ r \in \mathbb{Z} \\ 0 & \text{otherwise} \end{cases} \tag{3.55}$$

$$\lambda_{bd}(t) = \begin{cases} \lambda_{bd}(t - rT_m) & t_{bd1} \leq t \leq t_{bd2},\ r \in \mathbb{Z} \\ 0 & \text{otherwise} \end{cases} \tag{3.56}$$

$$\lambda_{cd}(t) = \begin{cases} \lambda_{cd}(t - rT_m) & t_{cd1} \leq t \leq t_{cd2},\ r \in \mathbb{Z} \\ 0 & \text{otherwise} \end{cases} \tag{3.57}$$

where $d = 1, 2, ..., \mathcal{D}$. It is to be noted that $\mathcal{D}$ is the number of sample groups over one cycle of each reference-modulating signal. Figure 3.18 shows $\lambda_a(t)$, $\lambda_b(t)$ and $\lambda_c(t)$ evaluated for two adjacent sample groups d and $d + 1$ for each reference-modulating signal.

The definition of the three interpolating functions leads to stating the sampling-based model of a 3ϕ six-pulse inverter as:

$$V_{ab}(t) = V_{DC} \sum_{r} \sum_{d=1}^{\mathcal{D}} \lambda_{ad}(t - rT_m) \tag{3.58}$$

$$V_{bc}(t) = V_{DC} \sum_{r} \sum_{d=1}^{\mathcal{D}} \lambda_{bd}(t - rT_m) \tag{3.59}$$

$$V_{ca}(t) = V_{DC} \sum_{r} \sum_{d=1}^{\mathcal{D}} \lambda_{cd}(t - rT_m) \tag{3.60}$$

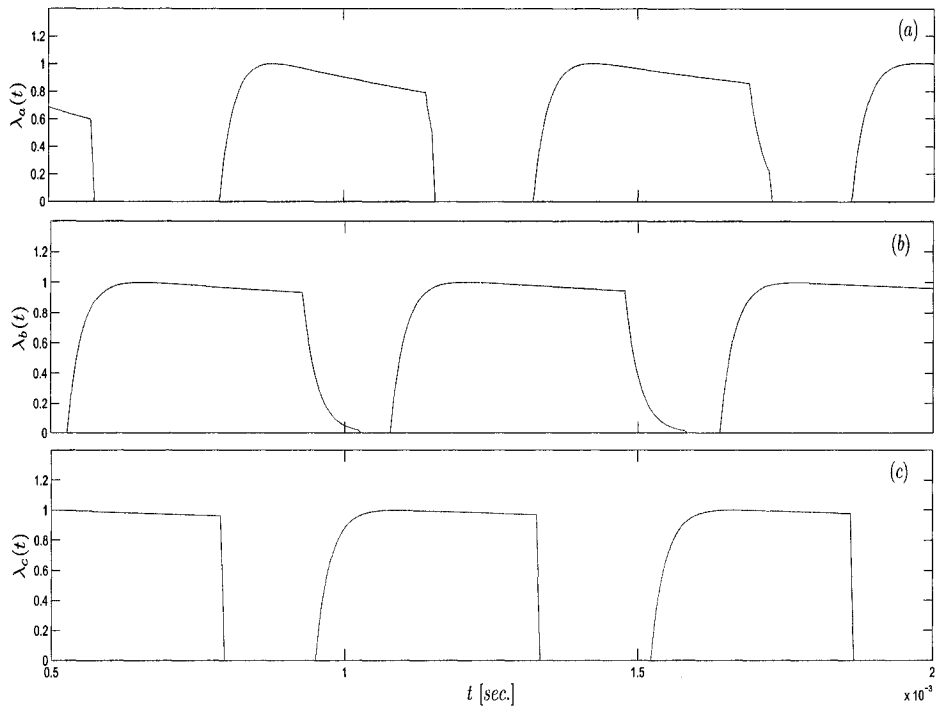

Figure 3.18: The three interpolation function for two adjacent groups of samples: (a) the interpolation function for phase a leg: $\lambda_a(t)$, (b) the interpolation function for phase b leg: $\lambda_b(t)$ and (c) the interpolation function for phase c leg: $\lambda_c(t)$.

Line-to-neutral output voltages can be derived from line-to-line ones as:

$$V_{an}(t) = \frac{V_{ab}\left(t - \frac{T_m}{12}\right)}{\sqrt{3}} \tag{3.61}$$

$$V_{bn}(t) = \frac{V_{bc}\left(t - \frac{T_m}{12}\right)}{\sqrt{3}} \tag{3.62}$$

$$V_{cn}(t) = \frac{V_{ca}\left(t - \frac{T_m}{12}\right)}{\sqrt{3}} \tag{3.63}$$

Figure 3.19 shows the three sets of interpolating functions used to reconstruct 3ϕ line-to-line output voltages for a 3ϕ VS PWM six-pulse inverter. Figure 3.20 shows the three sets of interpolating functions used to reconstruct 3ϕ line-to-neutral output voltages for a 3ϕ VS PWM six-pulse inverter.

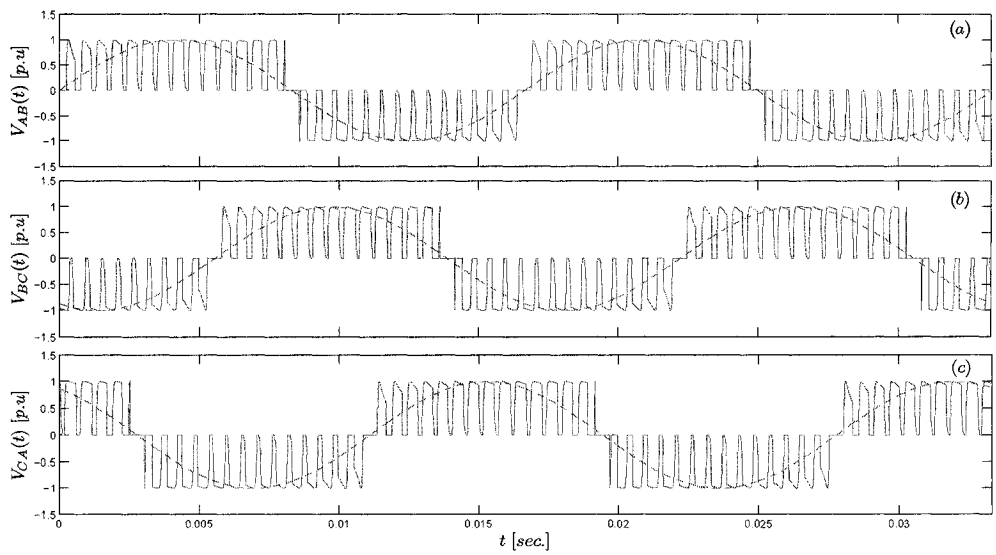

Figure 3.19: Reconstructing 3ϕ line-to-line output voltages for a 3ϕ VS PWM six-pulse inverter: (a) output of phase a leg: $V_{ab}(t)$, (b) output of phase b leg: $V_{bc}(t)$ and (c) output of phase c leg: $V_{ca}(t)$.

The developed non-uniform recurrent sampling-based approach is used to model a 3ϕ six-pulse inverter. Furthermore, the input data to this model includes f_m, f_c and the set of intersection points over one cycle of each reference-modulating signal $\{(t_{dp})_a\}$, $\{(t_{dp})_b\}$ and $\{(t_{dp})_c\}$, where $p = 1, 2$, $d = 1, 2, ..., \mathcal{D}$ [3]:

$$d = q + 1 \tag{3.64}$$

Phase A normalized line-to-line $V_{AB}(t)$ and line-to-neutral $V_{AN}(t)$ voltages obtained using the proposed sampling-based model are compared with phase A voltages obtained on the output of a 3ϕ six-pulse VS PWM inverter. Figure 3.21 shows inverter actual phase A voltages along with their spectra and phase A voltages obtained using the sampling-based model along with their spectra.

As shown in Figure 3.21, phase A voltages obtained using the sampling-based

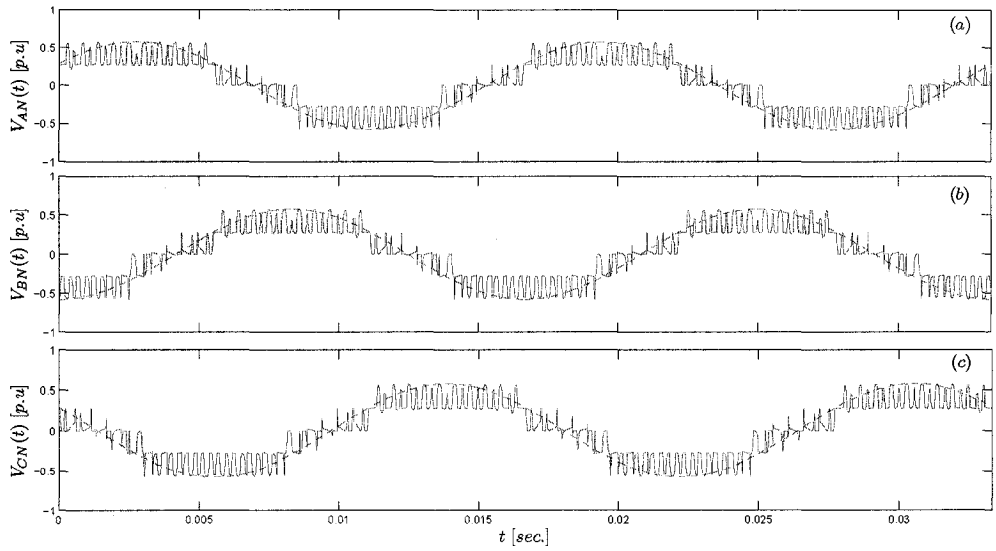

Figure 3.20: Reconstructing 3ϕ line-to-neutral output voltages for a 3ϕ VS PWM six-pulse inverter: (a) output of phase a: $V_{an}(t)$, (b) output of phase b: $V_{bn}(t)$ and (c) output of phase c: $V_{cn}(t)$.

model are almost identical to the actual voltages. Also, the spectra of both types of voltages are very close, which demonstrates the accuracy of the proposed non-uniform recurrent sampling-based model of 3ϕ inverters.

This chapter has provided a brief review of available inverter models along with their structures, conditions for validation, limitations and relations with switching techniques. Also, this chapter presented a new approach based on concepts from the sampling theorem to construct models for 1ϕ and 3ϕ inverters. The main concept from the sampling theorem has been the non-uniform recurrent sampling-reconstruction of CT signals. The connection between the sampling theorem and the wavelet theory can be utilized to develop an ideal sampling-reconstruction process for operating any inverter to achieve an optimal performance. The next chapter provides a method for optimizing the non-uniform recurrent sampling-reconstruction of CT signals using new wavelet basis functions

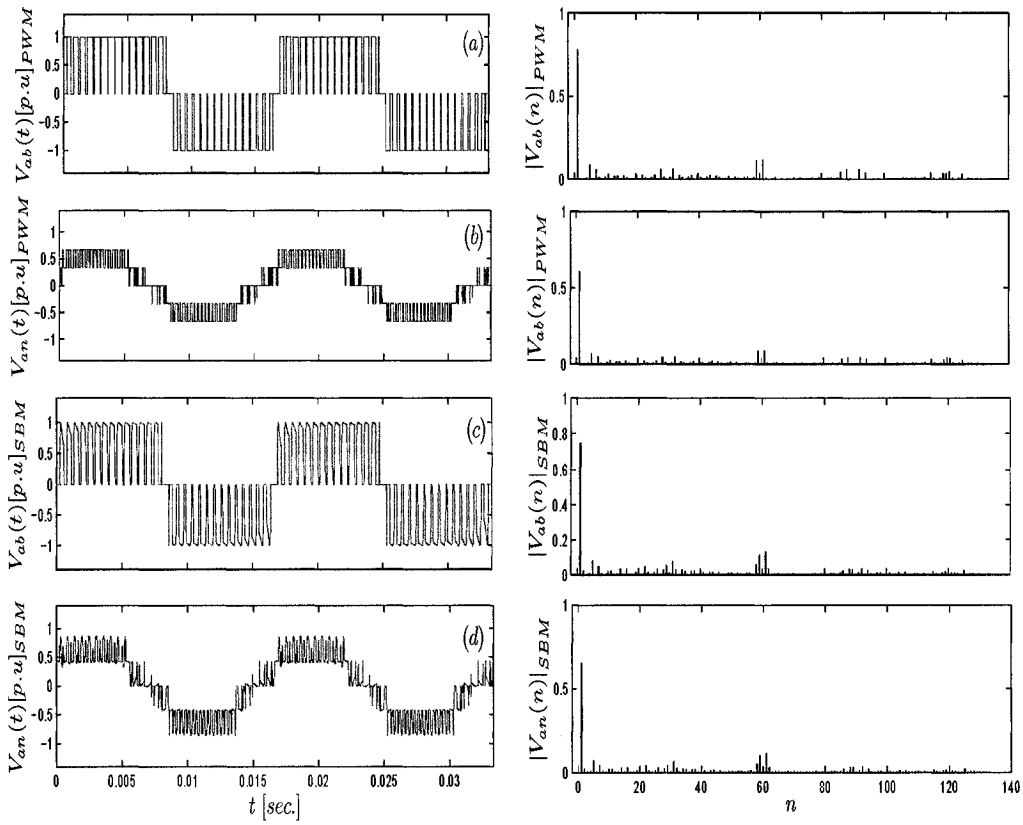

Figure 3.21: The output voltage of 3ϕ VS six-pulse inverter: (a) the output voltage of phase a leg: $V_{ab}(t)$ (actual inverter output) along with its spectrum, (b) the output voltage of phase a leg: $V_{an}(t)$ (actual inverter output) along with its spectrum, (c) the output voltage of phase a leg: $V_{ab}(t)$ using interpolating functions $\{\lambda_d(t)\}_{d=1,2,...,\mathcal{D}}$ along with its spectrum and (d) the output voltage of phase a leg: $V_{an}(t)$ using interpolating functions $\{\lambda_d(t)\}_{d=1,2,...,\mathcal{D}}$ along with its spectrum.

that can be employed for switching 1ϕ and 3ϕ inverters.

Chapter 4

Scale-Based Linearly-Combined Wavelet Bases

4.1 General

The previous chapter has presented a new model for both single-phase (1ϕ) and three-phase (3ϕ) inverters based on the non-uniform sampling-reconstruction of continuous-time (CT) signals. As chapter 2 has shown, sampling a CT signal can be represented as an N-dimensional approximation case. Such a representation has been used to interpret the sampling theorem in the context of the wavelet-based multiresolution analyses (MRA) [35, 41, 42, 44–46]. There are different types of wavelet basis functions that are capable of constructing MRAs, which can support sampling structures. However, such constructed MRAs are capable of supporting uniform sampling structures [41, 42, 45]. The different types of available wavelet basis functions along with the main characteristics of their associated MRAs are reviewed in this chapter. Furthermore, this chapter presents a new type

of wavelet basis functions that are capable of supporting a non-uniform recurrent sampling-reconstruction structure.

One of the most effective methods for decomposing CT signals is through a MRA that is constructed by orthogonal basis functions. In this type of signal processing, a CT signal is broken into orthogonal time-localized frequency channels (scales). The required orthogonal basis functions are generated by integer-indexed translations and dyadic (*powers of* 2) dilations of a single function that is known as the scaling function ($\phi(t)$) [47–51]. This scaling function $\phi(t)$ when dilated to scale j as $\phi_j(t)$ is orthogonal to its translations at that dilation (scale) j. The generated basis functions at scale j span a space V_j that provides an approximation to the signal in that space, which can be defined as [47–52]:

$$V_j(\varphi) = \text{clos}_{L^2} \langle \{\phi_{j,k}(t)\} \rangle, \quad j = 0, 1, 2, 3, .., \; k \in \mathbb{Z} \tag{4.1}$$

where the set $\{\phi_{j,k}(t)\}$ is given as:

$$\{\phi_{j,k}(t)\} = \left\{\phi_1\left(2^j t - k\right)\right\} j = 0, 1, 2.. \; k \in \mathbb{Z} \tag{4.2}$$

The notation clos_{L^2} is the closure of all linear combinations of all inner products of the set $\{\phi_{j,k}(t)\}$ over L^2. The clos operation can be defined as:
Definition: Let $\{g_n(x)\}$ be a collection of functions that can form a linear space $\mathcal{P}$ as [52]:

$$\mathcal{P} = \text{span}\{g_n(x)\} \tag{4.3}$$

The closure of the linear space $\mathcal{P}$ denoted by $\text{clos}_{L^2}\{\mathcal{P}\}$ can be stated as:
a function $f(x) \in \text{clos}_{L^2}\{\mathcal{P}\}$ if for every $\epsilon > 0$, there is a function $g(x) \in \mathcal{P}$ such

that:

$$\|f(x) - g(x)\|_2 < \epsilon \tag{4.4}$$

The collection of the spanned spaces $\{V_j\}$ allows the construction of a dyadic type multiresolution analysis (MRA). Since scaling basis functions $\{\phi_{j,k}\}$ are generated through shifting and dilating the scaling function $\phi(t)$, the spanned scaling spaces are nested such that [47, 48, 51]:

$$...V_{j-1} \subset V_j \subset V_{j+1} \subset V_{j+2}.... \tag{4.5}$$

Although the generated basis functions at a certain dilation (scale) j ($\{\phi_{j,k}\}$) are orthogonal, they are not complete with respect to $L^2(\mathbb{R})$. A more complete set $\{\phi_{j-1,k}\}$ is also orthogonal but is twice as dense. The difference between the successive spaces V_j and V_{j-1} yields a difference space spanned by another set of basis functions that are known as the wavelet basis functions. That is, for each space V_j, there exists an orthogonal complement space W_j, which is spanned by the set $\{\psi_{j,k}\}$, and can be defined as [47–52]:

$$W_j(\varphi) = \text{clos}_{L^2} \langle \{\psi_{j,k}(t)\} \rangle , \quad j = 1, 2, 3, .., \ k \in \mathbb{Z} \tag{4.6}$$

where $\{\psi_{j,k}(t)\}$ is defined as:

$$\{\psi_{j,k}(t)\} = \left\{\psi_1 \left(2^j t - k\right)\right\} j = 0, 1, 2.. \ k \in \mathbb{Z} \tag{4.7}$$

In general, a spanned space V_j in a MRA can be constructed using both spaces V_{j+1} and W_{j+1} as [47–51]:

$$V_j = V_{j+1} \bigoplus W_{j+1} \tag{4.8}$$

There are four major types of wavelet basis functions used in different signal and image processing applications. These types are:

1. Orthogonal wavelet basis function.
2. Semi-orthogonal wavelet basis functions.
3. Bi-orthogonal wavelet basis functions.
4. Shift-orthogonal wavelet basis functions.

These types of wavelet basis functions are capable of spanning spaces such as V_j and W_j above; a collection of these spaces allows the construction of dyadic-type MRAs. Furthermore, these constructed dyadic-type MRAs can support uniform ideal sampling processes [47–52].

This chapter introduces a new type of wavelet basis functions capable of spanning spaces that allow the construction of non-dyadic-type MRAs. The next section provides a review of conventional wavelet basis functions along with the characteristics of their spanned spaces and associated MRAs.

4.2 Wavelet Basis Functions

Wavelet Basis functions provide a system of coordinates in which several classes of linear operators are sparse. This system of coordinates is capable of expanding signals at different levels of resolution using coefficients in linear combinations of sets of basis functions. Temporal expansion is performed with contracted and high-frequency bases, while frequency analysis is performed with dilated and low-frequency ones. In general, wavelet basis functions can expand (decompose) signals and provide a time location for each frequency component present in such

decomposed signals. These basis functions are usually related to a single function that is known as the scaling function $\phi(t)$. A scaling function is a non-zero solution to a dilation equation of the form [47–49]:

$$\phi(t) = \sum_{k=0}^{N} c_k \phi(2t - k) \quad c_k \in \mathbb{R}, \;\; k \in \mathbb{Z} \tag{4.9}$$

As has been discussed in chapter 2, any function has to meet certain conditions to be categorized as a scaling function. If a function satisfies such conditions, then it is capable of generating a stable basis or *Riesz basis* of the form [47–51]:

$$\{\phi(t - k) : k \in \mathbb{Z}\} \tag{4.10}$$

A set of *Riesz basis* functions is capable of spanning a space $V(\phi)$ such that;

$$V(\phi) := \text{clos}_{L^2} \langle \{\phi(t - k)\} : k \in \mathbb{Z} \rangle \tag{4.11}$$

This property is valid if there exist two positive constants A and B called *Riesz bounds* for all functions $s(t) \in \mathcal{C}_n$ such that [51, 52]:

$$A \left\| s(t) \right\|_2^2 \leq \sum_k |\langle s(t), \phi(t - k) \rangle|^2 \leq B \left\| s(t) \right\|_2^2 \;\; \text{with } 0 < A \leq B < \infty \tag{4.12}$$

where $\mathcal{C}_n$ is the space of complex functions and the term $\|s(t)\|_2^2$ is given by [52]:

$$\|s(t)\|_2^2 = \int_t |s(t)|^2 \, dt \tag{4.13}$$

Scaling functions satisfying the *Riesz basis* condition can generate convenient

sets of basis functions through integer dilations and translations. Moreover, these generated basis functions are localized in time and frequency, which makes them capable of spanning complete linear spaces. In general, a set of functions is a basis if it can meet the following conditions [47–50, 56, 63].

- Completeness:

  A set $\{v_k(t)\}_{k\in\mathbb{Z}}$ is complete if its span is dense in a normed space V such that:

$$V = \text{clos}\left(\text{span}\left(\{v_k(t)\}\right)\right) \tag{4.14}$$

  where $\text{span}\left(\{v_k(t)\}\right)$ is given by:

$$\text{span}\left(\{v_k(t)\}\right) = \left\{\sum_{k\in\mathbb{Z}} \alpha_k v_k(t) \;|\alpha_k \in \mathbb{R} \text{ or } \mathbb{C}\right\} \tag{4.15}$$

  where $\mathbb{C}$ is the set of complex numbers.

- Linear independence:

  A set $\{v_k(t)\}_{k\in\mathbb{Z}}$ is linearly independent, if and only if none of the basis functions $v_k(t)$ is contained in the linear span of the other basis functions, which can be expressed as:

$$\sum_{k\in\mathbb{Z}} \alpha_k v_k(t) = 0 \quad \text{if and only if } \alpha_k = 0, \text{ for all } k \tag{4.16}$$

- Being a basis for the Hilbert space H:

  A set $\{v_k(t)\}_{k\in\mathbb{Z}}$ is a basis for a Hilbert space H if every function $f(t) \in H$ can

be uniquely expressed as [47, 51]:

$$f(t) = \sum_{k \in \mathbb{Z}} c_k v_k(t) \quad c_k \in \mathbb{C} \tag{4.17}$$

If a set of functions is complete and linearly independent, then it is a basis for Hilbert space H. However, the converse is not valid. Wavelet bases are special cases of Hilbert space basis functions with capabilities of constructing stable MRAs. This section provides brief descriptions of conventional classes of wavelet basis functions along with main characteristics of their spanned spaces.

4.2.1 Orthogonal Wavelet Basis Functions

Orthogonal basis functions are the first forms of well defined sets of basis functions used for processing signals. Fourier and Haar bases are among the earliest well defined and popular basis functions that have been used in different signal and image processing applications. The latest advancements in the theory of signal processing have made wavelets very popular tools in other engineering areas such power systems, where orthogonal wavelets have been used in developing protection systems and in improving power quality [41].

In general, orthogonal wavelets are characterized by the ability to generate sets of orthogonal basis functions. A set of functions $\{\chi_n(t)\}_{n \in \mathbb{Z}}$ is orthogonal if:

$$\langle \chi_d(t), \chi_s(t) \rangle = 0 \quad d \neq s \quad d, s \in \mathbb{Z} \tag{4.18}$$

where $\langle \chi_d(t), \chi_s(t) \rangle$ is the inner product of $\chi_d(t)$ and $\chi_s(t)$ that is given by [51]:

$$\langle \chi_d(t), \chi_s(t) \rangle = \int_{-\infty}^{\infty} \chi_d(t) \chi_s^*(t) dt \tag{4.19}$$

If a set of functions satisfies the conditions to be a basis for a Hilbert space H and satisfies the orthogonality condition, then it is an orthogonal basis for the Hilbert space H [48, 49, 51, 52, 62].

A scaling function $\phi(t)$ that satisfies the *Riesz basis* condition is capable of generating sets of basis functions in H. According to the $Mallat$ theory, any set of basis functions in H can be characterized by a pair of the form (Γ, A_M) [48, 52], where:

- A_M is an expanding matrix with its all eigenvalues $|\lambda_i| < 1$.
- Γ is an invariant lattice of A_M such that $A_M(\Gamma) \subseteq \Gamma$.

The matrix A_M is called dilation matrix for Γ, and it has $|\det(A_M)| \in \mathbb{R}$. The dilation equation for any scaling function $\phi(t)$ can be written in terms of the pair (Γ, A_M) as:

$$\phi(t) = \sum_{\gamma \in \Gamma} a_\gamma \left|\det(A_M)\right|^{\frac{1}{2}} \phi(t - \gamma) \tag{4.20}$$

The set $\{\phi(t-\gamma) : \gamma \in \Gamma\}$ is an orthogonal basis and the set of coefficients $\{a_\gamma\} \in \mathbb{R}$ or $\mathbb{C}$. The set $\{\phi(t-\gamma)\}$ can span a space $V(\phi)$. Also, high order spaces V_j can be spanned by related orthogonal sets of the form $\left\{\phi\left(A_M^j t - \gamma\right) : \gamma \in \Gamma\right\}$, $j = 0, 1, 2...$ These sets of orthogonal functions are bases in H, which imply that $\{V_j\}_{j=0,1,2..} \in H$. Among all orthogonal basis functions in H, orthonormal basis functions play a very important role in constructing wavelet-based MRAs [48, 49, 52, 57, 63].

A set of orthogonal basis functions can be changed into a set of orthonormal basis functions using the *Gram-Schmidt* orthogonalization procedure [51]. Using

this procedure, a set of orthonormal basis functions can be constructed from another set of orthogonal basis functions. Let $\{\mu_1, \mu_2, ..., \mu_g\}$ be a set of orthogonal basis functions that span a linear space Λ. A set of orthonormal basis functions $\{\lambda_1, \lambda_2, ..., \lambda_g\}$ can be constructed with the same span as $\{\mu_i\}$ as:

$$\lambda_1 = \frac{\mu_1}{\|\mu_1\|} \tag{4.21}$$

Then, recursively evaluate:

$$\lambda_i = \frac{\mu_i - v_i}{\|\mu_i - v_i\|} \tag{4.22}$$

where v_i is given by:

$$v_i = \sum_{p=0}^{g-1} \langle \lambda_p, \mu_i \rangle \lambda_p \tag{4.23}$$

The set of orthonormal basis functions $\{\lambda_1, \lambda_2, ..., \lambda_g\}$ obtained using the *Gram-Schmidt* procedure is capable of spanning the same linear space Λ that is spanned by the orthogonal set of basis functions [47–49, 52].

It is to be noted that if a set of orthonormal basis functions is generated from a *Riesz basis*, then the *Riesz bounds* become $A = B = 1$ [45]. These values of *Riesz bounds* satisfy the stability conditions, which have the following frequency-domain form [51].

$$\sum_{n=-\infty}^{\infty} \left|\hat{\phi}(\omega + 2\pi n)\right|^2 = 1 \tag{4.24}$$

where $\hat{\phi}(\omega)$ is the Fourier transform (FT) of $\phi(t)$.

A set of spaces $\{V_j\}_{j=0,1,2...}$ can be spanned by a set of orthonormal basis functions generated by a scaling function $\phi(t)$ such that:

$$\{\lambda_1, \lambda_2, ..., \lambda_g\} = \left\{\phi\left(A_M^j t - \gamma\right) : \gamma \in \Gamma\right\},\ j = 0, 1, 2.. \tag{4.25}$$

Such a set of spaces has an important characteristic that is:

$$\bigcap_{j=0,1,2\ldots} V_j = \{0\} \quad \text{and} \quad \bigcup_{j=0,1,2\ldots} V_j = L^2(\mathbb{R}) \tag{4.26}$$

This characteristic ensures the existence of $|\det(A_M)| - 1$ sets of basis functions that span a set of spaces $\{W_j\}_{j=1,2,..}$ as an orthogonal complement of $\{V_j\}_{j=1,2,..}$. This set of spaces $(\{W_j\})$ is spanned by sets of basis functions that are known as wavelet basis functions. These sets of basis functions are generated as an orthogonal complement to the set $\{\phi_j^k\}$ of basis functions as [48, 49]:

$$\psi_j(t) = \sum_{\gamma\in\Gamma} b_\gamma \left|\det(A_M)\right|^{\frac{1}{2}} \phi\left(A_M^j t - \gamma\right) \tag{4.27}$$

The function $\psi_j(t)$ is known as the wavelet function associated with $\phi_j(t)$ and the set of coefficients $\{b_\gamma\} \in \mathbb{R}$ or $\mathbb{C}$. The two sets of coefficients $\{a_\gamma\}$ and $\{b_\gamma\}$ are related as:

$$b_f = (-1)^f a_{\Gamma-f} \qquad 0 < f \leq \Gamma \tag{4.28}$$

The basis functions $\{\psi(t)^k\}$ span a linear space W that is orthogonal to V as [51, 52]:

$$W = \text{clos}\left(\text{span}\left(\{\psi^k(t)\}\right)\right) \tag{4.29}$$

where $\text{span}(\{\psi_k(t)\})$ is given by:

$$\text{span}(\{\psi_k(t)\}) = \left\{\sum_{k\in\mathbb{Z}} \beta_k \psi_k(t) \,|\beta_k \in \mathbb{R} \text{ or } \mathbb{C}\right\} \tag{4.30}$$

The collection of these spanned spaces constructs a multiresolution analysis (MRA). There are several common scaling functions that are capable of gener-

ating such sets of orthogonal and orthonormal basis functions, among them are *Daubechies* and *Haar* scaling functions [48, 49, 52].

4.2.2 Semi-Orthogonal Wavelet Basis Functions

The semi-orthogonal wavelet basis functions are very close to orthogonal ones in spanning multiresolution spaces ($\{W_j\}$ and $\{V_j\}$) [56]. These basis functions are characterized using B-splines that are related to fractional differential operators [65]. The semi-orthogonality condition forces wavelet spaces $\{W_j\}$ to be orthogonal to one another, which ensures that scaling spaces $\{V_j\}$ have the same orthogonal structure. However, scaling functions are selected to be generalized fractional B-splines, which are intimately related to a broad class of differential operators ∂_τ^γ with the γ^{th} order derivative having a shift τ [65, 66].

The generalized fractional B-spline of degree $\alpha \geq 0$ ($\alpha \in \mathbb{R}$) and a shift of τ can be best defined as [65, 66]:

$$\hat{\beta}_\tau^\alpha(\omega) = \left(\frac{1-e^{j\omega}}{-j\omega}\right)^{\frac{\alpha+1}{2}-\tau} \left(\frac{1-e^{-j\omega}}{j\omega}\right)^{\frac{\alpha+1}{2}+\tau} \tag{4.31}$$

A set of scaling spaces $\{(V_j)_{SO}\}$ can be defined using these basis functions as:

$$(V_j)_{SO} = \text{clos}\left\{\sum_k \epsilon_k \beta_\tau^\alpha(2^{-j}t-k) \mid \epsilon_k \in l^2(\mathbb{Z})\right\} \tag{4.32}$$

The fractional B-spline basis functions have *Riesz bounds* such that [65, 66]:

$$0 < A_{SO} \leq \sum_{k=-\infty}^{\infty} \left|\hat{\beta}_\tau^\alpha(\omega+2\pi k)\right|^2 \leq B_{SO} < \infty \tag{4.33}$$

where $\hat{\beta}_\tau^\alpha(\omega)$ is the FT of $\beta_\tau^\alpha(t)$. Complementary basis functions can be defined

using the fractional B-spline scaling function $\beta_\tau^\alpha(t)$ as:

$$\psi_\tau^\alpha(t) = \sum_{k\in\mathbb{Z}} w_k \beta_\tau^\alpha(2t-k) \quad w_k \in l^2(\mathbb{Z}) \tag{4.34}$$

In the frequency domain, this relation takes the following form:

$$\hat{\psi}_\tau^\alpha(\omega) = W(\omega)\frac{\hat{\beta}_\tau^\alpha(\omega)}{2} \tag{4.35}$$

A wavelet spanned space W_{SO} can be defined as:

$$(W_j)_{SO} = \text{span}\left\{\psi_\tau^\alpha(2^{-j}t)\right\} \tag{4.36}$$

The two spaces $(V_j)_{SO}$ and $(W_j)_{SO}$ are spanned by non-orthonormalized B-splines basis functions. These features make semi-orthogonal sets of basis functions always behave asymptotically as a fractional differential operator. Consequently, analyzing a signal $f(t)$ with wavelet semi-orthogonal basis functions yields samples of the operator ∂_τ^γ applied to a smoothed version of $f(t)$ [65, 66]:

$$\langle f(t), \psi(t-k)\rangle = \partial_\tau^\gamma \left\{\xi * f\right\}[k] \tag{4.37}$$

where $\xi[k]$ is a smoothing function defined in the frequency domain as:

$$\hat{\xi}(\omega) = \frac{\hat{\psi}(\omega)}{\hat{\partial}_\tau^\gamma(-\omega)} \tag{4.38}$$

where $\hat{\partial}_\tau^\gamma(\omega)$ is the FT of ∂_τ^γ operator, and is given by [65, 66]:

$$\hat{\partial}_\tau^\gamma(\omega) = (-j\omega)^{\frac{\gamma}{2}-\tau}(j\omega)^{\frac{\gamma}{2}+\tau} \tag{4.39}$$

It is to be noted that spaces spanned by sets of semi-orthogonal basis functions are orthogonal $\left((W_j)_{SO} \perp (V_j)_{SO}\right)$ for some values of γ that satisfy the following condition [43, 52, 65, 66]:

$$\gamma \approx \alpha + 1 \tag{4.40}$$

4.2.3 Bi-Orthogonal Wavelet Basis Functions

Orthogonal and semi-orthogonal basis functions provide series expansions of signals that have finite energy with a general form as.

$$f(t) = \sum_{j,k} d_{j,k}\psi_{j,k}(t) \quad f(t) \in L^2, \; d_{j,k} \in \mathbb{R} \text{ or } \mathbb{C} \tag{4.41}$$

The set of expansion coefficients $\{d_{j,k}\}$ has information about the time-frequency structure of the expanded signal $f(t)$. These coefficients can be determined as [44, 52]:

$$d_{j,k} = \int_{-\infty}^{\infty} f(t)\psi_{j,k}(t)dt = (E_\psi f)\left(\frac{k}{2^j}, \frac{1}{2^j}\right) \tag{4.42}$$

where $(E_\psi f)(a, b)$ is the integral wavelet transform (IWT) given as [45]:

$$(E_\psi f)(a, b) = \frac{1}{\sqrt{a}} \int_{-\infty}^{\infty} f(t)\psi\left(\frac{t-b}{a}\right) dt, \text{ with } (a, b) = \left(\frac{k}{2^j}, \frac{1}{2^j}\right) \tag{4.43}$$

In such expansion the function $\psi_{j,k}(t)$ is used to analyze the signal $f(t)$ as well as to provide time-locations of different frequencies present in it. Moreover, the spanned spaces $(W_j)_\psi$ and $(V_j)_\phi$ have to satisfy the orthogonality condition for every scale j such that [43, 47, 48, 52, 55, 65, 66]:

$$(W_j)_\psi \perp (V_j)_\phi \tag{4.44}$$

The fundamental concept of bi-orthogonal wavelet basis functions is based on selecting two scaling functions ($\phi(t)$ and $\tilde{\phi}(t)$) that are dual to each other such that [52–54, 65]:

$$\left\langle \phi(t-k), \tilde{\phi}(t-m) \right\rangle = \delta_{k,m} \quad k, m \in \mathbb{Z} \tag{4.45}$$

If wavelet functions ($\psi(t)$ and $\tilde{\psi}(t)$) are associated with $\phi(t)$ and $\tilde{\phi}(t)$ respectively, then these wavelet functions are dual such that [52–54, 65]:

$$\left\langle \psi(t-l), \tilde{\psi}(t-q) \right\rangle = \delta_{l,q} \quad l, q \in \mathbb{Z} \tag{4.46}$$

These dual functions can span four different spaces at each scale, which are $(V_j)_\phi$, $\left(\tilde{V}_j\right)_\phi$, $(W_j)_\psi$ and $\left(\tilde{W}_j\right)_\psi$. Some of these spaces satisfy the orthogonality conditions such that.

$$V_j \cap W_j = \{0\} \quad \text{Non-orthogonal} \tag{4.47}$$

$$\tilde{V}_j \cap \tilde{W}_j = \{0\} \quad \text{Non-orthogonal} \tag{4.48}$$

$$\tilde{V}_j \perp W_j \quad \text{Orthogonal} \tag{4.49}$$

$$\tilde{W}_j \perp V_j \quad \text{Orthogonal} \tag{4.50}$$

Bi-orthogonal scaling and wavelet functions can generate different sets of basis functions for analyzing and synthesizing signals. These different sets of basis functions can offer better representation than orthogonal and semi-orthogonal basis functions for certain types of signals [45, 52, 63].

4.2.4 Shift-Orthogonal Wavelet Basis Functions

Shift-orthogonal wavelet basis functions are sets of basis functions that span spaces, which are orthogonal with respect to translations in each scale. However, these spaces are not orthogonal with respect to dilations across scales. These basis functions are generated by scaling and wavelet functions that satisfy the duality principle (bi-orthogonality). The construction of shift-orthogonal scaling functions is based on selecting any two analysis and synthesis scaling functions $\zeta_a(t)$ and $\zeta_s(t)$ and defining an autocorrelation sequence $ac[k]$ as [57]:

$$ac_{s,a}[k] = \langle \zeta_a(t-k), \zeta_s(t) \rangle = \left(\zeta_a^T * \zeta_s\right)[k] \tag{4.51}$$

A synthesis scaling function $\phi_s(t)$ can be constructed as an orthogonalized version of $\zeta_s(t)$ as:

$$\phi_s(t) = \sum_{k \in \mathbb{Z}} \left(ac_{s,s}\right)^{1/2}[k] \zeta_s(t-k) \tag{4.52}$$

where $\left(ac_{s,s}\right)^{1/2}[k]$ is given by:

$$\left(ac_{s,s}\right)^{1/2}[k] \overset{DTFT}{\longleftrightarrow} \frac{1}{\sqrt{\hat{ac}_{s,s}(\omega)}} \tag{4.53}$$

The analysis scaling function $\phi_a(t)$ can be constructed as the dual of $\phi_s(t)$ as:

$$\phi_a(t) = \tilde{\phi}_s(t) = \sum_{k \in \mathbb{Z}} \left(\left(ac_{s,s}\right)^{1/2}[k] * \left(ac_{a,s}^T\right)^{-1}[k] \right) \zeta_a(t-k) \tag{4.54}$$

where $\left(ac_{a,s}^T\right)^{-1}[k]$ is given by:

$$\left(ac_{a,s}^T\right)^{-1}[k] \overset{DTFT}{\longleftrightarrow} \frac{1}{\hat{ac}_{a,s}(\omega)} \tag{4.55}$$

The definition of the analysis scaling function $\phi_a(t)$ indicates that it is not orthogonal to its own shifts. This feature can be expressed as [57]:

$$\langle \phi_a(t), \phi_a(t-k) \rangle = ac_\phi[k] \neq 0 \tag{4.56}$$

The sequence $ac_\phi[k]$ is an auto correlation sequence that can be determined as:

$$ac_\phi[k] = \left(ac_{s,s} * \left(ac_{a,s} * ac_{a,s}^T \right)^{-1} * ac_{a,a} \right)[k] \tag{4.57}$$

Two wavelet functions can be constructed using both $\zeta_a(t)$ and $\zeta_s(t)$ as :

$$\psi_s(t) = \sum_{k \in \mathbb{Z}} p[k] \zeta_s(2t-k) \tag{4.58}$$

$$\psi_a(t) = \sum_{k \in \mathbb{Z}} \hat{p}[k] \zeta_a(2t-k) \tag{4.59}$$

where the two sequences $p[k]$ and $\hat{p}[k]$ are extended dual filter sequences. The derivation of both $p[k]$ and $\hat{p}[k]$ is detailed in reference [57]. The two wavelet functions $\psi_a(t)$ and $\psi_s(t)$ satisfy the duality condition. Also, $\psi_a(t)$ wavelet function is not orthogonal to its own shifts, where a similar auto correlation sequence $ac_\psi[k]$ can be derived as a non-zero sequence. The spanned spaces by shift-orthogonal basis functions are not orthogonal to each other such that:

$$V_j \cap W_j = \{0\} \quad \text{Non-orthogonal} \tag{4.60}$$

$$\tilde{V}_j \cap \tilde{W}_j = \{0\} \quad \text{Non-orthogonal} \tag{4.61}$$

$$\tilde{V}_j \cap W_j = \{0\} \quad \text{Non-orthogonal} \tag{4.62}$$

$$\tilde{W}_j \cap V_j = \{0\} \quad \text{Non-orthogonal} \tag{4.63}$$

Different types of wavelet basis functions have been constructed for various applications in signal and image processing areas. The diversity of approaches employed in constructing such basis functions has been motivated to meet the requirements of various applications. In general, wavelet basis functions are capable of spanning spaces through integer dilations and translations. Furthermore, the collection of the spaces spanned by one set of basis functions defines its associated MRA. Each defined MRA can support only a uniform sampling-reconstruction process due to the dyadic (2^n dilations) nature of these spanned spaces. The review provided in the previous section has briefly described different types of available wavelet basis functions and the main characteristics of their associated MRAs.

In some applications of signal and image processing as well as switched power electronic converters, uniform sampling has been found redundant and may suffer from implementation problems. In such applications, non-uniform sampling has been found more practical for implementation [36, 63, 67]. As a result, new MRA structures are required to support non-uniform sampling-reconstruction processes that include the non-uniform recurrent sampling. The next section presents a new type of wavelet basis functions that are capable of spanning spaces to construct a non-dyadic type MRA to support non-uniform recurrent sampling-reconstruction processes.

4.3 Scale-Based Linearly-Combined Wavelet Basis Functions

The fundamental idea of constructing an MRA is to define a scale j such that sets of basis functions can span a collection of complete and dense spaces. Such sets of

basis functions are expressed as:

$$\{\{\phi_{j,k}(t)\},\{\psi_{j,k}(t)\}\} = \left\{\left\{\phi\left(2^j t-k\right)\right\},\left\{\psi\left(2^j t-k\right)\right\}\right\}, \quad j,k \in \mathbb{Z} \tag{4.64}$$

where $\phi(t)$ is a scaling function and $\psi(t)$ is a wavelet function. At each scale j, two spaces are spanned by one set of scaling basis functions $V_j(\phi)$, and one set of wavelet basis functions $W_j(\psi)$. These spaces can be related to the desired MRA as:

$$MRA(j) = V_j(\phi) \oplus W_j(\psi) \tag{4.65}$$

where $\oplus$ is the orthogonal sum operation. This structure of an MRA can be used to expand a signal $f(t)$ using sets of basis functions up to scale j as:

$$f(t) = \sum_{k\in\mathbb{Z}} \langle f(t), \phi_{j,k}(t)\rangle \, \tilde{\phi}_{j,k}(t) + \sum_{j\in\mathbb{Z}} \sum_{k\in\mathbb{Z}} \langle f(t), \psi_{j,k}(t)\rangle \, \tilde{\psi}_{j,k}(t) \tag{4.66}$$

where $\tilde{\phi}_{j,k} = \tilde{\phi}(2^j t - k)$ is a synthesis scaling function and $\tilde{\psi}_{j,k} = \tilde{\psi}(2^j t - k)$ is a synthesis wavelet function.

In general, any MRA characteristic depends on the nature of its nested spaces ($V_j(\phi)$ and $W_j(\psi)$) that are spanned by sets of basis functions. The scaling function is considered as the key element for defining the nature of an MRA [46, 52, 56, 63, 64]. Moreover, the convergence of the iterated filter banks and the denseness of the wavelet representation in L^2 are two major considerations that have to be taken into account when defining any scaling function [55, 61].

Definition 4.1: let $\varphi(t) = \varphi_1(t)$ be a scaling function defined as:

$$\varphi_j(t) = \phi_H\left(2^{j+1}t\right) + \phi_H\left(2^{j+1}\left(t-1+2^{-(j+1)}\right)\right), \quad j = 1,2,... \tag{4.67}$$

where $\phi_H(t)$ is the Haar scaling function. The selection of the Haar scaling function $\phi_H(t)$ as a building block to design the scale-based linearly-combined scaling function $\varphi(t)$ is based on the following features of $\phi_H(t)$ [35]:

- The Haar scaling function $\phi_H(t)$ is the only orthogonal scaling function of compact support.
- The Haar scaling function $\phi_H(t)$ is the basic building block for constructing scaling and wavelet functions.

The new designed scale-based linearly-combined scaling function $\varphi(t)$ is an Lth-order scaling function, *if and only if* it satisfies the following three conditions [56].

- *Condition* 1:

$$0 < A \leq \hat{a}_{\varphi}(\omega) < B < +\infty \tag{4.68}$$

where A and B are the *Riesz bounds* of φ. The term $\hat{a}_{\varphi}(\omega)$ is DTFT of $a[k]$, which is an autocorrelation sequence, and is defined as [52, 56]:

$$\hat{a}_{\varphi}(\omega) = \sum_{k \in \mathbb{Z}} |\hat{\varphi}(\omega + 2\pi k)|^2 \tag{4.69}$$

where

$$\hat{\varphi}(\omega) \overset{FT}{\longleftrightarrow} \varphi(t) \tag{4.70}$$

$$\hat{a}_{\varphi}(\omega) \overset{FT}{\longleftrightarrow} a[k] \tag{4.71}$$

- *Condition* 2:

$$\varphi(t) = \sqrt{2}\sum_{k\in\mathbb{Z}} h_\varphi[k]\varphi(2t-k) \tag{4.72}$$

where $h_\varphi[k]$ is the refinement filter associated with $\varphi(t)$.

- *Condition* 3: $\hat{\varphi}(0) = 1$ and

$$\frac{d^m\hat{\varphi}(\omega)}{d\omega^m}|_{\omega=2\pi k} = 0 \tag{4.73}$$

where $k \neq 0$, $m = 0, 1, ..., L-1$ and L is the number of vanishing moments of $\varphi(t)$.

For condition 1, $\hat{\varphi}(\omega)$ can be determined using Fourier transform properties and $\hat{\phi}_H(\omega)$ as:

$$\hat{\varphi}(\omega) = \hat{\phi}_H\left(\frac{\omega}{4}\right) + \left(e^{-i\frac{3}{4}\omega}\right)\hat{\phi}_H\left(\frac{\omega}{4}\right) \tag{4.74}$$

The auto correlation sequence $\hat{a}_\varphi(\omega)$ can be expressed as:

$$\hat{a}_\varphi(\omega) = \sum_k \left|\hat{\phi}_H\left(\frac{\omega+2\pi k}{4}\right) + \left(e^{-i\frac{3}{4}(\omega+2\pi k)}\right)\hat{\phi}_H\left(\frac{\omega+2\pi k}{4}\right)\right|^2 \tag{4.75}$$

$$\hat{a}_\varphi(\omega) = \sum_k \left|\hat{\phi}_H\left(\frac{\omega+2\pi k}{4}\right)\left(1 + e^{-i\frac{3}{4}(\omega+2\pi k)}\right)\right|^2 \tag{4.76}$$

The auto correlation sequence $\hat{a}_\varphi(\omega)$ is bounded, since $\hat{\phi}_H(\omega)$ is also bounded. Furthermore, the term $\hat{\phi}_H\left(\frac{\omega+2\pi k}{4}\right)$ is a decaying function as $\omega \longrightarrow \infty$. The refinement filter $h_\varphi[k]$ can be determined by solving the refinement equation from condition 2 that depends on $\phi_H(t)$ [56, 67]:

$$\varphi(t) = \sqrt{2}\sum_{k=0}^{L-1} h_\varphi[k]\varphi(2t-k) \tag{4.77}$$

The refinement equation can be rewritten as:

$$\phi(4t) + \phi(4t-3) = \sqrt{2}\sum_{k=0}^{L-1} h_\varphi[k]\phi(8t-k) + \sqrt{2}\sum_{k=0}^{L-1} h_\varphi[k]\phi(8t-6-k) \quad (4.78)$$

Haar scaling function has (L=2), which makes scaling filter coefficients as:

$$h_\varphi = [0.7071 \;\; 0.7071] \quad (4.79)$$

The scaling filter $h_\varphi[k]$ is identical to the Haar scaling filter $(h_\phi)_H[k]$. This result comes due to the linear combination approach in designing $\varphi(t)$.

For condition 3, the derivative of $\hat{\varphi}(\omega)$ will be (for $j = 1$):

$$\frac{d\hat{\varphi}}{d\omega} = \frac{1}{4}\left[\frac{d\hat{\phi(\omega}/4)}{d\omega}\left(1 + e^{-i\frac{3}{4}\omega}\right) - i3e^{-i\frac{3}{4}\omega}\hat{\phi}(\omega/4)\right] \quad (4.80)$$

The value of the derivatives of $\hat{\varphi}(\omega)$ at $\omega = 2\pi k$ are zeros, since $\phi_H(t)$ satisfies the conditions of a scaling function, which include [52, 56]:

$$\frac{d^m\hat{\phi}_H}{d\omega^m}|_{\omega=2\pi k} = 0, \; m = 0, 1, \; k = 0, 1, 2, ... \quad (4.81)$$

As a result:

$$\frac{d^m\hat{\varphi}}{d\omega^m}|_{\omega=2\pi k} = 0, \; m = 0, 1, \; k = 0, 1, 2, ... \quad (4.82)$$

The scale-based linearly-combined scaling function $\varphi(t)$ is shown in Figure 4.1 along with the magnitude of its FT ($\hat{\varphi}(\omega)$) and $\left|\frac{d^m\hat{\varphi}}{d\omega^m}\right|$ (the magnitude of the derivative of its FT).

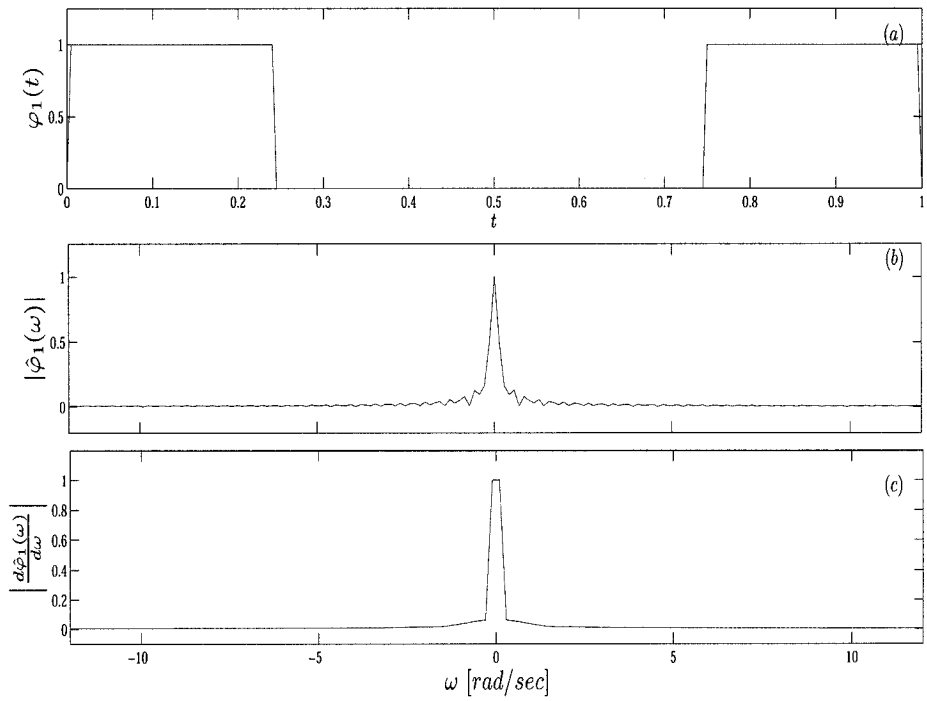

Figure 4.1: The scale-based linearly-combined scaling function $\varphi(t)$ for $j = 1$: (a) the scaling function $\varphi_1(t)$, (b) the magnitude of its FT $|\hat{\varphi}_1(\omega)|$ and (c) the magnitude of the derivative of $\hat{\varphi}(\omega)$ $\left(\left|\frac{d\hat{\varphi}_1(\omega)}{d\omega}\right|\right)$.

4.3.1 Balancing the Order of $\varphi(t)$

The refinement filter associated with the scaling function $\varphi(t)$ is identical to the refinement filter associated with the Haar scaling functions $\phi_H(t)$. This feature is ensured by the linear-combination approach to construct $\varphi(t)$ using $\phi_H(t)$. Also, this feature ensures that both scaling functions $\varphi(t)$ and $\phi_H(t)$ have the same number of vanishing moments. Furthermore, the refinement filter and the number of vanishing moments are consistent due to the scale-based shift of $(\phi_H(t))_{j+1}$. This shift in $\phi_H(t)$ when constructing $\varphi_j(t)$ provides a balance of the order of $\varphi_j(t)$ with respect to the used $\phi_H(t)$ [67]. As a consequence, $\varphi(t)$ will have similar properties as $\phi_H(t)$, in particular, the ability to span closed spaces $\{V_j(\varphi)\}$.

The scale-based linearly-combined scaling function $\varphi(t)$ features of the scaling filter and the number of vanishing moments make it capable of generating basis functions at each scale. These basis functions can be defined as:

$$\{\varphi_{j,k}(t)\} = \left\{\varphi_1\left(2^{j-1}t - k\right)\right\} j = 1, 2.. \; k \in \mathbb{Z} \tag{4.83}$$

The generated basis functions $\{\varphi_{j,k}(t)\}$ span spaces $\{V_j\}$, from a collection of which a MRA can be constructed. However, this constructed MRA will not be dyadic due to the scale-based shift inherent in $\varphi(t)$, as well as due to the fact that as $j \rightarrow \infty$, $\varphi(t) \nrightarrow \delta(t)$.

If a CT periodic signal $x_c(t) \neq 0, \; t \in [t_{1j}, t_{2j}]$ then the inner product $\langle x_c(t), \varphi_{1,k}(t)\rangle$ will have a non-zero value. Limits of the interval of support $[t_1, t_2]$ are defined as:

$$\begin{aligned} t_{1j} &= d + 2^{-(j+1)} \\ t_{2j} &= d + 1 - 2^{-(j+1)}, \; d = 1, 2, ..., \mathcal{D}_\varphi, \; j = 1, 2... \end{aligned} \tag{4.84}$$

where $\mathcal{D}_\varphi$ is the number of sample groups created by $\varphi(t)$ over one period of $S_M(t)$. It is to be noted that $\varphi_j(t)$ creates one group of non-uniform samples at each translation k. However, for the dc-ac inverter successive ON switching pulses have to be of different widths. These pulses aim to reconstruct the CT signal from its non-uniform sample groups. As a consequence, a sample group d is created by $\varphi_1(t)$ scaled to a different scale j that aims to generate different switching pulses over each period of the sampled CT signal $x_c(t)$. The constructed MRA can be generalized as [67]:

$$V_j = \{x_c(t) \neq 0, t \in [t_{1j}, t_{2j}] \; ; \; j = 1, 2, 3, ..\} \tag{4.85}$$

provided that $x_c(t)$ is continuous and differentiable over the interval $[t_{1j}, t_{2j}]$. The generalized MRAs spaces can be formulated as:

$$V_j(\varphi) = \text{clos}_{L^2}\left(\{\varphi_{j,k}(t)\}\right), \quad j = 1, 2, 3, .., \; k \in \mathbb{Z} \tag{4.86}$$

The scaling function $\varphi(t)$ is composed of two Haar scaling functions. This indicates that if $\varphi(t)$ is used as a sampling function, two samples will be created at each translation. Each translation depends on both k and the scale-based quantity $(1 - 2^{-(j+1)})$. These translations cause the spacings between samples to be non-uniform. As a consequence, the constructed non-dyadic-type MRA can support a non-uniform sampling case.

4.3.2 Scale-Based Linearly-Combined Wavelet Function

The refinement filter associated with the designed scaling function $\varphi(t)$ is determined, which makes it possible to define a wavelet function associated with $\varphi_j(t)$. Using the refinement equation, a wavelet function can be defined as [55, 65]:

$$\psi_\varphi(t) = \sqrt{2}\sum_{k=0}^{L-1} g_\varphi[k]\varphi(2t - k) \tag{4.87}$$

where $\varphi(2t)$ is given by:

$$\varphi(2t) = \phi_H(8t) + \phi_H(8t - 6) \tag{4.88}$$

The vector $g_\varphi[k]$ is related to the refinement filter $h_\varphi[k]$ by the following relation [51, 56, 67]:

$$g_\varphi[k] = (-1)^k h_\varphi[L - k] \quad k = 0, 1, ..., L - 1 \tag{4.89}$$

Evaluating equation (4.89) yields that $g_\varphi[k] = g_\phi[k]$. As a consequence, the wavelet function $\psi_\varphi(t)$ can be expressed as:

$$\psi_\varphi(t) = \sqrt{2}\sum_{k=0}^{L-1} g_\varphi[k]\phi_H(8t-k) + \sqrt{2}\sum_{k=0}^{L-1} g_\varphi[k]\phi_H(8t-6-k) \tag{4.90}$$

Recalling the relation between Haar scaling and wavelet functions as:

$$\psi_H(t) = \sqrt{2}\sum_{k=0}^{L-1} g_H[k]\phi_H(2t-k) \tag{4.91}$$

Using the fact that $g_\varphi[k] = g_H[k]$, the scale-based linearly-combined wavelet function can be expressed in terms of Haar wavelet function $\psi(t)$ as:

$$(\psi_\varphi)_j(t) = \psi_H\left(2^{j+1}t\right) + \psi_H\left(2^{j+1}\left(t-1+2^{-(j+1)}\right)\right) \tag{4.92}$$

Figure 4.2 shows scale-based linearly-combined wavelet function $\psi_\varphi(t)$ and the magnitude of its Fourier transform $\hat{\psi}_\varphi(\omega)$.

A signal can be expanded using the generated basis functions by both $\varphi(t)$ and $\psi_\varphi(t)$ as [65]:

$$f(t) = \sum_j \left(\sum_k \langle f(t), \varphi_{j,k}(t)\rangle \tilde{\varphi}_{j,k}(t) + \sum_k \left\langle f(t), (\psi_\varphi)_{j,k}(t)\right\rangle \left(\tilde{\psi}_\varphi\right)_{j,k}(t) \right) \tag{4.93}$$

where $\tilde{\varphi}_{j,k}(t)$ is a synthesis scaling function and $\left(\tilde{\psi}_\varphi\right)_{j,k}(t)$ is the synthesis wavelet function at scale j. The inner product term can be written as:

$$\langle f(t), \varphi_{j,k}(t)\rangle = \int_0^{t_{1j}} f(t)\left(\phi_H\right)_k\left(2^{j+1}t\right)dt + \int_{t_{2j}}^{1} f(t)\left(\phi_H\right)_k\left(2^{j+1}\left(t-1+2^{-(j+1)}\right)\right)dt \tag{4.94}$$

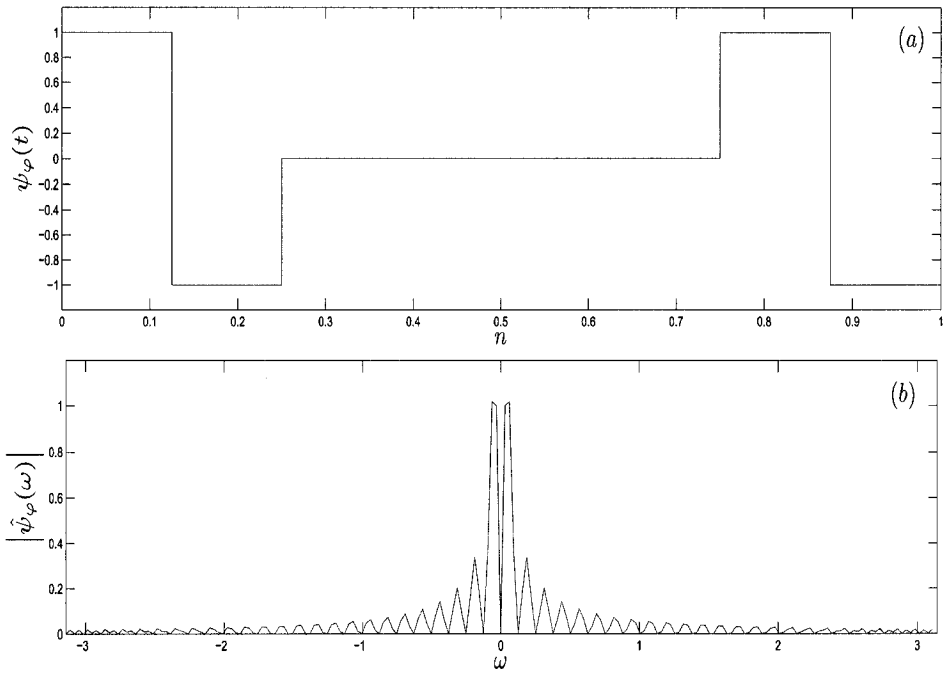

Figure 4.2: Scale-Based Linearly-Combined wavelet functions: (a) $\psi_\varphi(t)$ and (b) the magnitude of its FT $\left|\hat{\psi}_\varphi(\omega)\right|$.

where $t_{1j} = d + 2^{-(j+1)}$ and $t_{2j} = d + 1 - 2^{-(j+1)}$. In general, expanding any function as a linear combination of weighted basis functions is a form of series expansion. For the case of the scale-based linearly-combined basis functions, each coefficient of such a series is composed of two terms that offer a better and more accurate representation of signals.

4.3.3 Construction of Scale-Based Linearly-Combined Synthesis Scaling Functions

The linearly combined scaling function $\varphi(t)$ is defined along with its associated refinement filter $h_\varphi[k]$ and wavelet function $\psi_\varphi(t)$. The remaining step toward the

complete characterization of the proposed basis functions is to define a linearly-combined synthesis scaling and wavelet functions.

The series expansion approach can be used to define a synthesis scaling $\tilde{\varphi}(t)$ and wavelet $\tilde{\psi}_{\varphi}(t)$ functions. The series expansion of a CT signal $f(t)$ can be written as:

$$\begin{aligned} f(t) = & \sum_{j=1,2..} \sum_{k\in\mathbb{Z}} \left\langle f(t), (\phi_H)_k \left(2^{j+1}t\right)\right\rangle \tilde{\varphi}_{j,k}(t) \\ & + \sum_{j=1,2..} \sum_{k\in\mathbb{Z}} \left\langle f(t), (\phi_H)_k \left(2^{j+1}\left(t-1+2^{-(j+1)}\right)\right)\right\rangle \tilde{\varphi}_{j,k}(t) \\ & + \sum_{j=1,2..} \sum_{k\in\mathbb{Z}} \left\langle f(t), (\psi_H)_k \left(2^{j+1}t\right)\right\rangle \left(\tilde{\psi}_{\varphi}\right)_{j,k}(t) \\ & + \sum_{j=1,2..} \sum_{k\in\mathbb{Z}} \left\langle f(t), (\psi_H)_k \left(2^{j+1}\left(t-1+2^{-(j+1)}\right)\right)\right\rangle \left(\tilde{\psi}_{\varphi}\right)_{j,k}(t) \end{aligned} \tag{4.95}$$

The previous two summations can be expressed in terms of their inner products over the interval $[0, t_{1j}]$ as:

$$\begin{aligned} \sum_{k\in\mathbb{Z}} \left\langle f(t), (\phi_H)_k \left(2^{j+1}t\right)\right\rangle \tilde{\varphi}_{j,k}(t) &= \sum_{k\in\mathbb{Z}} \left(\int_0^{t_{1j}} f(t)\phi_H\left(2^{j+1}t-k\right)dt\right) \tilde{\varphi}\left(2^j t-k\right) \\ \sum_{k\in\mathbb{Z}} \left\langle f(t), (\psi_H)_k \left(2^{j+1}t\right)\right\rangle \left(\tilde{\psi}_{\varphi}\right)_{j,k}(t) &= \sum_{k\in\mathbb{Z}} \left(\int_0^{t_{1j}} f(t)\psi_H\left(2^{j+1}t-k\right)dt\right) \tilde{\psi}_{\varphi}\left(2^j t-k\right) \end{aligned} \tag{4.96}$$

These two inner products have non-zero values over the interval $[0, t_{1j}]$ that can be interpreted as taking one sample from the signal $f(t)$ over that interval. The other two summations can be expressed in terms of their inner products over the interval $[t_{2j}, 1]$ as:

Let $u_j = 1 + 2^{j+1}$

$$\sum_{k\in\mathbb{Z}} \left\langle f(t), (\phi_H)_k \left(2^{j+1}t - u_j\right)\right\rangle \tilde{\varphi}_{j,k}(t) = \sum_{k\in\mathbb{Z}} \left(\int_{t_{2j}}^{1} f(t)\phi_H \left(2^j t - u_j - k\right) dt \right) \tilde{\varphi}_{j,k}(t)$$

$$\sum_{k\in\mathbb{Z}} \left\langle f(t), (\psi_H)_k \left(2^{j+1}t - u_j\right)\right\rangle \left(\tilde{\psi}_{\varphi}\right)_{j,k}(t) = \sum_{k\in\mathbb{Z}} \left(\int_{t_{2j}}^{1} f(t)\psi_H \left(2^j t - u_j - k\right) dt \right) \left(\tilde{\psi}_{\varphi}\right)_{j,k}(t) \tag{4.97}$$

These inner products have non-zero values over the interval $[t_{2j}, 1]$, which again can be interpreted as taking another sample of the signal $f(t)$ over the interval $[t_{2j}, 1]$. The summations represent interpolation process to synthesize $f(t)$ from the samples taken by $\varphi(t)$ using $\tilde{\varphi}_{j,k}(t)$ and $\left(\tilde{\psi}_{\varphi}\right)_{j,k}(t)$ basis functions over the interval $[t_{1j}, t_{2j}]$.

Three possibilities can be considered for $\tilde{\varphi}_j(t-k)$, which are:

- $\tilde{\varphi}_j(t-k)$ has an interval of support as $[0, 1]$, which indicates that $\tilde{\varphi}_j(t-k) = \phi_j(t-k)$. This possibility can not be true due to the structure of $\varphi_j(t-k)$.

- $\tilde{\varphi}_j(t-k) = \varphi_j(t-k)$, which indicates that there will be cross inner products such as:
  $\left\langle \phi_j(t-k)\tilde{\phi}_j\left(t-k-\left(1-2^{-(j+1)}\right)\right)\right\rangle \neq 0.$
  This possibility also can not be true due to the orthogonality of the used scaling functions $\phi_H(t)$.

- A combination of the previous possibilities, where $\tilde{\varphi}_{j,k}(t)$ has an interval of support related to $\varphi_{j,k}(t)$ can meet orthogonality conditions, the dilation equation and the structure of $\varphi(t)$. Moreover, $\tilde{\varphi}_{j,k}(t)$ has to have a continuity over its interval of support. This possibility can meet the conditions required for $\tilde{\varphi}_{j,k}(t)$ to be a scaling function.

Using the third possibility, the synthesis scaling function can be defined as:

$$\tilde{\varphi}_j(t) = \phi_H\left(2^j t\right) - \left(\phi_H\left(2^{j+1}t\right) + \phi_H\left(2^{j+1}t - u_j\right)\right) \tag{4.98}$$

The above equation can be expressed in terms of $\varphi_j(t)$ as:

$$\tilde{\varphi}_j(t) = \phi_H\left(2^j t\right) - \varphi_j(t),\ j = 1, 2, ... \tag{4.99}$$

The scale-based linearly-combined scaling and wavelet functions are capable of spanning orthogonal spaces at each scale j such that:

$$W_j\left(\psi_\varphi\right) \perp V_j(\varphi) \tag{4.100}$$

Although the spanned spaces are orthogonal, the constructed MRA is not a dyadic one. This nature of such spaces can construct MRAs for supporting non-uniform sampling forms. The next section presents a non-dyadic MRA structure using scale-based linearly-combined basis functions.

4.4 Non-Dyadic MRA Structure

The defined linearly-combined scaling function $\varphi(t)$ can generate sets of basis functions that span successive spaces $\{V_j(\varphi)\}$. Also, the wavelet function $\left(\psi_\varphi\right)_j(t)$, associated with $\varphi(t)$, can generate sets of basis functions that span successive spaces $\{W_j\left(\psi_\varphi\right)\}$. These spaces satisfy orthogonality and completeness conditions that is:

$$V_j(\varphi) = V_{j-1}(\varphi) \bigoplus W_{j-1}\left(\psi_\varphi\right) \tag{4.101}$$

The set of spaces $\{V_j(\varphi)\}$, composed of orthogonal spaces spanned by scaling and wavelet basis functions, has a nested structure such that:

$$... \subset V_{-1} \subset V_0 \subset V_1 \subset V_2 ... \subset V_m \subset L^2(\mathbb{R}) \tag{4.102}$$

The collection of such spanned spaces constructs a stable MRA. It is to be noted that both $\varphi(t)$ and $\psi_\varphi(t)$ have dilations as the the level j changes. Also, both of $\varphi(t)$ and $\psi_\varphi(t)$ have translations that are created by the change in k as well as $(1 - 2^{-(j+1)})$. These types of dilations and translations create a unique non-dyadic MRA. Such a MRA can be employed to support non-uniform sampling forms. The next subsection provides the non-uniform recurrent sampling form that is supported by the developed non-dyadic MRA.

4.4.1 MRA for Non-Uniform Recurrent Sampling

The scale-based linearly-combined scaling function $\varphi(t)$ creates two samples over its interval of support. Moreover, the spacing between these samples depends on the scale j. A CT signal $x_c(t)$ can be reconstructed from its non-uniform recurrent samples $x_c(t_p)$ using the Lagrange general interpolation formula as [36]:

$$x_c(t) = \sum_{n=-\infty}^{\infty} \sum_{p=1}^{2} x(t_p) \frac{G(t)}{G'(t_p)(t - t_p)} \tag{4.103}$$

An interpolation function $\lambda(t)$ can be defined as:

$$\lambda_j(t) = \sum_{p=1}^{2} x(t_{pj}) \frac{G(t)}{G'(t_{pj})(t - t_{pj})} \tag{4.104}$$

The two samples created by $\varphi(t)$ at each scale j can be considered as one group

of non-uniform samples that can be described by:

$$\{t_{pj}\} = \left\{t_{1j} = d + 2^{-(j+1)}, t_{2j} = d + 1 - 2^{-(j+1)}\right\},\ p = 1, 2,\ d = 1, 2..., \mathcal{D}_{\varphi} \quad (4.105)$$

The set of sampling instants $\{t_{pj}\}$ for the sample group d that is related to the scale j, can be used to evaluate the function $G(t)$ at the scale j, $(j = 1, 2, 3, ..., \infty)$ as:

$$G_j(t) = t\left(1 - \frac{t}{2^{-j-1}}\right)\left(1 - \frac{t}{1 - 2^{-j-1}}\right) \quad (4.106)$$

It should be noted that the value of t_0 is considered *zero* to indicate the beginning of each cycle of the sampled CT signal $x_c(t)$. The function $G(t)$ can be simplified to:

$$G_j(t) = t - \frac{2^{2j+2}t^2}{2^{j+1} - 1} + \frac{2^{2j+2}t^3}{2^{j+1} - 1} \quad (4.107)$$

Evaluating the derivative of $G(t)$ at t_1 and t_2 gives the following values:

$$G'_j(t_{1j}) = \frac{1}{2^{j+1} - 1} - 1 \quad (4.108)$$

$$G'_j(t_{2j}) = 2^{j+1} - 2 \quad (4.109)$$

The quantities $G_j(t)$, $G'_j(t_1)$ and $G'_j(t_2)$ can be employed to evaluate the interpolation function $(\lambda_j(t))$ for $j = 1$:

$$\lambda_{j=1}(t) = -x(t_{11})\frac{3t - 16t^2 + 16t^3}{2\left(t - \frac{1}{4}\right)} + x(t_{12})\frac{3t - 16t^2 + 16t^3}{6\left(t - \frac{3}{4}\right)} \quad (4.110)$$

For $j = 2$, the interpolation function $\lambda_j(t)$ is:

$$\lambda_{j=2}(t) = -x(t_{21})\frac{t - 64t^2 + 64t^3}{\frac{6}{7}\left(t - \frac{9}{8}\right)} + x(t_{22})\frac{t - 64t^2 + 64t^3}{6\left(t - \frac{15}{8}\right)} \tag{4.111}$$

Figure 4.3 shows the two interpolation functions $\lambda_{j=1}(t)$ and $\lambda_{j=2}(t)$.

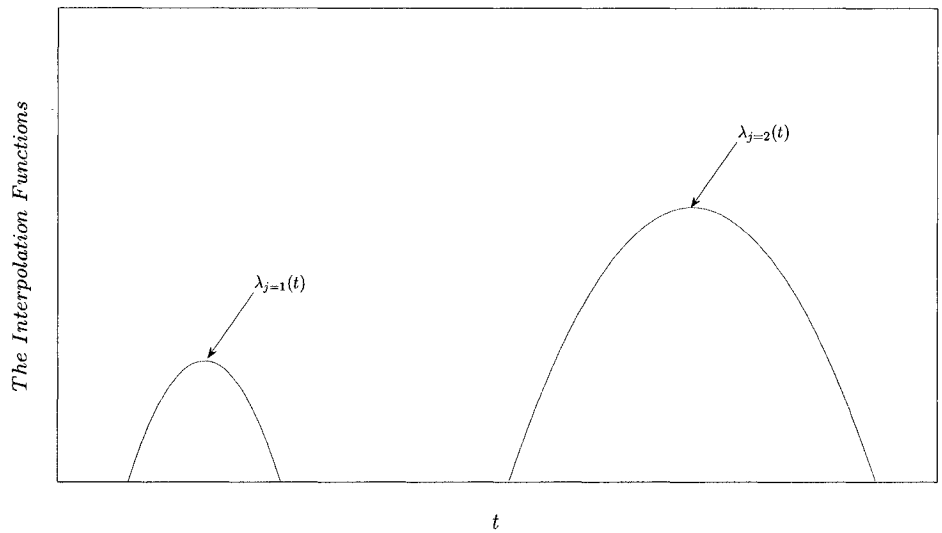

Figure 4.3: The interpolation function $\lambda_{j=1}(t)$ and $\lambda_{j=2}(t)$.

The two examples of the interpolation function $\lambda_j(t)$ provided in equations (4.110) and (4.111) suggest that at each scale j and translation k there is one group of samples created. Also, it indicates that a set of interpolation functions $\{\lambda_j(t)\}_{j=1,2..}$ will have a set of intervals of support such that $t \in [t_{1j}, t_{2j}]$, where t_j indicates that the interpolation is done over the sample group d that is created by $\varphi(t)$ at scale j. Moreover, each interpolation function is continuous and differentiable over its interval of support.

This work focuses on developing a new modulation technique for dc-ac inverters. These inverters are composed of switching elements that are operated either fully ON or fully OFF. As a result, inverter outputs are trains of rectangular pulses

with variable widths and locations, which represent a synthesized version of the sinusoidal reference-modulating signal $S_M(t)$. The sampling-based inverter model developed in chapter 3 defines these rectangular pulses as stages in an interpolation process, which is consistent with the developed non-dyadic MRA. Each interpolation function $\lambda_j(t)$ defines an ON switching pulse. This ON pulse will be translated to a rectangular pulse by an activated switching element(s) appearing on inverter output terminals. Such output due to $\lambda_j(t)$ comes consistent with defined scale-based linearly-combined synthesis scaling function $\tilde{\varphi}(t)$.

Figure 4.4 shows the interpolating function $\lambda_j(t)$ for $j = 2$ and the corresponding synthesis scale-based linearly-combined scaling function $\tilde{\varphi}(t)$.

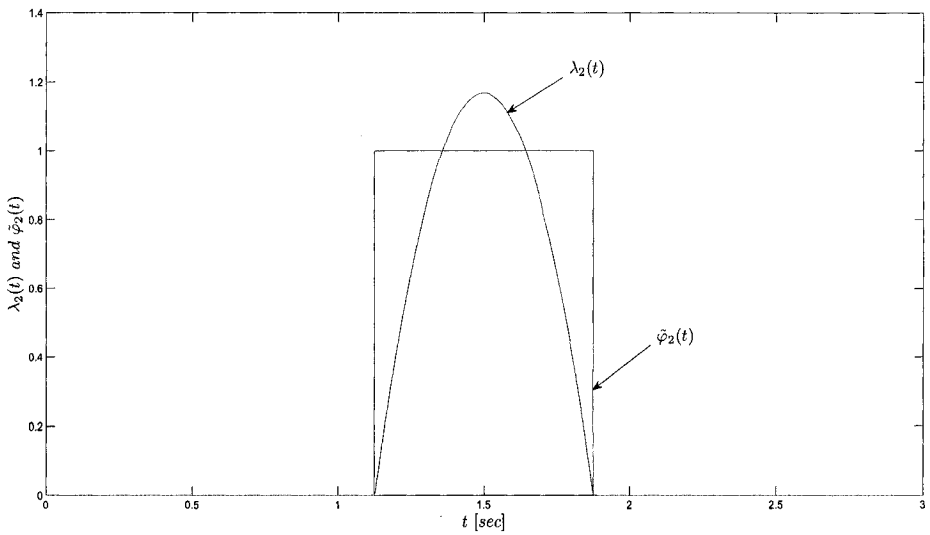

Figure 4.4: The interpolation function $\lambda_j(t)$ for $j = 2$ and the corresponding synthesis scaling function $\tilde{\varphi}_2(t)$.

Two samples are created over each interval of support for $\varphi(t)$. Furthermore, the spacing between the samples in each sample group increases as the scale j increases. It is to be noted that the change in the scale j affects the translation

of $\varphi_j(t)$, but does not allow successive groups of samples to overlap. The MRA associated with this form of sampling can be created by the defined scale-based linearly-combined scaling function ($\varphi_j(t)$). The reconstruction of a CT signal $x_c(t)$ from its non-uniform recurrent samples the scale-based linearly-combined synthesis scaling function using $\tilde{\varphi}(t)$ can be expressed as [47, 48, 52]:

$$x_c(t) = \sum_j \sum_{k \in \mathbb{Z}} \langle x_c(t), \varphi_j(t-k) \rangle \, \tilde{\varphi}_j(t-k) \tag{4.112}$$

The defined scale-based linearly-combined scaling functions $\varphi(t)$ and $\tilde{\varphi}(t)$ as well as their corresponding wavelet function $\psi_\varphi(t)$ are capable of spanning spaces that defines a stable non-dyadic MRA to support a non-uniform recurrent sampling. It is to be noted that the structure of $\varphi(t)$ using $\phi_H(t)$ guarantees creating two samples over its interval of support at each scale j. This consideration is important for meeting the requirements of the sampling-based inverter model developed in chapter 3. However, in other applications, such scaling and wavelet functions may be constructed to create more than two samples using other scaling functions than the Haar one.

There are different types of wavelet basis functions that are capable of spanning spaces to construct MRAs. In general, these MRAs are based on dyadic structure that can only support uniform sampling. Wavelet basis functions can be designed using the dilation matrix-based method, convolution of dual basis functions, fractional $B-spline$ basis functions and autocorrelation sequence-based method. These methods of designing wavelet basis functions guarantee different combinations of scaling and wavelet spaces within dyadic MRA structures. The need for non-dyadic MRAs in applications that include modeling inverters has motivated the development of a new type of scaling and wavelet basis functions to

construct such types of MRA.

The new scale-based linearly-combined basis functions are constructed using a new design method, which is based on a linear combination of dilated scaling and wavelet functions. This design method has produced a new type wavelet basis functions that has been verified to support a non-uniform recurrent sampling-reconstruction process. The newly designed scale-based linearly-combined basis functions will be used to develop a modulation technique to operate dc-ac inverters. The next chapter describes a procedure to implement the wavelet modulation technique to generate switching pulses for operating a single-phase (1ϕ) voltage-source (VS) four-pulse inverter.

Chapter 5

Developing and Simulating the Wavelet Modulation Technique

5.1 General

The fundamental function of a dc-ac inverter is to convert dc voltages into ac ones [1]. This function is achieved through activating inverter switching elements in a sequential manner that guarantees periodic changes of the output voltage polarity. Many techniques have been developed and tested to activate inverter switching elements to produce output voltages as close to sinusoidal waveforms as possible. Such techniques have limited capabilities to produce sinusoidal output waveforms due to the presence of harmonic components in their outputs. In general, achieving inverter outputs with reduced harmonics has been considered as a trade off between the complexity of the switching scheme and the efficiency of the inverter itself [1]. The lack of accurate modeling of dc-ac inverters has limited the development of new modulation techniques that are capable of producing high

quality output.

In this chapter, a new technique for generating switching pulses to activate inverter switching elements is to be developed. The proposed technique is based on the non-dyadic wavelet-based multiresolution analysis (MRA) that can be constructed using the scale-based linearly-combined basis functions presented in chapter 4. The sampling-based inverter model developed in chapter 3 will be the basic building component for the desired wavelet modulation technique. The next section provides inverter constraints that have to be considered before implementing the wavelet modulation technique.

5.2 Inverter Constraints

Inverter outputs can be improved by reducing and/or canceling output harmonic components through generating sequences of switching pulses to activate their switching elements. Switching element functions are part of the proposed technique in that their functions constitute the synthesis part of the non-uniform recurrent sampling-reconstruction process. From a practical point of view, switching elements need time (ON time and OFF time) to change their status (ON to OFF or OFF to ON). Recall that the scale-based linearly-combined synthesis functions are defined over time intervals of sample groups, which are separated by small time intervals due to locations of samples. These time intervals can provide the switching elements with the needed switching times. The other constraint for operating an inverter is the energy in the reconstructed signal (inverter outputs). In general, any modulation technique has to be capable of concentrating the energy of the reconstructed signal in the fundamental frequency component. This constraint ensures that minimum energy be distributed in undesired frequency bands.

If these constraints are taken into account when operating an inverter, output voltage and current will have very low harmonic components [1, 59–61].

5.3 Implementing the Wavelet Modulation Technique

The main idea of the proposed wavelet modulation technique is the realization of a non-dyadic multiresolution analysis process (MRA), in particular, sampling the reference-modulating signal in a non-uniform recurrent manner, and then reconstructing it through the dc-ac inverter switching actions. The implementation of the wavelet modulation technique can be divided into 2 parts, which are:

- Implementing a non-uniform recurrent sampling with a period of T_m that is the period of the reference-modulating signal $S_M(t)$. These samples are created by dilated and shifted versions of the scale-based linearly-combined scaling function $\varphi_1(t)$, and arranged in groups of two samples each.
- Generating switching pulses that are dilated and shifted versions of the synthesis scaling function $\tilde{\varphi}_1(t)$.

The developed scale-based linearly-combined scaling function $\varphi_j(t)$ creates a group of samples at each dilation (change in scale j) and shift (change in k). For each cycle of $S_M(t)$, a finite number of sample groups $\mathcal{D}_\varphi$ is created. The time interval of each group can be defined as:

$$t \in [t_{1j}, t_{2j}] \tag{5.1}$$

where t_{1j} and t_{2j} are the time locations of the first and second samples of the sample group d created by $\varphi_j(t)$, respectively. Also, the time interval of each sample group

represents the interval of support for the scaling function $\varphi_1(t)$ at scale j and shift k. The length of the time interval of the sample group changes as the scale j changes. This relation between the scale j and the time interval of each sample group can be stated as:

$$t_{1j} = d + 2^{-(j+1)}$$
$$t_{2j} = d + 1 - 2^{-(j+1)},\ d = 1, 2, ..., \mathcal{D}_{\varphi},\ j = 1, 2, ... \tag{5.2}$$

It is to be noted that the scale j has to start with $j_0 = 1$ in order to avoid uniform sampling that takes place for $j = 0$.

The reconstruction of the reference-modulating signal $S_M(t)$ from its non-uniform recurrent samples is carried out using dilated and shifted versions of the synthesis scaling function $\tilde{\varphi}_1(t)$. Each dilated and shifted version of the synthesis scaling function $\tilde{\varphi}\left(2^j t - k\right)$ has an interval of support that is given by:

$$t \in [t_{1j}, t_{2j}] \tag{5.3}$$

Both scaling function functions $\varphi_1(t)$ and $\tilde{\varphi}_1(t)$ at scale j and shift k have identical intervals of support. This property is consistent with properties of the Haar scaling function $\phi_H(t)$ that is used to construct $\varphi(t)$.

The synthesis scaling function $\tilde{\varphi}_1(t)$ at scale j and shift k creates an ON switching pulse with a duration $ON_{\tilde{\varphi}}$ that can be defined as:

$$ON_{\tilde{\varphi}} = t_{2j} - t_{1j} \tag{5.4}$$

It is to be noted that the location d is taken with respect to an arbitrary reference. In general, inverter switching elements are activated by successive sets of synthesis scaling functions $\{\tilde{\varphi}_{j,k}(t)\}$ that have their adjacent intervals of support placed such that:

$$t_{d1} = t_{sp} + t_{(d-1)2} \tag{5.5}$$

where t_{sp} is a time interval separating time intervals of sample groups d and $d-1$. The set of these time intervals $\{t_{sp}\}_d$ can provide switching elements with the needed ON and OFF switching times. Figure 5.1 shows two sample groups and their time intervals and the location of the time interval $(t_{sp})_d$ that separates them.

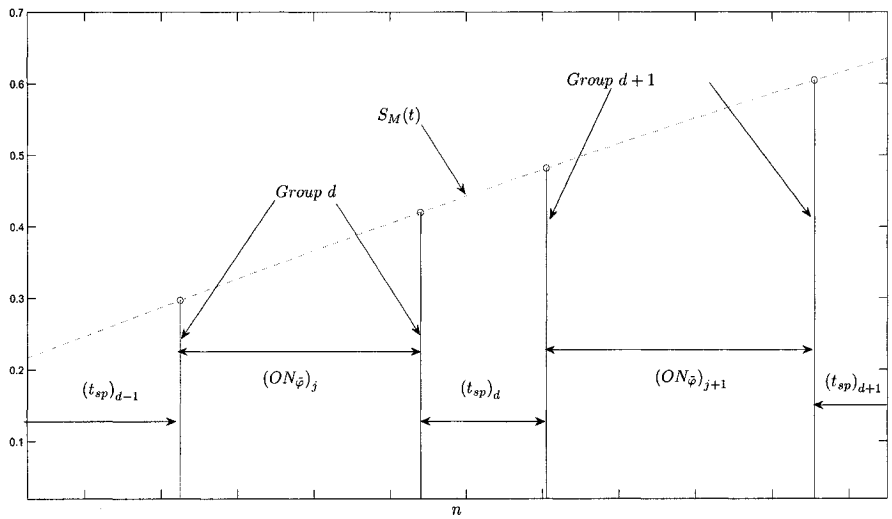

Figure 5.1: Two groups (d and $d+1$) of non-uniform recurrent samples and the location of the time interval $(t_{sp})_d$ that separates them. Also, the durations on the associated ON switching pulses $(ON_{\tilde{\varphi}})_j$ and $(ON_{\tilde{\varphi}})_{j+1}$.

The wavelet modulation technique can be realized through a procedure with the following steps:

1. Set the scale j to $j_0 = 1$ and the index of sample groups d to $d_0 = 1$.

2. Create one sample at $t_{1j} = d + 2^{-(j+1)}$, and another sample at $t_{2j} = d + 1 - 2^{-(j+1)}$ (the sampling part $\langle S_M(t), \varphi_j(t) \rangle$).

3. Evaluate the derivative $S'_M(t)|_{t_{2j}}$:

   - If $S'_M(t_{2j}) > 0$, the scale j is increased by 1 for the next sample group.
   - If $S'_M(t_{2j}) < 0$, the scale j is decreased by 1 for the next sample group.

4. Generate an ON switching pulse over the time interval for the sample group d (the reconstruction part $\langle S_M(t), \varphi_j(t) \rangle \tilde{\varphi}_j(t)$).

5. If $t \geq T_m$, set j to j_0 and d to d_0. Otherwise, increase the index d by 1.

6. Go to step 2.

It is to be noted that the evaluation of $S'_M(t)|_{t_{2j}}$ is performed to ensure that the scale j has finite maximum value. Also, the evaluation of of $S'_M(t)|_{t_{2j}}$ is performed to ensure that the number of sample groups $\mathcal{D}_\varphi$ over one cycle of $S_M(t)$ is finite.

The aforementioned procedure to implement the wavelet modulation technique has to consider the inverter constraints mentioned in section 5.2. Also, physical and operational specifications of switching elements used in such inverters have to be considered when testing the wavelet modulation technique experimentally. Figure 5.2 shows a flowchart to implement the proposed wavelet modulation technique for an inverter.

5.4 Simulating the Wavelet Modulation Technique

The previous section has presented a procedure for implementing the proposed wavelet modulation technique for operating a single-phase inverter through processing (sampling and reconstructing) the CT signal $S_M(t)$. This procedure can be

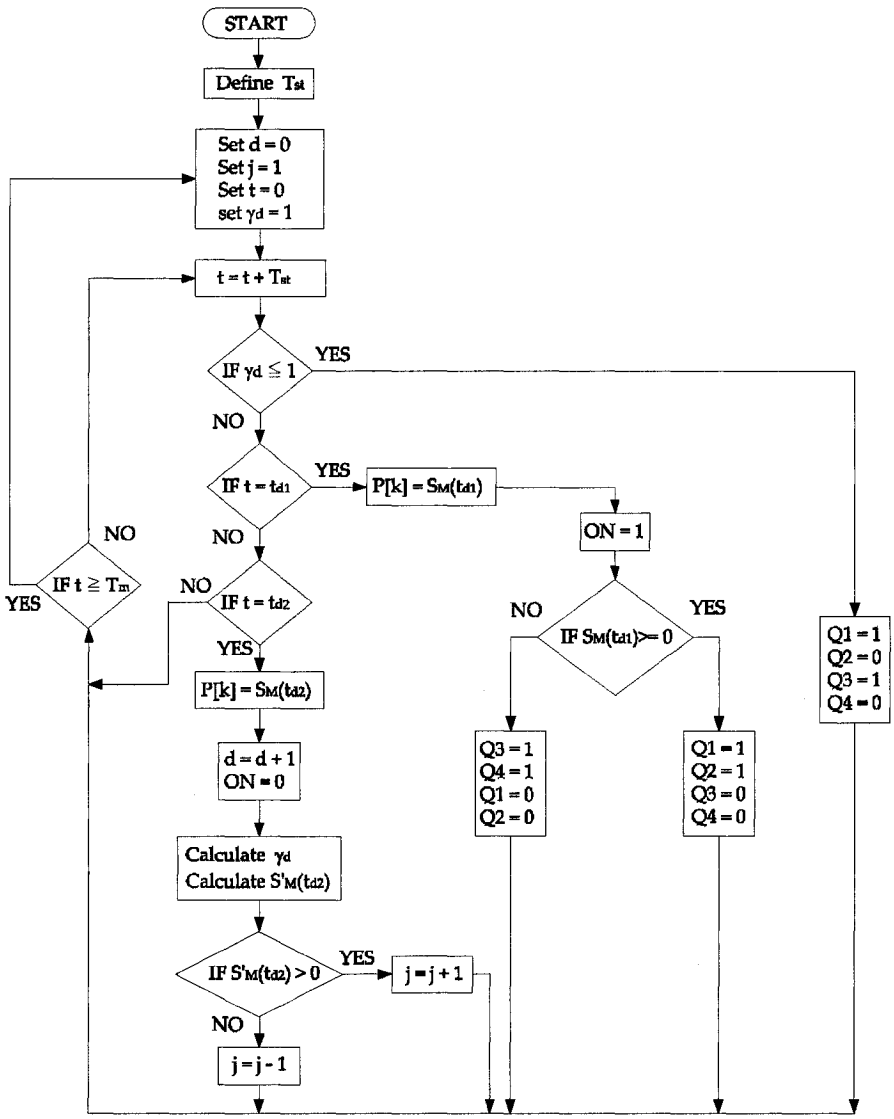

Figure 5.2: A flowchart for an algorithm to implement the wavelet modulation technique. Time instants t_{d1} and t_{d2} are defined in equation (5.2). The reference-modulating signal $S_M(t)$ is given by $S_M(t) = \sin(\omega_m t)$.

converted into an executable program using a MATLAB code. Such a code carries out sampling $S_M(t)$ using dilated and shifted versions of the scaling function $\varphi_1(t)$. Also, it can generate switching pulses using dilated and shifted versions of

the scaling function $\tilde{\varphi}_1(t)$. These generated switching pulses are used to operate a SIMULINK model of a single-phase (1ϕ) voltage-source (VS) four-pulse dc-ac inverter. Figure 5.3 shows a schematic diagram of a single-phase four-pulse inverter.

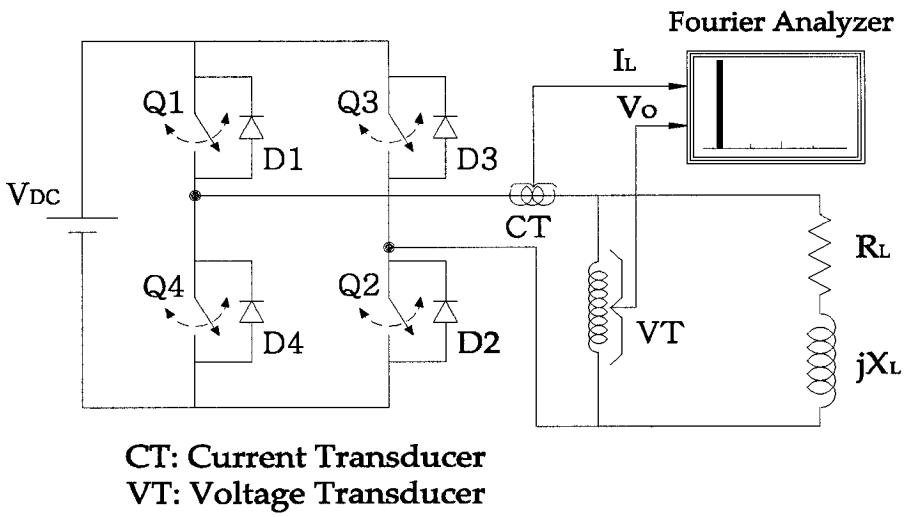

Figure 5.3: A schematic diagram of a single-phase four-pulse voltage source inverter.

Two SIMULINK load models are used to test the performance of the 1ϕ inverter. These load models are as the following:

- A static $R-L$ load with an impedance of $Z_L = 10 + j7.45\ \Omega$.
- A single-phase universal motor.

The SIMULINK model of the 1ϕ four-pulse VS inverter and one of the loads are shown in Figure 5.4. The ON switching pulses generated by the developed MATLAB code to operate the 1ϕ VS four-pulse inverter model are shown in Figure 5.5.

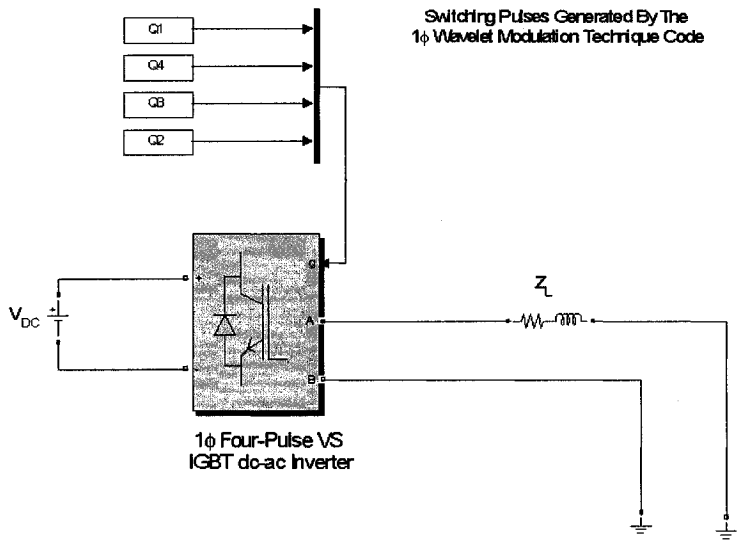

Figure 5.4: A SIMULINK model for a single-phase voltage-source dc-ac inverter supplying a $R-L$ load to simulate the performance of the wavelet modulation technique.

5.4.1 The Static $R-L$ Load

The SIMULINK model of the wavelet-modulated 1ϕ VS four-pulses inverter supplies a $R-L$ load with an impedance of $Z_L = 10 + j7.45\ \Omega$. The inverter model has a dc voltage supply of 50 V. The quality of inverter output voltage and load current are usually expressed in terms of the total harmonic distortion factor. This factor is defined as [1]:

$$THD_A = \frac{A_h}{A_1} \tag{5.6}$$

where A_1 is the RMS value of the fundamental component of the inverter output voltage or load current. Also, A_h is the summation of all other harmonic compo-

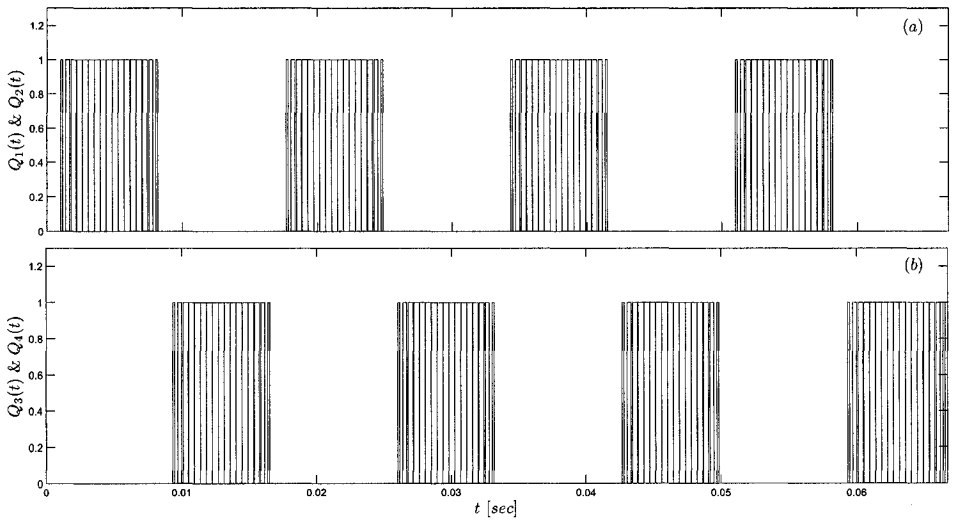

Figure 5.5: Generated ON switching pulses for inverter switching elements: (a) switching pulses for Q_1 and Q_2 switches and (b) switching pulses for Q_3 and Q_4 switches.

nents RMS values, which is defined as [1]:

$$A_h = \sqrt{(A_2^2 + A_3^2 + ... + A_n^2)} \tag{5.7}$$

where A_h; $h = 2, 3, ..., n$ is the RMS value of the h harmonic component. The THD factors can be evaluated using built-in MATLAB functions.

The inverter output voltage and its spectrum are shown in Figure 5.6. The load current along with its spectrum are shown in Figure 5.7. The fundamental component of the output voltage is 49.2714 V, and the fundamental component of the output current is 3.075 A.

5.4.2 The Universal Motor Load

The simulated 1ϕ VS four-pulse wavelet-modulated inverter is used to supply a SIMULINK model of a 1ϕ, 110 V, 60 Hz, 0.75 hp, 2400 RPM universal motor. This

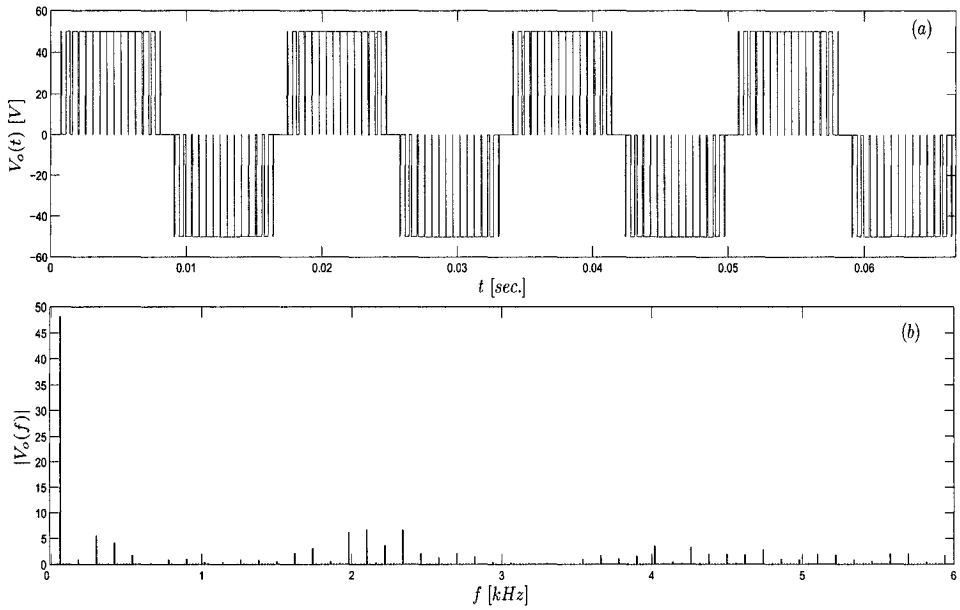

Figure 5.6: The inverter output voltage for an inductive load: (a) the wavelet modulated dc-ac inverter output voltage $V_o(t)$ and (b) its magnitude spectrum $|V_o(f)|$. The total harmonic distortion factor THD_V = 17.64%.

load is selected to investigate the performance of the inverter for supplying a dynamic load. The same MTALB code generates ON-switching pulses to activate the simulated 1ϕ inverter. The dc input voltage is set to 110 V to meet the 1ϕ motor model rating values. The inverter output voltage and its spectrum are shown in Figure 5.8. The motor current along with its spectrum are shown in Figure 5.9.

The simulation results have demonstrated quite encouraging results in terms of harmonic contents of inverter output voltage and current. Furthermore, total harmonic distortion factors (THD_V and THD_I) evaluated for several tests show significant reduction of the energy distributed in the harmonic frequencies that provides an indication of high quality outputs. Also, different tests for different loads have shown significant magnitudes of output fundamental components of both inverter output voltages and load currents. The next section presents a performance com-

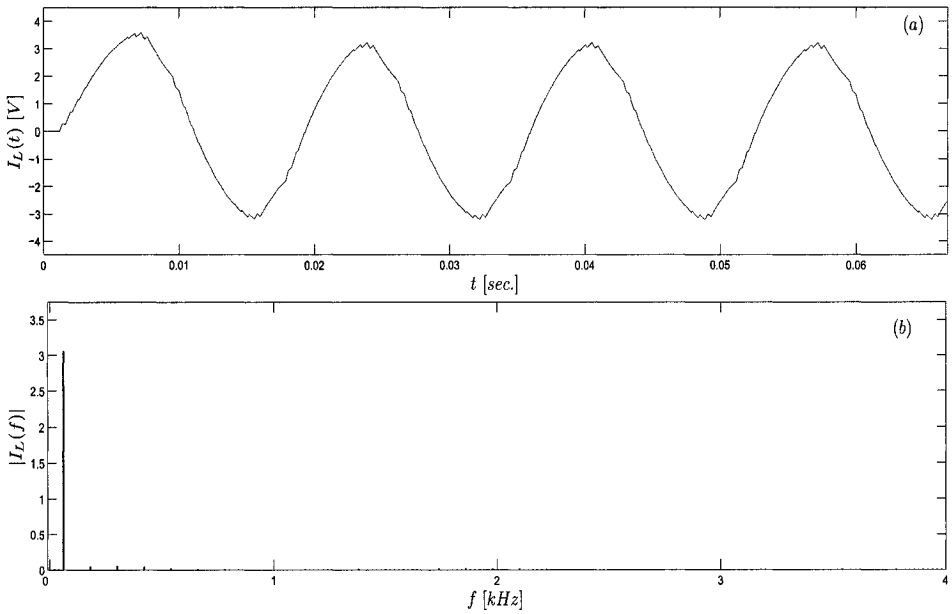

Figure 5.7: The load current $I_L(t)$ and its spectrum: (a) the load current $I_L(t)$ and (b) its magnitude spectrum $|I_L(f)|$. The total harmonic distortion factor THD_I = 2.15%.

parison of the proposed wavelet modulation technique and the SPWM one under the same loading conditions.

5.4.3 Comparison with a Typical SPWM Inverter

The simulated wavelet-modulated inverter has shown significant performance improvement when supplying different loads. To further demonstrate the significant capabilities of the proposed wavelet modulation technique, a performance comparison between the WM inverter and the SPWM one is conducted. Furthermore, simulation results of both inverters are compared under the same loading conditions. The 1ϕ VS four-pulse inverter model is used to supply both load models using ON switching pulses generated by both modulation techniques. SPWM ON switching pulses are generated with a carrier frequency $f_s = 1080\ Hz$ and a modu-

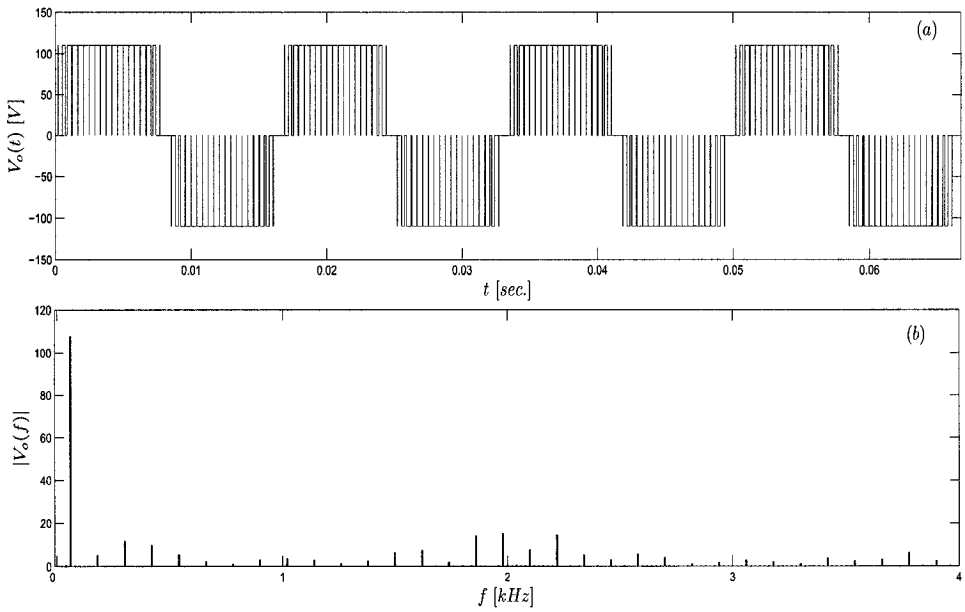

Figure 5.8: The output voltage of the inverter and its spectrum: (a) the inverter output voltage supplied to the motor $V_o(t)$ and (b) its spectrum $|V_o(f)|$.

lation index $m_a = 0.8$. These generated SPWM ON switching pulses are shown in Figure 5.10.

The static $R - L$ load voltages obtained by both inverters along with their spectra are shown in Figure 5.11. Currents supplied to the $R - L$ load by WM and SPWM inverters and their spectra are shown in Figure 5.12. The dynamic load (the 1ϕ universal motor) currents supplied by the WM inverter as well as the SPWM inverter along with their spectra are shown in Figure 5.13.

Simulation results obtained from the SPWM inverter are mainly used here for comparison purposes with their analog results obtained from the proposed wavelet-modulated one. Table 5.1 summarizes these results.

Table 5.1 clearly demonstrates that the WM inverter yields a higher fundamental component and lower total harmonic distortion factors than the SPWM for the

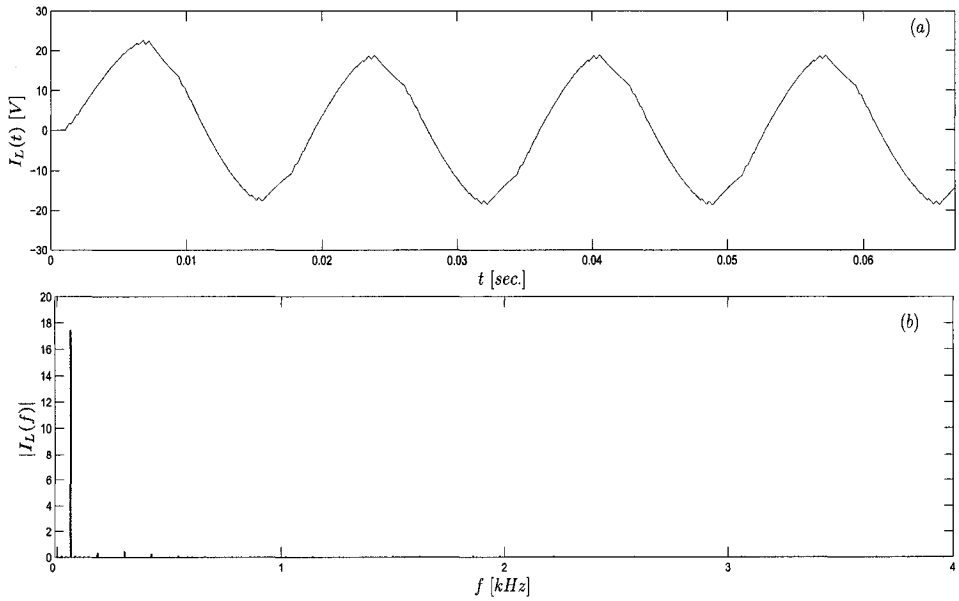

Figure 5.9: The motor current $I_M(t)$ and its spectrum: (a) the motor current and (b) the spectrum of the motor current $|I_M(f)|$.

Table 5.1: Performance comparison between simulated WM and SPWM inverters for the $R-L$ load and the universal motor.

Load	Parameter	WM	SPWM
$L-R$	$\|V_1\|$	49.27 V	41.66 V
	$\|I_1\|$	3.08 A	2.87 A
	THD_V	17.64%	24.7%
	THD_I	2.15%	3.77%
Motor	$\|V_1\|$	108.78 V	92.86 V
	$\|I_1\|$	17.62 A	14.44 A
	THD_V	16.92%	25.2%
	THD_I	1.26%	1.84%

same $R-L$ and motor loads. Such performance comparisons confirm that the wavelet-modulated inverter has capabilities to transfer higher power with reduced harmonic components than the SPWM inverter. The data of Table 5.1 along with the previous discussion illustrate the efficacy of the developed wavelet modulation

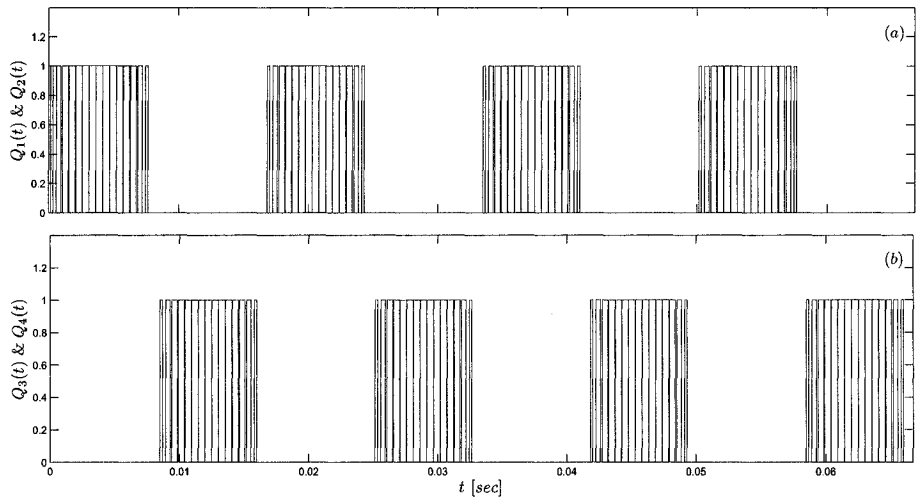

Figure 5.10: SPWM generated switching pulses for inverter switching elements: (a) switching pulses for Q_1 and Q_2 and (b) switching pulses for Q_3 and Q_4.

technique.

Simulating the performance of the proposed wavelet modulation technique has shown very good results for both static and dynamic loads. However, all the simulation results presented here have been carried out at one output frequency of 60 Hz. The next section extends simulations to include other output frequencies.

5.5 Performance of a WM Inverter for Different Output Frequencies

The previous section has presented quite encouraging results of the proposed wavelet modulation techniques. These results have included different load types for an output frequency of 60 Hz. Other output frequencies are tested to investigate the capabilities of the proposed wavelet modulation technique to operate inverters for different output frequencies. This section provides simulation results for output

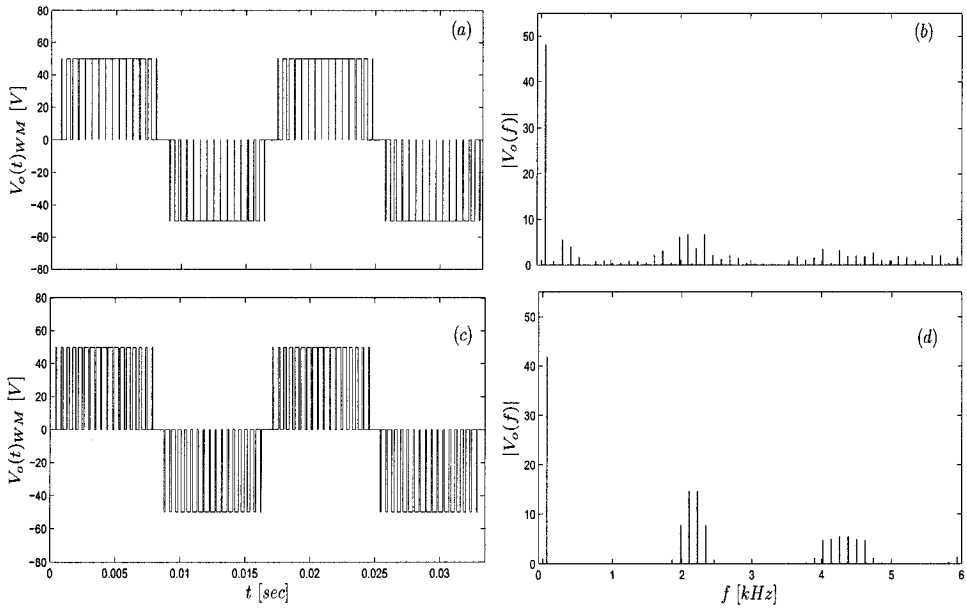

Figure 5.11: The output voltages of WM and SPWM inverters and their spectra for the static $R-L$ load: (a) the output voltage of the WM inverter, (b) the spectrum of the WM inverter output voltage, (c) the output voltage of the SPWM inverter and (d) the spectrum of the SPWM inverter output voltage.

frequencies of 50, 90 and 400 Hz.

The inverter model described in the previous section supplies the same $R-L$ load ($Z_L = 10 + j7.45\ \Omega$) with an input dc voltage of 50 V for an output frequency of 50 Hz. It should be noted that the output frequency can be varied by setting the frequency of the reference-modulating signal ($S_M(t)$) to the desired value. Figure 5.14 shows the inverter output voltage and the load current along with their spectra at 50 Hz.

The frequency of the reference-modulating signal is set to 90 Hz. Figure 5.15 shows the inverter output voltage and the $R-L$ load current along with their spectra at 90 Hz.

The simulated 1ϕ inverter supplies the same $R-L$ load and the frequency of

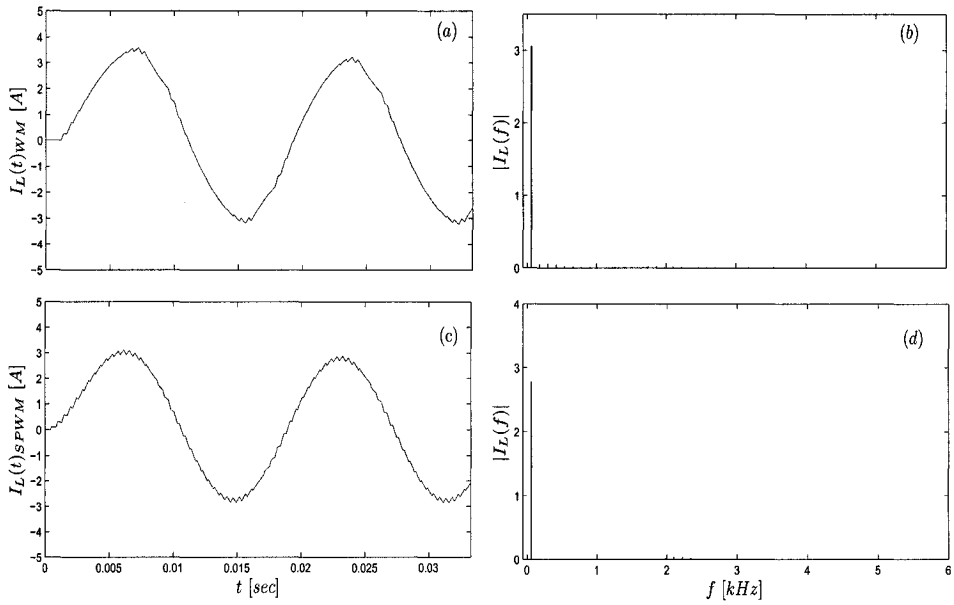

Figure 5.12: The static $R-L$ load currents supplied by WM and SPWM inverters and their spectra: (a) the load current supplied by the WM inverter $I_M(t)_{WM}$, (b) the spectrum of the load current $|I_M(f)_{WM}|$, (c) the load current supplied by the SPWM inverter $I_M(t)_{SPWM}$ and (d) the spectrum of the load current $|I_M(f)_{SPWM}|$.

$S_M(t)$ is set to 400 Hz. The inverter output voltage and the load current along with their spectra at 400 Hz are shown in Figure 5.16. The 1ϕ universal motor model is supplied by the same inverter with an output frequency of 90 Hz. Figure 5.17 shows the inverter output voltage and the motor current along with their spectra.

The simulation results of operating the 1ϕ VS four-pulse wavelet modulated inverter for different output frequencies show that the spectral location of the fundamental components of output voltage and load current are shifted, while their magnitudes are almost unchanged. Moreover, the voltage as well the current THD factors are slightly changed. The operation of the inverter for various output frequencies is achieved by changing the frequency of $S_M(t)$, which is the sampled CT signal. These results indicate that the reconstruction of $S_M(t)$ using the developed

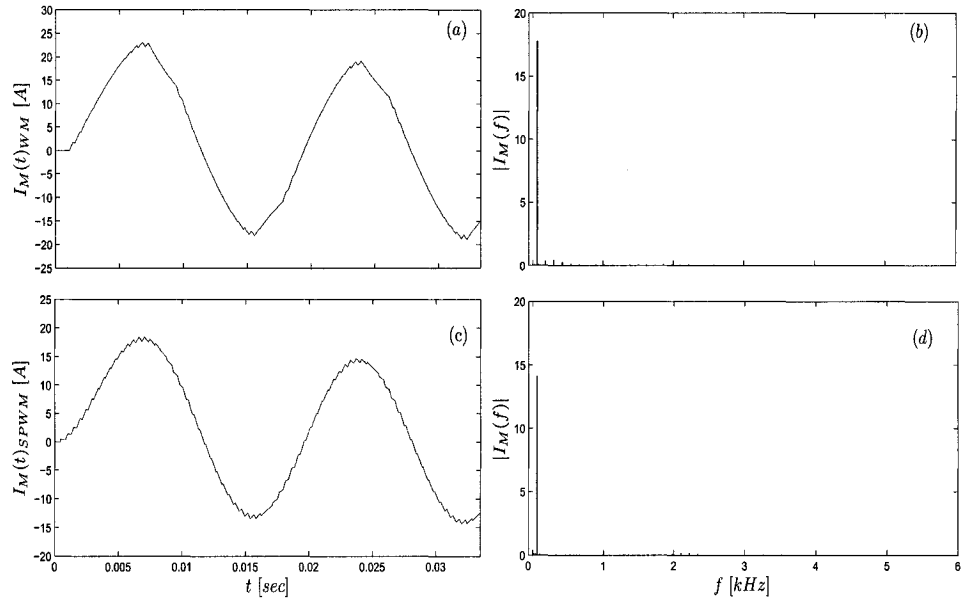

Figure 5.13: The 1ϕ universal motor currents supplied by WM and SPWM inverters and their spectra: (a) the motor current supplied by the WM inverter $I_M(t)_{WM}$, (b) the spectrum of the motor current $|I_M(f)_{WM}|$, (c) the motor current supplied by the SPWM inverter $I_M(t)_{SPWM}$ and (d) the spectrum of the motor current $|I_M(f)_{SPWM}|$.

non-dyadic type MRA is independent of the frequency of the sampled CT signal. Also, the accuracy of the reconstructed signals is almost unaffected by the change in the frequency of $S_M(t)$ as indicated by the THD factor values.

Simulation results for different loads supplied by the proposed wavelet modulated inverter output voltages with different frequencies have been presented. Also, some of these simulation results have been compared with their counterparts obtained using a typical SPWM inverter under the same loading conditions. In all simulated results, the performance of the proposed WM inverter has shown significant capabilities to produce high quality outputs regardless of load type or output frequency over the SPWM inverter one. Also, the wavelet modulated inverter has a better ability to transfer power than the SPWM inverter, (as the higher output

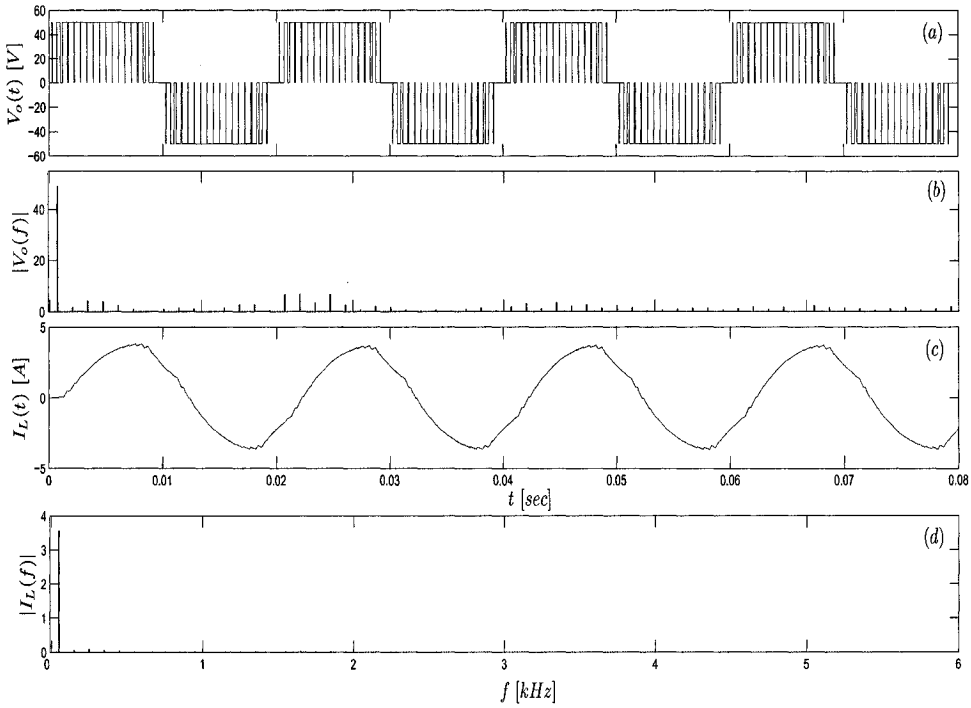

Figure 5.14: The inverter output voltage and the load current for an output frequency of $f = 50\ Hz$: (a) the inverter output voltage $V_o(t)$, (b) the spectrum of the inverter output voltage $|V_o(f)|$ with $|V_1| = 47.14\ V$ and $\text{THD}_V = 18.73\ \%$, (c) the load current $I_L(t)$ and (d) the spectrum of the load current $|I_L(f)|$ with $|I_1| = 3.31\ A$ and $\text{THD}_I = 2.78\ \%$.

voltage fundamental frequency component magnitudes indicate). This ability for high power transfer can be linked to the effective switching that improves both magnitudes of output fundamental components and the inverter efficiency. The next section introduces a new factor that can monitor the scale j changes during the creation of non-uniform recurrent samples of $S_M(t)$ as well as during its reconstruction by the synthesis scaling function.

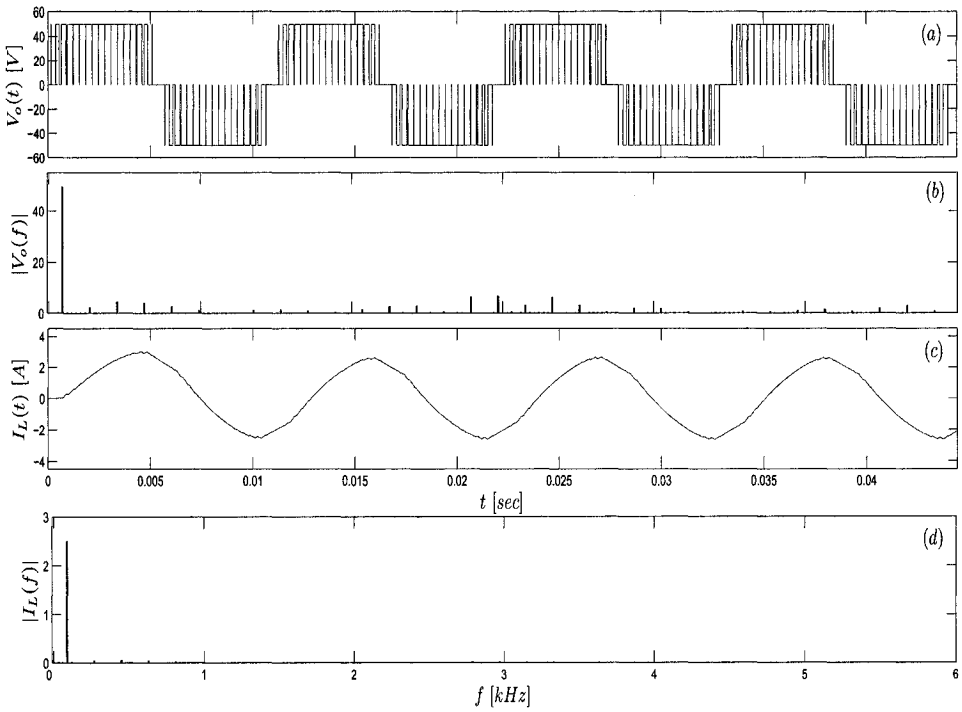

Figure 5.15: The inverter output voltage and the load current for an output frequency of $f = 90\ Hz$: (a) the inverter output voltage $V_o(t)$, (b) the spectrum of the inverter output voltage $|V_o(f)|$ with $|V_1| = 49.56\ V$ and $\text{THD}_V = 15.21\ \%$, (c) the load current $I_L(t)$ and (d) the spectrum of the load current $|I_L(f)|$ with $|I_1| = 2.73\ A$ and $\text{THD}_I = 1.92\ \%$.

5.6 The Scale-Time Interval Factor

Switching pulses generated to operate the inverter represent a set of synthesis scaling functions ($\{\tilde{\varphi}_j(t)\}$) created to reconstruct the reference-modulating signal $S_M(t)$ from its non-uniform recurrent samples. As the scale j changes, the duration and the location of each dilated and translated version of the synthesis scaling function ($\tilde{\varphi}_{j,k}(t)$) change over each half cycle of $S_M(t)$. However, the scale is constant over the interval of support of $\tilde{\varphi}_{j,k}(t)$. On the other hand, the changes of the scale j with time show the location of sample groups along with their density. This indication can help to improve the quality of the inverter outputs. Also, the

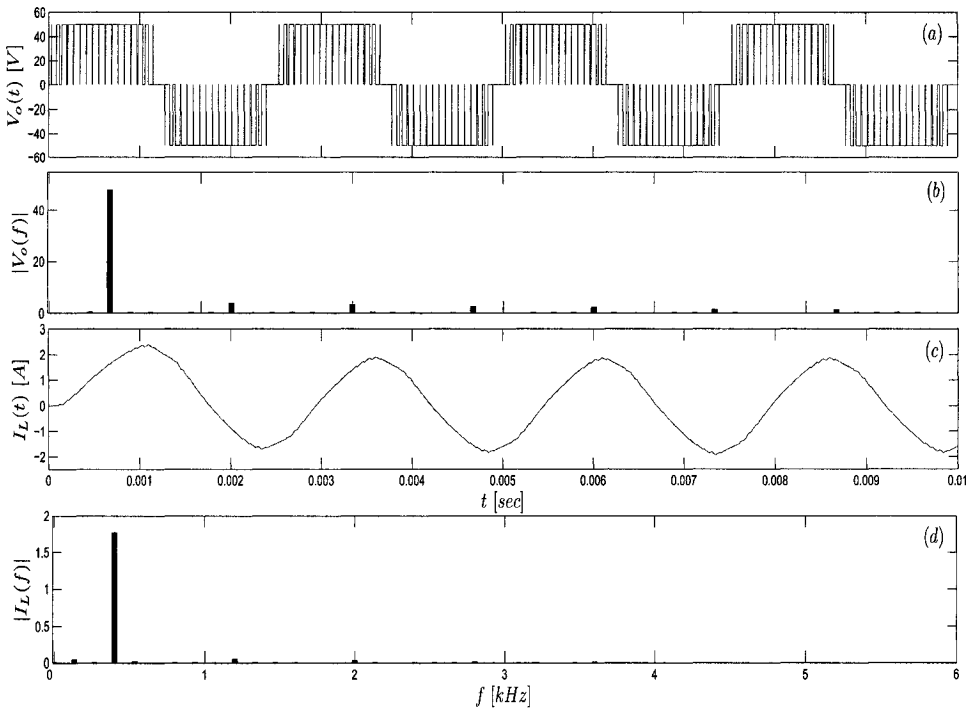

Figure 5.16: The inverter output voltage and the load current for an output frequency of $f = 400\ Hz$: (a) the inverter output voltage $V_o(t)$, (b) the spectrum of the inverter output voltage $|V_o(f)|$ with $|V_1| = 49.87\ V$ and $\text{THD}_V = 12.95\ \%$, (c) the load current $I_L(t)$ and (d) the spectrum of the load current $|I_L(f)|$ with $|V_1| = 1.10\ A$ and $\text{THD}_I = 0.73\ \%$.

value of the scale j that is associated with the switching pulses of the maximum width can be located. Furthermore, as the scale is increasing, the derivative of the sampled reference-modulating signal is positive, which imply that the sampled signal is changing toward its maximum value. The previous discussion is important when considering adjusting the inverter output during its operation as will be discussed in chapter 7.

A factor γ can be defined as a $scale-time\ interval$ factor to provide a time-scale relation that can produce time localized values of the scale over a half-cycle of the reference-modulating signal $S_M(t)$. Recall that the maximum value of the scale j is reached before the derivative of the sampled reference-modulating signal changes

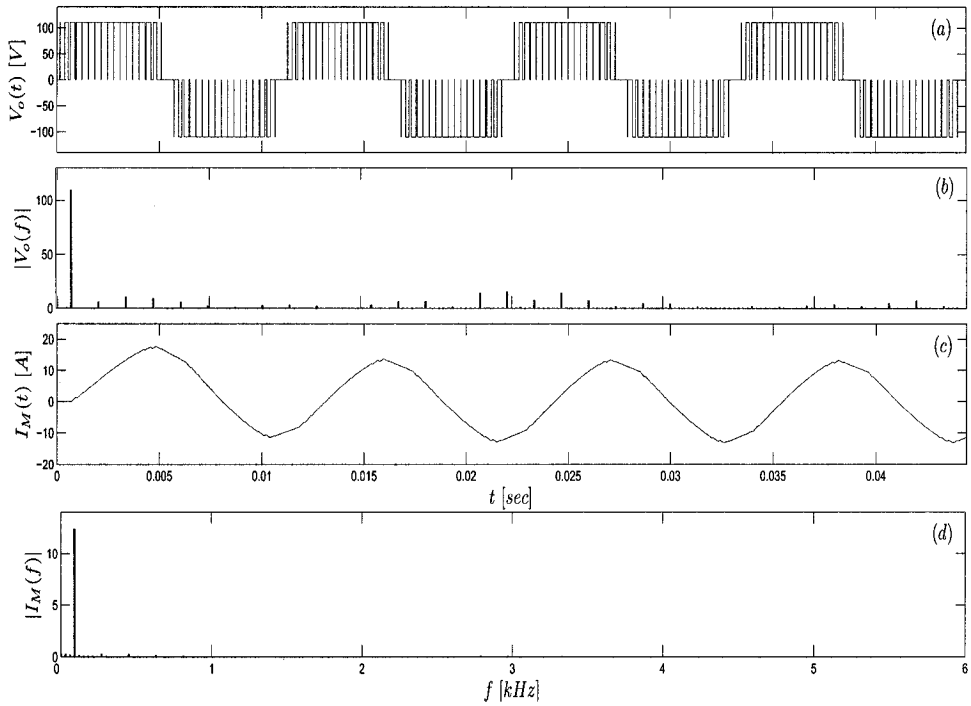

Figure 5.17: The inverter output voltage and the motor current for an output frequency of $f = 90\ Hz$: (a) the inverter output voltage $V_o(t)$, (b) the spectrum of the inverter output voltage $|V_o(f)|$ with $\text{THD}_V = 15.21\ \%$, (c) the load current $I_M(t)$ and (d) the spectrum of the load current $|I_M(f)|$ with $\text{THD}_I = 1.07\ \%$.

it sign. This factor can be defined as:

Definition 5.1: let γ be a $scale - time\ interval$ factor for sample group d defined as:

$$\gamma_d = \gamma_{d-1} + \frac{S'_M(t_{d2})}{|S'_M(t_{d2})|} \sum_{m=1}^{j} m2^m \left(t_{m2} - t_{m1}\right) \tag{5.8}$$

where γ_d is the scale-time interval factor for the sample group d and j is the scale.

The factor γ changes its increasing pattern into a decreasing one following a change in the sign of the first derivative of the reference modulating signal $S'_M(t)$. As a consequence, the term $\frac{S'_M(t_{d2})}{|S'_M(t_{d2})|}$ ensures changing k from an increasing sequence to a decreasing one follows any change in the sign of $S'_M(t)$. This can be

very important when relating the change in the scale to the change in a sampled signal. Figure 5.18 shows the scale-time interval factor γ for one of the simulated cases for the static $R-L$ load at an output frequency of 60 Hz. Figure 5.19 shows

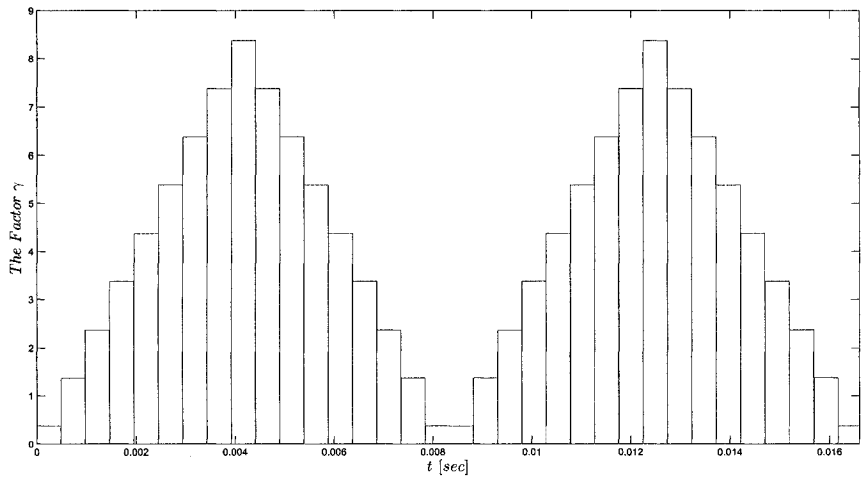

Figure 5.18: The scale-time interval factor γ for the inverter output voltage with a frequency of $f = 60$ Hz.

the factor γ for the case of supplying the 1ϕ universal motor at an output frequency of $f = 90$ Hz.

The scale-time interval factor γ can provide instantaneous values of time durations for each interval of support for any synthesis function over one cycle of $S_M(t)$. Such values can be used to change locations of sample groups that can be employed to adjust magnitudes as well as frequencies of inverter outputs. As a result, changing intervals of support for dilated and shifted versions of the synthesis scaling function $(\tilde{\varphi}_{j,k}(t))$can change durations as well as locations of ON switching pulses.

The results of simulating the performance of a 1ϕ wavelet-modulated inverter demonstrates significantly high quality output voltages and load currents. This

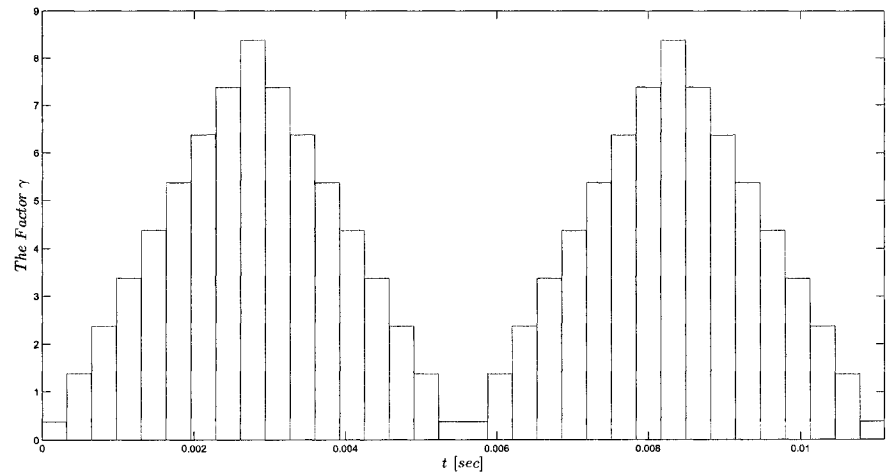

Figure 5.19: The scale-time interval factor γ for the inverter output voltage with a frequency of $f = 90$ Hz.

high quality has been demonstrated through low harmonic contents as well as high fundamental components of output voltages and currents. Moreover, simulation results have shown that the proposed wavelet modulated (WM) inverters have the ability to transfer more power to the load side. Simulation results of the WM inverter have included cases with different output frequencies, where harmonic contents as well as fundamental component of outputs have not been significantly affected. Also, a typical SPWM inverter has been simulated for the same loading conditions. These simulations have been compared with their counterpart results obtained from simulating the wavelet modulated inverter.

Simulation results obtained from the proposed wavelet modulated inverters have demonstrated quite encouraging performance. These simulation results need to be confirmed by the performance of an experimental inverter. The next chapter presents real-time implementation and experimental testing of a 1ϕ wavelet-modulated inverter for different loads at different output frequencies. Also, the

next chapter presents a performance comparison between the proposed wavelet modulation technique and the conventional SPWM one under same loading conditions.

Chapter 6

Experimental Testing of a Wavelet-Modulated Inverter

6.1 General

The previous chapter presented the development and an implementation of the wavelet modulation technique using MATLAB software and SIMULINK tools. Also, chapter 5 has provided results of simulating the performance of a single-phase voltage-source four-pulse dc-ac wavelet-modulated inverter for different loads under several output frequencies. The presented simulation results have demonstrated the method's high ability to substantially eliminate harmonics from output voltages and currents. Furthermore, simulation results have shown significant capabilities of the wavelet modulation technique to concentrate output energy in the fundamental frequency component, which resulted in improved inverter outputs. It should be noted that the test results of chapter 5 are obtained using models of inverters, loads and supplies that are used for simulation purposes.

In this chapter, the wavelet modulation technique (WM) is implemented for operating a single-phase (1ϕ) voltage-source (VS) four-pulse IGBT dc-ac inverter. Moreover, experimental test results of the WM technique are compared to results obtained from the same inverter activated using sinusoidal pulse-width modulation (SPWM) switching pulses. At the beginning, an experimental setup for a 1ϕ VS four-pulse IGBT inverter is developed for conducting experimental tests.

6.2 The Experimental Setup

The wavelet modulation (WM) technique is tested on a 1ϕ VS four-pulse IGBT inverter that supplies two types of loads that are:

1. A static $R-L$ load with an impedance $Z_L = 12 + j5.31\ \Omega$.
2. A $\frac{1}{2}$ hp, 110 V, 60 Hz, 1750 RPM single-phase capacitor-run induction motor.

The experimental setup needed for testing the 1ϕ VS four-pulse IGBT inverter for the aforementioned loads is composed of the following elements:

- A 1ϕ VS four-pulse inverter composed of four insulated gate bipolar transistor (IGBTs) switching elements with a free-wheeling diode across each IGBT.
- Hall-effect current and voltages sensors to collect currents and voltages for performing spectral analysis using $FLUKE\ 41$ power harmonic analyzer.
- A digital signal processing board $dSPACE\ ds1102$ DSP board for executing the wavelet modulation technique $Turbo-C$ code.
- An isolation and amplification circuit to supply generated switching pulses on $dSPACE\ ds1102$ DSP board output ports to gates of IGBT switches.

It is worth mentioning that the used 1ϕ VS four-pulse IGBT inverter is equipped with snubber circuits in parallel with each IGBT switch. These circuits are meant to limit the change of voltage across each IGBT switch during the ON-OFF switching. The design of these circuits along with their schematic diagrams are detailed in Appendix C.

The aforementioned elements are connected to build the experimental setup that is shown in Figure 6.1. Figure 6.2 shows a picture for the experimental setup

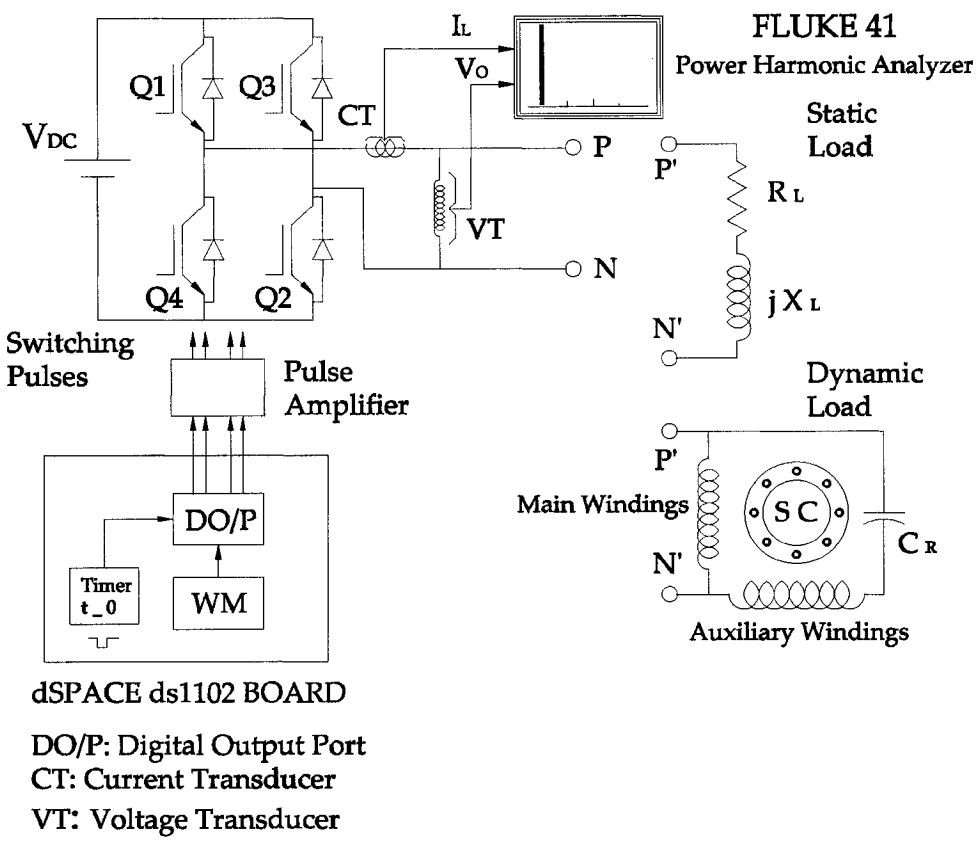

Figure 6.1: The experimental setup schematic for testing a wavelet modulated single-phase voltage-source four-pulse IGBT dc-ac inverter and the tested loads.

taken in the Energy Laboratory.

Figure 6.2: A picture for the laboratory setup of the inverter along with the measuring instruments taken at the Energy Laboratory.

An algorithm for implementing the proposed wavelet modulation technique has been developed in chapter 5. The proposed WM technique algorithm is realized using a $Turbo - C$ code, compiled using the Texas Instrument compiler and loaded to the $dSPACE\ ds1102$ DSP board to generate switching pulses. These switching pulses are taken from digital-output port (DO/P) of the $dSPACE\ ds1102$ DSP board and applied to activate inverter IGBT switches. It should be noted that these switching pulses are applied to IGBT switches through an opto-coupler pulse amplifier for isolating and protecting the DSP board. A dc voltage (V_{DC}) of 50 V is used to supply the inverter on the input side.

The tested inverter output voltages and load currents are measured using the hall-effect sensors, displayed and downloaded to a computer using a 2-channel

Tektronics 2212 storage digital oscilloscope that has a sampling frequency of 10 kHz. The software package *Grab* 2212 is used to download the collected waveforms from the storage oscilloscope to a computer. Also, inverter output voltages and load currents are fed into the $FLUKE$ 41 harmonic analyzer to obtain their spectra and total harmonic distortion (THD) factors.

6.3 Experimental Test Results

An experimental setup prepared to test the performance of the wavelet modulation technique consists of the 1ϕ VS four-pulse IGBT inverter with a dc voltage supply, loads and measuring instruments. When the developed $Turbo - C$ code is executed using the $dSPACE$ $ds1102$ DSP board, switching pulses are generated and sent to the digital output port (DO/P) of the DSP board. These switching pulses are collected using the *Tektronics* 2212 storage digital oscilloscope. The software package *Grab* 2212 is used to download the collected waveforms from the storage oscilloscope to a computer. Figure 6.3 shows switching pulses generated by the proposed WM technique.

6.3.1 The Static $R - L$ Load

A static load that has an impedance of $Z_L = 12 + j5.31\ \Omega$ is connected across the inverter output terminals (terminals P and N shown in Figure 6.1). This load is tested for several frequencies including the standard 60 Hz frequency.

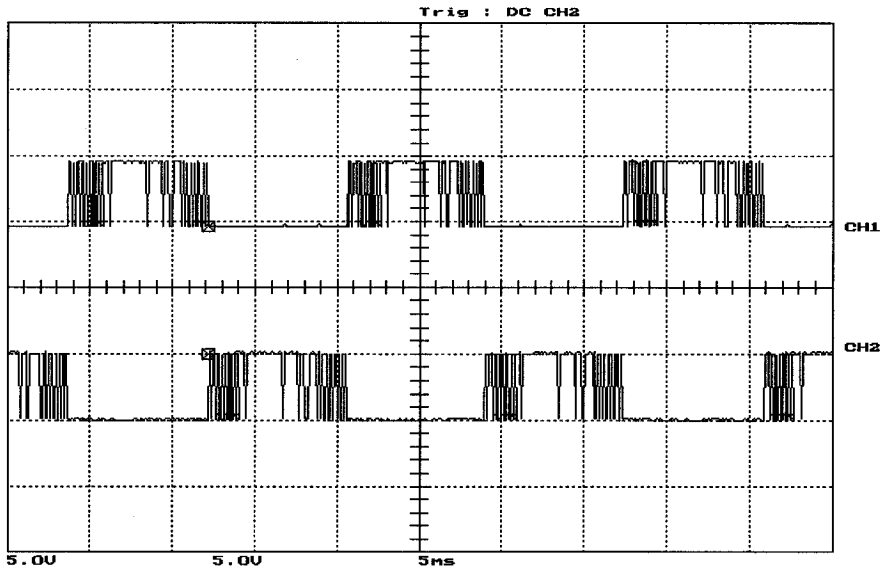

Figure 6.3: Switching pulses generated by the proposed WM technique and collected from the DO/P of the $ds1102$ DSP board using the $Tektronics$ 2212 storage digital oscilloscope.

Results for an Output Frequency of 60 Hz

Switching pulses generated by the wavelet modulation technique aim to activate the inverter IGBT switching elements to reconstruct the reference-modulating signal $S_M(t)$ from its non-uniform recurrent samples. As a consequence, the frequency of a wavelet-modulated inverter output voltage is identical to the frequency of $S_M(t)$. The first set of tests is conducted for an inverter output voltage with a frequency of 60 Hz. As switching pulses are applied to the gates of the IGBT switches with the dc voltage supply turned on, an output voltage appears across the $R-L$ load. Figure 6.4 shows the inverter output voltage $V_o(t)$ and its harmonic spectrum. This voltage is collected using a hall-effect voltage sensor that is connected in parallel with inverter output terminals (P, N as in Figure 6.1). Also, the collected inverter output voltage is fed into the $FLUKE$ 41 power harmonic analyzer to provide the spectrum of $V_o(t)$. It is to be noted that the collected results using

the $FLUKE$ 41 power harmonic analyzer are always RMS values.

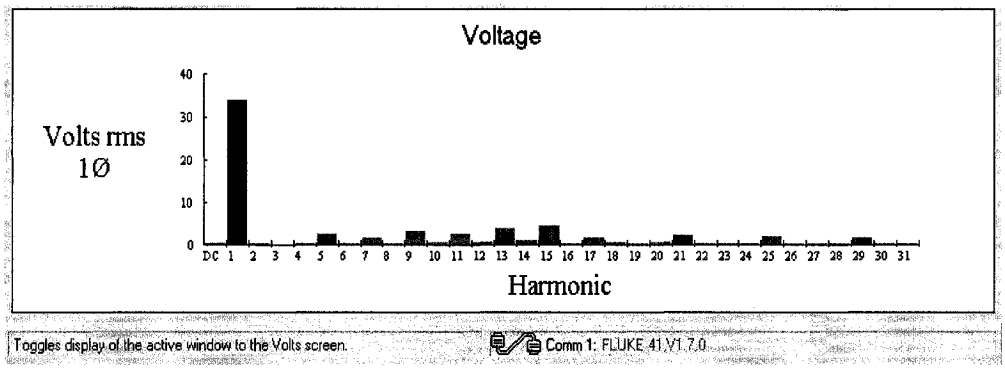

Figure 6.4: The experimental inverter output voltage and its spectrum obtained using the $FLUKE$ 41 power harmonic analyzer. The THD_V is 16.10%.

The $R - L$ load connected across the inverter output terminals (P, N), draws a current $I_L(t)$ that flows through Z_L, and is collected using a series-connected hall-effect current sensor. Moreover, the load current is passed through a clamp meter connected to the $FLUKE$ 41 power harmonic analyzer to provide the spectrum of $I_L(t)$. Figure 6.5 shows the load current along with its spectrum. The

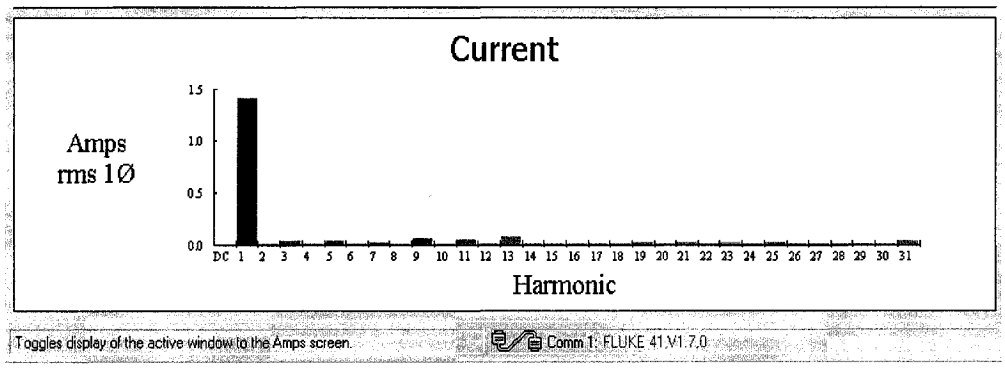

Figure 6.5: The experimental load current $I_L(t)$ and its spectrum obtained using the $FLUKE$ 41 power harmonic analyzer. The THD_I is 1.86%.

inverter output voltage and load current waveforms have been collected using the $Tektronics$ 2212 storage digital oscilloscope. Figure 6.6 shows waveforms of the

inverter output voltage and load current. It is to be noted that the inverter output voltage and load current have been measured using different hall-effect sensors, which caused their scales to be different.

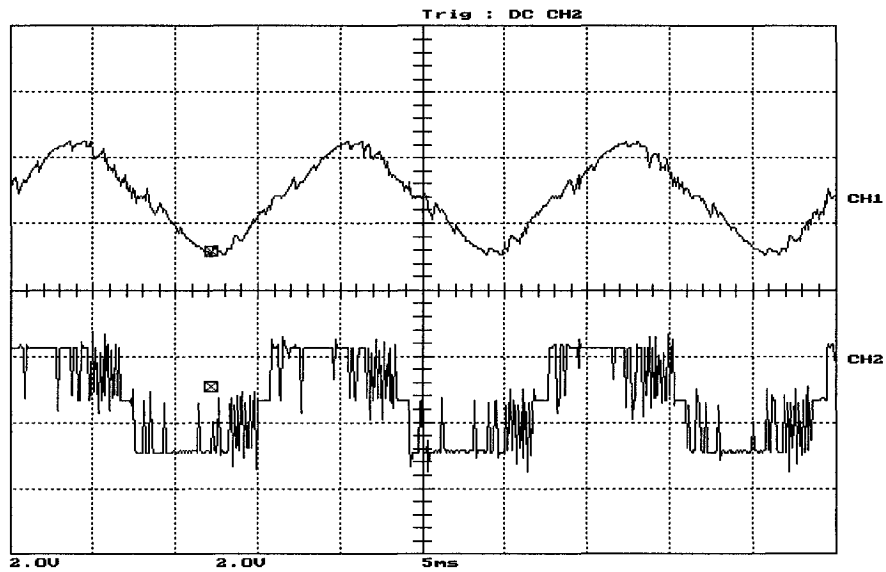

Figure 6.6: The experimental inverter output voltage and the load current collected using the *Tektronics* 2212 storage digital oscilloscope. The voltage scale is 25 V/Div and the current scale is 1.5 A/Div.

Experimental Test Results for Different Output Frequencies

The previous results have demonstrated the experimental performance of a 1ϕ VS four-pulse wavelet-modulated inverter supplying a static load ($R - L$) for an output frequency of 60 Hz. To extend the experimental testing of the wavelet modulation technique, other output frequencies were also considered. These frequencies include:

- 50 Hz
- 90 Hz

- 120 Hz
- 150 Hz

Test results for an output frequency of $f = 50\ Hz$ are presented in this chapter, while results for the rest of tested frequencies are presented in Appendix A. The same experimental setup as described for testing $f_m = 60\ Hz$ with the same $R - L$ load is used to test the performance of the 1ϕ VS wavelet-modulated inverter for an output frequency of 50 Hz. Moreover, the same procedures for collecting and analyzing output voltages and load currents are applied. Figure 6.7 shows the inverter output voltage and its harmonic spectrum. The spectrum of the output voltage has been determined using the $FLUKE\ 41$ power harmonic analyzer.

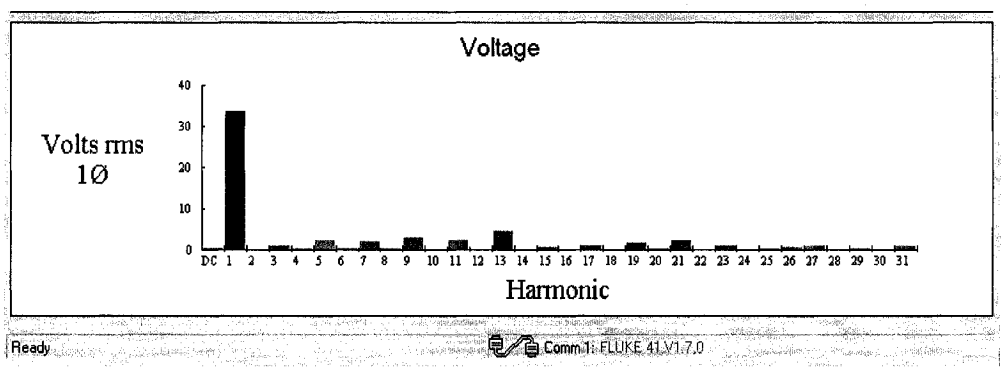

Figure 6.7: The experimental inverter output voltage for an output frequency of $f = 50\ Hz$ and its spectrum obtained using the $FLUKE41$ power harmonic analyzer. The THD_V is 17.8%.

The $R - L$ load connected across the output terminals of the tested 1ϕ VS wavelet-modulated inverter draws a current $I_L(t)$. This current is collected using a hall-effect current sensor, and fed into the $FLUKE\ 41$ power harmonic analyzer to obtain its spectrum. Figure 6.8 shows the load current along with its spectrum. It is to be noted that the load impedance value is lower than the value for $f = 60\ Hz$ due to the existence of the inductive element.

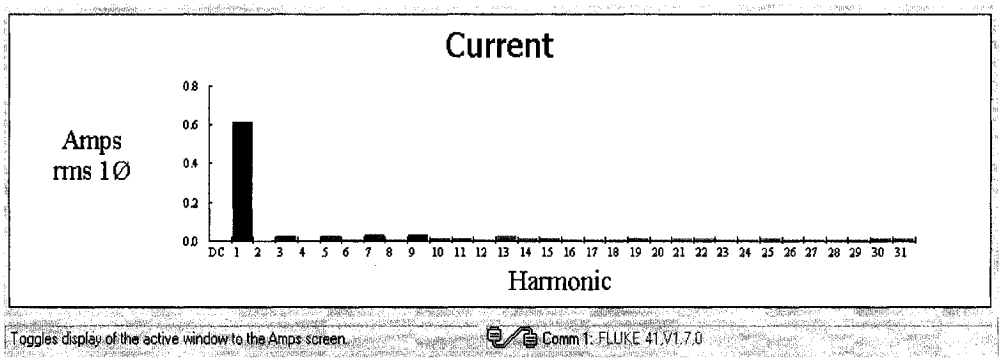

Figure 6.8: The experimental load current for an output frequency of $f = 50\ Hz$ and its spectrum using the $FLUKE\ 41$ power harmonic analyzer. The THD_I is 2.2%.

Experimental test results show the significant capabilities for harmonic elimination of the tested 1ϕ VS wavelet-modulated inverter based on the output voltage and load current. This is clearly indicated by the low values of THD factors of the collected inverter output voltages and load currents. Moreover, the fundamental components of the collected voltages as well as currents have peak values that are very close to the input dc values, indicating effective output energy concentration in the desired output frequency component. The next subsection presents results from testing a single-phase induction motor load.

6.3.2 The Single-Phase Capacitor-Run Induction Motor

This motor is tested to examine the behavior of the 1ϕ VS wavelet-modulated inverter when supplying a dynamic load. The 1ϕ capacitor-run induction motor is rated at 60 Hz, but it will be tested for other frequencies as well.

Results for an Output Frequency of 60 Hz

The experimental setup for the tested 1ϕ VS inverter and measuring instruments is kept the same as in the case of the $R - L$ load as described before. The 1ϕ induction motor terminals (P, N shown in Figure 6.1) are connected to the output terminals of the tested inverter. Switching pulses are applied to the gates of IGBT switches, and the dc voltage supply is set to 110 V. It is to be noted that the inverter output voltage is an amplified version of the one shown in Figure 6.3 because the same switching pulses are used. Figure 6.9 shows the inverter output voltage and its harmonic spectrum. The spectrum of the output voltage has been determined using the $FLUKE\ 41$ power harmonic analyzer.

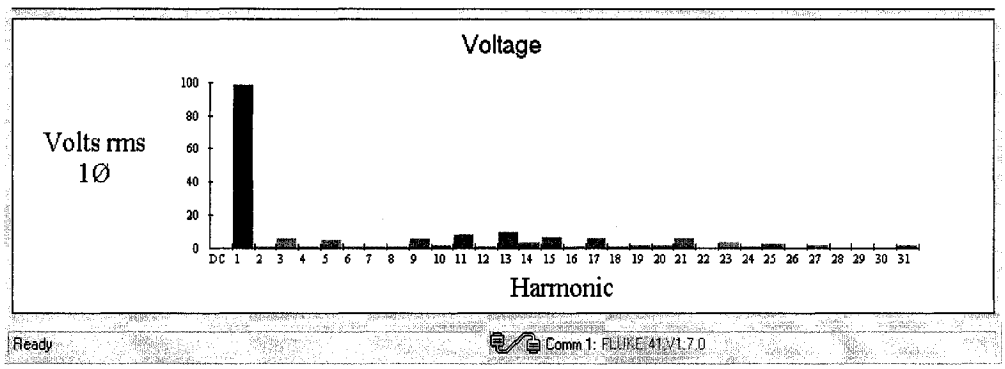

Figure 6.9: The experimental inverter output voltage for an output frequency of $f = 60\ Hz$ and its spectrum obtained using the $FLUKE41$ power harmonic analyzer. The THD_V is 17.4%.

As the tested 1ϕ capacitor-run induction motor draws current from the inverter, its speed begins to build up until it reaches its rated value. The motor current is collected using the hall-effect current sensor and fed into the $FLUKE\ 41$ power harmonic analyzer to obtain its spectrum. Figure 6.10 shows the motor current along with its spectrum. It is to be noted that this output current is obtained for an output frequency of 60 Hz. Figure 6.11 shows the inverter output voltage and the motor

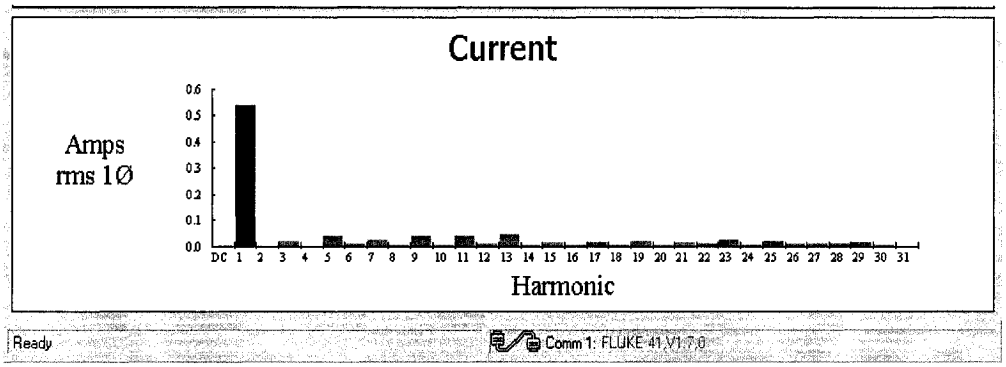

Figure 6.10: The experimental 1ϕ capacitor-run induction motor current and its spectrum using the $FLUKE$ 41 power harmonic analyzer. The THD_I is 2.72%.

current waveforms. These waveforms are collected using the $Tektronics$ 2212 storage digital oscilloscope.

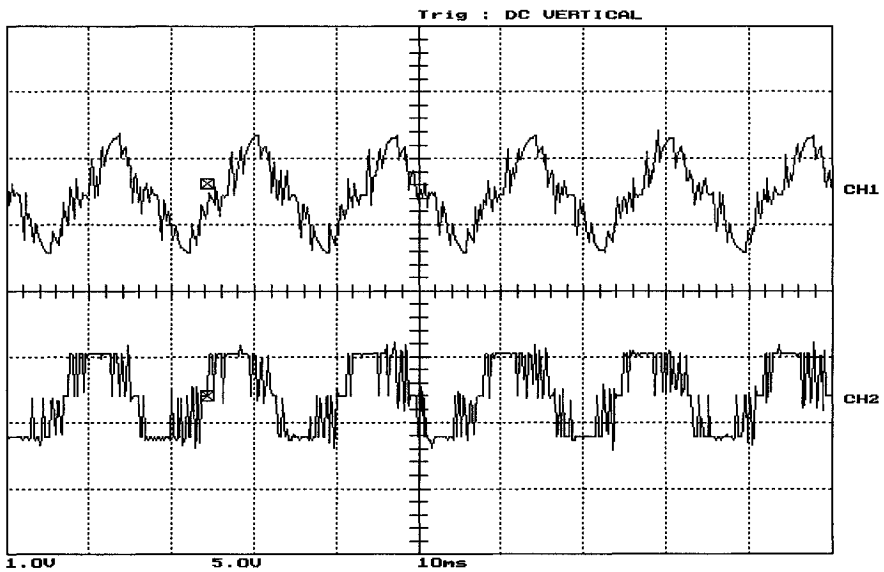

Figure 6.11: The experimental inverter output voltage and the 1ϕ capacitor-run induction motor current waveforms collected using the $Tektronics$ 2212 storage digital oscilloscope. The voltage scale is 150 V/Div and the current scale is 1 A/Div.

Experimental Test Results for Different Output Frequencies

The tested 1ϕ capacitor-run induction motor is rated at 60 Hz. However, it is tested for several other output frequencies. These frequencies provide additional performance testing for different operating conditions. Such tests include the following frequencies:

- 50 Hz
- 90 Hz
- 120 Hz
- 150 Hz

Test results for the output frequency of $f = 90\ Hz$ are presented in this chapter, while results for the rest of tested frequencies are presented in Appendix A. The same experimental setup for supplying the 1ϕ capacitor-run induction motor as described for testing $f_m = 60\ Hz$ is used for testing the performance of the wavelet modulated inverter for an output frequency of 90 Hz. Also, the inverter output voltage and motor current are collected and analyzed using the same procedures and instruments. Figure 6.12 shows the inverter output voltage and its harmonic spectrum along with its spectrum that is determined using the $FLUKE\ 41$ power harmonic analyzer.

The 1ϕ capacitor-run induction motor draws a current that is collected using the hall-effect current sensor and fed to the $FLUKE\ 41$ power harmonic analyzer device to obtain its spectrum. The 1ϕ induction motor current along with its spectrum are shown in Figure 6.13.

The previous experimental results for the 1ϕ VS four-pulse wavelet modulated inverter supplying a dynamic load have demonstrated the significant capabilities

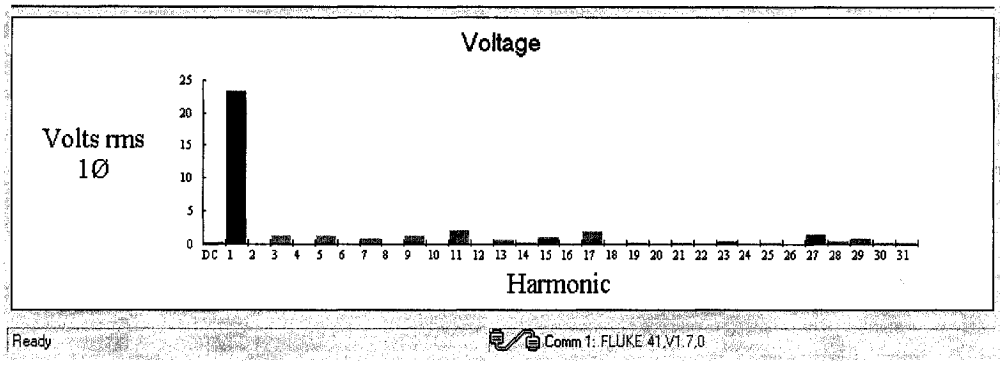

Figure 6.12: The experimental inverter output voltage for an output frequency of $f = 90\ Hz$ and its spectrum using the $FLUKE\ 41$ power harmonic analyzer. The THD_V is 12.7%. The voltage scale is 1:4.

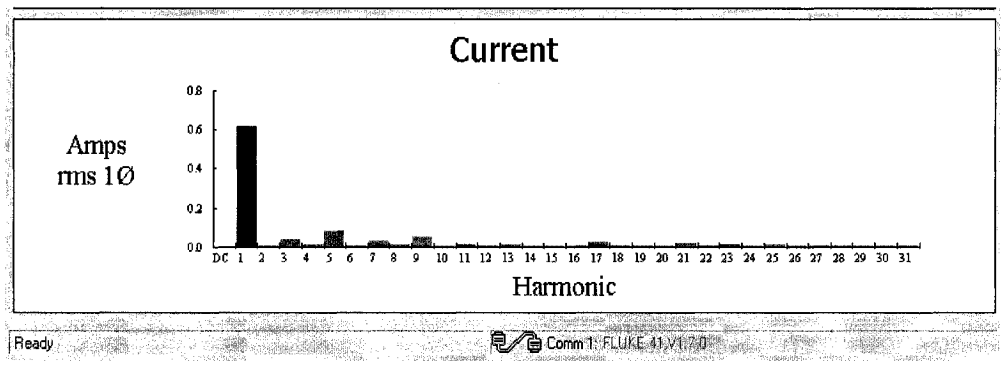

Figure 6.13: The experimental 1ϕ capacitor-run induction motor current for an output frequency of $f = 90\ Hz$ and its spectrum obtained using the $FLUKE\ 41$ power harmonic analyzer. The THD_I is 6.2%.

for harmonic elimination from output voltages and currents. This is clearly indicated by the low values of THD factors of output voltages and load currents. Moreover, output waveforms have shapes very close to sinusoidal with fundamental components very close to the dc supply voltages and currents.

Experimental test results presented for both static and dynamic loads clearly show the high quality performance of the tested 1ϕ VS four-pulse wavelet modulated inverter. Also, they show significant capabilities to concentrate the output

energy in the desired frequency bands. These features of the tested inverter performance confirm the efficacy of the wavelet modulation technique.

Sinusoidal pulse-width modulated (SPWM) inverters are very popular in wide ranges of industrial applications. In order to demonstrate the advantages of the developed wavelet-modulated inverter, it is convenient to compare both modulated inverters for the same loading conditions. The next section presents experimental test results of a 1ϕ VS four-pulse SPWM inverter tested for the same loading conditions presented in the previous section for testing the WM inverter.

6.4 Experimental Tests of an SPWM Inverter

The previous section has presented experimental test results for a 1ϕ wavelet-modulated inverter for different loads and output frequencies . This sections aims to provide a performance comparison between a wavelet-modulated and a sinusoidal pulse-width modulated (SPWM) inverters for the same loading conditions. In order to carry out such performance comparison, a typical SPWM technique is implemented to generate switching pulses for the same 1ϕ VS four-pulse inverter for same loads. The implemented SPWM has a triangular carrier signal with a switching frequency of $f_s = 2\ kHz$ and an amplitude modulation index $m_a = 0.8$ for an output frequency of 60 Hz.

SPWM switching pulses are applied to inverter IGBT gates and the dc voltage supply is turned on. This causes an output voltage to appear on inverter output terminals (P and N as in Figure 6.1). The inverter output voltage is collected using a hall-effect voltage sensor and is fed into the $FLUKE\ 41$ power harmonic analyzer to obtain its spectrum. Figure 6.14 shows the inverter output voltage along with its spectrum.

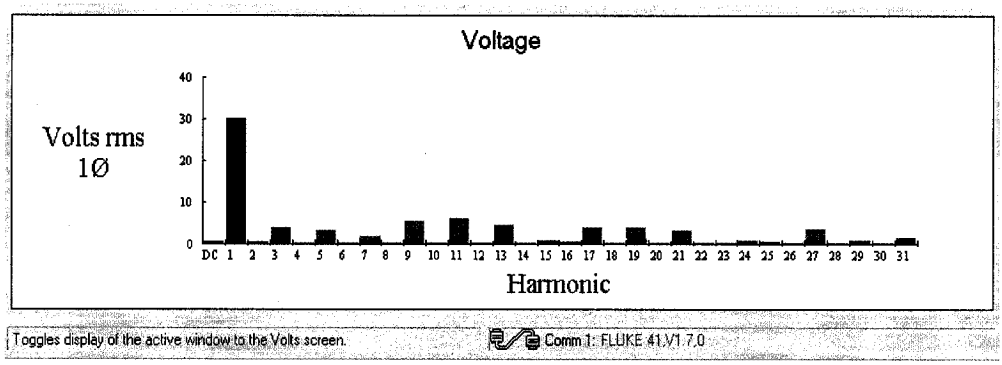

Figure 6.14: The experimental SPWM inverter output voltage with $f_s = 2\ kHz$ and $m_a = 0.8$ and its spectrum using the $FLUKE\ 41$ power harmonic analyzer device. The THD_V is 32.7%.

A static $R-L$ load is connected between inverter output terminals, which draws a current $I_L(t)$. This current is collected using the hall-effect current sensors and fed into the $FLUKE\ 41$ power harmonic analyzer to obtain its spectrum. Figure 6.15 shows the load current along with its spectrum. The same 1ϕ VS four-pulse

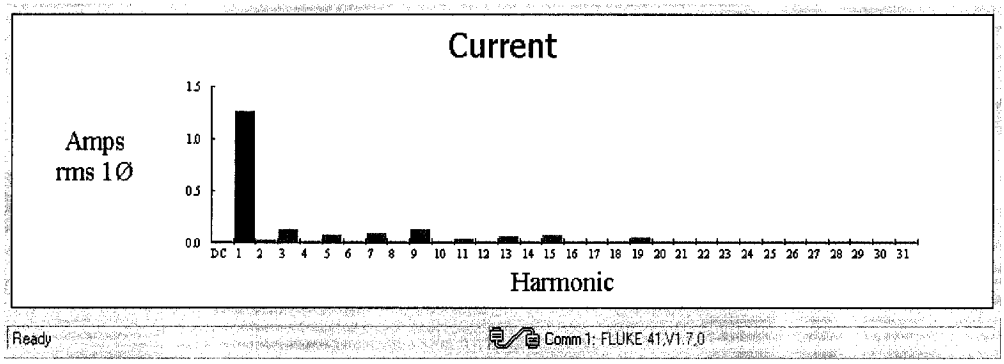

Figure 6.15: The experimental $R-L$ load current supplied by a 1ϕ VS SPWM inverter with $f_s = 2\ kHz$ and $m_a = 0.8$ along with its spectrum using the $FLUKE\ 41$ power harmonic analyzer. The THD_I is 11.5%.

SPWM inverter is used to supply the 1ϕ capacitor-run induction motor. The inverter output voltage is collected using a hall-effect voltage sensor and fed into the $FLUKE\ 41$ power harmonic analyzer to obtain its spectrum. Figure 6.16 shows

the inverter output voltage along with its spectrum. The motor current is collected

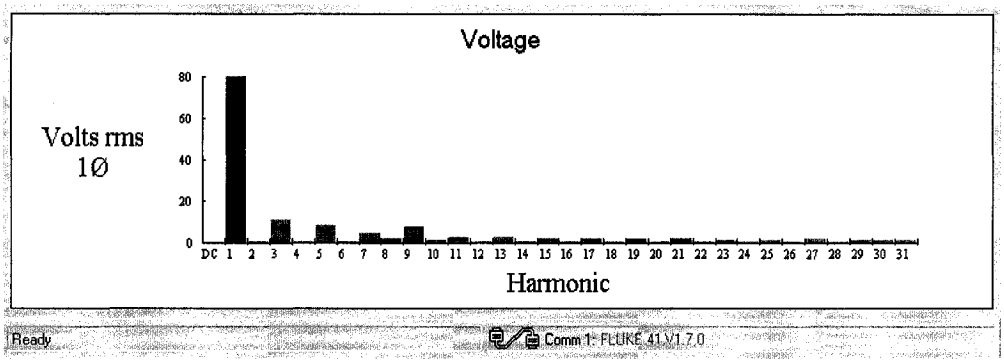

Figure 6.16: The experimental SPWM inverter output voltage with $f_s = 2\ kHz$ and $m_a = 0.8$ and its spectrum using the $FLUKE\ 41$ power harmonic analyzer device. The THD_V is 25.7%.

using a hall-effect current sensor and fed into the $FLUKE\ 41$ power harmonic analyzer to obtain its spectrum. Figure 6.17 shows the motor current along with its spectrum. Figure 6.18 shows the SPWM inverter output voltage and the motor cur-

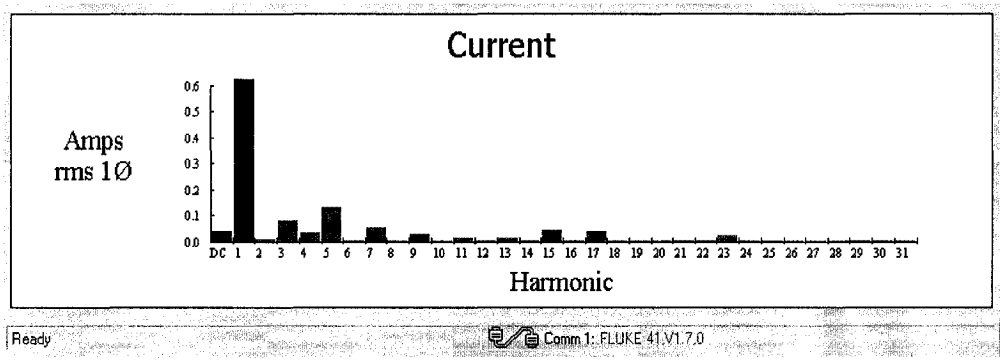

Figure 6.17: The experimental 1ϕ induction motor current supplied by a 1ϕ VS SPWM inverter with $f_s = 2\ kHz$ and $m_a = 0.8$ along with its spectrum using the $FLUKE\ 41$ power harmonic analyzer. The THD_I is 12.96%.

rent waveforms. These waveforms are collected using the $Tektronics\ 2212$ storage digital oscilloscope.

Experimental test results obtained from the SPWM inverter for comparison pur-

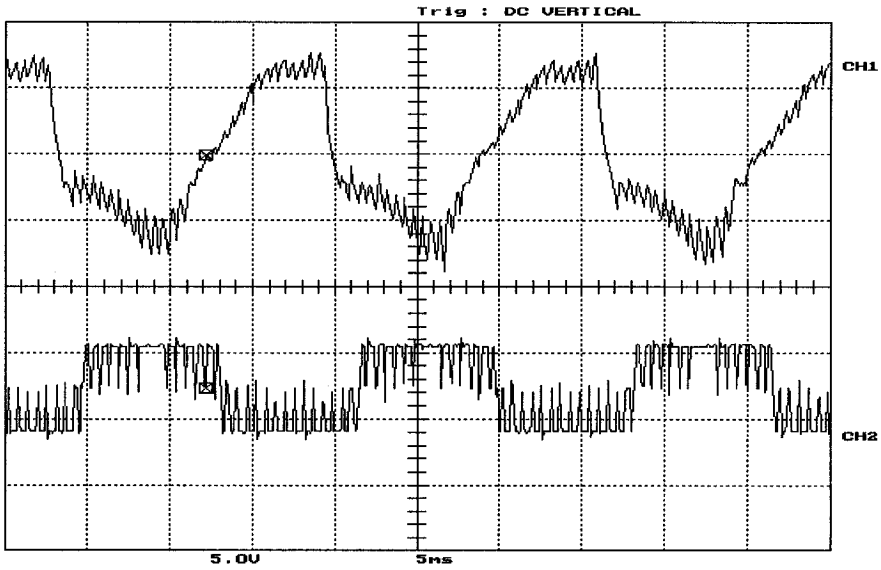

Figure 6.18: The experimental SPWM inverter output voltage and the 1ϕ capacitor-run induction motor current collected using the *Tektronics* 2212 storage digital oscilloscope. The voltage scale is 50 V/Div and the current scale is 0.2 A/Div.

poses with their analog results obtained from the wavelet-modulated one. Table 6.1 summarizes these results. THD_V is the total harmonic distortion factor of the in-

Table 6.1: Performance comparison between experimental WM and SPWM inverters for the $R-L$ load and the 1ϕ capacitor-run induction motor.

Load	Parameter	WM	SPWM
$R-L$	$\lvert V_1\rvert$	49.27 V	39.71 V
	$\lvert I_1\rvert$	3.66 A	2.95 A
	THD_V	16.1%	32.7%
	THD_I	1.86%	11.5%
Motor	$\lvert V_1\rvert$	108.26 V	82.4 V
	$\lvert I_1\rvert$	1.02 A	1.68 A
	THD_V	17.40%	25.42%
	THD_I	2.72%	12.96%

verter output voltage and THD_I is the total harmonic distortion factor of the load current. The THD factor is defined in equation (5.6).

Table 6.1 demonstrates clearly that the WM inverter has higher fundamental components and lower output harmonic contents than the SPWM one. Such performance comparisons confirm the results obtained from simulating both inverters in chapter 5, in particular, that the wavelet-modulated inverter has capabilities to transfer higher power than does the SPWM inverter. The data of Table 6.1 along with the previous discussion provide an experimental confirmation of the efficacy of the developed wavelet modulation technique. The next section provides experimental evaluations and test results of the $scale - time\ interval$ factor γ.

6.5 The Scale-Time Interval Factor

The $scale-time\ interval$ factor γ (defined in chapter 5 by equation (5.8)) provides an insight about the change in time interval of each group of non-uniform recurrent samples with the change in the scale j. Also, this factor provides a time-scale relation that can provide time localized values of the scale over a half-cycle of the reference-modulating signal $S_M(t)$. Such a time-scale relation is important when considering adjusting the inverter output during its operation as will be discussed in chapter 7. The factor γ can be evaluated as one step of the wavelet modulation technique implementation algorithm developed in section 5.2.

The scale-time interval factor γ is defined as:

$$\gamma_d = \gamma_{d-1} + \frac{S'_M(t_{d2})}{|S'_M(t_{d2})|} \sum_{m=1}^{j} m2^m \left(t_{m2} - t_{m1}\right) \tag{6.1}$$

where γ_d is the scale-time interval factor for non-uniform recurrent samples group d and j is the scale. The factor γ changes its increasing pattern into a decreasing one following a change in the sign of the derivative of the reference modulating signal

$S'_M(t)$. As a consequence, the term $\frac{S'_M(t_{d2})}{|S'_M(t_{d2})|}$ ensures changing γ from an increasing sequence to a decreasing one following any change in the sign of $S'_M(t)$. This can be very important when relating the change in the scale to the change in the sampled signal. Figure 6.19 shows the γ factor for an output frequency of 60 Hz.

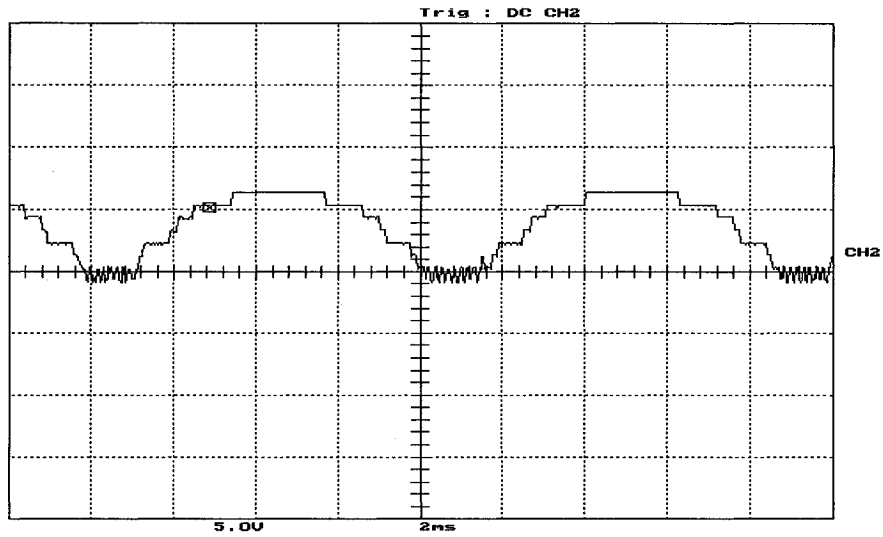

Figure 6.19: The scale-time interval factor γ for an output frequency of $f = 60\ Hz$ collected using *Tektronics* 2212 storage digital oscilloscope.

The factor γ has also been collected for an output frequency of $f = 90\ Hz$, and is shown in Figure 6.20. The experimental results for evaluating the factor γ for the rest of the tested inverter output frequencies are provided in Appendix A.

Experimental results for evaluating the scale-time interval factor γ are almost identical to the simulation results presented in chapter 5; Figures 5.18 and 5.19. Such close results demonstrate that the proposed wavelet modulation technique functions the same regardless of the computational hardware.

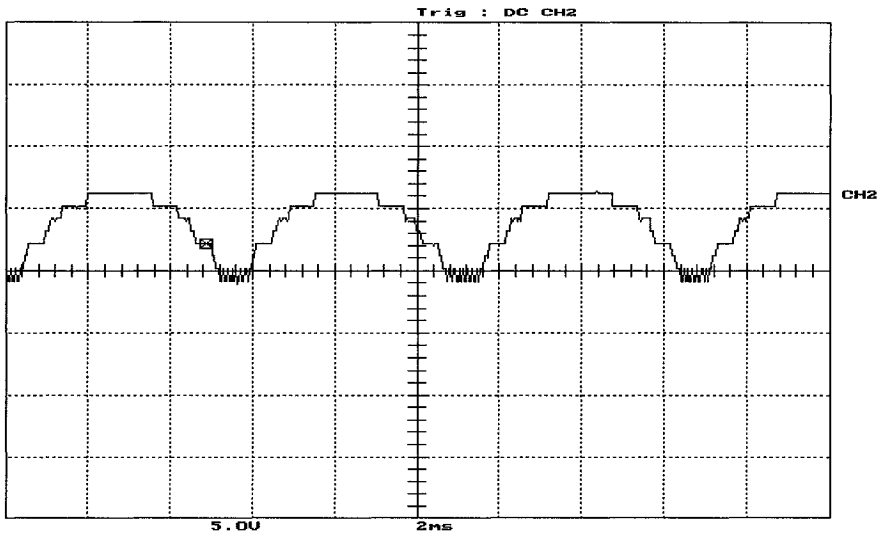

Figure 6.20: The scale-time interval factor γ for an output frequency of $f = 90\ Hz$ collected using $Tektronics$ 2212 storage digital oscilloscope.

6.6 Comments on Experimental Test Results

Several experimental tests are conducted to demonstrate the performance of the 1ϕ WM inverter for different loads at different output frequencies. In all these tests, the proposed wavelet modulation technique has been implemented through a $Turbo - C$ code, which is complied using the Texas Instrument Complier and executed by the $dSPACE\ ds1102$ board. Also, all the produced voltage and current waveforms are collected using hall-effect sensors, and are converted to images using the 2-channel $Tektronics$ digital oscilloscopes. Finally, the spectral analysis to determine the THD factors as well as the magnitude of V_1 is carried out using the $FLUKE41$ Power Harmonic Analyzer.

The instrumentation devices and components used for collecting and analyzing the waveforms of the experimental tests have some functional limitations that are summarized as follows:

- The sampling rate: This factor affects the $ds1102$ board, the $Tektronics$ digital oscilloscopes and the $FLUKE41$ Power Harmonic Analyzer. The limited sampling rate of these instrumentations can cause some deformations in the collected waveforms (voltages and currents), can lower the resolution of the obtained images for the collected waveforms, and spectra and may limit the performances of the $ds1102$ board

- Anti-aliasing filters: These filters are used to smooth out any spikes when carrying out the analog-to-digital conversion of both data and images. Personal computers, $Tektronics$ digital oscilloscopes and $FLUKE41$ Power Harmonic Analyzer have anti-aliasing filters at their input/output ports. These filters can cause deformation in the waveforms when displayed as images as well as filtered version of other images as in the waveforms produced by the $FLUKE41$.

- Limited operating frequency bandwidth: The used hall-effect sensors have operating frequency bandwidth that may not be wide enough to accommodate all the frequencies present in the collected voltage and current waveforms. This limitation can be responsible for additional distortion in the experimental test results.

The aforementioned features of the employed instrumentations can deform some images showing experimental test results. However, these minor deformations in the presented experimental results do not change the fact that these results provide strong evidence for the significant performance of the proposed WM inverters.

This chapter presented experimental results for testing a 1ϕ VS four-pulse wavelet modulated inverter. This developed wavelet-modulated inverter has been

tested with two types of loads for different output frequencies. Experimental results for both loads have demonstrated a powerful capability to eliminate harmonics from inverter output voltages and currents. Some results obtained using a typical 1ϕ SPWM inverter are presented for comparison purposes. The comparison of these two techniques has shown the high quality performance of the proposed WM technique. In all tests, the load nature (static or dynamic) has little effect on switching the inverter as well as the quality of inverter outputs. The scale-time interval factor is determined for all the tested loads, and is used to demonstrate the change of the resolution level of the synthesis scaling function $\{\tilde{\varphi}_j(t)\}$.

In all the experimental tests, the laboratory 1ϕ four-pulse IGBT inverter is supplied with a dc voltage that is produced using an ac-dc rectifier. This dc voltage supply delivers its current with some harmonic contents. The waveforms of the input dc voltage and current along with their spectra for all the tested loads are provided in Appendix A.

The next chapter, chapter 7, presents a control strategy for adjusting the magnitudes and the frequencies of a 1ϕ WM inverter when supplying different load types under different operating conditions. Simulation and experimental test results for the performance of the controlled WM inverter are provided and discussed.

Chapter 7

Analysis and Testing of Resolution-Level Controlled 1ϕ WM Inverters

7.1 General

The last two chapters, chapter 5 and chapter 6, have presented various performance test results for single-phase (1ϕ) wavelet-modulated (WM) inverters. The presented results have included different load types supplied at different frequencies. In all these tests, the proposed WM inverter has shown remarkable capabilities to produce high quality outputs. Also, the presented test results have been conducted to investigate the performance of the WM inverter for constant output mode of operation (i.e. inverter output voltages are not varied during the operation).

In several industrial applications, inverters are operated within control loops

to adjust the magnitudes as well as frequencies of their outputs. Such modes of operation are usually required to meet the continuous changes in the supplied load demands. These industrial applications include adjusting the speed in ac motor drives, voltage compensation in power quality applications, varying the energy distributed in harmonic frequencies for power conditioning applications, etc. [11, 15, 27, 68–72]. The key approach for achieving adjustable inverter output magnitudes and frequencies is through changing the widths and the locations of the generated switching pulses. Several control strategies have been developed and tested to carry out this approach including the following [68–79]:

1. Proportional-integral (PI) controllers;
2. Dead-beat current controllers;
3. Sliding mode controllers;
4. State-space controllers;
5. Fuzzy logic controllers;
6. Hysteresis-band current controllers;
7. Intelligent controllers;

The aforementioned control strategies are developed to adjust magnitudes and/or frequencies of the inverter outputs, while maintaining predefined levels of the output quality (pre-defined maximum values of THD factors). It is worth mentioning that the aforementioned strategies are mostly developed to control the outputs of PWM inverters [70–77]. This chapter aims to provide a control approach to vary magnitudes and frequencies of the wavelet modulated (WM) inverter output. The proposed approach is based on changing the scale j (dilation) of the

synthesis scaling functions $\{\tilde{\varphi}_j(t)\}_{j=1,2,..}$. This control strategy will be called the resolution-level control strategy.

7.2 Resolution-Level Control Strategy

The fundamental idea of the wavelet modulation technique is the construction of a non-dyadic-type multiresolution analysis (MRA). The synthesis part of such a MRA is carried out by inverter switching elements. The synthesized inverter output is composed of a train of variable-width pulses that represent dilated and translated versions of the scale-based linearly-combined synthesis scaling function $\tilde{\varphi}_1(t)$. Moreover, the interval of support of $\tilde{\varphi}_1(t)$ at each dilation and translation depends on the value of the scale j. These dilated and translated versions of $\tilde{\varphi}_1(t)$ have a repetitive nature due to the periodicity and the quarter-cycle symmetry of the sampled sinusoidal reference-modulating signal $S_M(t)$. As a result, the output voltage of the 1ϕ voltage-source (VS) WM inverter over one cycle of the reference-modulating signal ($S_M(t)$) can be expressed as:

$$\frac{V_o(t)}{V_{DC}} = \sum_{d=1}^{\mathcal{D}_\varphi} \langle S_M(t), \varphi_d(t) \rangle \, \tilde{\varphi}_d(t) - \sum_{d=1}^{\mathcal{D}_\varphi} \left\langle S_M(t), \varphi_d\left(t - \frac{T_m}{2}\right) \right\rangle \tilde{\varphi}_d\left(t - \frac{T_m}{2}\right) \quad (7.1)$$

It is to be noted that the term $\langle S_M(t), \varphi_d(t) \rangle$ represents the values of the samples created by $\varphi(t)$. However, the inverter switching elements are operated either fully ON or OFF, which causes their outputs to be either the input dc voltage or 0. This mode of operating the inverter switching elements in addition to the quarter cycle symmetry can simplify the expression of the WM inverter output voltage over one

cycle of $S_M(t)$ to the following:

$$\frac{V_o(t)}{V_{DC}} = \sum_{j=1}^{J} \tilde{\varphi}_j(t) + \sum_{j=1}^{J-1} \tilde{\varphi}_{(J-j)}(t) - \sum_{j=1}^{J} \tilde{\varphi}_j\left(t - \frac{T_m}{2}\right) - \sum_{j=1}^{J-1} \tilde{\varphi}_{(J-j)}\left(t - \frac{T_m}{2}\right) \quad (7.2)$$

where J is the maximum value of the scale j. The sample groups index d is replaced by the scale j due to the fact that one group of samples is created by $\varphi(t)$ at each scale j. Figure 7.1 shows one cycle of the output voltage of 1ϕ WM inverter with the $\tilde{\varphi}_J(t)$ labeled.

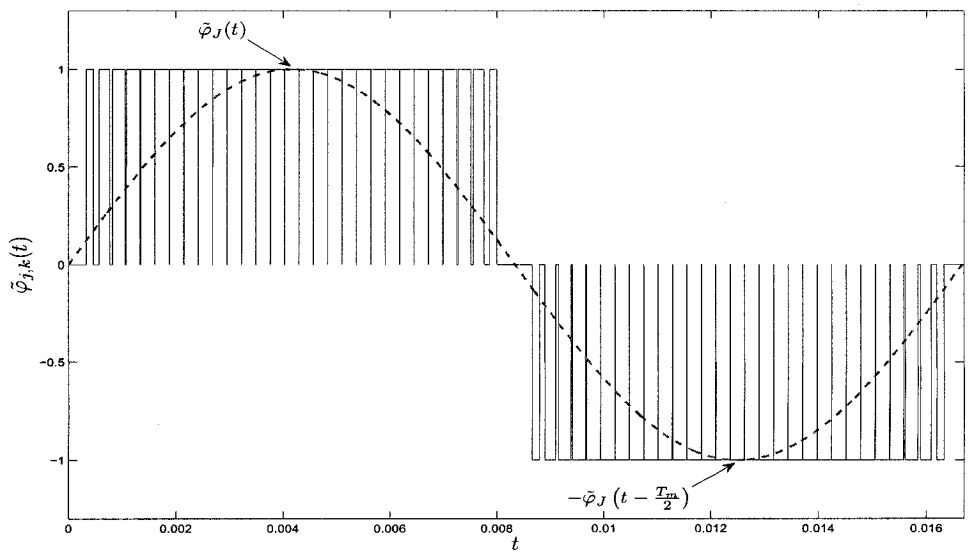

Figure 7.1: One cycle of $V_o(t)$ and shifted and dilated versions of the scale-based linearly-combined synthesis scaling function $\tilde{\varphi}_1(t)$.

Equation (7.2) indicates that changing the value of J will change the durations and the locations of the dilated and shifted versions of $\tilde{\varphi}_1(t)$. Hence, the output voltage of the WM inverter can be changed through adjusting the value of J. Figure 7.2 shows the effects of changing J on the magnitude of the fundamental frequency component of the WM inverter output voltage $|V_1|$ along with the total harmonic

distortion (THD_V) factor for several values of the output frequency (f_m). On the

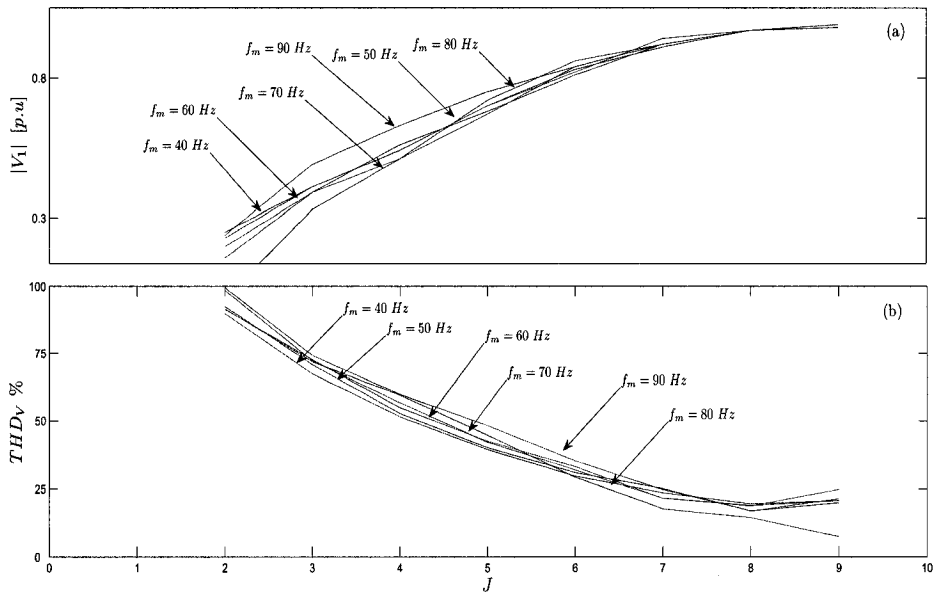

Figure 7.2: The effects of changing J on $|V_1|$ and THD_V for several values of f_m: (a) the magnitude of the fundamental frequency component of the WM inverter output voltage and (b) the total harmonic distortion (THD_V) factor. The base value of the voltage is inverter input dc voltage.

other hand, the scale-time interval factor γ defined in chapter 5, provides a relation between the interval of support (duration) of $\tilde{\varphi}_j(t)$ and the scale j. The factor γ is a piece-wise continuous function in time with its increasing and decreasing behaviors directly related to the first derivative ($S'_M(t)$) of the reference-modulation signal $S_M(t)$. Also, the factor γ changes from an increasing to a decreasing function when the scale $j = J$.

The scale j of successive synthesis scaling functions $\{\tilde{\varphi}_j(t)\}_{j=1,2,..}$ changes either up or down by 1. Further, the change in the scale j depends on the sign of the derivative $S'_M(t)$ evaluated at the $t = t_2$ of each group of non-uniform recurrent samples. This relation between the scale j and the sign on $S'_M(t)$ suggests that

both the durations and the locations of successive synthesis scaling functions can be adjusted depending of the sign of $S'_M(t)$. The relation between the scale j and the sign of $S'_M(t)$ is characterized using the definition of the factor γ as:

$$\gamma_d = \gamma_{d-1} + \frac{S'_M(t_{d2})}{|S'_M(t_{d2})|} \sum_{m=1}^{j} m2^m \left(t_{m2} - t_{m1}\right) \tag{7.3}$$

where γ_d is the scale-time interval factor for the group d of non-uniform recurrent samples.

The previous discussion suggests that the width and the location of each $\tilde{\varphi}_j(t)$ can be changed by changing the value of J. This suggested change in the value of J can be achieved , as the factor γ shows, by varying the time instants at which the derivative $S'_M(t)$ changes its sign from positive to negative or vice versa. The reference-modulating signal $S_M(t)$ is a sine function, which indicates that $S'_M(t)$ is a cosine function. The time instants a cosine function changes its sign can be expressed as [74, 79]:

$$\{t_c\} = \left\{ T_m \left(\frac{1}{4} + \frac{c}{2} \right), \; c \in \mathbb{Z} \right\} \tag{7.4}$$

where T_m is the period of $S_M(t)$. The set $\{t_c\}$ represents the set of time instants, where $S'_M(t)$ changes its sign from positive to negative or vice versa. Figure 7.3 shows the first derivative $S'_M(t)$, the factor γ and the inverter output voltage along with its spectrum for a normal mode of operation.

In general, the time instants of sign changes for a cosine function can be changed using one of the following methods:

1. Shifting $S'_M(t)$ such that:

$$S'_M(t, \omega, \theta) = A_M \cos\left(\omega_m t + \theta\right) \tag{7.5}$$

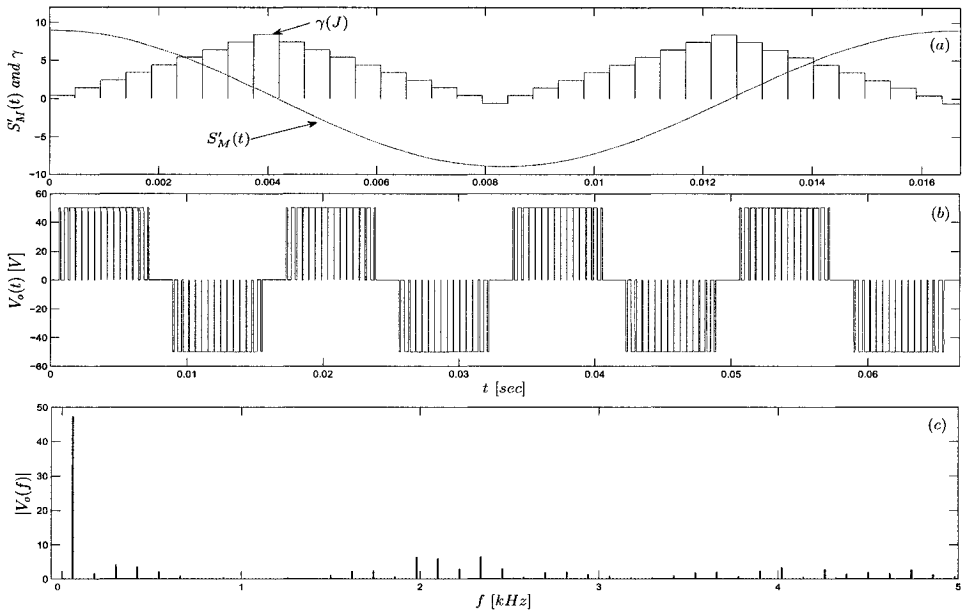

Figure 7.3: The normal mode of operation for the WM inverter: (a) the scale-time interval factor γ and the first derivative of the reference-modulating signal $S'_M(t)$, (b) the inverter output voltage for $f_m = 60\ Hz$ at $V_{DC} = 50\ V$ and (c) the spectrum of the output voltage. $|V_1| = 49.27\ V$ and $\text{THD}_V = 17.64\%$.

where A_M is the peak value of $S'_M(t)$, ω_m is the angular frequency of $S_M(t)$ and θ is a phase shift. The phase shift θ causes the scale j either to exceed J or to begin decreasing before reaching the value of J. As a result, the widths and the locations of successive synthesis scaling functions will be changed that will affect the magnitude of the output fundamental frequency component.

2. Changing the frequency of $S_M(t)$ such that:

$$S'_M(t, \omega, \theta) = A_M \cos(\omega_2 t) \tag{7.6}$$

where ω_{m2} is a new angular frequency of $S_M(t)$. This change in the frequency of $S_M(t)$ results in generating synthesis scaling functions that will reconstruct

$S_M(t)$ at the new frequency f_2. This can be interpreted as shifting the spectral location of the fundamental frequency component of the inverter output from f_{m1} to f_{m2}.

3. A combination of changing the frequency of $S_M(t)$ and introducing a phase shift in $S'_M(t)$ such that:

$$S'_M(t, \omega, \theta) = A_M \cos(\omega_3 t + \theta) \tag{7.7}$$

This combination of shifting $S'_M(t)$ and changing the frequency of $S_M(t)$ results in changing the widths and the locations of the synthesis scaling functions to reconstruct $S_M(t)$ at the new frequency f_{m3}. Also, the phase shift θ vary the magnitude of the fundamental frequency component of the inverter output at the new frequency.

Figure 7.4 shows the effects of changing the phase shift θ on the value of J for several values of f_m.

The aforementioned methods of changing the time instants where the first derivative $S'_M(t)$ changes its sign can adjust the frequency and the magnitude of the WM inverter output that can provide the basis for realizing the proposed resolution-level control strategy. As Figure 7.4 shows, the relation between the θ and J is linear for $\theta \in [-0.5, 0.5]$ rad. The next section presents simulation test results for the performance of 1ϕ VS WM inverter with the resolution level control.

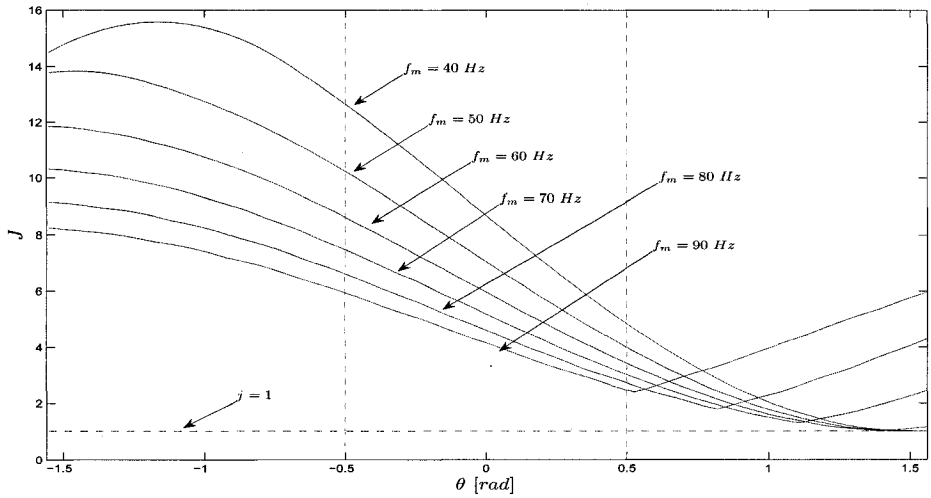

Figure 7.4: The effects of changing the phase shift θ on the maximum value of the scale J for several values of f_m.

7.3 Testing A Resolution-Level Controlled WM Inverter

The previous section presented the resolution-level control approach for adjusting magnitudes as well as frequencies of the WM inverter outputs. This approach is based on changing the time instants where $S'_M(t)$ changes its sign. Furthermore, three methods to realize the resolution-level control approach have been suggested [73, 74]. The resolution-level control strategy can be implemented as a part of the wavelet modulation technique by adding both the frequency of $S_M(t)$ and phase shift θ as variables to be updated while generating the inverter switching pulses. Figure 7.5 shows a flowchart diagram for implementing the resolution-level control strategy.

This section presents simulation test results for a resolution-level controlled WM VS inverter. It should be noted that simulation tests are conducted for a 1ϕ

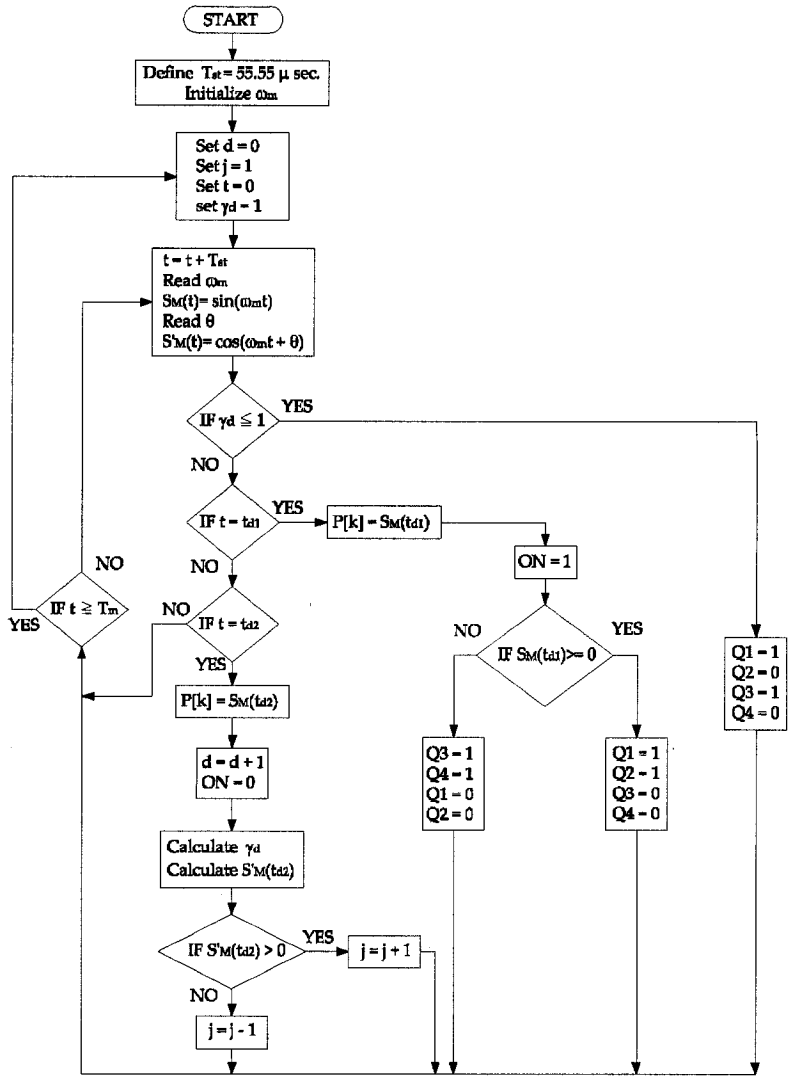

Figure 7.5: A flowchart for implementing the resolution-level control strategy to operate a 1ϕ WM inverter.

VS four-pulse WM inverter when supplying a $R - L$ load. Moreover, the experimental test results for a 1ϕ VS four-pulse IGBT WM inverter when supplying a $R - L$ load are presented in Appendix B.

7.3.1 Simulating the Performance of a Resolution-Level Controlled WM Inverter

The performance of a 1ϕ VS four-pulse WM inverter is simulated using MATLAB/SIMULINK software under resolution-level control. The simulated inverter supplies an $R-L$ load of $Z_L = 10 + j7.45\ \Omega$ with an input dc voltage of 50 V. The resolution-level control is added as a part of the developed $MATLAB$ code for implementing the wavelet modulation technique. This code generates switching pulses to activate a SIMULINK model of a 1ϕ VS inverter and the $R-L$ load. Three cases are simulated to investigate the performance of the resolution-level controlled WM inverter including the following:

- Introducing a phase shift of $\theta = -\frac{\pi}{12}$.
- Changing the output frequency to $f_m = 75\ Hz$.
- Changing the output frequency to $f_m = 50\ Hz$ with $\theta = \frac{\pi}{10}$.

Simulation Results for $\theta = -\frac{\pi}{12}$

The case represents introducing a negative phase shift in the first derivative $(S'_M(t))$. The phase shift is set to $\theta = -\frac{\pi}{12}$, which makes $(S'_M(t))$ have the following expression:

$$S'_M(t,\theta) = \cos\left(120\pi t - \frac{\pi}{12}\right) \tag{7.8}$$

Figure 7.6 shows $S'_M(t)$, the factor γ along with the inverter output voltage and its spectrum for this case. The load current for $\theta = -\frac{\pi}{12}$ along with its spectrum are shown in Figure 7.7. It should be noted that all the spectra in the following simulation tests are determined after changing θ and/or f_m.

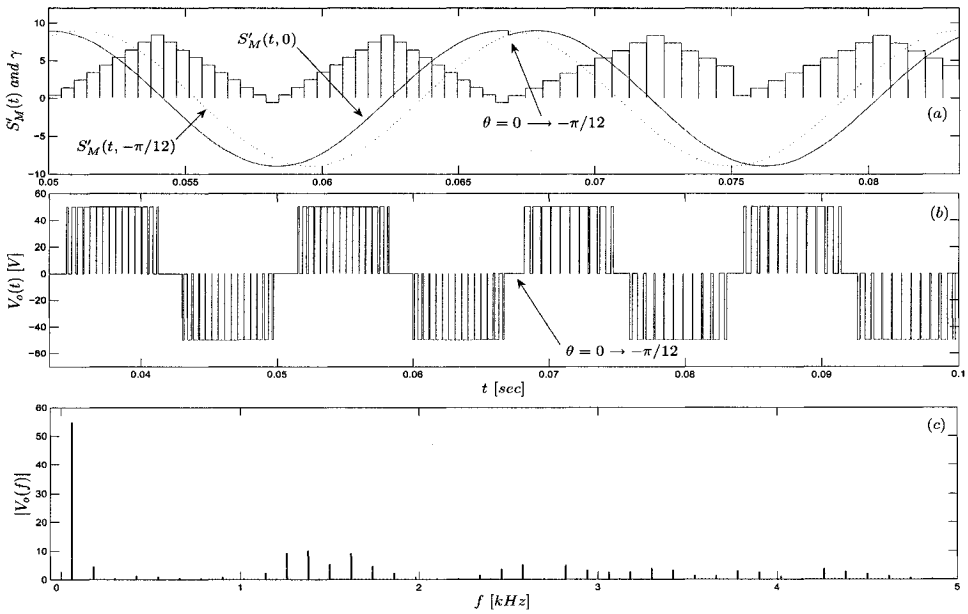

Figure 7.6: Introducing a phase shift of $\theta = -\frac{\pi}{12}$ in $S'_M(t)$: (a) the derivative $S'_M(t)$ and the factor γ, (b) the inverter output voltage and (c) the spectrum of the inverter output voltage. $|V_1| = 54.12\ V$ and $\text{THD}_V = 18.97\%$.

The simulation result shows an increase in the magnitude of the fundamental frequency component of the inverter output voltage ($|V_1| = 49.27\ V \longrightarrow 54.12\ V$) with a small change in the THD_V factor ($\text{THD}_V = 17.64\% \longrightarrow 18.97\%$). Also, the fundamental frequency component of the load current has increased ($|I_1| = 3.08\ A \longrightarrow 3.48\ A$) with a small change in the THD_I factor ($\text{THD}_I = 2.15\% \longrightarrow 2.77\%$).

Simulation Results for $f_{m2} = 75\ Hz$

The performance of the WM inverter with the output frequency set at $f_{m2} = 75\ Hz$ is simulated for the $R - L$ load. For this case, the frequency of the reference-

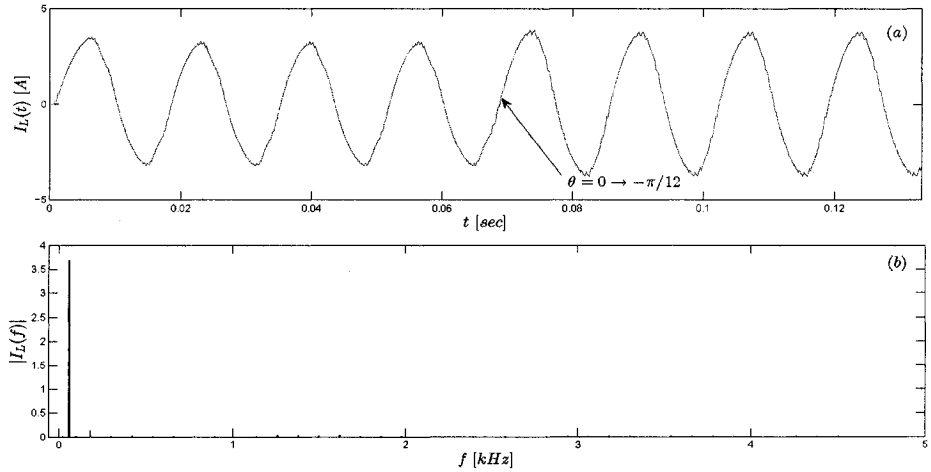

Figure 7.7: The load current $I_L(t)$ and its spectrum: (a) the load current $I_L(t)$ and (b) its magnitude spectrum $|I_L(f)|$. $|I_1| = 3.48\ A$ THD_I = 2.77%.

modulating signal $S_M(t)$ is set at $f_{m2} = 75\ Hz$, which makes $S'_M(t)$ expressed as:

$$S'_M(t, f_m) = \cos(150\pi t) \tag{7.9}$$

Figure 7.8 shows $S'_M(t)$, factor γ, the inverter output voltage and its spectrum for this case. The load current for $f_{m2} = 75\ Hz$ along with its spectrum are shown in Figure 7.9.

The simulation result shows almost no change in the magnitude of the fundamental frequency component of the inverter output voltage ($|V_1| = 49.27\ V \longrightarrow 48.46\ V$) with a small change in the THD_V factor ($\text{THD}_V = 17.64\% \longrightarrow 16.94\%$. Also, the fundamental frequency component of the load current has decreased ($|I_1| = 3.08\ A \longrightarrow 2.56\ A$) with a small change in the THD_I factor ($\text{THD}_I = 2.15\% \longrightarrow 2.93\%$). It is to be noted that the decrease in the current is due to the increase in the load impedance when f_m is increased to 75 Hz.

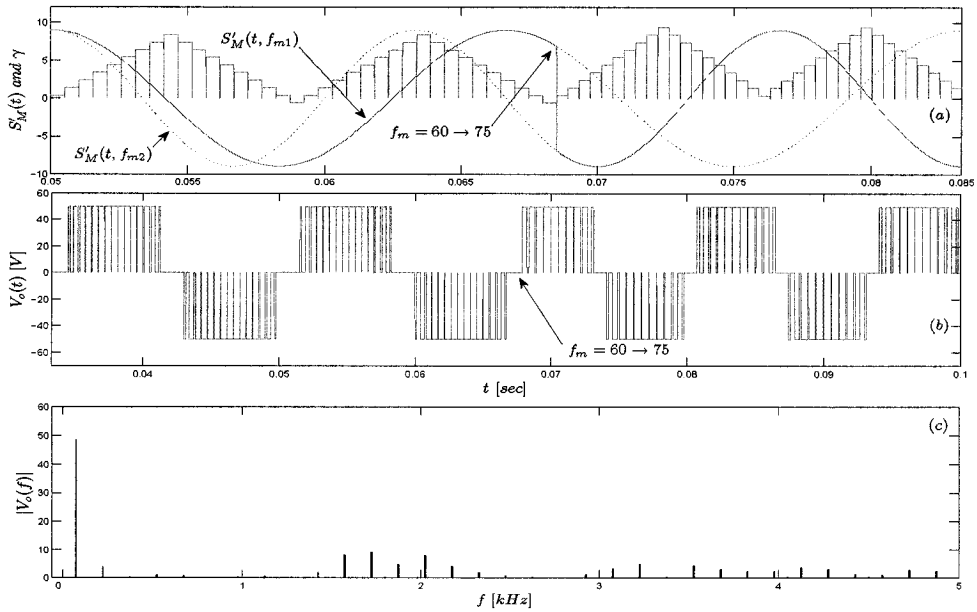

Figure 7.8: Changing the frequency of $S_M(t)$ $f_m = 60 \rightarrow 75$ Hz: (a) the derivative $S'_M(t)$ and the factor γ, (b) the inverter output voltage and (c) the spectrum of the inverter output voltage. $|V_1| = 48.46$ V and $\text{THD}_V = 16.94\%$.

Simulation Results for $f_{m3} = 50$ Hz with $\theta = \frac{\pi}{10}$

The performance of the WM inverter with the output frequency set at $f_{m2} = 50$ Hz and the phase shift $\theta = \frac{\pi}{10}$ is simulated for the $R - L$ load. For this case, the first derivative $S'_M(t)$ has the following expression:

$$S'_M(t, \theta) = \cos\left(100\pi t + \frac{\pi}{10}\right) \tag{7.10}$$

Figure 7.10 shows $S'_M(t)$, factor γ, the inverter output voltage and its spectrum for this case. The load current for $f_{m3} = 50$ Hz with $\theta = \frac{\pi}{10}$ along with its spectrum are shown in Figure 7.11.

The simulation result shows a decrease in the magnitude of the fundamental

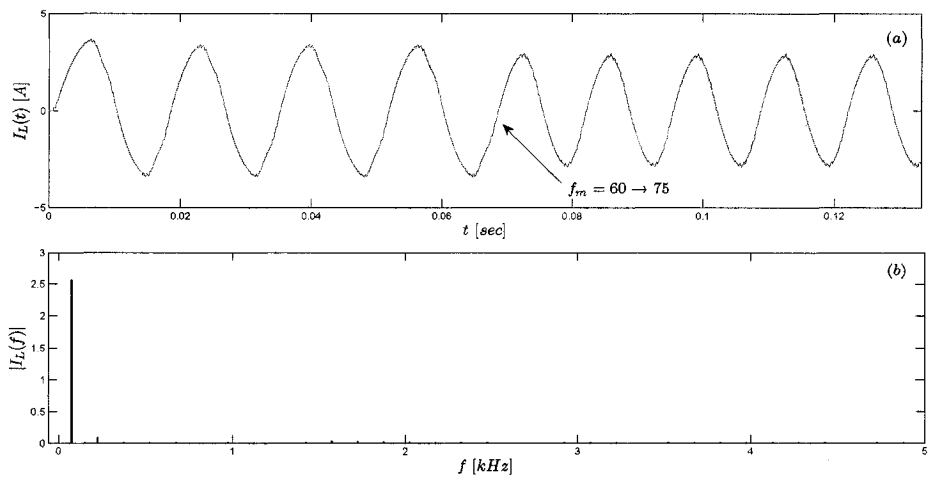

Figure 7.9: The load current $I_L(t)$ and its spectrum: (a) the load current $I_L(t)$ and (b) its magnitude spectrum $|I_L(f)|$. $|I_1| = 2.56\ A$ THD_I = 2.93%.

frequency component of the inverter output voltage ($|V_1| = 49.27\ V \longrightarrow 43.17\ V$) with a small change in the THD_V factor ($\text{THD}_V = 17.64\% \longrightarrow 19.22\%$). Also, the fundamental frequency component of the load current has increased ($|I_1| = 3.08\ A \longrightarrow 3.19\ A$) with a small change in the THD_I factor ($\text{THD}_I = 2.15\% \longrightarrow 3.76\%$). It is to be noted that the increase in the current is due to the decrease in the load impedance when f_m is decreased to 50 Hz.

Simulation test results of the 1ϕ resolution-level controlled WM inverter has shown stable and fast responses for increasing and decreasing the magnitude of the output voltage. Moreover, the same features have been observed for the controlled WM inverter when the output frequency is changed. The stable and fast responses for changing the magnitudes and frequencies have negligible effects on the harmonic contents of the inverter outputs. The simulation results have demonstrated encouraging performances of the 1ϕ resolution-level controlled WM inverter for responding to different adjustments on the WM inverter output. The next section

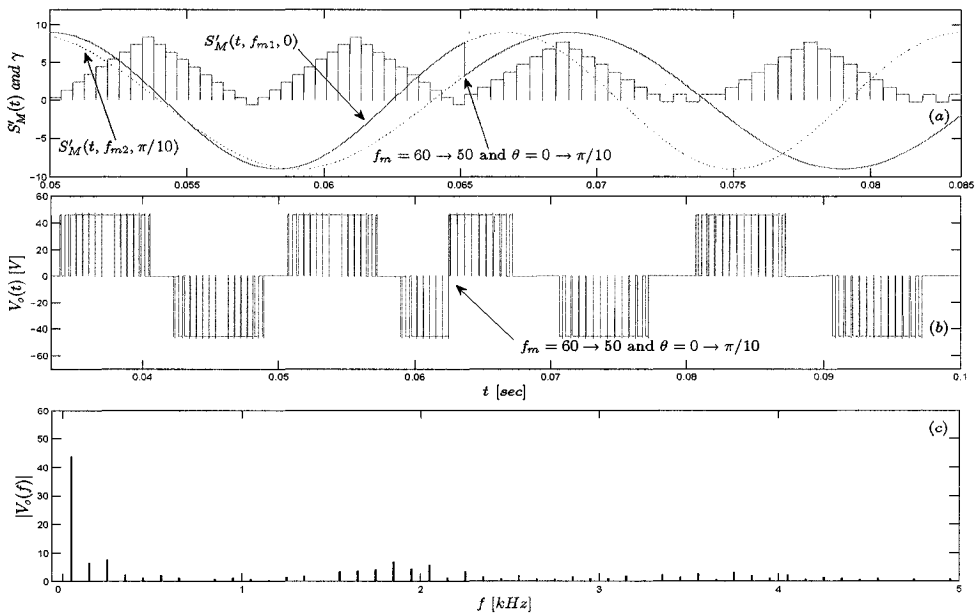

Figure 7.10: Changing the frequency of $S_M(t)$ $f_m = 60 \rightarrow 50$ Hz with $\theta = \frac{\pi}{10}$: (a) the derivative $S'_M(t)$ and the factor γ, (b) the inverter output voltage and (c) the spectrum of the inverter output voltage. $|V_1| = 43.17$ V and $\text{THD}_V = 19.22\%$.

provides experimental test results for a 1ϕ VS four-pulse resolution-level controlled WM inverter for supplying a single-phase capacitor-run induction motor.

7.4 Experimental Testing of a Resolution-level Controlled WM Inverter

The previous section has presented simulation results for 1ϕ resolution-level controlled WM inverter when supplying a $R - L$ load. The presented simulation results have clearly shown that changing the magnitude and/or the frequency of the controlled WM inverter has little effects on the quality of its outputs. This section presents experimental tests of a 1ϕ VS four-pulse IGBT resolution-level con-

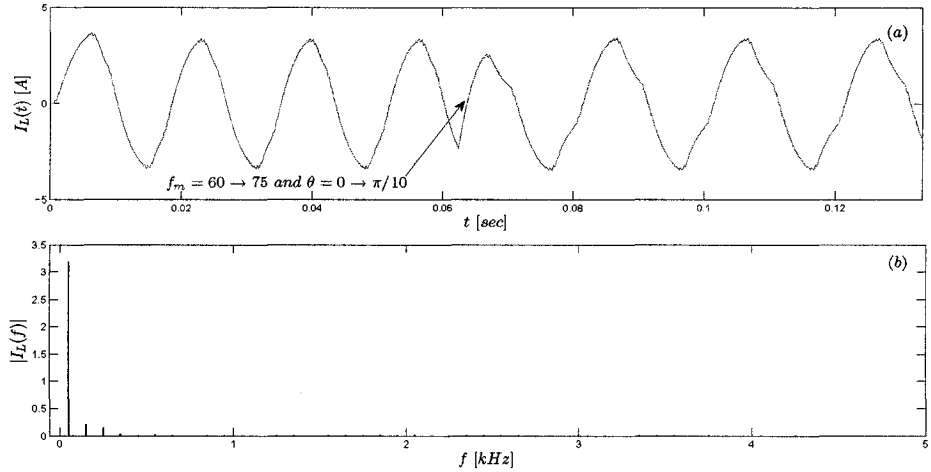

Figure 7.11: The load current $I_L(t)$ and its spectrum: (a) the load current $I_L(t)$ and (b) its magnitude spectrum $|I_L(f)|$. $|I_1| = 3.19\ A$ THD_I = 3.76%.

trolled WM inverter when supplying a 1ϕ capacitor-run induction motor. It is to be noted that the speed response of the tested 1ϕ capacitor-run induction motor are presented in Appendix B.

An experimental setup identical to the one used in chapter 6 (Figure 6.1), is used to test the 1ϕ resolution-level controlled WM inverter when supplying the 1ϕ capacitor-run induction motor. Also, the voltage and current waveforms are collected using the same procedure reported in chapter 6. The resolution-level control strategy is realized as a part of the developed $Turbo - C$ code for implementing the wavelet modulation technique by adding f_m and θ as variables to be updated while generating the switching pulses. Experimental tests include:

1. Introducing a phase-shift in $S'_M(t)$ of $\theta = -\frac{\pi}{12}$.

2. Changing the output frequency f_m from 60 Hz to 75 Hz

3. Changing the output frequency f_m from 60 Hz to 50 Hz with a phase-shift $\theta = \frac{\pi}{10}$.

Figure 7.12 shows the factor γ, the motor current and the inverter output voltage for the normal operation ($f_m = 60\ Hz$ and $\theta = 0$) with an input dc voltage of 110 V. For normal operation, $|V_1| = 108.26\ V$ and $\text{THD}_V = 17.40\%$ and $|I_1| = 1.02\ A$ and $\text{THD}_I = 2.72\%$ (see Table 6.1).

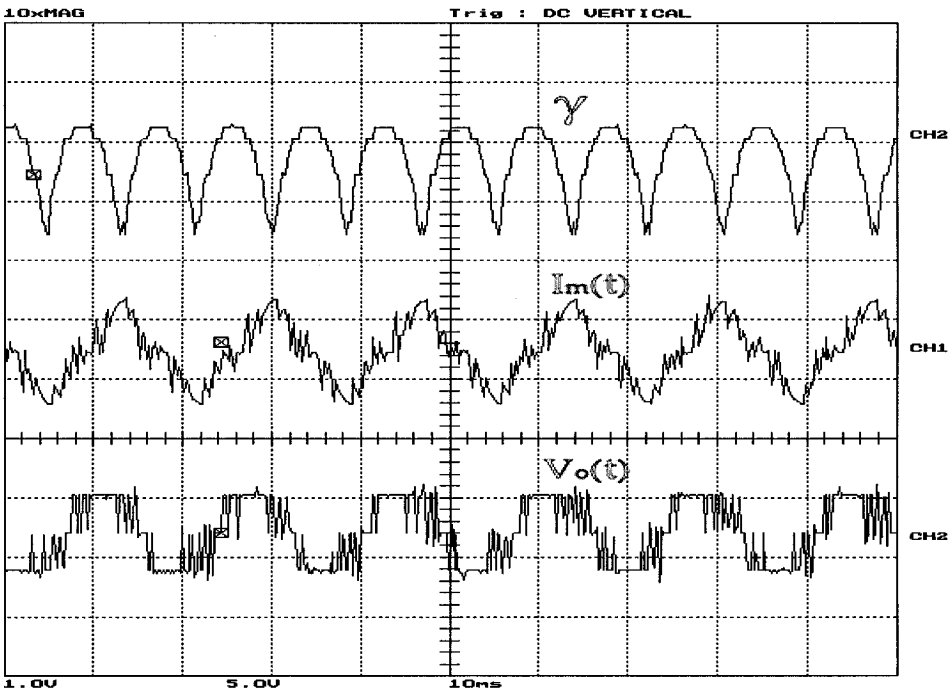

Figure 7.12: The experimental inverter normal operation for $f_m = 60\ Hz$ and $\theta = 0$: the factor γ, the motor current and the inverter output voltage. The voltage scale is 150 V/Div. and current scale is 2 A/Div.

Experimental Test Results for $\theta = -\frac{\pi}{12}$

This test aims to increase fundamental component of the inverter output voltage. As indicated by the simulation results, the negative phase shift θ in $S'_M(t)$ changes the durations as well as the locations of synthesis scaling functions that results in increasing the magnitude of the output fundamental frequency component. It is

to be noted that the phase shift θ is changed while the inverter is supplying the motor such that $\theta = 0 \rightarrow \frac{-\pi}{12}$. Figure 7.13 shows the factor γ, the motor current and the inverter output voltage for this case. Figure 7.14 shows spectra of the motor

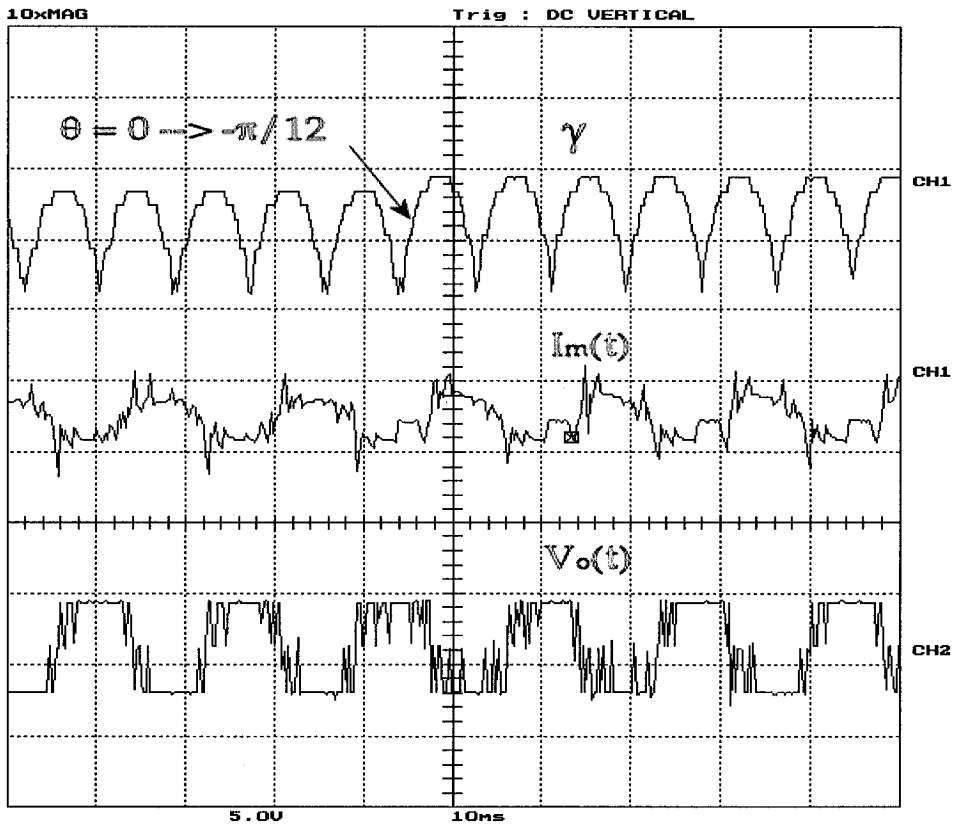

Figure 7.13: Test results for shifting $S'_M(t)$ by $\theta = -\frac{\pi}{12}$: the scale-time interval factor γ, the motor current and the inverter output voltage. The voltage scale is 80 V/Div. and current scale is 1 A/Div.

current and the inverter output voltage for $\theta = -\frac{\pi}{12}$ obtained using the $FLUKE\ 41$ harmonic analyzer. It is to be noted that the spectra in Figure 7.11 are determined after changing θ to $\frac{-\pi}{12}$.

Experimental test results show an increase in the magnitude of the fundamental frequency component of the inverter output voltage ($|V_1| = 108.26\,V \longrightarrow 117.34\,V$)

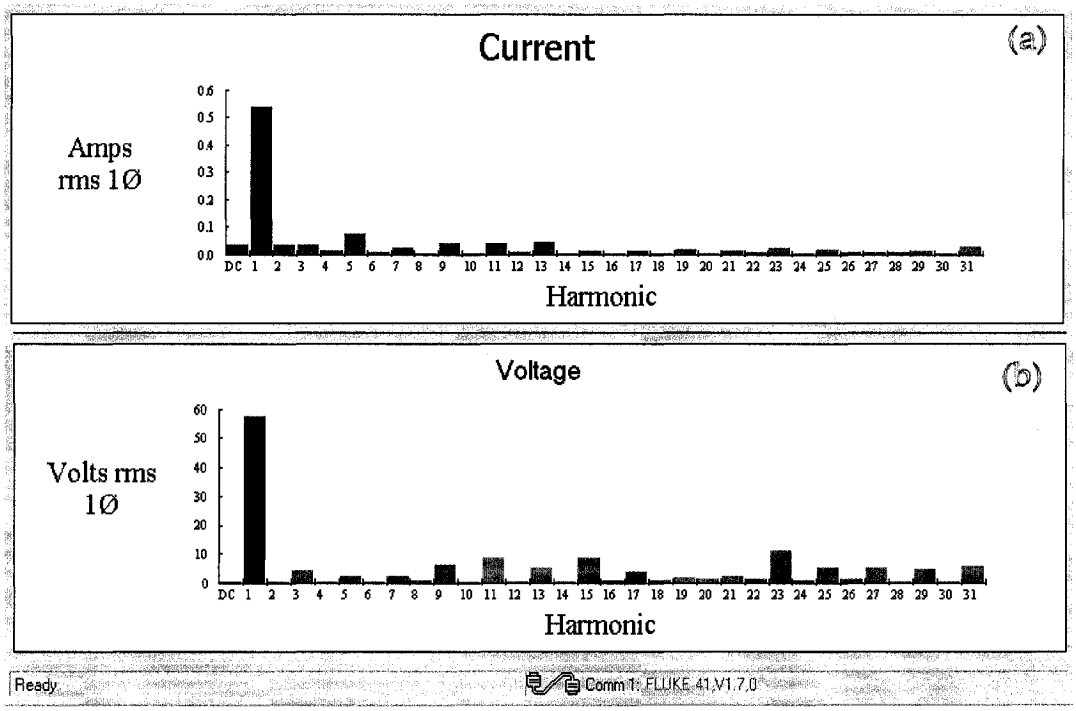

Figure 7.14: Experimental test results for shifting $S'_M(t)$ by $\theta = -\frac{\pi}{12}$: (a) the spectrum of the motor current and (b) the spectrum of the inverter output voltage. $|I_1| = 1.32\ A$ and $\text{THD}_I = 3.62\%$ $|V_1| = 117.34\ V$ and $\text{THD}_V = 19.46\%$. Scale 1:2.

with a small change in the THD_V factor ($\text{THD}_V = 17.40\% \longrightarrow 19.46\%$). Also, the fundamental frequency component of the load current has increased ($|I_1| = 1.02\ A \longrightarrow 1.32\ A$) with a small change in the THD_I factor ($\text{THD}_I = 2.72\% \longrightarrow 3.62\%$).

Experimental Test Results for Changing f_m

This test aims to investigate the performance of the WM inverter when the output frequency is changed. This test is conducted by changing the frequency of the reference-modulating signal $S_M(t)$ from 60 to 75 Hz while the inverter is supplying the motor. Figure 7.15 shows the factor γ, the motor current and the inverter

output voltage for this case. Figure 7.16 shows spectra of the motor current and the

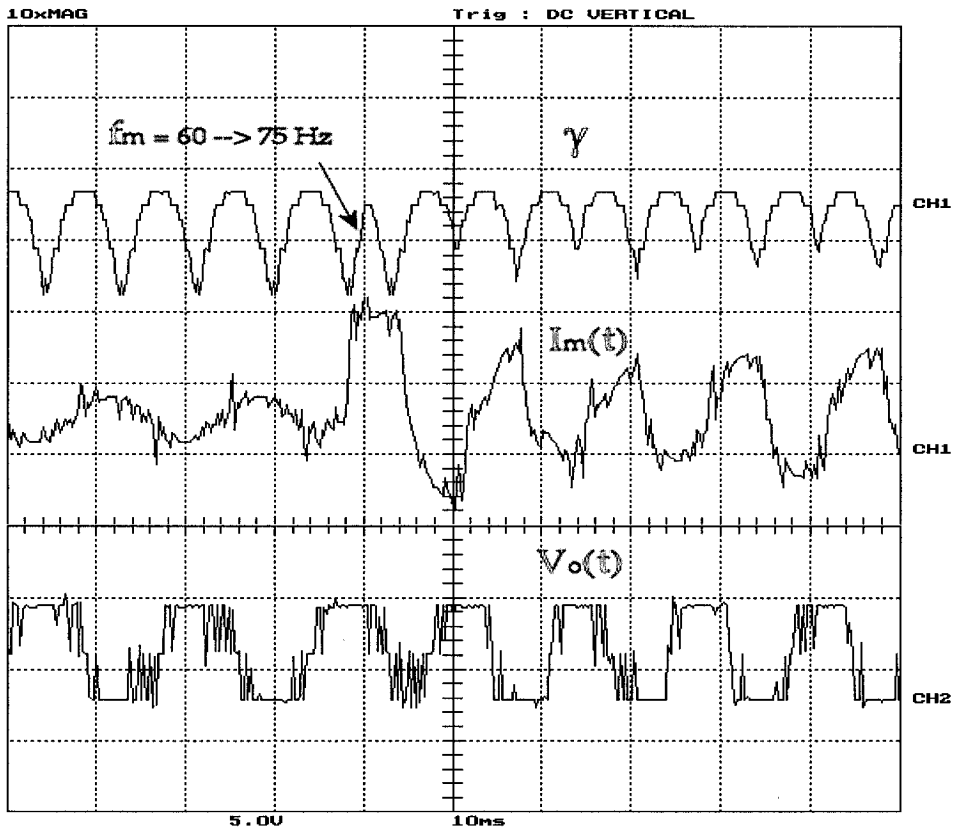

Figure 7.15: Experimental test results for changing the output frequency f_m from 60 to 75 Hz: the scale-time interval factor γ, the motor current and the inverter output voltage. The voltage scale is 80 V/Div. and current scale is 0.5 A/Div.

inverter output voltage for $f_m = 75\ Hz$ obtained by using the $FLUKE$ 41 harmonic analyzer.

Experimental test results show a decrease in the magnitude of the fundamental frequency component of the inverter output voltage ($|V_1| = 108.26\ V \longrightarrow 98.56\ V$) with a small change in the THD_V factor ($\text{THD}_V = 17.40\% \longrightarrow 20.26\%$). Also, the fundamental frequency component of the load current has decreased ($|I_1| = 1.02\ A \longrightarrow 0.78\ A$) with a small change in the THD_I factor ($\text{THD}_I = 2.72\% \longrightarrow$

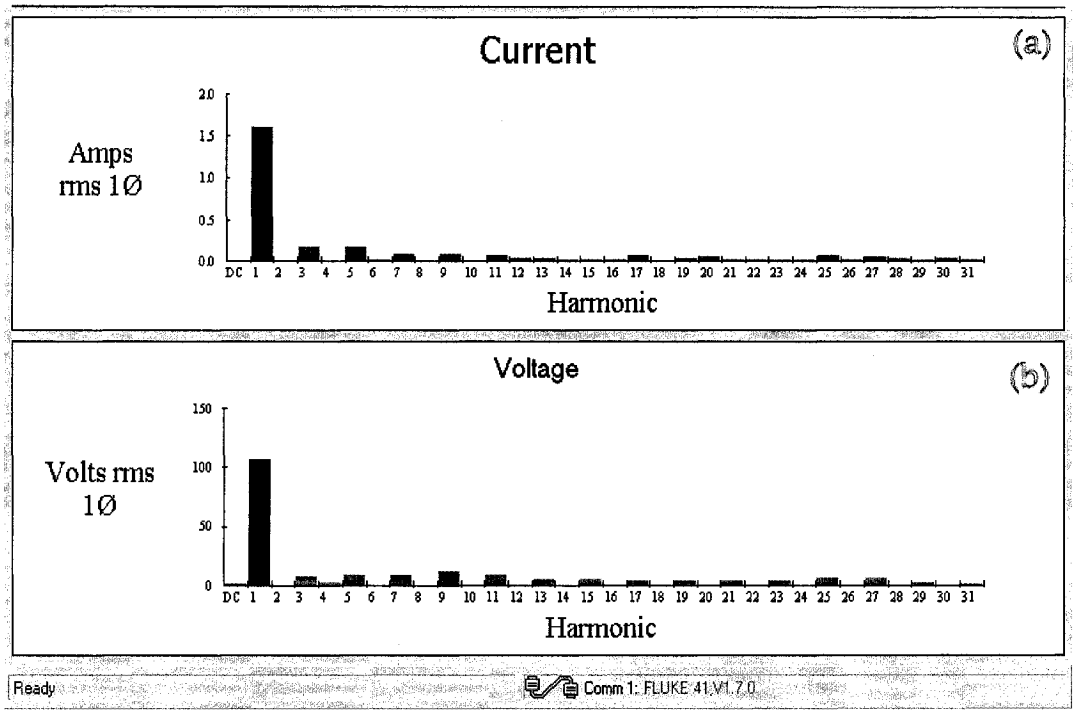

Figure 7.16: Experimental test results for changing the output frequency f_m from 60 to 75 Hz: (a) the spectrum of the motor current and (b) the spectrum of the inverter output voltage. $|I_1| = 0.78\ A$ and $\text{THD}_I = 1.87\%$ $|V_1| = 107.68\ V$ and $\text{THD}_V = 20.26\%$. Scale 1:1.

1.87%). It is to be noted that the motor current has decreased due to the increase in the speed for the same motor output mechanical power.

Experimental Test Results for Changing f_m with a Phase-shift θ

This test aims to examine the performance of the WM inverter when the output frequency is changed with the introduction of a phase-shift θ in $S'_M(t)$. This test is conducted by changing the frequency of the reference-modulating signal $S_M(t)$ from 60 to 50 Hz and setting $\theta = \frac{\pi}{10}$ while the inverter is supplying the motor. The frequency change and the introduction of a phase shift cause durations of switching pulses to narrow, which shifts the spectral location of the fundamental frequency

component. Figure 7.17 shows the factor γ and the inverter output voltage for this case. Figure 7.18 shows spectra of the motor current and the inverter output

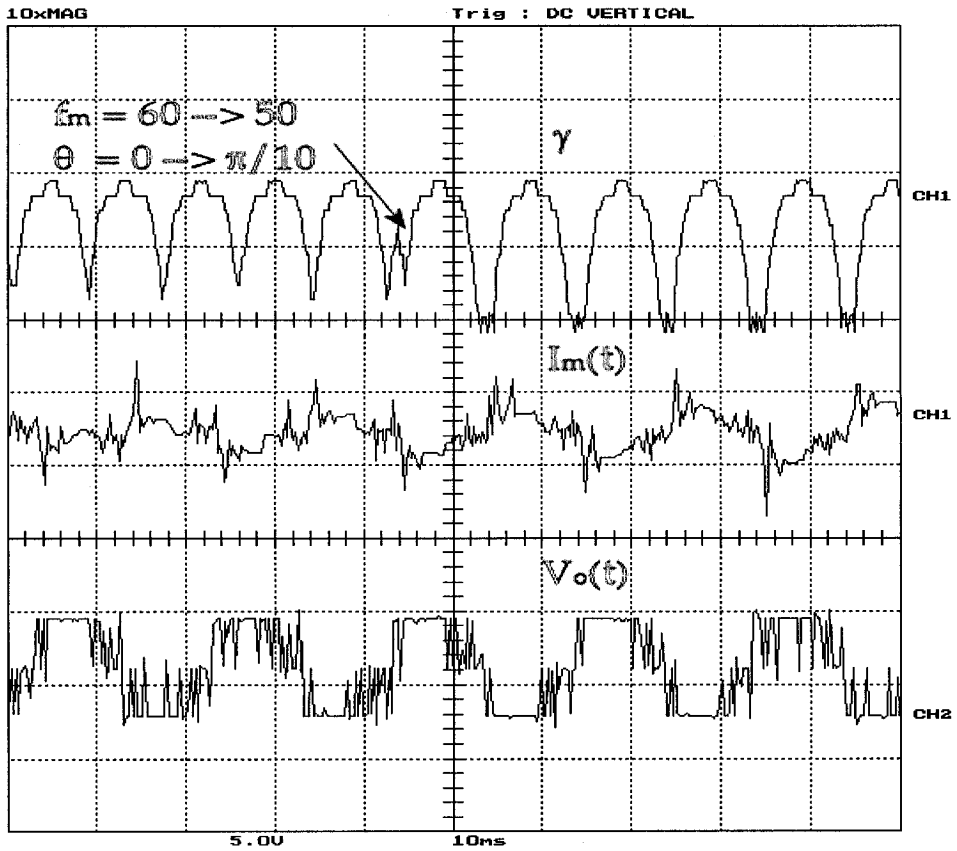

Figure 7.17: Experimental test results for changing the output frequency f_m from 60 to 50 Hz with a phase-shift $\theta = \frac{\pi}{10}$: the scale-time interval factor γ, the motor current and the inverter output voltage. The voltage scale is 80 V/Div. and current scale is 0.5 A/Div.

voltage for $f_m = 50\ Hz$ with $\theta = \frac{\pi}{10}$ obtained by using the $FLUKE\ 41$ harmonic analyzer.

Experimental test results show a decrease in the magnitude of the fundamental frequency component of the inverter output voltage ($|V_1| = 108.26\ V \longrightarrow 96.12\ V$) with a small change in the THD_V factor ($\text{THD}_V = 17.40\% \longrightarrow 18.74\%$). Also, the fundamental frequency component of the load current has increased ($|I_1| =$

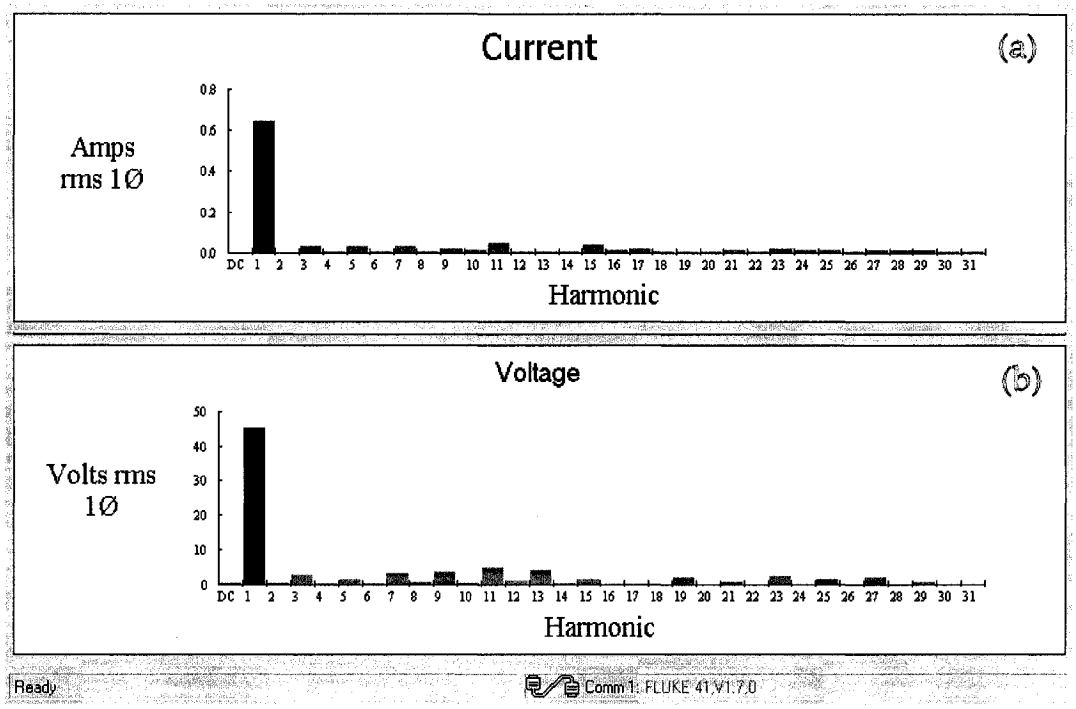

Figure 7.18: The test results for changing the output frequency f_m from 60 to 50 Hz with $\theta = \frac{\pi}{10}$: (a) the spectrum of the motor current and (b) the spectrum of the inverter output voltage. $|I_1| = 1.28\ A$ and $\text{THD}_I = 3.44\%$ $|V_1| = 96.12\ V$ and $\text{THD}_V = 18.74\%$. Scale 1:2.

$1.02\ A \longrightarrow 1.28\ A$) with a small change in the THD_I factor ($\text{THD}_I = 2.72\% \longrightarrow 3.44\%$). It is to be noted that the decrease in the motor speed ($f_m = 60 \rightarrow 50\ Hz$) causes an increase in the motor current for the same motor output mechanical power.

This chapter has presented a new control strategy that aims to a adjust magnitudes and frequencies of the 1ϕ WM inverter outputs. This strategy is called the resolution-level control that is based on changing the scale j of the successive dilated and shifted versions of the synthesis scaling functions. This change in the scale j has varied the durations and locations of $\tilde{\varphi}_j(t)$ by introducing a phase-shift (θ) in the derivative $S'_M(t)$. Furthermore, the phase shift θ has been able to allow the

scale j to exceed the value of J (for $\theta < 0$) and begin decreasing before reaching the value of J (for $\theta > 0$). Simulation and experimental test results of a 1ϕ resolution-level controlled WM inverter have demonstrated stable and fast responses to meet any change in the inverter output. Moreover, the quality of the inverter outputs has been maintained high in all the tested cases. Table 7.1 summarizes all the results obtained from testing the 1ϕ resolution-level controlled WM inverter. The

Table 7.1: Performance test results of the 1ϕ resolution-level controlled WM inverter for different load types.

Load	θ	f_m	$\lvert V_1 \rvert$	$\lvert I_1 \rvert$	THD_V	THD_I
$R-L$	$\theta = 0$	$f_m = 60\ Hz$	49.27 V	3.66 A	17.64%	2.15%
	$\theta = \frac{-\pi}{12}$	$f_m = 60\ Hz$	54.12 V	3.48 A	18.97%	2.77%
	$\theta = 0$	$f_m = 75\ Hz$	48.46 V	2.56 A	16.94%	2.93%
	$\theta = \frac{\pi}{10}$	$f_m = 50\ Hz$	43.17 V	3.19 A	19.22%	3.76%
Motor	$\theta = 0$	$f_m = 60\ Hz$	108.26 V	1.02 A	17.40%	2.72%
	$\theta = \frac{-\pi}{12}$	$f_m = 60\ Hz$	117.34 V	1.32 A	19.46%	3.62%
	$\theta = 0$	$f_m = 75\ Hz$	107.68 V	0.78 A	20.26%	1.87%
	$\theta = \frac{\pi}{10}$	$f_m = 50\ Hz$	96.12 V	1.28 A	18.74%	3.44%

presented performance test results prove the functionality and the validity of the proposed 1ϕ VS resolution-level controlled WM inverters for supplying different load types under different operating conditions.

All the developments and performance tests have been focused on 1ϕ VS four-pulse inverters. The next chapter extends the development and the tests of the proposed wavelet modulation technique to operate three-phase (3ϕ) VS six-pulse inverters.

Chapter 8

Developing and Testing the Three-phase Wavelet Modulation Technique

8.1 General

The last three chapters of this work have presented different test results of single-phase (1ϕ) WM inverters for supplying different types of loads under different operating conditions. These test results have demonstrated significant capabilities to produce high quality outputs and transfer high power to the load side. Also, test comparisons have shown that the proposed wavelet modulate inverters can outperform the conventional SPWM inverters under the same loading conditions. In general, dc-ac inverters can be designed as single-phase (1ϕ) or three-phase (3ϕ) configurations. 3ϕ inverters are very popular in a wide range of industrial applications such as power systems, ac motor drives, renewable energy utilization, power

supplies, etc. [80–83].

This chapter presents the development of extended non-dyadic type multiresolution analyses (MRAs) that can be employed to generate switching pulses for operating a 3ϕ six-pulse inverter. The basis for the desired MRAs will depend on the non-uniform recurrent sampling model of 3ϕ inverters developed in chapter 3, in particular, sampling shifted continuous-time (CT) signals.

8.2 Scale-based Linearly-Combined Scaling Functions for Three-Phase Inverters

In chapter 3, the non-uniform recurrent sampling-based model of a single-phase inverter was extended to develop a model for a three-phase inverter. Such an extension was based on considering a 3ϕ inverter as three independent 1ϕ inverters. This consideration was justified by the principle of operating 3ϕ inverters, where the switching pulses are generated using reference-modulating signals representing 3ϕ line quantities. The developed 3ϕ inverter sampling-based model was composed of three shifted single-phase ones. This extension of the non-uniform recurrent sampling-based model can be employed for developing non-dyadic-type MRAs to generate switching pulses for operating a 3ϕ inverter.

The basis of the wavelet modulation technique lies in the definition of the scale-based linearly-combined scaling function $\varphi_1(t)$, which is used to sample the reference-modulating signal in a non-uniform recurrent manner. In a 3ϕ six-pulse inverter, three reference-modulating signals are used to generate the required switching pulses. As a consequence, three scaling functions are needed to sample these three signals. It is to be noted that these three reference-modulating signals

have the same frequency and magnitude with a phase shift of $\frac{2\pi}{3}$ from each other. The three reference-modulating signals, each one of them is related to one phase of the desired 3ϕ output, can be defined as [1, 29, 80–83]:

$$S_{Ma}(t) = \sin(\omega_m t) \tag{8.1}$$

$$S_{Mb}(t) = \sin\left(\omega_m t - \frac{2\pi}{3}\right) \tag{8.2}$$

$$S_{Mc}(t) = \sin\left(\omega_m t + \frac{2\pi}{3}\right) \tag{8.3}$$

The non-uniform recurrent sampling of these three CT reference-modulating signals can be achieved using one sampling function for each CT signal. As a consequence, three scaling functions with a phase shift of $\frac{2\pi}{3}$ from each other are required to sample the three reference-modulating signals in a non-uniform recurrent manner. These three scale-based linearly-combined scaling functions can be defined as:

$$(\varphi_a(t))_j = \phi_H\left(2^{j+1}t\right) + \phi_H\left(2^{j+1}(t-u)\right) \tag{8.4}$$

$$(\varphi_b(t))_j = \phi_H\left(2^{j+1}t - z_b\right) + \phi_H\left(2^{j+1}(t-u) - z_b\right) \tag{8.5}$$

$$(\varphi_c(t))_j = \phi_H\left(2^{j+1}t - z_c\right) + \phi_H\left(2^{j+1}(t-u) - z_c\right) \tag{8.6}$$

where $u = 1 - 2^{-(j+1)}$, $j = 1, 2, ...$ and the shifts z_b and z_c are given by:

$$z_b = \frac{2^{2-j}}{3} \tag{8.7}$$

$$z_c = \frac{2^{3-j}}{3} \tag{8.8}$$

Figure 8.1 shows the three scaling functions $(\varphi_a(t))_1$, $(\varphi_b(t))_1$ and $(\varphi_c(t))_1$

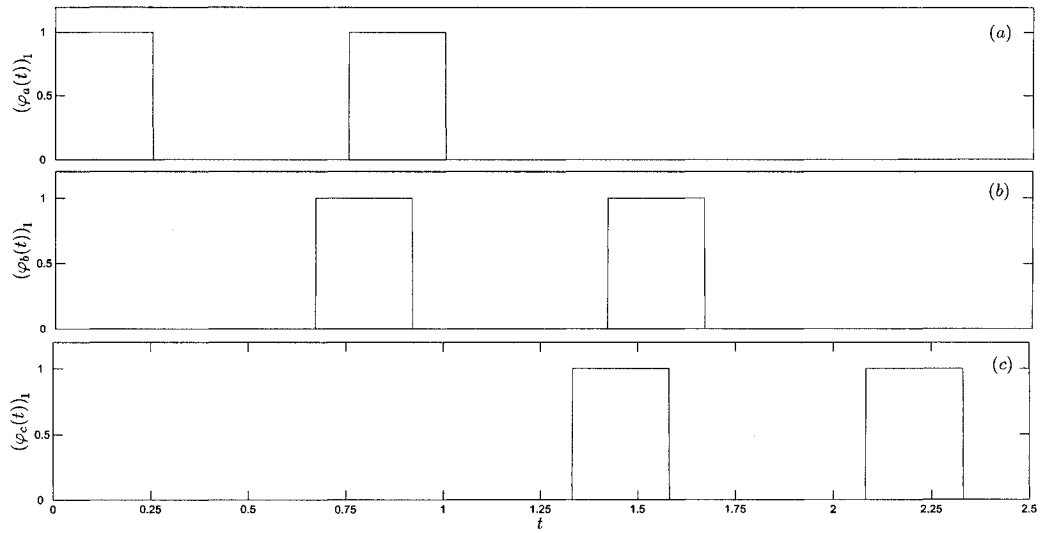

Figure 8.1: The three scale-based linearly-combined scaling functions: (a) $(\varphi_a(t))_1$, (b) $(\varphi_b(t))_1$ and (c) $(\varphi_c(t))_1$.

The three scale-based linearly-combined scaling functions $(\varphi_a(t))$, $(\varphi_b(t))$ and $(\varphi_c(t))$ are capable of creating sets of non-uniform recurrent sample groups for the three reference-modulation signals $S_{Ma}(t)$, $S_{Mb}(t)$ and $S_{Mc}(t)$. It is to be noted that the three scale-based linearly-combined scaling functions are required to meet the conditions for constructing a MRA using dilated and translated versions of each scaling functions. This condition is necessary to ensure the reconstruction of the CT signals using dilated and translated versions of the dual synthesis scaling functions [47–53].

Reconstructing the three CT reference-modulation signals $S_{Ma}(t)$, $S_{Mb}(t)$ and $S_{Mc}(t)$ is carried out by the synthesis scaling functions, where each one of them is the dual of one scale-based linearly-combined scaling function. These scale-based

linearly-combined synthesis scaling functions can be defined as:

$$(\tilde{\varphi}_a(t))_j = (\phi_H)_j(t) - (\varphi_a(t))_j \tag{8.9}$$

$$(\tilde{\varphi}_b(t))_j = (\phi_H)_j(t - z_b) - (\varphi_b(t))_j \tag{8.10}$$

$$(\tilde{\varphi}_c(t))_j = (\phi_H)_j(t - z_c) - (\varphi_c(t))_j \tag{8.11}$$

where $j = 1, 2, \ldots$. Figure 8.2 shows the three synthesis scaling functions $(\tilde{\varphi}_a(t))_1$, $(\tilde{\varphi}_b(t))_1$ and $(\tilde{\varphi}_c(t))_1$. These synthesis scaling functions are used to ac-

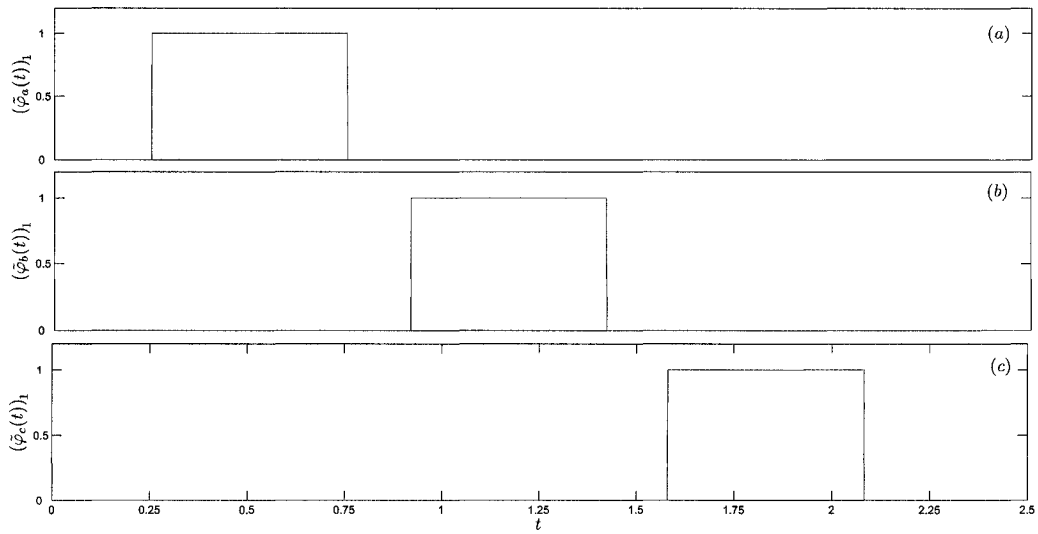

Figure 8.2: The three scale-based linearly-combined synthesis scaling functions: (a) $(\tilde{\varphi}_a(t))_1$, (b) $(\tilde{\varphi}_b(t))_1$ and (c) $(\tilde{\varphi}_c(t))_1$.

tivate the switching elements of the 3ϕ inverter. Each of the three scaling functions $(\varphi_a(t))_j$, $(\varphi_b(t))_j$ and $(\varphi_c(t))_j$ is composed of two Haar scaling functions. This feature indicates that each scaling function creates two samples at each dilation j and translation k. On the other hand, changing in the scale j will cause both dilations and translations of each scaling function. Further, each translation is dependent on

both the translation integer k and the scale-dependent quantity $(1-2^{-(j+1)})$. These translations cause the spacings between samples to be non-uniform. This feature guarantees that synthesis scaling functions will have different locations with different intervals of support [67].

Using the three developed scale-based linearly-combined scaling functions $(\varphi_a(t))_j$, $(\varphi_b(t))_j$ and $(\varphi_c(t))_j$ and their dual synthesis ones $(\tilde{\varphi}_a(t))_j$, $(\tilde{\varphi}_b(t))_j$ and $(\tilde{\varphi}_c(t))_j$, the three CT reference-modulating signals $S_{Ma}(t)$, $S_{Mb}(t)$ and $S_{Mc}(t)$ can be expanded as [67]:

$$S_{Ma}(t) = \sum_j \sum_{k\in\mathbb{Z}} \left\langle S_{Ma}(t), (\varphi_a(t-k))_j \right\rangle (\tilde{\varphi}_a(t-k))_j \tag{8.12}$$

$$S_{Mb}(t) = \sum_j \sum_{k\in\mathbb{Z}} \left\langle S_{Mb}(t), (\varphi_b(t-k))_j \right\rangle (\tilde{\varphi}_b(t-k))_j \tag{8.13}$$

$$S_{Mc}(t) = \sum_j \sum_{k\in\mathbb{Z}} \left\langle S_{Mc}(t), (\varphi_c(t-k))_j \right\rangle (\tilde{\varphi}_c(t-k))_j \tag{8.14}$$

The inner products in the above equations can be written as:

$$\left\langle S_{Ma}(t), (\varphi_a(t))_j \right\rangle = \int_0^{t_{ad1}} S_{Ma}(t)\,(\phi_H)_{j+1}(t)dt + \int_{t_{ad2}}^{1} S_{Ma}(t)\phi_H(l)dt \tag{8.15}$$

$$\left\langle S_{Mb}(t), (\varphi_b(t))_j \right\rangle = \int_0^{t_{bd1}} S_{Mb}(t)\,(\phi_H)_{j+1}(t-z_b)\,dt + \int_{t_{bd2}}^{1} S_{Mb}(t)\phi_H(l-z_b)\,dt \tag{8.16}$$

$$\left\langle S_{Mc}(t), (\varphi_c(t))_j \right\rangle = \int_0^{t_{cd1}} S_{Mc}(t)\,(\phi_H)_{j+1}(t-z_c)\,dt + \int_{t_{cd2}}^{1} S_{Mc}(t)\phi_H(l-z_c)\,dt \tag{8.17}$$

where $\phi_H(l) = \phi_H\left(2^{j+1}\left(t-1+2^{-(j+1)}\right)\right)$. The aforementioned inner products ensure the creation of two samples over the interval of support of each scaling function at each scale j and translation k. It should be noted that the scale j has to

start from $j_0 = 1$ in order to avoid uniform sampling that takes place for $j = 0$ [45–47, 67].

8.3 Implementing the Wavelet Modulation Technique for a Three-Phase Inverter

The structure of the scale-based linearly-combined scaling functions and their dual synthesis scaling functions indicates the creation of three non-dyadic type MRAs. Each one of these MRAs is associated with one reference-modulating signal. These MRAs are realized through sampling the reference-modulating signals in a non-uniform recurrent manner, then reconstructing them through switching actions. The implementation of the wavelet modulation technique for a 3ϕ six-pulse inverter can be divided into 2 parts as [67]:

- Implementing a non-uniform recurrent sampling with period $T_m = 1/f_m$, where f_m is the frequency of reference-modulating signals $S_{Ma}(t)$, $S_{Mb}(t)$ and $S_{Mc}(t)$. The required sampling times are determined by dilated and translated versions of the three scale-based linearly-combined scaling functions $(\varphi_a(t))_1$, $(\varphi_b(t))_1$ and $(\varphi_c(t))_1$.

- Generating switching pulses using the three developed synthesis scale-based linearly-combined scaling functions $(\tilde{\varphi}_a(t))_1$, $(\tilde{\varphi}_b(t))_1$ and $(\tilde{\varphi}_c(t))_1$.

The resulting samples (for the three reference-modulating signals) are arranged in groups, where each group of each reference-modulating signal contains two samples. Also, each group of each reference-modulating signal defines a time interval for one dilated and translated version of its associated synthesis scaling

function. It is to be noted that the time interval of each sample group of each reference-modulating signal changes due to the change of the scale j.

The developed procedure for implementing the wavelet modulation technique for operating a 1ϕ inverter can be extended for a 3ϕ six-pulse one by creating switching pulses for each leg to reconstruct one reference-modulating signal. In other words, treating each leg of the 3ϕ inverter as one non-dyadic type MRA. Figure 8.3 shows a flowchart for implementing the wavelet modulation for a 3ϕ six-pulse inverter.

The flowchart of Figure 8.3 shows a simple procedure for implementing the proposed wavelet modulation for a 3ϕ six-pulse inverter. This procedure can be realized using a MATLAB code. A SIMULINK model of a 3ϕ six-pulse inverter can be used for simulating the performance of a 3ϕ six-pulse wavelet-modulated (WM) inverter. The next section presents simulation results for a 3ϕ VS six-pulse inverter supplying an $R-L$ load.

8.4 Simulating the Performance of a 3ϕ VS Six-Pulse Wavelet-Modulated Inverter

The procedure for implementing the three-phase wavelet modulation technique developed in the previous section can be realized using a MATLAB code. This code generates the required switching pulses to activate a 3ϕ VS six-pulse inverter. A SIMULINK model is constructed for simulating the performance of the inverter when supplying a 3ϕ Y-connected $R-L$ load. Figure 8.4 shows a schematic diagram of a three-phase six-pulse inverter with the 3ϕ Y-connected $R-L$ load. Figure 8.5 shows the constructed SIMULINK model for a 3ϕ VS six-pulse IGBT inverter

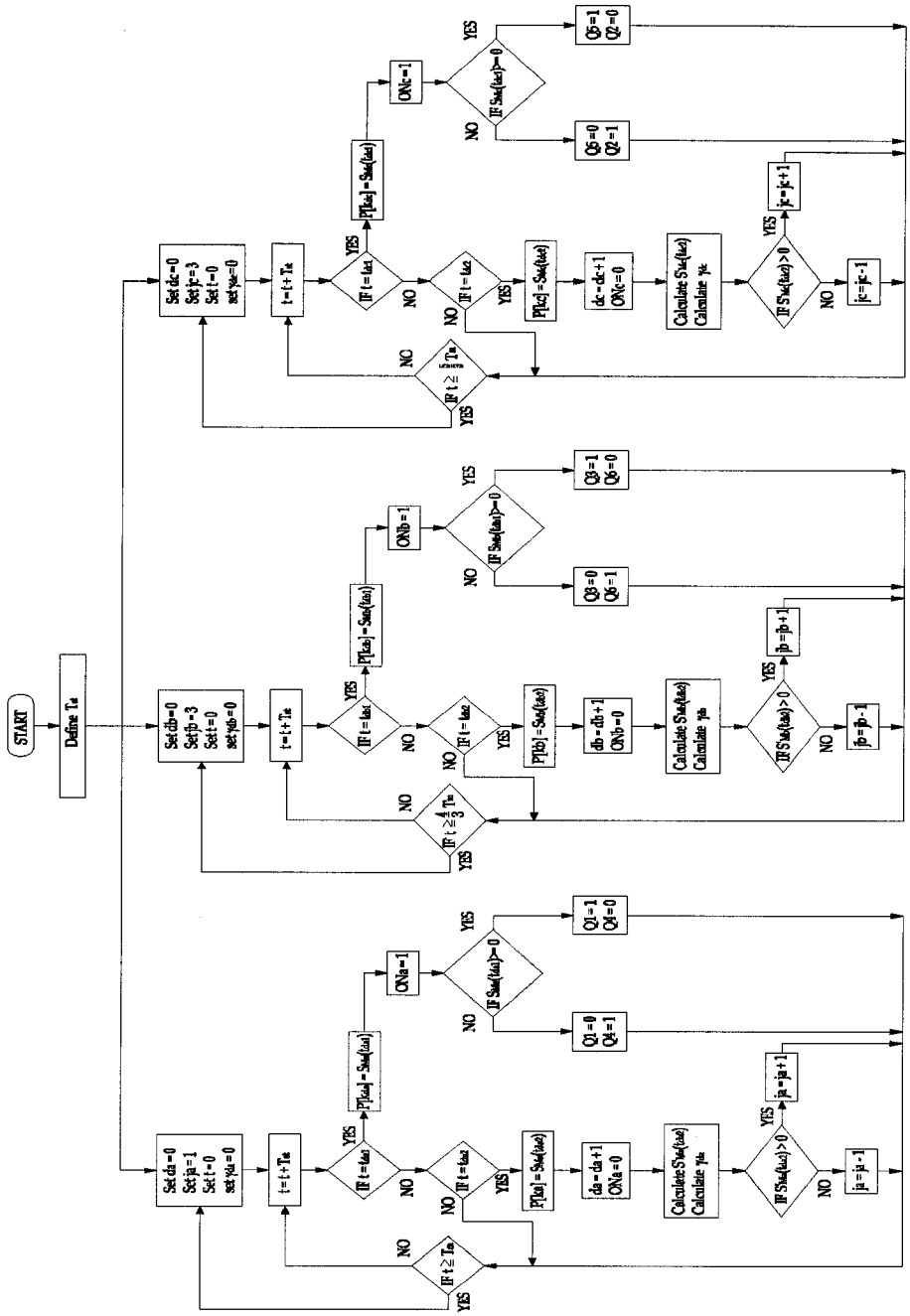

Figure 8.3: The flowchart for an algorithm to implement the 3ϕ WM that generates switching pulses for a 3ϕ six-pulse inverter.

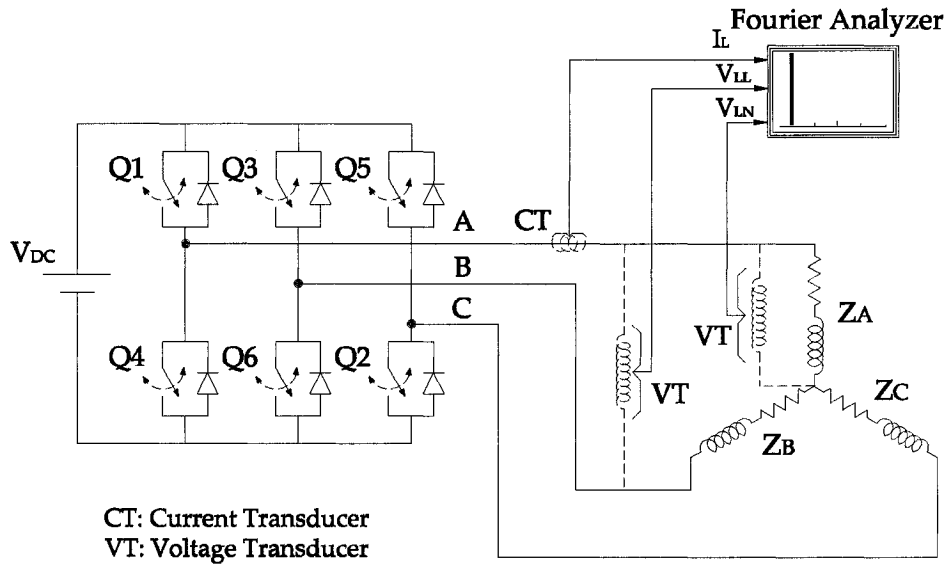

Figure 8.4: The schematic diagram of a 3ϕ six-pulse voltage source inverter supplying a 3ϕ Y-connected $R-L$ load.

with the 3ϕ Y-connected $R-L$ load.

The three-phase wavelet modulation technique code generates switching pulses for the three legs of the 3ϕ VS six-pulse inverter. Figure 8.6 shows the switching pulses generated by the developed MATLAB code.

The quality of inverter output voltage and load current are usually expressed in terms of the total harmonic distortion factor (THD) that has been defined in section 5.4.1. The constructed SIMULINK model is composed of a six-pulse IGBT inverter with a dc voltage supply of 50 V. This model supplies a 3ϕ Y-connected $R-L$ load of $Z_L = 10 + j3.77\ \Omega/phase$. Figure 8.7 shows the 3ϕ line-to-line inverter output voltages. Figure 8.8 shows the 3ϕ line-to-neutral inverter output voltages.

Line-to-line as well as line-to-neutral inverter output voltages are analyzed us-

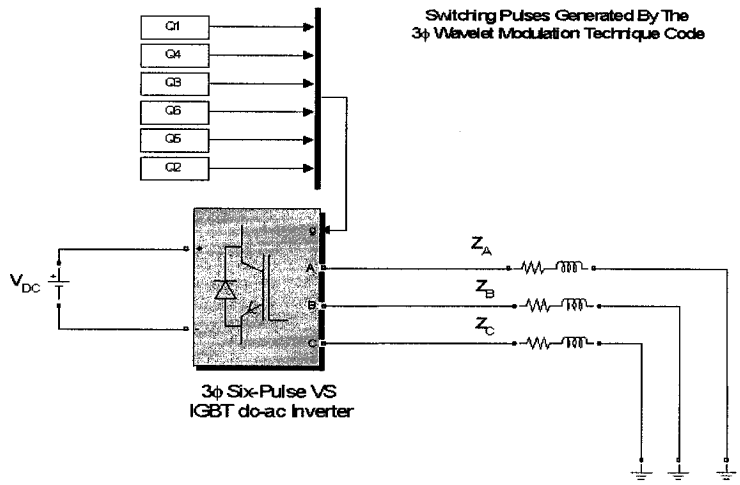

Figure 8.5: The SIMULINK model of a 3ϕ VS six-pulse inverter with the 3ϕ Y-connected $R-L$ load to simulate the performance of the 3ϕ wavelet modulation technique.

ing Fourier analysis to obtain their harmonic spectra as well as the values of their THD factors. Figure 8.9 shows the voltages $V_{AB}(t)$ and $V_{AN}(t)$ along with their spectra. The 3ϕ Y-connected $R-L$ load draws three-phase currents that are shown in Figure 8.10. Line currents are analyzed using Fourier analysis to obtain their spectra as well as the values of their THD factors. Figure 8.11 shows phase A current along with its spectrum.

The scale-time interval factor γ defined in chapter 5 for the 1ϕ case, can be defined for the 3ϕ one. For the three phase wavelet modulation, three non-dyadic type MRAs are required to operate the 3ϕ inverter so that each MRA is responsible for operating one of the three legs of the inverter. As a consequence, three factors γ_a, γ_b and γ_c can be defined for the case of the 3ϕ WM inverter. These factors are

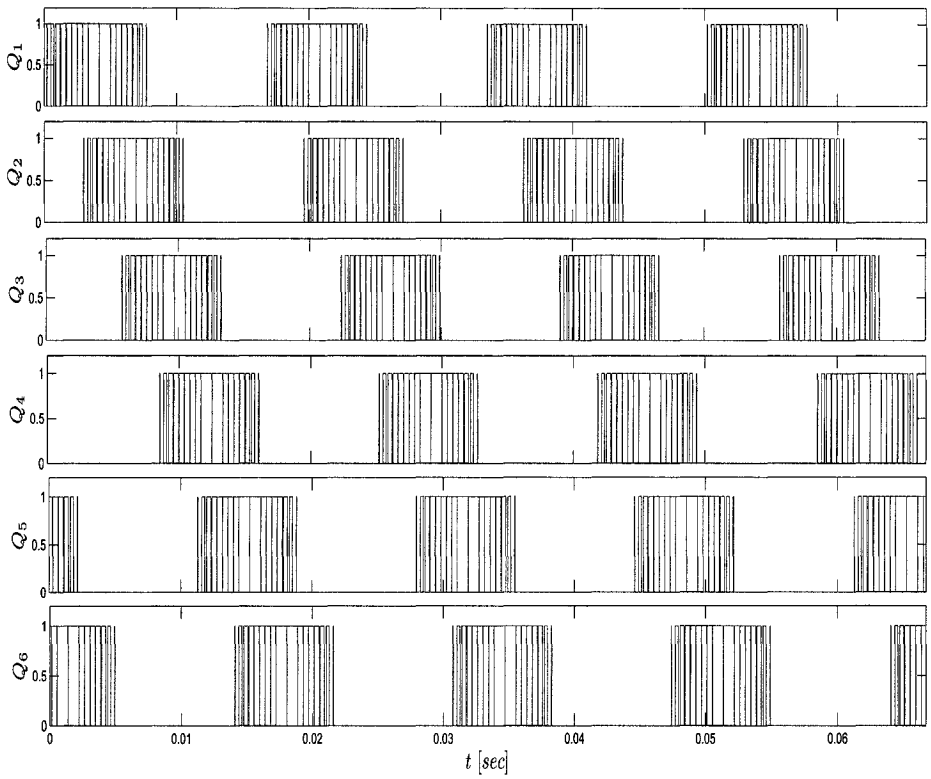

Figure 8.6: The switching pulses generated by the 3ϕ wavelet modulation technique MATLAB code for activating three legs of the 3ϕ VS six-pulse inverter.

defined as:

$$(\gamma_a)_{ad} = (\gamma_a)_{ad-1} + \frac{(S'_M(t_{ad2}))_a}{|(S'_M(t_{ad2}))_a|} \sum_{m=1}^{j} m2^m \left(t_{am2} - t_{am1}\right) \tag{8.18}$$

$$(\gamma_b)_{bd} = (\gamma_b)_{bd-1} + \frac{(S'_M(t_{bd2}))_b}{|(S'_M(t_{bd2}))_b|} \sum_{m=1}^{j} m2^m \left(t_{bm2} - t_{bm1}\right) \tag{8.19}$$

$$(\gamma_c)_{cd} = (\gamma_c)_{cd-1} + \frac{(S'_M(t_{cd2}))_c}{|(S'_M(t_{cd2}))_c|} \sum_{m=1}^{j} m2^m \left(t_{cm2} - t_{cm1}\right) \tag{8.20}$$

The scale-time interval factors γ_a, γ_b and γ_c are evaluated for the three non-dyadic MRAs. Figure 8.12 shows the factors γ_a, γ_b and γ_c for the simulated three-

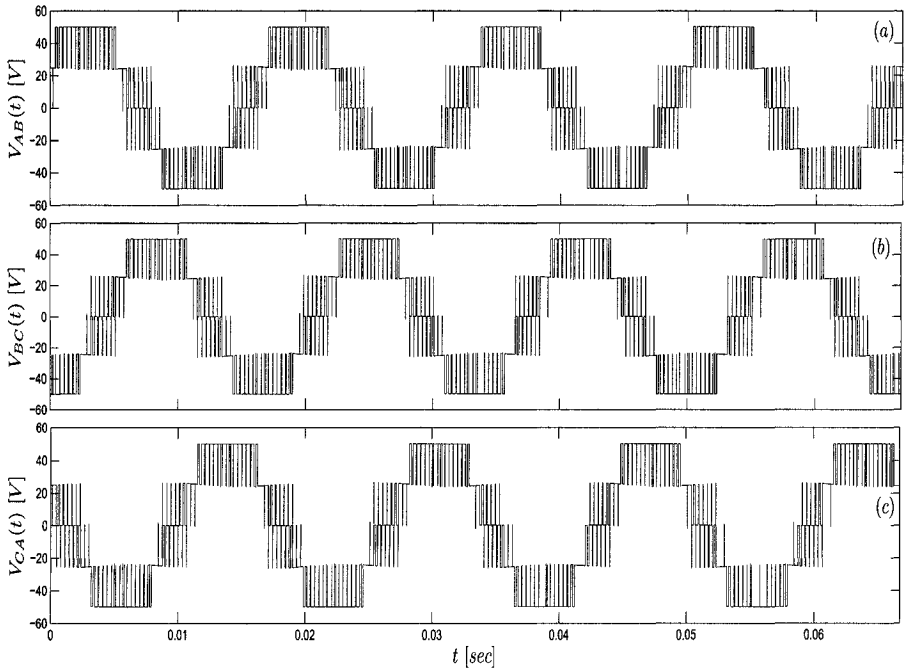

Figure 8.7: The 3ϕ six-pulse VS WM inverter line-to-line output voltages: (a) phase A-to-phase B voltage V_{AB}, (b) phase B-to-phase C voltage V_{BC} and (c) phase C-to-phase A voltage V_{CA}.

phase six-pulse WM inverter.

To further investigate the performance of the proposed 3ϕ WM inverter, the same load is supplied from the conventional three-phase sinusoidal pulse-width modulated (3ϕ SPWM) inverter. For simulating the 3ϕ SPWM inverter, a SIMULINK built-in block is used with a switching frequency of $f_c = 1.8kHz$ and a modulation index of $m_a = 0.85$. Figure 8.13 shows the spectra of $V_{AB}(t)$ and $V_{AN}(t)$ output voltages. Also, the spectrum of the phase A line current for the SPWM case is determined, and is shown in Figure 8.14.

Simulation results of the 3ϕ six-pulse VS WM inverter have demonstrated an encouraging performance in terms of the magnitude and the quality of inverter

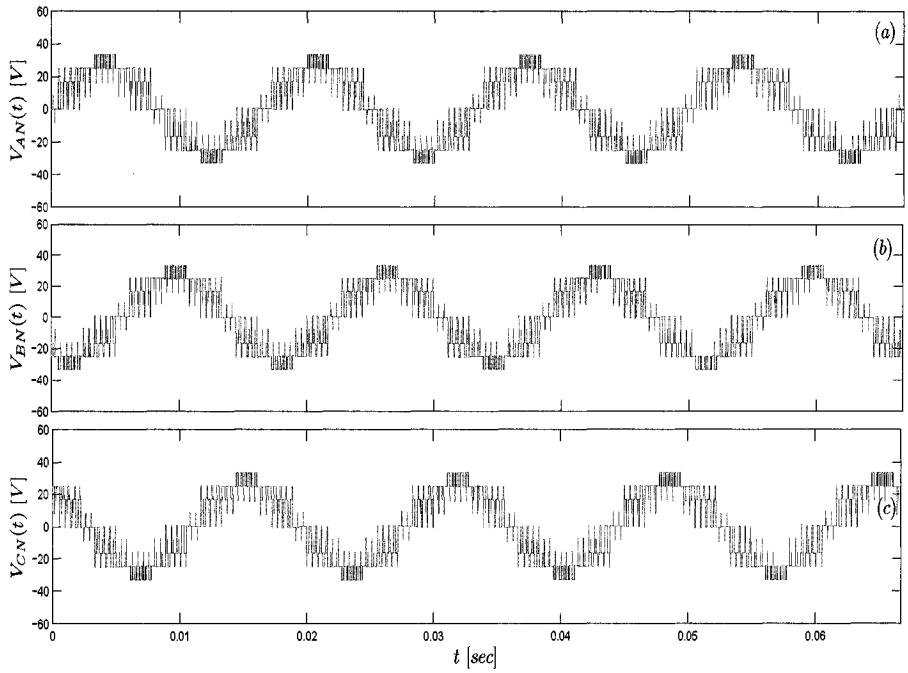

Figure 8.8: The 3ϕ six-pulse VS WM inverter line-to-neutral output voltages: (a) phase A-to-neutral voltage V_{AN}, (b) phase B-to-neutral voltage V_{BN} and (c) phase C-to-neutral voltage V_{CN}.

outputs. The output voltages have low THD_V factor values with the line-to-line fundamental component magnitudes close to the input dc voltage. Moreover, line currents have negligible THD_I factor values with almost sinusoidal waveforms. The comparison of the proposed 3ϕ WM inverter with the 3ϕ SPWM one shows that:

- Fundamental component magnitudes of output voltages and currents for the proposed 3ϕ WM inverter are higher than their counterparts obtained from the 3ϕ SPWM one: $|V_{AB}(1)|_{WM} = 49.8V$ and $|V_{AB}(1)|_{SPWM} = 42.53V$.

- The quality of the proposed 3ϕ WM inverter outputs is much higher than the 3ϕ SPWM inverter outputs. This is clearly indicated by the values of THD_V

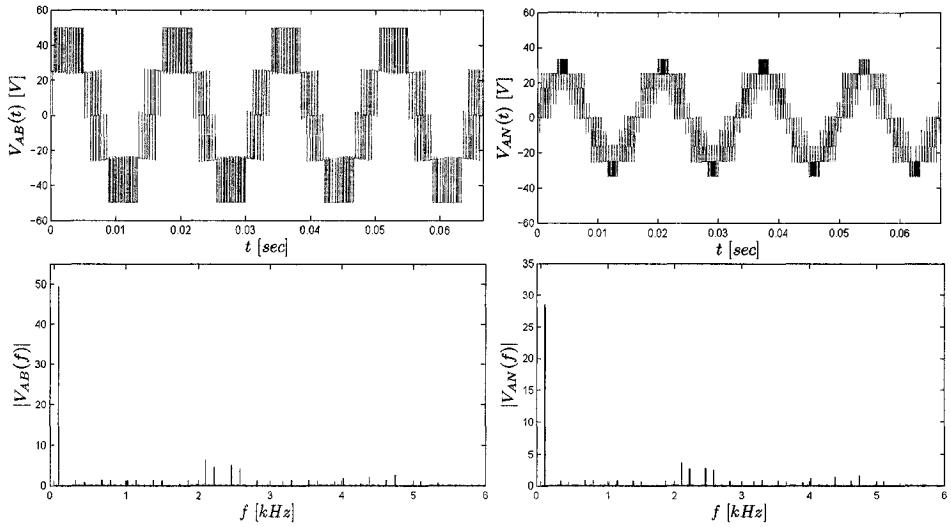

Figure 8.9: The harmonic spectra of the 3ϕ six-pulse VS WM inverter output voltages: (a) phase A line-to-line voltage ($V_{AB}(t)$), (b) phase A line-to-neutral voltage ($V_{AN}(t)$), (c) the spectrum of $V_{AB}(t)$; THD$_V$ = 12.3% and (d) the spectrum of $V_{AN}(t)$; THD$_V$ = 12.3%.

and THD$_I$ factors for both inverters: $(THD_V)_{WM} = 12.3\%$, $(THD_V)_{SPWM} = 39.1\%$, $(THD_I)_{WM} = 2.6\%$ and $(THD_I)_{SPWM} = 7.6\%$.

The presented simulation results of a 3ϕ VS six-pulse wavelet-modulated inverter have shown an encouraging performance with output voltage fundamental components having magnitudes close to the input dc voltage. Also, inverter output voltages have negligible harmonic components. Moreover, simple static 3ϕ $R-L$ load currents are very close to sinusoidal waveforms. It is worth mentioning that line-to-neutral output voltages of the simulated 3ϕ VS six-pulse inverter are composed of multi-level waveform due to the shift in the developed three scaling functions. This capability can be very significant when comparing 3ϕ WM inverters to other modulated 3ϕ ones. The extended non-dyadic MRA for generating 3ϕ switching pulses is implemented for operating a laboratory 3ϕ VS six-pulse IGBT inverter. The next section provides preliminary experimental test results for a 3ϕ

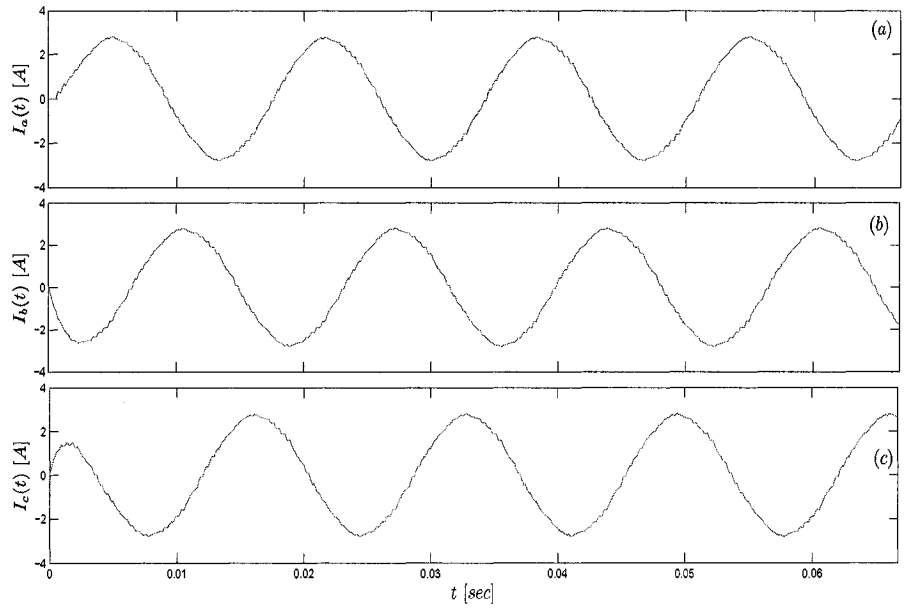

Figure 8.10: The 3ϕ load currents: (a) phase A current I_a, (b) phase B current I_b and (c) phase C current I_c.

Y-connected static $R-L$ load.

8.5 Experimental Test Results of a 3ϕ Wavelet Modulated Inverter

The three-phase WM technique is realized using a $Turbo-C$ code, compiled using the Texas Instrument compiler and loaded to a $dSPACE\ ds1102$ DSP board to generate switching pulses. These switching pulses are taken from digital-output port (DO/P) of the $dSPACE\ ds1102$ DSP board and applied to activate inverter IGBT switches. It should be noted that the generated switching pulses are applied to IGBT switches through an opto-coupler pulse amplifier for isolating and protecting the DSP board. An input dc voltage (V_{DC}) of 50 is used to supply the inverter

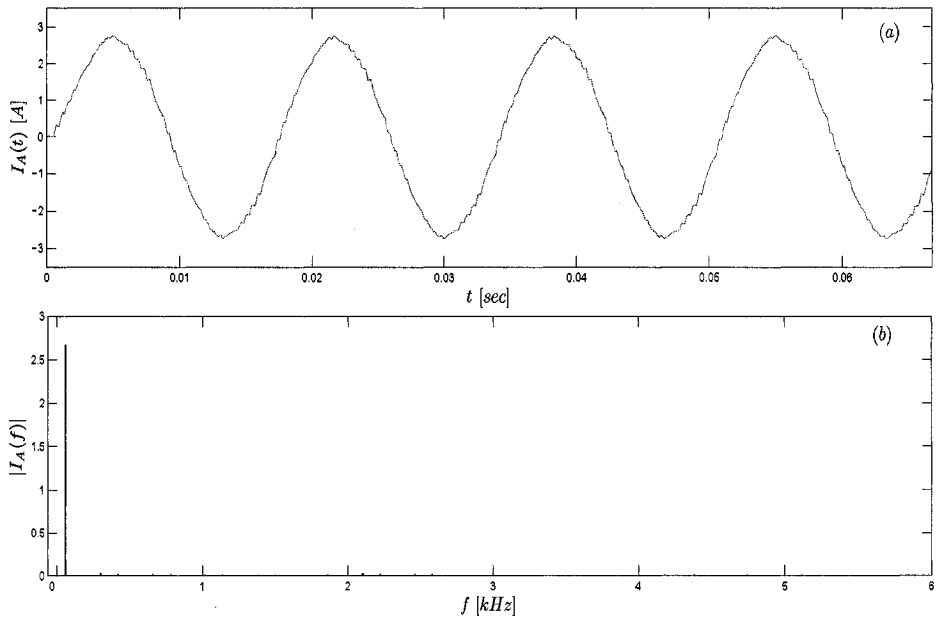

Figure 8.11: The harmonic spectrum of phase A current: (a) the phase A current $I_a(t)$ and (b) the magnitude of its spectrum $|I_a(n)|$; $\text{THD}_I = 1.16\%$.

on the input side. The tested inverter output line-to-line as well as line-to-neutral voltages and load currents are measured using the hall-effect sensors. The inverter output voltage and load current waveforms are displayed and downloaded to a computer using a 2-channel *Tektronics* 2212 storage digital oscilloscope that has a sampling frequency of 10 kHz. The software package *Grab* 2212 is used to download the collected waveforms from the storage oscilloscope to computer. Also, the inverter output voltages and the load currents are fed into the *FLUKE* 41 harmonic analyzer to obtain their spectra and total harmonic distortion (THD) factors.

8.5.1 Experimental Setup for a 3ϕ VS Six-Pulse IGBT Inverter

The elements used to build the experimental setup for the single-phase four-pulse inverter presented in chapter 6 are used for preparing a setup for the 3ϕ VS six-

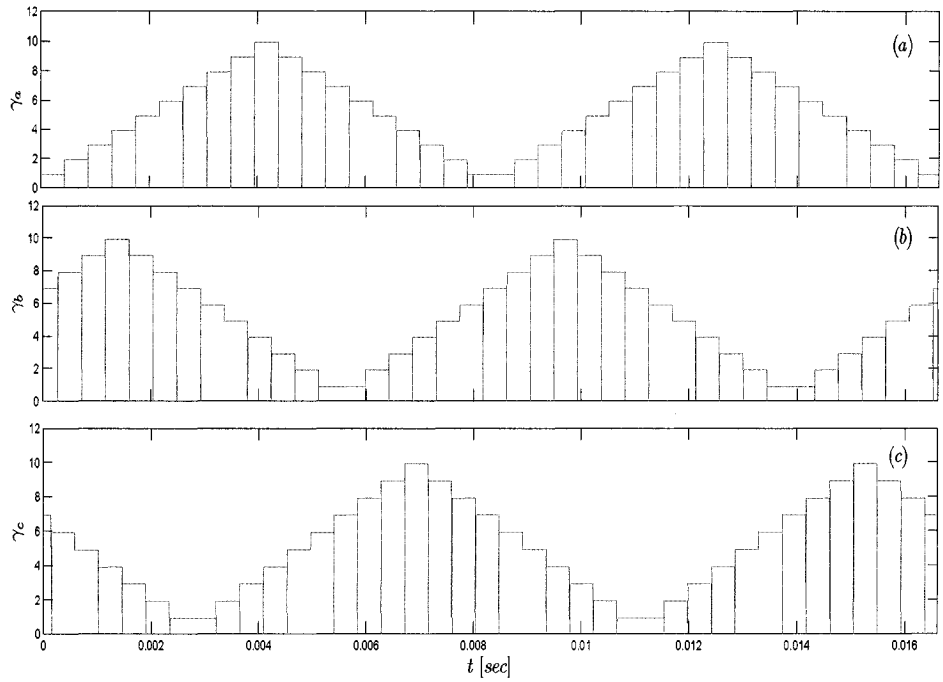

Figure 8.12: The scale-time interval factor γ for three non-dyadic type MRAs: (a) the phase A factor γ_a, (b) the phase B factor γ_b and (c) the phase C factor γ_c.

pulse IGBT inverter. However, this inverter has three legs, each of which supplies one phase of the Y-connected $R-L$ load. The experimental setup for the 3ϕ VS six-pulse IGBT inverter is shown in Figure 8.15.

8.5.2 Experimental Test Results

The experimental setup of the 3ϕ VS six-pulse IGBT inverter is prepared to test the performance of the proposed three-phase wavelet modulation technique. The setup of the 3ϕ IGBT inverter has an input dc voltage of 50 V and supplies a Y-connected $R-L$ load of $Z = 23.33 + j10\ \Omega/phase$. When the developed $Turbo-C$ code is executed by the $dSPACE\ ds1102$ DSP board, switching pulses are generated and sent to the digital output port (DO/P). These switching pulses are col-

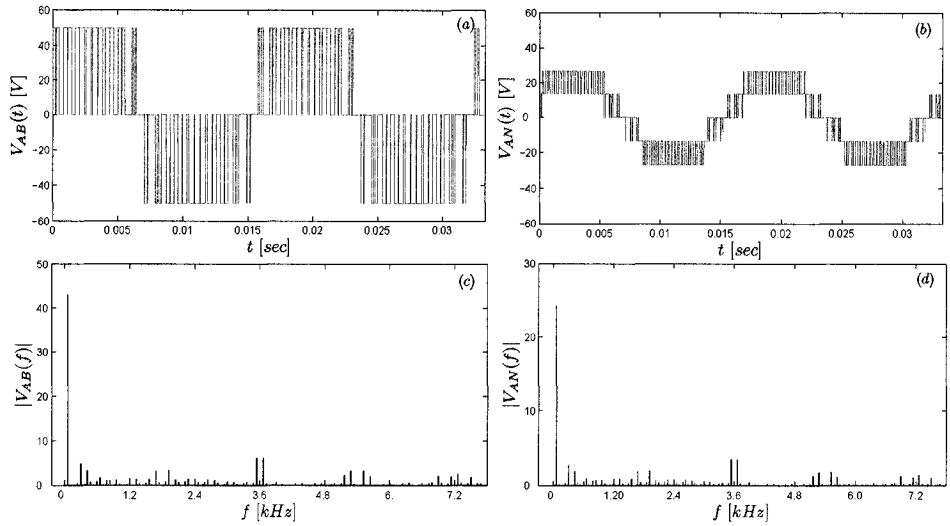

Figure 8.13: The harmonic spectra of the 3ϕ six-pulse VS SPWM inverter output voltages: (a) phase A line-to-line voltage ($V_{AB}(t)$), (b) phase A line-to-neutral voltage ($V_{AN}(t)$), (c) the spectrum of $V_{AB}(t)$; $\text{THD}_V = 39.1\%$ and (d) the spectrum of $V_{AN}(t)$; $\text{THD}_V = 39.1\%$.

lected using the *Tektronics* 2212 storage digital oscilloscope, and downloaded to a computer using the software package *Grab* 2212. Figure 8.16 shows the generated switching pulses that activate the inverter IGBT switches.

As the switching pulses are applied to the gates of IGBT switches and the dc voltage supply is turned on, an output voltage appears across the $R-L$ load. This voltage is collected using a hall-effect sensor and fed into the $FLUKE$ 41 power harmonic analyzer to determine its spectrum $|V_{BC}(f)|$ and the value of its THD factor. Figure 8.17 shows the inverter output line-to-line voltage $V_{BC}(t)$ and its harmonic spectrum. The inverter output line-to-neutral voltage is also collected and its spectrum is determined along with the value of its THD factor using the $FLUKE$ 41 power harmonic analyzer. Figure 8.18 shows the output line-to-neutral voltage $V_{BN}(t)$ along with its spectrum.

The Y-connected $R-L$ load draws three phase currents $I_A(t)$, $I_B(t)$ and $I_C(t)$.

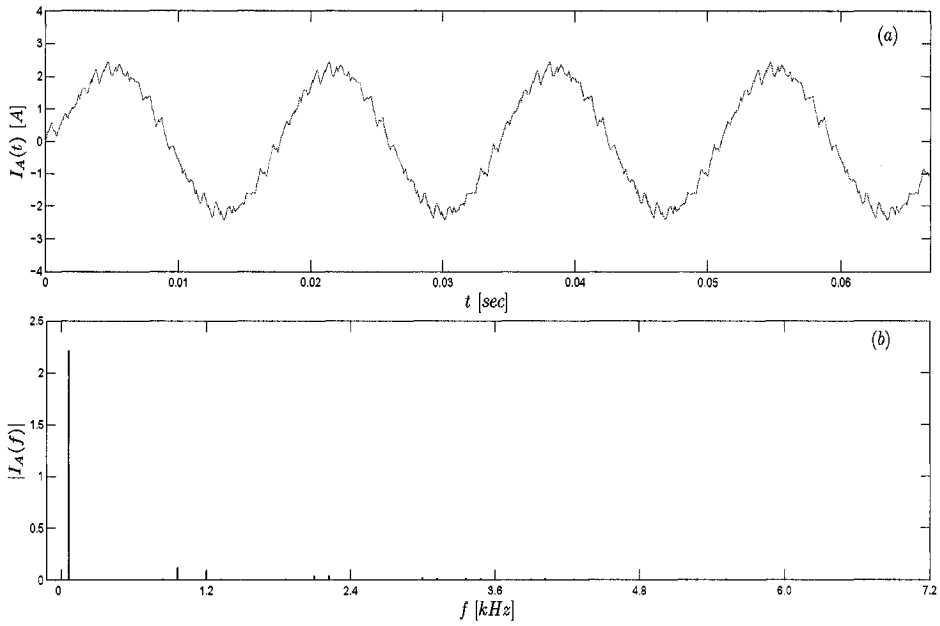

Figure 8.14: The harmonic spectrum of phase A current for the SPWM case: (a) the phase A current $I_a(t)$ and (b) the magnitude of its spectrum $|I_a(n)|$; $\text{THD}_I = 7.6\%$.

Phase A current is collected using a hall-effect sensor and fed into the $FLUKE$ 41 power harmonic analyzer to determine its spectrum as well as the value of its THD factor. Figure 8.19 shows the phase A load current along with its spectrum. The waveforms of the inverter output line-to-line and line-to-neutral voltages as well as the 3ϕ load currents are collected using the $Tektronics$ 2212 storage digital oscilloscope. Figure 8.20 shows the waveforms of the inverter output 3ϕ line-to-line voltages. Also, the inverter output 3ϕ line-to-neutral voltages collected using the $Tektronics$ 2212 storage digital oscilloscope are shown in Figure 8.21. Moreover, Figure 8.22 shows the waveforms of $I_A(t)$, $I_B(t)$ and $I_C(t)$, which are collected using the $Tektronics$ 2212 storage digital oscilloscope.

The scale-time interval factors γ_a, γ_b and γ_c defined in section 8.4 are evaluated for the experimental 3ϕ six-pulse WM inverter. Figure 8.23 shows the three factors

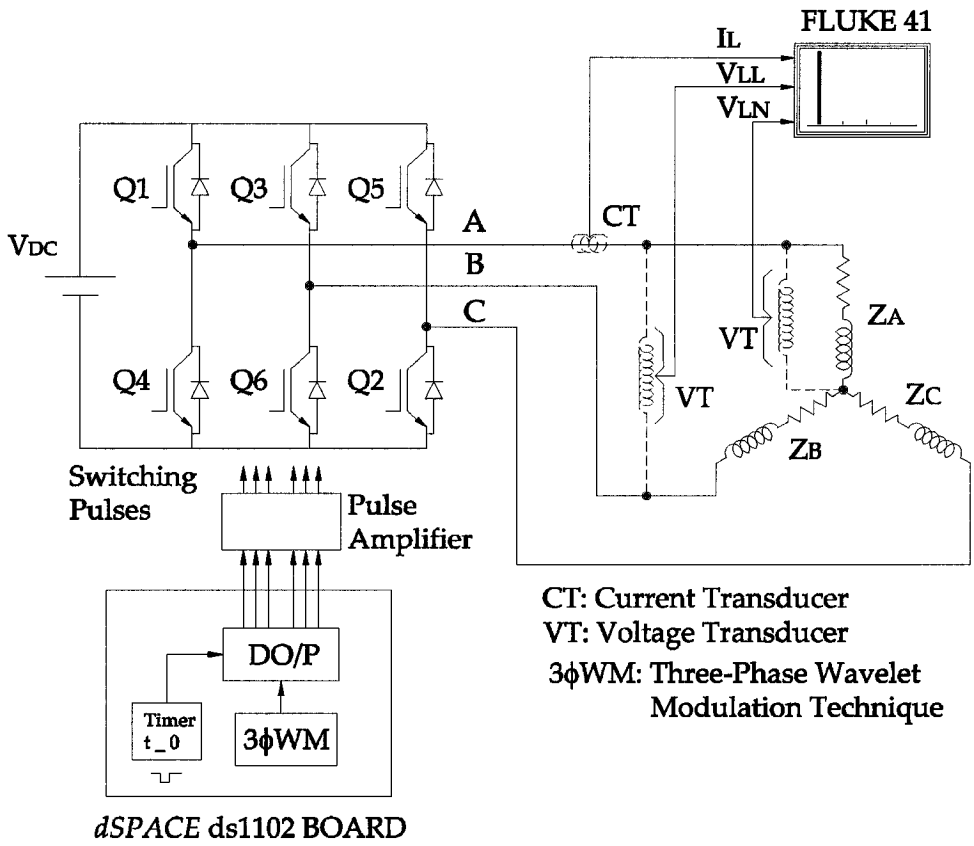

Figure 8.15: The experimental setup schematic for testing a 3ϕ VS six-pulse wavelet modulated IGBT dc-ac inverter and the 3ϕ Y-connected $R-L$ load.

γ_a, γ_b and γ_c.

Preliminary experimental test results of the 3ϕ wavelet modulated inverter have shown significant capabilities to eliminate harmonic components from the output voltages. Also, these results have demonstrated clear improvements on the 3ϕ VS output voltage quality that is indicated by the low values of THD_V and THD_I factors. Moreover, the fundamental components of the inverter output voltages have peak values close to the input dc voltage indicating effective concentration of output energies in the desired frequency components. Experimental test results are very consistent with simulation ones in both waveform shapes and inverter high

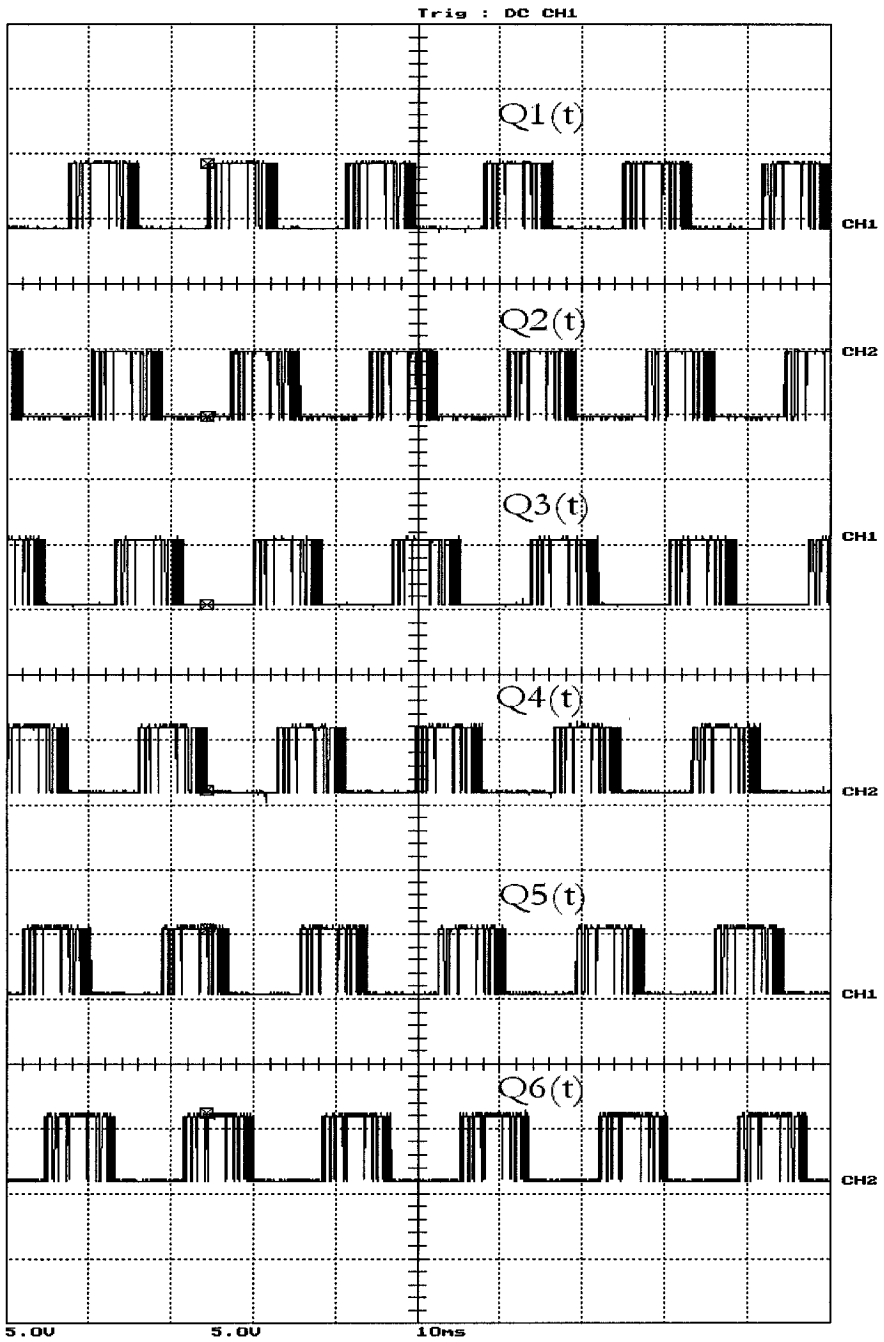

Figure 8.16: The switching pulses generated by the extended wavelet modulation technique $Turbo - C$ code collected from the digital output port of the ds1102 board using the *Tektronics* 2212 storage digital oscilloscope.

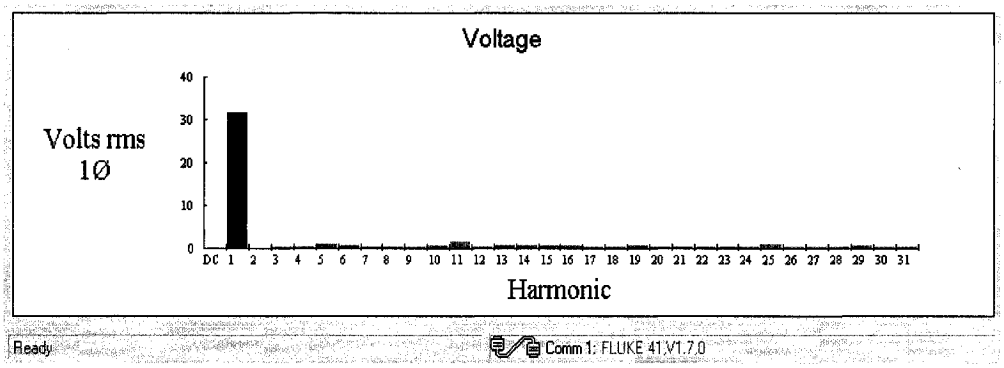

Figure 8.17: The experimental inverter output line-to-line voltage $V_{BC}(t)$ and its spectrum obtained using the $FLUKE$ 41 power harmonic analyzer. The THD_V is 3.2%.

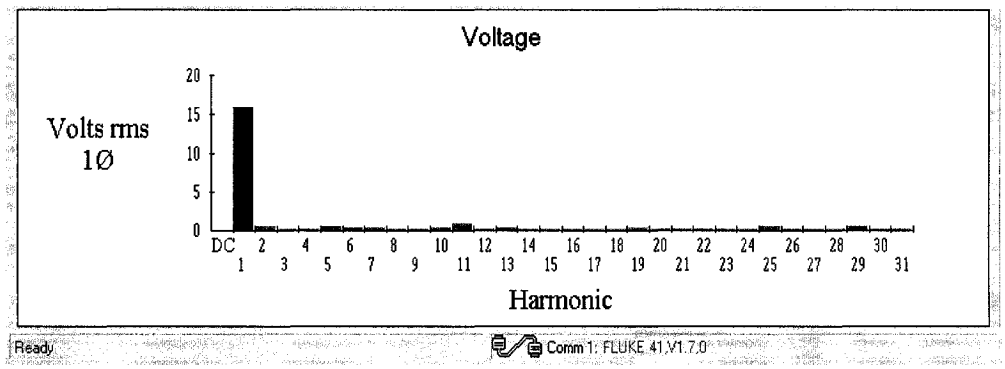

Figure 8.18: The experimental inverter output line-to-neutral voltage $V_{BN}(t)$ and its spectrum obtained using the $FLUKE$ 41 power harmonic analyzer. The THD_V is 3.2%.

quality outputs.

This chapter has presented the development and both simulation and experimental testing of the 3ϕ six-pulse WM inverter. The developed 3ϕ wavelet modulation technique has been based on constructing three non-dyadic type MRAs that are responsible for sampling and reconstructing three CT reference-modulating signals. Furthermore, each non-dyadic type MRA is responsible for generating switching pulses for one of the three inverter legs to reconstruct one reference-modulating signal. This approach for operating the 3ϕ inverter has been entirely based on the developed sampling-based model of 3ϕ inverters. The 3ϕ wavelet

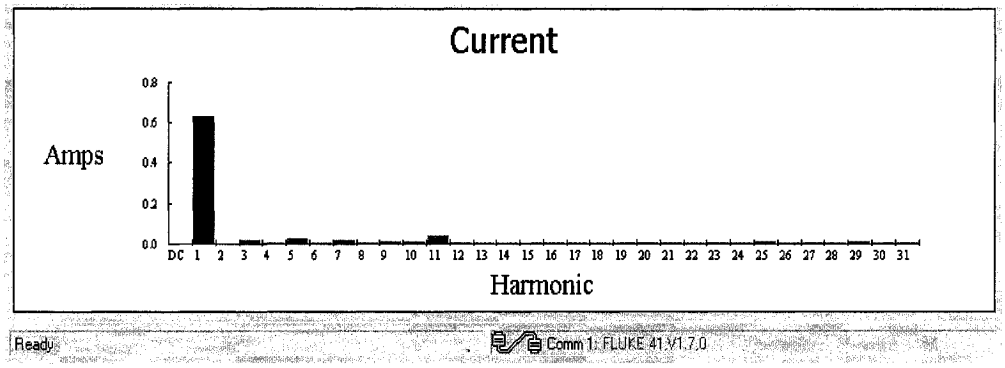

Figure 8.19: The experimental phase A load current $I_A(t)$ and its spectrum obtained using the $FLUKE$ 41 power harmonic analyzer. The THD_I is 0.68%.

modulation technique has been successfully implemented for simulation and experimental testing of a 3ϕ six-pulse inverter to supply a 3ϕ Y-connected $R-L$ load. The results obtained from the simulation and the experimental tests have shown robust and stable performance by the WM inverters along with high quality outputs. Furthermore, these test results have shown significant improvements in the magnitudes of the fundamental components of the inverter outputs over the conventional SPWM inverter. The test results along with simple implementation can provide evidence of the applicability of the proposed 3ϕ WM inverters in various industrial applications.

This chapter has been the last chapter to present developments and performance test results of the proposed wavelet modulation technique. The next chapter provides summary, concluding remarks and suggestions for future work in the line this research.

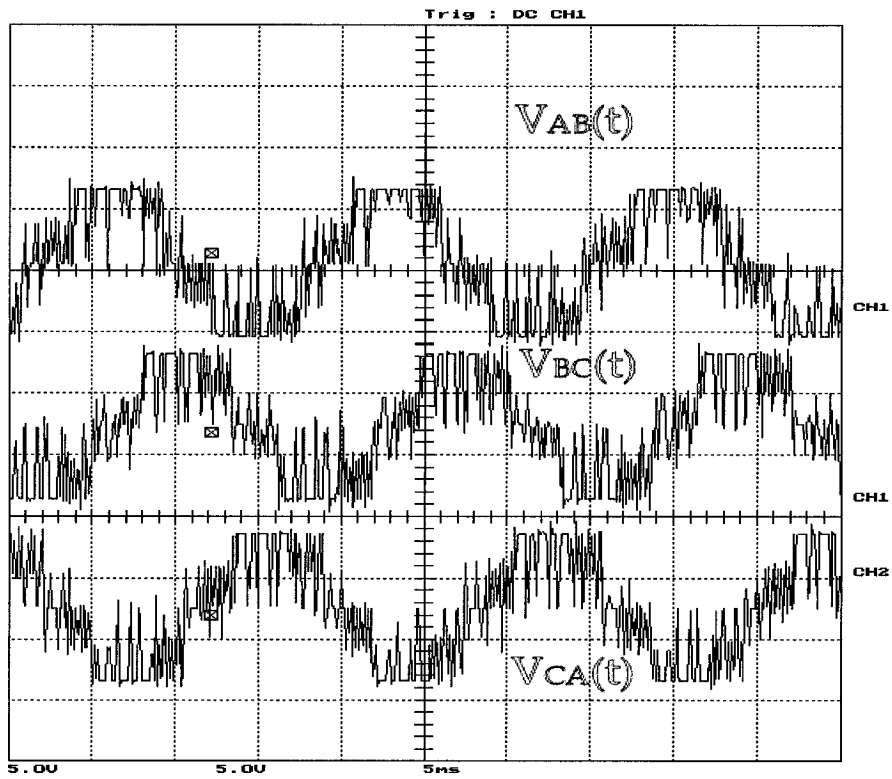

Figure 8.20: The 3ϕ six-pulse VS WM inverter experimental output line-to-line voltages $V_{AB}(t)$, $V_{BC}(t)$ and $V_{CA}(t)$ collected using the *Tektronics* 2212 storage digital oscilloscope. The voltage scale is 25 V/Div.

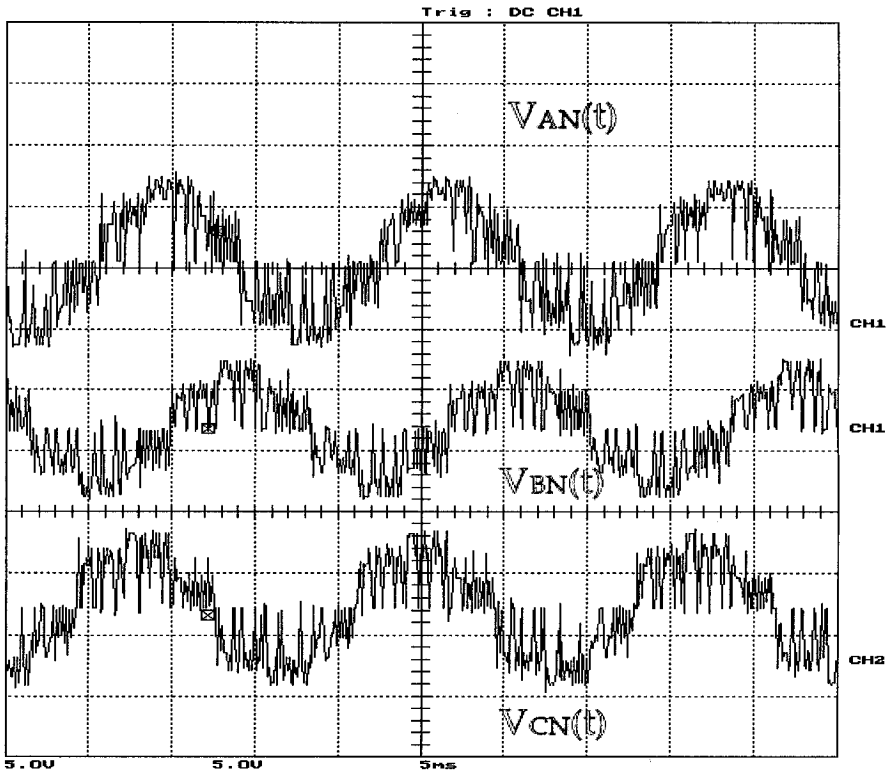

Figure 8.21: The 3ϕ six-pulse VS WM inverter experimental output line-to-neutral voltages $V_{AN}(t)$, $V_{BN}(t)$ and $V_{CN}(t)$ collected using the *Tektronics* 2212 storage digital oscilloscope. The voltage scale is 25 V/Div.

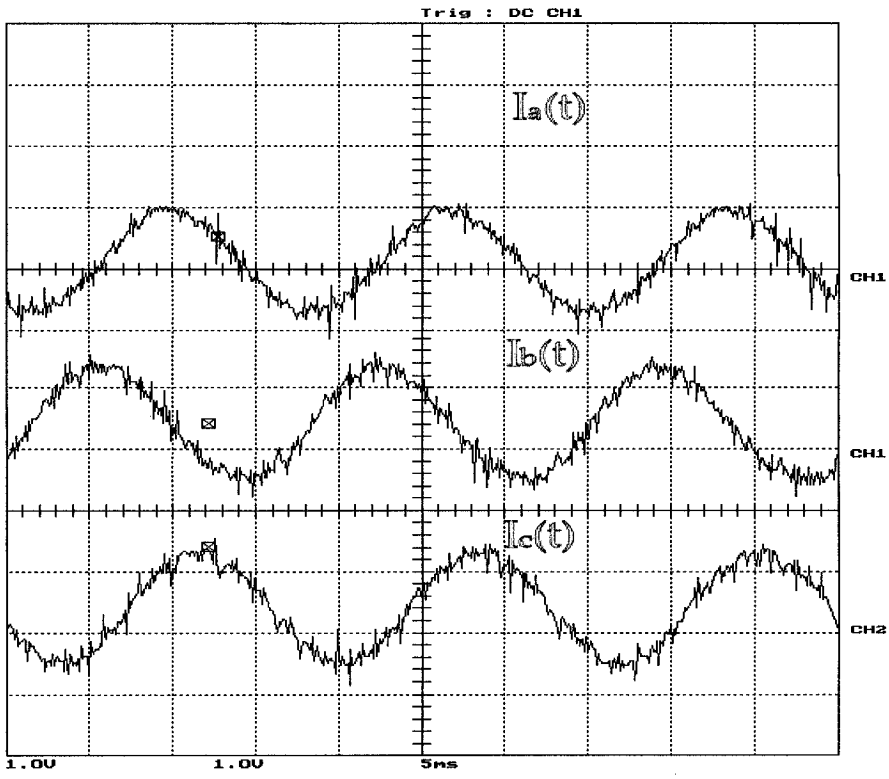

Figure 8.22: The 3ϕ load currents $I_A(t)$, $I_B(t)$ and $I_C(t)$ collected using the *Tektronics* 2212 storage digital oscilloscope. The current scale is 0.5 A/Div.

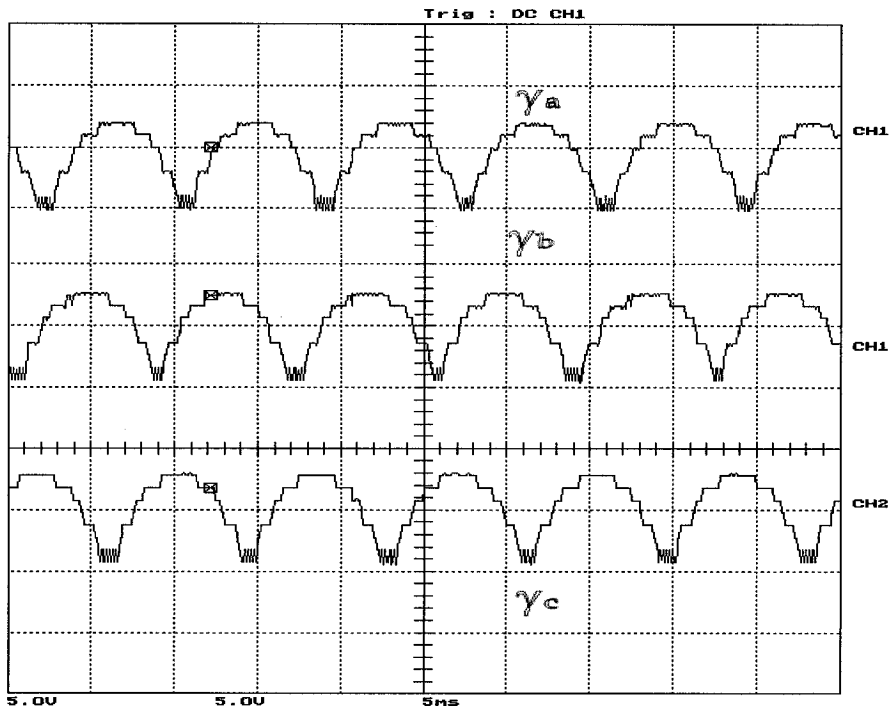

Figure 8.23: The scale-time interval factor γ for the extended non-dyadic MRA: the phase A factor γ_a, the phase B factor γ_b and the phase C factor γ_c.

Chapter 9

Conclusions and Future Work

9.1 Summary

The objectives established to investigate operating dc-ac inverters using wavelet basis functions were met through this research. A new technique was named the wavelet modulation technique, which was correlated with a non-uniform sampling-based model of inverters. The wavelet modulation technique required constructing a novel non-dyadic type multiresolution analysis (MRA) to support the non-uniform recurrent sampling. Constructing this MRA was achieved through defining a new set of basis functions that was called the scale-based linearly-combined basis functions. Furthermore, scale-based linearly-combined basis functions were proved to carry out non-uniform recurrent sampling on the analysis side of the non-dyadic MRA, while their dual basis functions reconstructed the reference-modulating signal on the synthesis side.

The first objective of this thesis was to develop an inverter model capable of considering instantaneous switching actions as a main part. This objective was met through the development and testing of the non-uniform recurrent sampling-

based model of inverters. In particular, the model interpreted the operation of an inverter as sampling the reference-modulating signal and reconstructing using the switching actions. The developed model showed accurate representation of inverter outputs for different switching frequencies. Moreover, the non-uniform recurrent sampling-based method was successfully extended to model three-phase inverters.

The second objective of this thesis was to design sets of basis functions that could construct a MRA to support a non-uniform recurrent sampling structure. This objective was met through the introduction of the scale-based linearly-combined scaling function along with its dual synthesis scaling function. These functions were found capable of generating basis functions to span spaces. Moreover, the collection of such spaces was found to construct a unique non-dyadic MRA capable of supporting a non-uniform recurrent sampling-reconstruction case.

The third objective of this thesis was to realize the non-dyadic MRA that generated switching signals for operating both 1ϕ and 3ϕ inverters. The realization of the required non-dyadic MRA and the generation of the switching signals were the two main components for implementing the proposed wavelet modulation technique. The implementation of the wavelet modulation technique was carried out using a MATLAB code for simulation purpose. Also, it was carried out using a $Turbo - C$ code for experimental testing purposes. Furthermore, this objective aimed at comparing the performance of wavelet modulated (WM) inverters with conventional sinusoidal pulse-width modulated (SPWM) ones. These comparisons were conducted for both simulation and experimental tests.

The final objective of this thesis was to develop and test a control strategy capable of adjusting the output magnitudes as well as frequencies of WM invert-

ers. This objective was achieved through the development of the resolution-level control strategy. This control strategy was based on the adjusting the level of the scale-based linearly-combined synthesis scaling function to vary the positions as well as widths of switching pulses. Such variation provided means of changing magnitudes and frequencies of inverter outputs. Furthermore, the resolution-level control strategy was implemented for both simulation and experimental tests.

Different simulation and experimental test results for different load types under different operating conditions demonstrated significant inverter output quality. Tested inverter output voltages as well as various load currents were analyzed using the the fast Fourier transform (FFT) to determine their harmonic spectra. Substantial improvements in magnitudes of output fundamental components were achieved indicating higher power transferred to the load side with high quality. Also, output voltages and load currents spectra showed remarkable capabilities of the wavelet modulation technique to eliminate undesired harmonic components, which resulted in low values of the total harmonic distortion factor. The next section summarizes the main contribution of this thesis.

9.2 Contributions

Major contributions and achievements of this work toward developing and testing wavelet modulated inverters are summarized as follows.:

- A novel non-uniform sampling-based model of inverters that considers instantaneous switching actions as interpolating functions to recover a CT signal has been developed. This model of inverters has been simulated for different inverter operating conditions. Furthermore, an extension of the

sampling-based model has been successfully constructed for three-phase 3ϕ six-pulse inverters.

- A new family of analysis and synthesis basis functions has been designed. This new family of basis functions is named scale-based linearly-combined basis functions that are able to span spaces. A collection of such spaces constructs a non-dyadic type MRA that supports a non-uniform recurrent sampling structure. Furthermore, all conditions required for the scale-based linearly-combined scaling function to be a scaling function have been verified.

- An innovative modulation technique that combines concepts of the sampling theorem, wavelet theory and power electronics has been successfully developed and tested. Also, a new algorithm has been introduced to implement the wavelet modulation technique for simulation and experimental tests. The performance of the developed technique has been compared to that of the conventional SPWM for the same loading conditions.

- A novel parameter that relates the scale with the interval of support in a non-dyadic MRA has been defined. This parameter has been named as the scale-time interval factor γ, and has been evaluated in all simulation and experimental tests. The scale-time interval factor γ has been utilized in monitoring the change in the scale of the synthesis scaling functions responsible for reconstructing the inverter output.

- A significant improvement of the inverter outputs has been obtained using the innovative wavelet modulation technique that has been demonstrated through low values of total harmonic distortion (THD) factors. Moreover,

high quality WM inverter outputs have been consistent in all simulation and experimental tests.

- A new control strategy has been developed, implemented and tested to adjust WM inverter output magnitude and frequency. This control strategy has been named as resolution-level control, and has been based on adjusting the scale of synthesis scaling functions to vary the widths as well the locations of switching pulses.

- An approach for extending the developed non-dyadic MRA to operate three-phase inverters has been developed and successfully tested. This approach has been based on the non-uniform sampling and reconstruction of three reference-modulating signals, each corresponding to one phase on the inverter output side. This extended non-dyadic MRA has been realized for simulation as well as for experimental testing. Both simulation and experimental test results have indicated significant quality improvement of inverter outputs.

9.3 Conclusions

This thesis presented a new analysis, successful development and testing of the wavelet modulation technique for single and three phase inverters. Test results of the new technique demonstrated significant performance regardless of load type or output frequency. Conclusions drawn from this work can be summarized as follows:

- The wavelet theory and its connection with the sampling theorem are fairly new concepts in power electronics applications, in particular, for modeling

and operating power electronic converters. In this work, an innovative modulation technique based on the non-uniform sampling and the wavelet theory was successfully developed and tested for operating inverters for the first time.

- Unlike other modulation techniques, the wavelet modulation technique was correlated with a non-uniform sampling-based model of inverters. Also, the new technique was developed through constructing a non-dyadic type MRA that supported a non-uniform recurrent sampling structure. The generation of switching pulses required to activate inverter switching elements was achieved without using carrier signals and aimed to reconstruct a CT signal from its samples. This approach showed remarkable concentration of the inverter output energy in a single frequency component. As a result, magnitudes of desired output frequency components were found high, while the energy distributed in undesired frequencies was almost negligible.

- The performance of the wavelet modulation technique was compared to that of the conventional SPWM one under same operating conditions. Results of such comparisons indicated that the WM inverter had better output quality than the SPWM one. Moreover, magnitudes of the WM inverter output fundamental frequency components were found much higher that their counter parts obtained using the SPWM inverter. As a consequence, the WM inverter showed better capabilities to transfer power to the load side than the SPWM one.

- The approach to design a new family of basis functions to span spaces that construct a non-dyadic type MRA was carried out successfully for the first

time. This new MRA was constructed to support non-uniform recurrent sampling structures. Also, the definition of a factor that related the scale to change in the interval of support of each synthesis scaling function showed ability to control a wavelet-modulated inverter output under varying load requirements.

- The consistent results obtained from simulations and experimental tests demonstrated practical aspects of the wavelet modulation technique to be employed for industrial applications. Furthermore, the simplicity of its implementation represented another advantage over existing modulation techniques.

- Test results for the inverter supplying different loads under different output requirements showed high quality output along with stable responses under changing load conditions.

- The developed non-dyadic type MRA was successfully extended and implemented to generate switching pulses for three-phase inverters. Simulation as well as experimental test results indicated significant performance with almost no output harmonic components.

- Simulation and experimental test results showed that high amounts of power could be transfered from the supply side to the load side using the innovative WM inverters. This feature of the WM inverters was consistent in all tested loads under different output frequencies.

9.4 Future Works

The developed wavelet modulation technique can be used for operating inverters for different applications. Additional research can be conducted on applying wavelet modulated inverters in ac motor drives, UPS, different applications in power systems and renewable energy utilization. Also, research can be carried out on designing and implementing resolution-level controlled wavelet modulated inverters for different industrial applications.

The wavelet modulation technique may be applied for other power electronic converters. Moreover, the developed technique along with the proposed wavelet basis functions design approach can open several areas of research that may include:

- Extending tests of the new wavelet modulation technique for three-phase voltage-source and current-source inverters. This can be applied in different areas, in particular, ac motor drives and renewable energy utilization.

- Designing new wavelet basis functions using different scaling functions for other potential applications in signal processing as well as power electronic converters operation and control. As a potential area, ac-dc converters may be operated by a modified version of the developed non-dyadic type MRA.

- Applying other signal processing concepts in modeling other power electronic switching circuits for different industrial applications.

- Implementing and testing the developed resolution-level control for other types of inverters. This can provide new approaches for controlling and operating existing modulated inverters.

Bibliography

[1] Holmes, D. G. and Lipo, T. A., *Pulse Width Modulation for Power Converters.* IEEE Press Series on Power Engineering, Wiley Inter-Science, NJ, 2003.

[2] Bowes, R. S. and Lai, Y. S., "The Relationship Between Space-Vector Modulation and Regular-Sampled PWM", *IEEE Trans. on Industrial Electronics*, Vol. 44, No. 5, 1997, pp. 670–679.

[3] Mohan, N., Undeland, T. M. and Robbins, W. P, *Power Electronics: Converters, Applications and Design*, John Willey & Sons, Inc., 1989.

[4] Saleh, S. A. and Rahman, M. A., "Discrete Time-Based Model of the Sinusoidal Pulse Width Modulation Technique", *IEEE IECON'05 Conference Proceeding*, Raleigh, NC., Nov. 2005, pp. 1082–1087.

[5] Royer, G. H., "A Switching Transistor D-C to A-C Converter Having an Output Frequency Proportional to the D-C Input Voltage", *AIEE Trans. on Communications and Electronics*, Vol. 74, Part. I, 1955, pp. 322–324.

[6] Uchrin, G. C. and Taylor, W. 0., "A New Self-Excited Square-Wave Transistor Power Oscillator", *Proc. of the IRE*, Vol. 43, pp. 99, 1955.

[7] Lee, Y. F. and Willson, T. G., "Analysis and Modeling of a Family of Two-Transistor Parallel Inverters", *IEEE Trans. on Magnetics*, Vol.Mag-9, No. 3, 1973, pp. 414–418.

[8] McMurry, W., "Multipurpose Power Converter Circuits", *U.S. Patent No. 3,487,289*, December, 1969.

[9] McMurry, W., "Analysis of Thyristor DC Chopper Power Converters Including Nonlinear Commutating Reactors", *IEEE Trans. on Magnetics*, Vol. MAG-1, 1970, pp. 16–21.

[10] Kirnick, A. and Heinrick, "Static Inverters with Neutralization of Harmonics", *AIEE Transactions*, Vol. 81, 1962, pp. 374–378.

[11] Mokrytzki, B., "Pulse Width Modulated Inverters for AC Motor Drives", *IEEE Trans. on IA*, Vol.-IGA-3, 1967, pp. 493–503.

[12] Schonubg, A. and Stemmler, H., "Static Frequency Changers with Subharmonic Control in Conjunction with Reversible Variable Speed AC Drives ", *Brown Boveri Rev.*, 1964, pp. 555–557.

[13] Grant, D. A. and Seinder, R., "Ratio Changing in Pulse Width Modulated Inverters", *Proc. IEE*, Vol. 128, Part B, No. 5, 1981, pp. 243–248.

[14] Bowes, S. R. and Clark, P. R., "Simple Microprocessor Implementation of New Regular-Sampled Harmonic Elimination PWM Techniques", *IEEE Trans. on Industry Applications*, Vol. 28, No. 1, 1992, pp. 89–95.

[15] Bowes, S. R., "New Sinusoidal Pulsewidth-Modulated Inverter", *Proc. IEE.*, Vol. 122, No. 11, 1975, pp. 1279–1285.

[16] Bowes, R. S. and Bird, B. M, "Novel Approach to the Analysis and Synthesis of Modulation Processes in Power Converters", *Proc. IEE.*, Vol. 122, No. 5, 1975, pp. 507–513.

[17] Bowes, S. R. and Mount, M. J., "Microprocessor Control of PWM Inverters", *IEE Proc.,B, Elect. Power Appl*, Vol. 128, No. 6, 1981, pp. 293–305.

[18] Maswood, A.I., Shen W. and Rahman, M. A., "A flexible Way to Generate PWM-SHE Switching Patterns Using Genetic Algorithm", *IEEE APEC 2001*, Vol. 2, 2001, pp. 1130–1134.

[19] Patel, H. S. and Hoft, R. G., "Generalised Techniques of Harmonic Elimination and Voltage Control in Thyristor Inverters: Part I Harmonic Elimination", *IEEE Trans. on Industry Applications*, IA-9(3), 1973, pp. 310-317.

[20] Patel, H. S. and Hoft, R. G., "Generalised Techniques of Harmonic Elimination and Voltage Control in Thyristor Inverters: Part II - Voltage Control Techniques", *IEEE Trans. on Industry Applications*, IA-10(5), 1974, pp. 666-673.

[21] Enjeti, P. and Lindsay, J. F., "Solving Nonlinear Equations of Harmonic Elimination PWM in Power Control", *IEE Electronics Letters*, 1987, Vol. 23, pp. 656–657.

[22] Enjeti, N., Ziogas, P. D. and Lindsay, J. F., "Programmed PWM Techniques to Eeliminate Harmonics: a Critical Evaluation", *IEEE Trans. on Industry Applications*, Vol. 26, No. 2, 1990, pp. 302–316.

[23] Liang, T. J., OConnell, R. M. and Hoft, R.G., "Inverter Harmonic Reduction Using Walsh Function Harmonic Elimination Method", *IEEE Trans. on Power Electronics*, Vol. 12, No. 6, 1997, pp. 971–982.

[24] Boost, M. A. and Ziogas, P. D., "State-of-the-art Carrier PWM Techniques: a Critical Evaluation", *IEEE Trans. on Industry Applications*, Vol. 24, No. 2, 1988, pp. 271–280.

[25] Trzynadlowski, A. M., "Nonsinusoidal Modulating Functions for Three-Phase Inverters", *IEEE Trans. on Power Electronics*, Vol. 4, No. 3, 1989, pp. 331–338.

[26] Holmes, D. G., "The Significance of Zero Space Vector Placement for Carrier-Based PWM Schemes", *IEEE Trans. on Industry Applications*, Vol. 32, No. 5, 1996, pp. 1122–1129.

[27] Plunckett, A. B., "A Current Controlled PWM Transistor Inverter Drive", *IEEE/IAS 1979 Annual Meeting Proc.*, 1979, pp. 785–792.

[28] Bose, B. K., "An Adaptive Hysteresis-Band Current Control Technique of a Voltage-Fed PWM Inverter for Machine Drive System", *IEEE Trans. on Industrial Electronics*, Vol. 37, No. 5, 1990, pp. 402–408.

[29] Rahman, K. M., Rezwan, M. K., Choudhury, M. A. and Rahman, M. A., "Variable-Band Hysteresis Current Controllers for PWM Voltage-Source Inverters", *IEEE Trans. on Power Electronics*, Vol. 12, No. 6, 1997, pp. 964–970.

[30] Holtz, J. and Stadtfeld, S., "A Predictive Controller for the Stator current Vector of AC Machines Fed from a Switched Voltage Source", *IPEC'83 Conference Record*, Tokyo, 1983, pp. 1165–1675.

[31] Trzynadlowski, A. M., Legowaki, S. and Kirlin, R. L., "Random Pulse Width Modulation Technique for Voltage-Controlled Power Inverters", *IEEE/IAS 1987 Annual Meeting Proc.*, 1987, pp. 863–868.

[32] Hui, S. R., Sathiakumar, S. and Sung, K. K., "Novel Random PWM Scheme with Weighted Switching Decision", *IEEE Trans. on Power Electronics*, Vol. 12, No. 6, 1997, pp. 945–952.

[33] Rahman, M. A., Quaicoe, J. E. and Choudhury, M. A., "Performance Analysis of Delta Modulated Inverters", *IEEE Trans. on Power Electronics*, Vol. 2, No. 3, 1987, pp. 227–233.

[34] Raman, V. and Yoram, B, "Optimal Sub-Nyquist Nonuniform Sampling and Reconstruction for Multiband Signals", *IEEE Trans. on Signal Processing*, Vol. 49, No. 10, 2001, pp. 2301–2313.

[35] Selesnick, I. W., "Interpolating multiwavelet bases and the sampling theorem.", *IEEE Trans. on Signal Processing*, Vol. 47, No. 6, 1999, pp. 1615–1621.

[36] Eldar C. Y. and Oppenheim, A. V., "Filterbank Reconstruction of Bandlimited Signals from Nonuniform and Generalized Samples", *IEEE Trans. on Signal Processing*, Vol. 18, No. 10, 2000, pp. 2864–2875.

[37] Papoulis, A., "Generalized sampling expansion", *IEEE Trans. on Circuits and Systems*, Vol. 24, No. 11, 1977, pp. 652–654.

[38] Paley, R. and Wiener, N., "Fourier Transform in the Complex Domain", *Amer. Math. Soc. Colloq. Publications*, Vol. 19, 1934.

[39] Unser, M. and Zerubia, J., "A Generalized Sampling Theory without bandlimiting constraints", *IEEE Trans. on Circuits and Systems II*, Vol. 45, No. 8, 1998, pp. 959–969.

[40] Zayed, A. I., "On Kramer's Sampling Theorem Associated with General Sturm-Liouville Problems and Lagrange Interpolation", *SIAM Journal Applied Math.*, Vol. 51, 1991, pp. 575–604.

[41] Kotsakis, C., Multiresolution Aspects of Linear Approximation Methods in Hilbert Spaces Using Gridded Data. *Ph.D. thesis*, University of Calgary, Calgary, AL, Canada, 2000.

[42] Aldroubi, A. and Grochenig, K., "Non-uniform Sampling and Reconstruction in Shift-Invariant Spaces", *SIAM Rev.*, Vol. 43, No. 4, 2001, pp. 585–620.

[43] Levinson, N., "Gap and Density Theorems", *Amer. Math. Soc. Colloq. Publications*, Vol. 26, 1940.

[44] Duffin, R. and Schaeffer, A., "A Class of Nonharmonic Fourier Series", *Trans. Amer. Math. Soc.*, Vol. 72, 1952, pp. 341–366.

[45] Gopinath, R. A., Odegard, J. E. and Burrus, C. S., "Optimal Wavelet Representation of Signals and the Wavelet Sampling Theorem", *IEEE Trans. on Circuits and Systems-II: Analog and Digital Signal Processing*, Vol. 41, No. 4, 1994, pp. 262–277.

[46] Walter, G.G., "A Sampling Theorem for Wavelet Subspaces", *IEEE Trans. on Information Theory*, Vol. 38, No. 2, 1992, pp. 881–884.

[47] Nashed, M. Z. and Walter, G.G., "General Sampling Theorems for Functions in Reproducing Kernel Hilbert Spaces", *Math. Control Signals Sys.*, Vol. 4, 1991, pp. 373–412.

[48] Mallat, S. G., "A Theory for Multiresolution Signal Decomposition: the Wavelet Representation", *IEEE Trans. on Pattern Analysis and Machine Intelligence*, Vol. 11, No. 7, 1989, pp. 674–693.

[49] Daubechies, I., "Orthonormal Bases of Compactly Supported Wavelets", *Comm. Pure & Appl. Math.*, Vol. 41, 1988, pp. 909–996.

[50] Gilbert, S., "Wavelet Transforms Versus Fourier Transforms", *Bull. Amer. Math. Soc.*, Vol. 28, 1993, pp. 288–305.

[51] Odegard, J.E., Gopinath, R.A. and Burrus, C.S., "Optimal Wavelets for Signal Decomposition and the Existence of Scale-Limited Signals", *IEEE International Conference on Acoustics, Speech, and Signal Processing, ICASSP-92 Record*, Philadelphia, PA, Vol. 4, 1992, pp. 597–600.

[52] Chui, C. K., *Wavelets: A Mathematical Tool for Signal Processing.* SIAM: Society of Industrial and Applied Mathematics Series, Philadelphia, PA, 1997.

[53] Xia, X. G. and Zhang, Z., "On Sampling Theorem, Wavelets, and Wavelet Transforms", *IEEE Trans. on Signal Processing*, Vol. 41, No. 12, 1993, pp. 3524–3535.

[54] Strang, G., "Wavelets and Dilation Equations: A Brief Introduction", *SIAM Rev.*, Vol. 31, 1989, pp. 614–627.

[55] Berry, F., "Steady State Mathematical Model for the DC-AC Inverters on the Space Shuttle", *IEEE Conference on 'Energy and Information Technologies in the Southeast*, Southeast Con'89 Proceedings, Vol. 2, 1989, pp. 455–458.

[56] Milosevic, M., "Decoupling Control of d and q Current Components in Three-Phase Voltage Source Inverter", *EEH Power Systems Laboratory, Technical Report*, Zuerich, Switzerland, 2004.

[57] Unser, M., Thevenaz, P. and Aldroubi, A., "Shift-Orthogonal Wavelet Bases", *IEEE Trans. on Signal Processing*, Vol. 46, No. 7, 1998, pp. 1827–1836.

[58] Jia, R. Q., Jiang, Q. and Shen, Z., "Distributional Solutions of Non-Homogenous Discrete and Continuous Refinement Equations", *SIAM Journal on Applied Math.*, Vol. 32, No. 2, 2000, pp. 420–434.

[59] Walker, G. and Ledwich, G., "Bandwidth Considerations for Multilevel Converters", *IEEE Trans. on Power Electronics*, Vol. 14, No. 1, 1999, pp. 74–81.

[60] Tymerski, R. E., "Frequency Analysis of Time-Interval-Modulated Switched Networks", *IEEE Trans. on Power Electronics*, Vol. 6, No. 2, 1991, pp. 287–295.

[61] Koutroulis, E., Chatzakis, J., Kalaitzakis, K. and Voulgaris, N. C., "A Bidirectional, Sinusoidal, High-Frequency Inverter Design", *IEE Proc.-Electr. Power Appl.*, Vol. 148, No. 4, 2001, pp. 315–321.

[62] Wood, P., *Switching Power Converters.*. Van Nostrand Reinhold, New York, 1981.

[63] T. Dogaru and L. Carin, "Multiresolution Time-Domain Using CDF Biorthogonal Wavelets", *IEEE Trans. on Microwave Theory and Techniques*, Vol. 49, No. 5, 2001, pp. 902–912.

[64] Zhang, J. K., Davidson, T. N. and Wong, K. M., "Efficient Design of Orthonormal Wavelet Bases for Signal Representation.", *IEEE Trans. on Signal Processing*, Vol. 52, No. 7, 2004, pp. 1983–1996.

[65] Unser, M., Aldroubi, A. and Eden, M., "On the Asymptotic Convergence of B-spline Wavelets to Gabor Functions", *IEEE Trans. on Information Theory*, Vol. 38, March 1992, pp. 864–872.

[66] Van De Ville, D., Blu, T., Forster, B. and Unser, M.,"Semi-Orthogonal Wavelets that Behave Like Fractional Differentiators", *Proceedings of the SPIE: Optical Engineering and Instrumentation (Wavelet XI)*, San Diego, CA, August, 2005.

[67] Saleh, S. A., Moloney, C., R. and Rahman, M. A., "Developing a Non-dyadic MRAS for Switching DC-AC Inverters", *The IEEE 12th Digital Signal Processing Workshop DSP06 Conference*, Jackson Lake Lodge, Wyoming, USA, September, 2006, pp. 544–549.

[68] Abdel-Rahim, N. and Quaicoe, J. E., "Analysis and design of a multiple feedback loop control strategy for single-phase voltage-source UPS inverters", *IEEE Trans. on Power Electronics*, Vol. 11, No. 4, 1996, pp. 532–541.

[69] Zhang, K., Kang, Y., Xiong, J. and Chen, J., "Direct repetitive control of SPWM inverter for ups purpose", *IEEE Trans. on Power Electronics*, Vol. 18, No. 3, 2003, pp. 784–792.

[70] Abdel-Rahim, N. and Quaicoe, J. E., "A Single-Phase Delta-Modulated Inverter for UPS Applications", *IEEE Trans. on Industrial Electronics*, Vol. 40, No. 3, 1993, pp. 347–354.

[71] Rech, C., Pinheiro, H., Grundling, H. A., Hey, H. L. and Pinheiro, J. R., "A Modified Discrete Control Law for UPS Applications", *IEEE Trans. on Power Electronics*, Vol. 18, No. 5, 2003, pp. 1138–1145.

[72] Stankovic, A. M., Verghese, G. C. and Perreault, D. J., "Randomized Modulation of Power Converters Via Markov Chains", *IEEE Trans. on Control System Technology*, Vol. 5, No. 1, 1997, pp. 61–73.

[73] Saleh, S. A. and Rahman, M. A., "Development and Experimental Testing of a Single-Phase B-Spline-Based SPWM Inverter", *IEEE ISIE'06 Conference Proceedings*, Montreal, Quebec, July, 2006, pp. 815–819.

[74] Saleh, S. A. and Rahman, M. A., "Experimental Testing of a Novel Control for Inverter-Fed Three-Phase Induction Motor", *IEEE PES'06 CD-ROM Conference Proceedings*, Montreal, Quebec, June, 2006.

[75] Bowes, S. R., "Novel Real-Time Harmonic Minimized PWM Control for Drives and Static Power Converters", *IEEE Trans. on Power Electronics*, Vol. 9, No. 3, 1994, pp. 256–262.

[76] Bowes, S. R. and Clark, P. R., "Transputer-Based Optimal PWM Control of Inverter Drives", *IEEE Trans. on Industry Applications*, Vol. 28, No. 1 Part 1, 1992, pp. 81–88.

[77] Bowes, S. R., "Advanced Regular-Sampled PWM Control Techniques for Drives and Static Power Converters", *IEEE Trans. on Industrial Electronics*, Vol. 42, No. 4, 1995, pp. 367–373.

[78] Bowes, S. R. and Jian L., "New Robust Adaptive Control Algorithm for High-Performance AC Drives", *IEEE Trans. on Industrial Electronics*, Vol. 47, No. 2, 2000, pp. 325–336.

[79] Czarkowski, D., Chudnovsky, D. V., Chudnovsky, G. V. and Selesnick, I. W., "Solving the Optimal PWM Problem for Single-Phase Inverters", *IEEE Trans.*

on Circuits and Systems -I: Fundamental Theory and Applications, Vol. 49, No. 4, 2002, pp. 465–475.

[80] Buja, G. and Indri, G., "Optimal PWM for feeding AC motors", *IEEE Trans. on Industry Applications*, Vol. 13, No. 1, 1977, pp. 34–42.

[81] Bowes, S. R. and Holliday, D., "Comparison of Pulse-Width-Modulation Control Strategies for Three-Phase Inverter Systems", *IEE Proceedings: Electric Power Applications*, Vol. 153, No. 4, 2006, pp. 575–584.

[82] Houndsworth, J. A. and Grant, D. A., "The Use of Harmonic Distortion to Increase Voltage of a Three Phase PWM Inverter", *IEEE Trans. on Industry Applications*, Vol. IA-20, 1984, pp. 1224–1228.

[83] Rowan, T. R. and Kerkman, R. L., "A New Synchronous Current Regulator and an Analysis of Current-Regulated PWM Inverters", *IEEE Trans. on Industry Applications*, Vol. 22, No. 4, 1986, pp. 678–690.

Appendix A

Extended Experimental Test Results:

1ϕ WM Inverters

A.1 Static $R - L$ Load

A.1.1 An Output Frequency of $f = 90\ Hz$

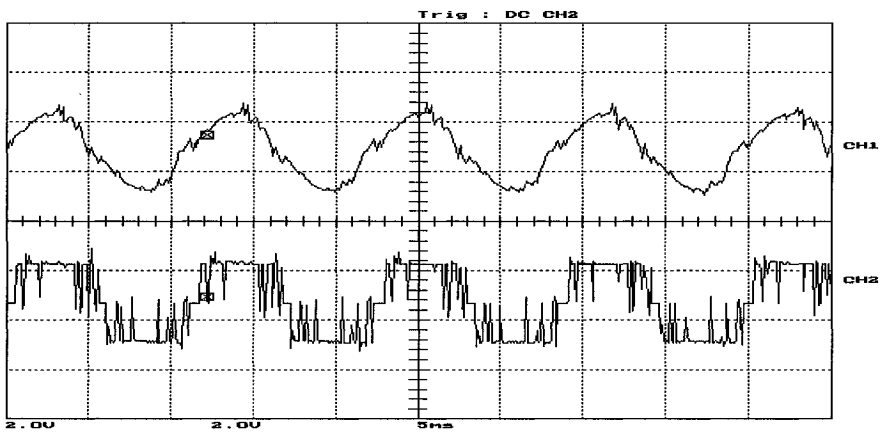

Figure A.1: Experimental inverter output voltage and $R - L$ load current for an output frequency of $f = 90\ Hz$ collected using the *Tektronics* 2212 storage digital oscilloscope. The voltage scale is 50 V/Div and the current scale is 0.2 A/Div.

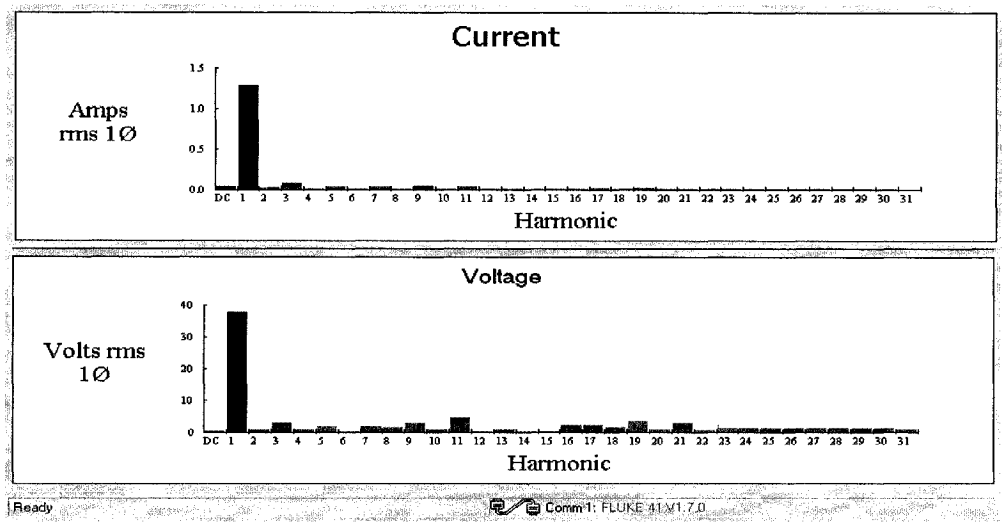

Figure A.2: The experimental $R - L$ load current and the inverter output voltage spectra for an output frequency of $f = 90\ Hz$ obtained using the $FLUKE41$ power harmonic analyzer. The THD_V is 15.1% and the THD_I is 1.4%.

A.1.2 An Output Frequency of $f = 120\ Hz$

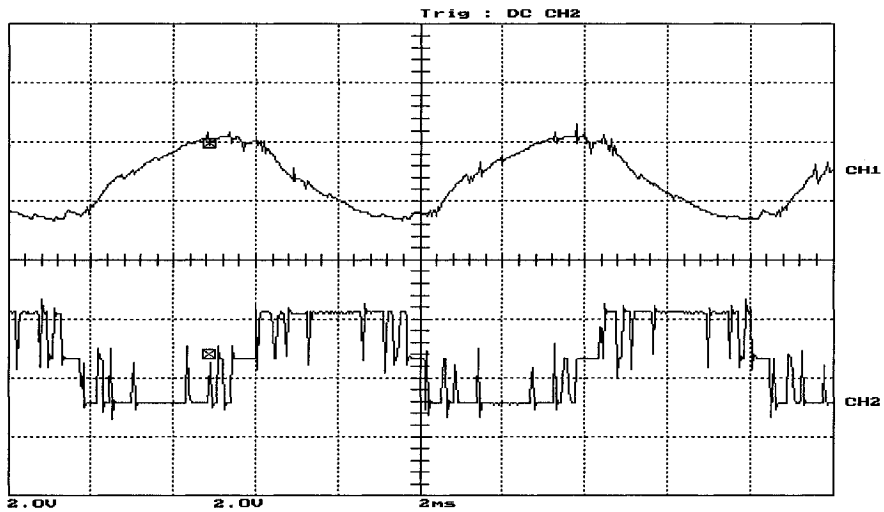

Figure A.3: Experimental results for an output frequency of $f = 120\ Hz$, the inverter output voltage and the $R - L$ load current collected using the *Tektronics* 2212 storage digital oscilloscope. The voltage scale is 50 V/Div and the current scale is 0.2 A/Div.

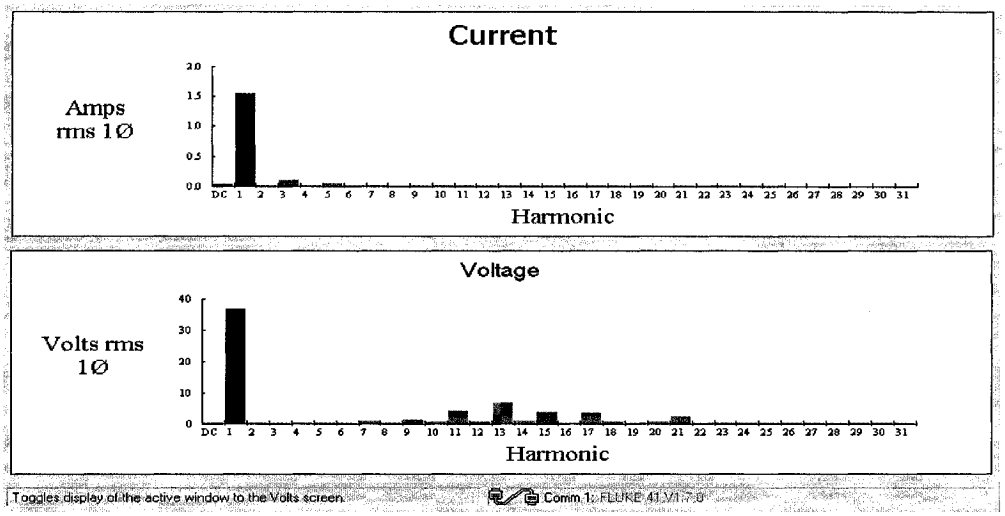

Figure A.4: The experimental $R - L$ load current and the inverter output voltage spectra for an output frequency of $f = 120\ Hz$ obtained using the $FLUKE41$ power harmonic analyzer. The THD_V is 14.3% and the THD_I is 0.8%.

A.1.3 An Output Frequency of $f = 150\ Hz$

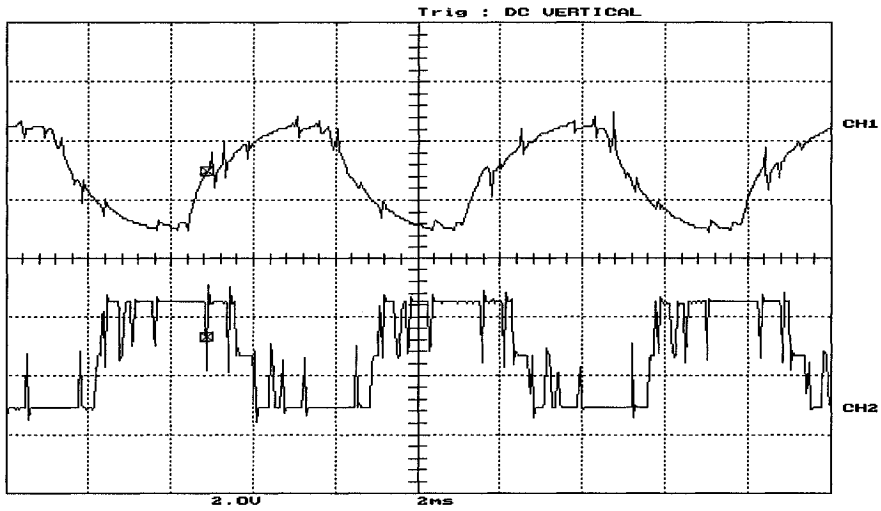

Figure A.5: Experimental inverter output voltage and $R - L$ load current for an output frequency of $f = 150\ Hz$ collected using the *Tektronics* 2212 storage digital oscilloscope. The voltage scale is 50 V/Div and the current scale is 0.2 A/Div.

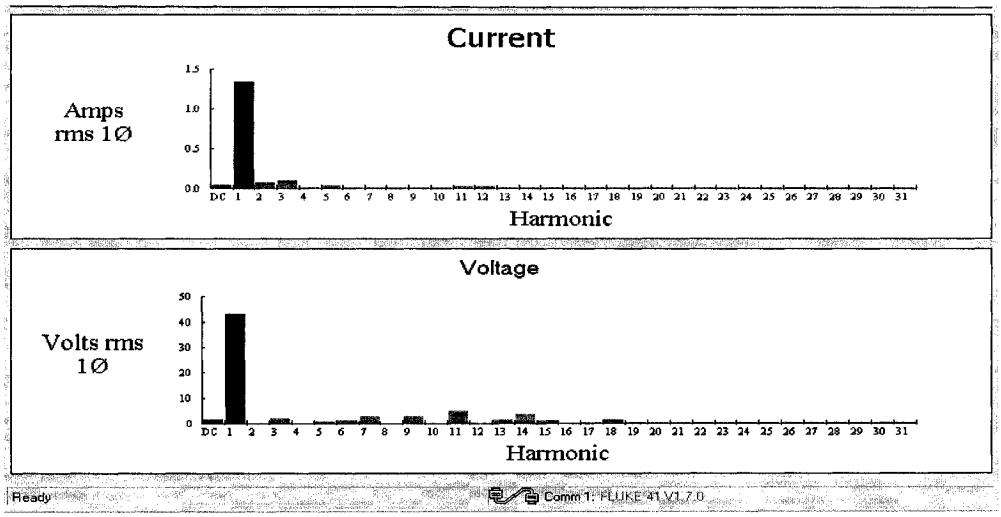

Figure A.6: The experimental $R-L$ load current and the inverter output voltage spectra for an output frequency of $f = 150\ Hz$ obtained using the $FLUKE\ 41$ power harmonic analyzer. The THD_V is 12.2% and the THD_I is 0.4%.

A.2 Single-Phase Capacitor-Run Motor

A.2.1 An Output Frequency of $f = 50\ Hz$

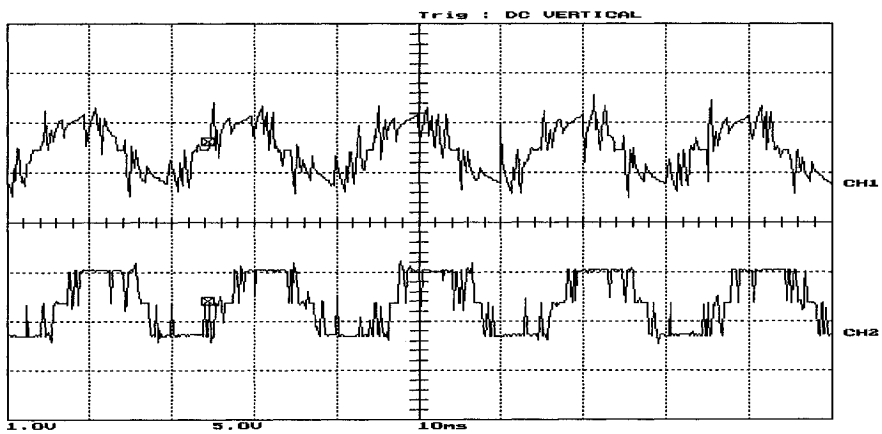

Figure A.7: Experimental results for an output frequency of $f = 50\ Hz$, the inverter output voltage and the 1ϕ induction motor current collected using the $Tektronics\ 2212$ storage digital oscilloscope. The voltage scale is 150 V/Div and the current scale is 0.2 A/Div.

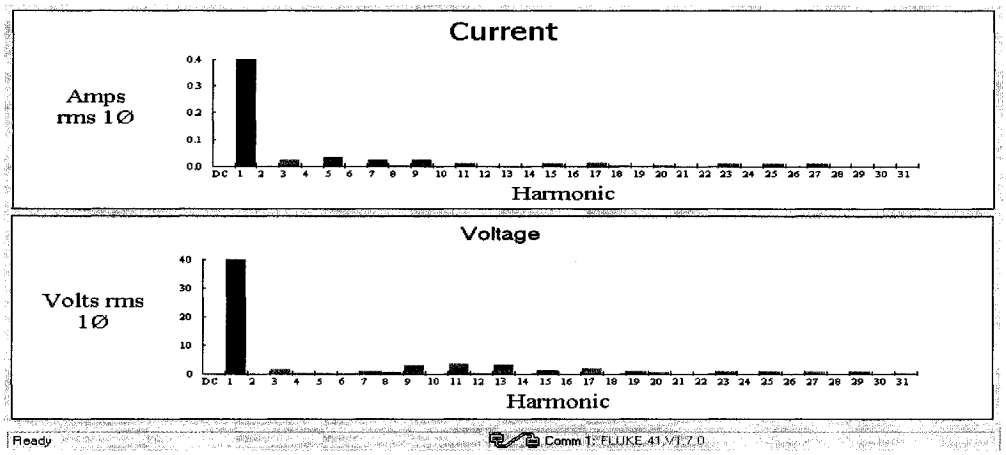

Figure A.8: The experimental 1ϕ IM current and the inverter output voltage spectra for an output frequency of $f = 50\ Hz$ obtained using the $FLUKE\ 41$ power harmonic analyzer. The THD_V is 15.2% and the THD_I is 6.3%. The voltage scale is 1:2.

A.2.2 An Output Frequency of $f = 120\ Hz$

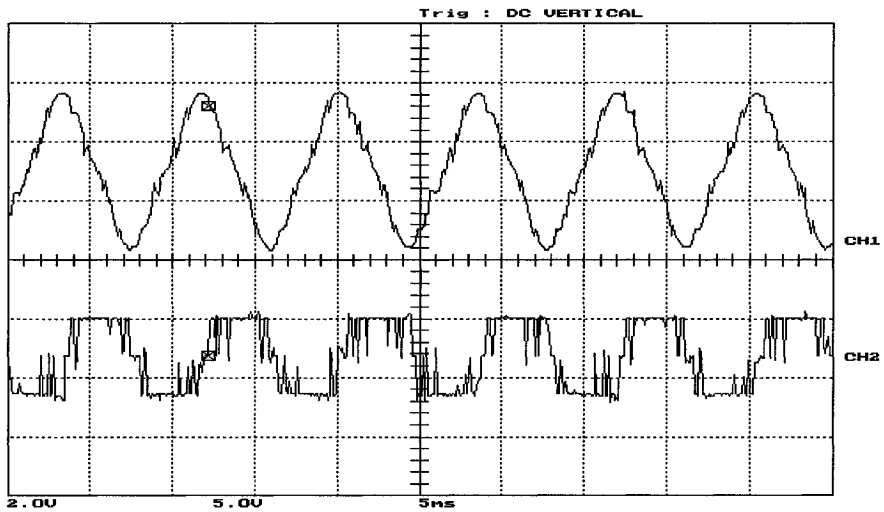

Figure A.9: Experimental results for an output frequency of $f = 120\ Hz$, the inverter output voltage and the 1ϕ induction motor current. The voltage scale is 75 V/Div and the current scale is 0.2 A/Div.

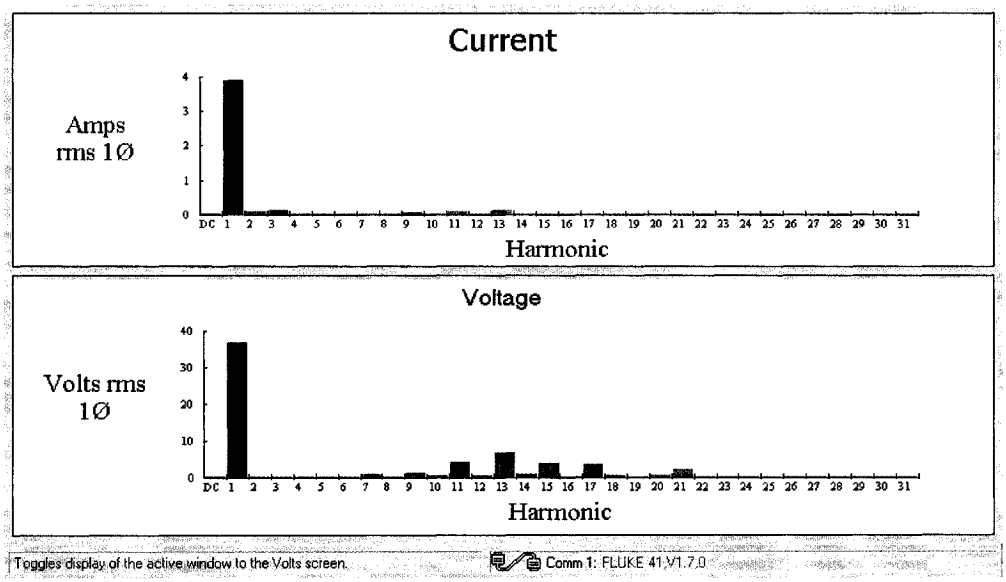

Figure A.10: The experimental 1ϕ IM current and the inverter output voltage spectra for an output frequency of $f = 120\ Hz$ obtained using the $FLUKE\ 41$ power harmonic analyzer. The THD_V is 15.5% and the THD_I is 1.7%. The voltage scale is 1:4.

A.2.3 An Output Frequency of $f = 150\ Hz$

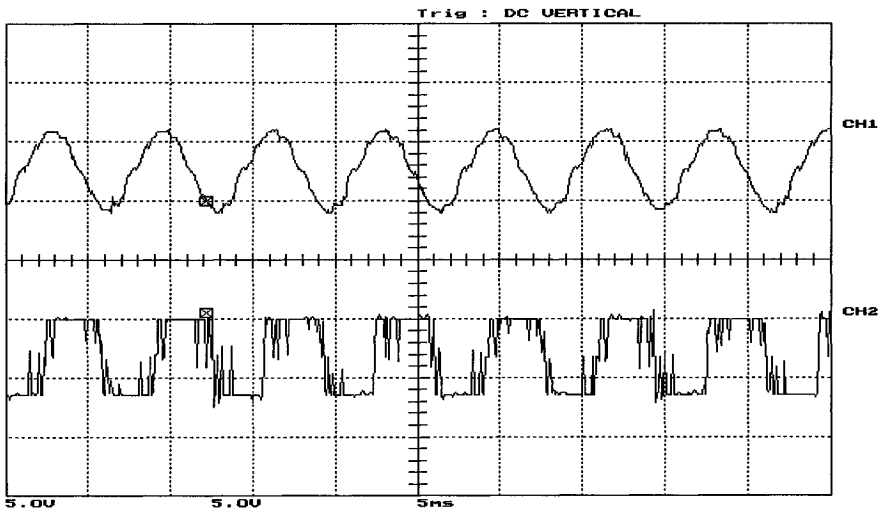

Figure A.11: Experimental results for an output frequency of $f = 150\ Hz$, the inverter output voltage and the 1ϕ induction motor current. The voltage scale is 75 V/Div and the current scale is 0.2 A/Div.

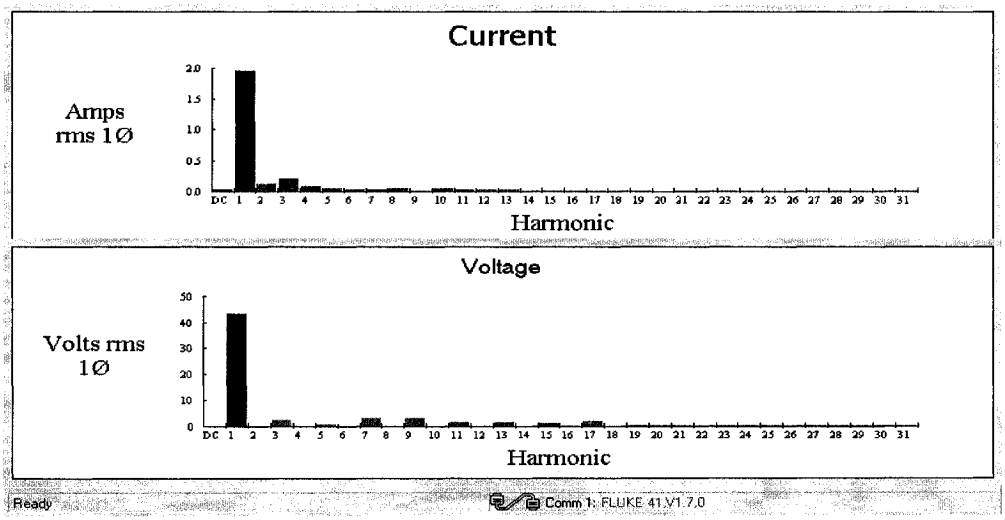

Figure A.12: The experimental 1ϕ IM current and the inverter output voltage spectra for an output frequency of $f = 150\ Hz$ obtained using the $FLUKE\ 41$ power harmonic analyzer. The THD_V is 12.2% and the THD_I is 0.8%. The voltage scale is 1:1.

A.3 The Scale-Time Interval Factor γ

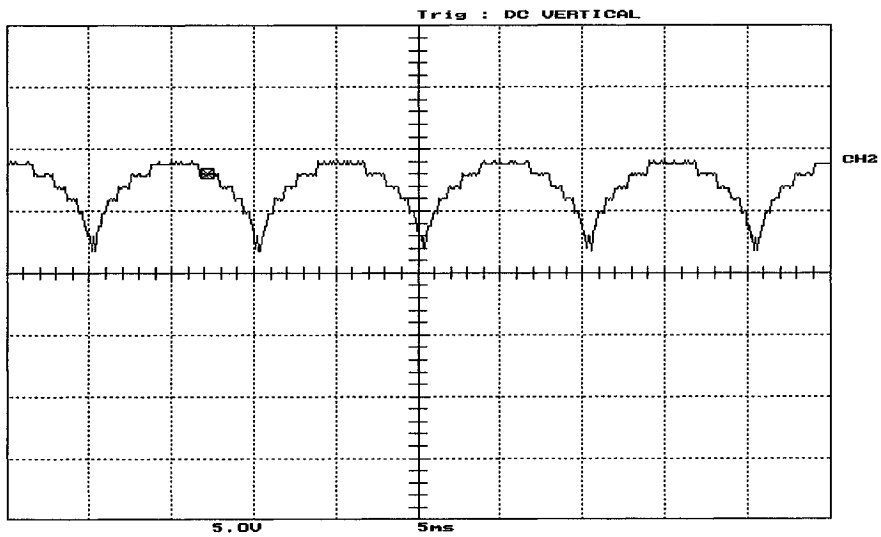

Figure A.13: The scale-time interval factor γ for an output frequency of $f = 50\ Hz$ collected using *Tektronics* 2212 storage digital oscilloscope.

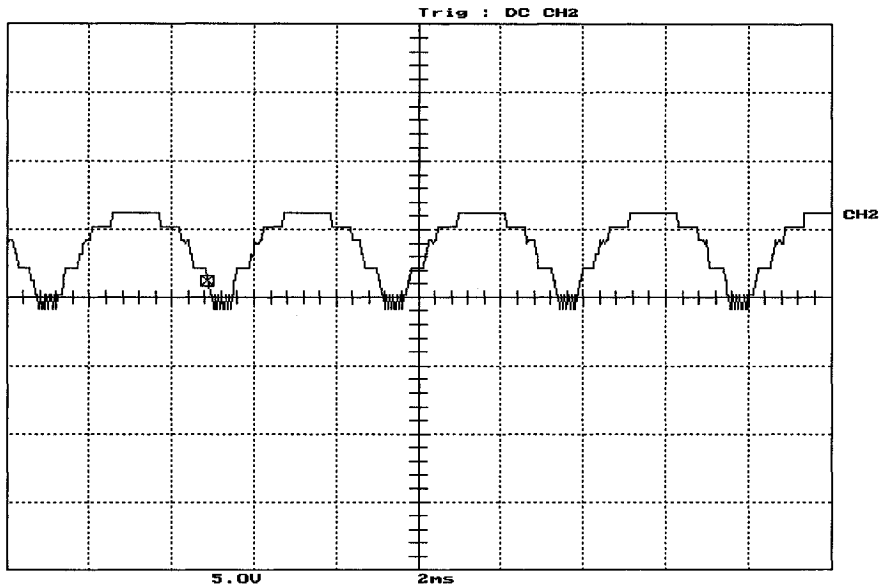

Figure A.14: The scale-time interval factor γ for an output frequency of $f = 120\ Hz$ collected using *Tektronics* 2212 storage digital oscilloscope.

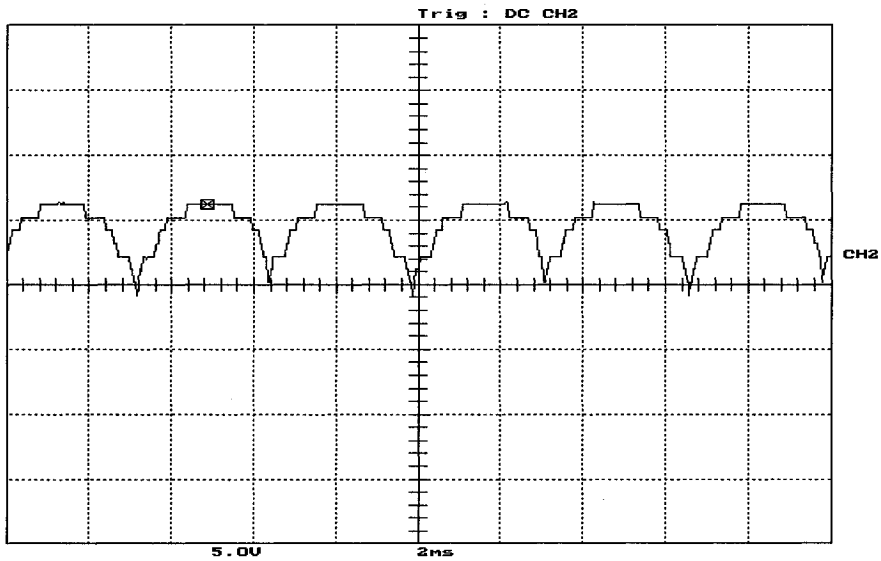

Figure A.15: The scale-time interval factor γ for an output frequency of $f = 150\ Hz$ collected using *Tektronics* 2212 storage digital oscilloscope.

A.4 The Inverter Input dc Voltage and Current

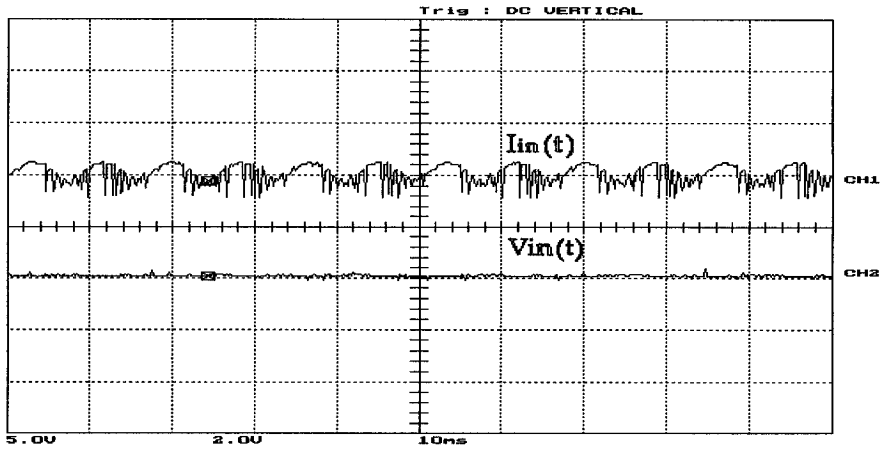

Figure A.16: Experimental waveforms of the tested 1ϕ WM inverter input dc current and voltage for the $R-L$ load. The voltage scale is 50 V/Div and the current scale is 2 A/Div.

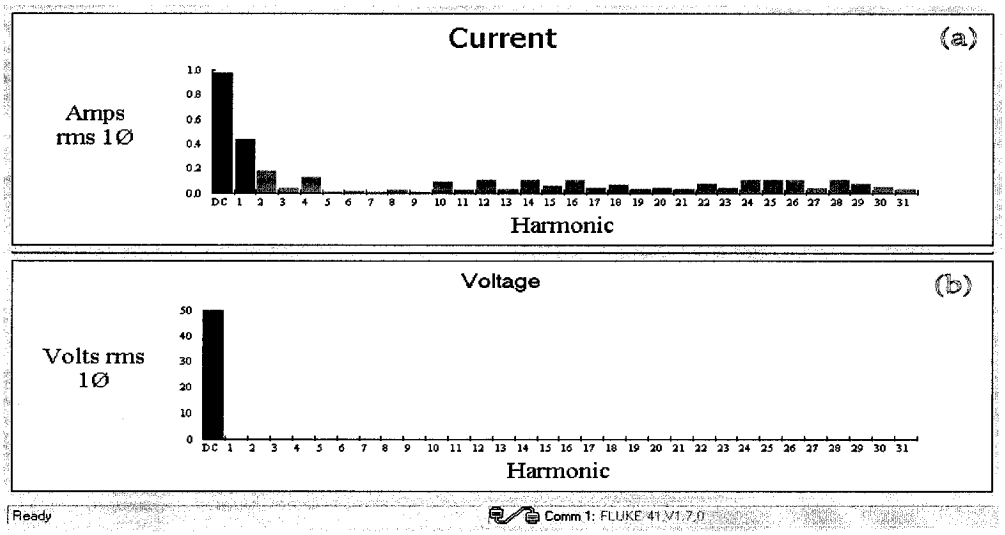

Figure A.17: Experimental spectra of the tested 1ϕ WM inverter input dc current and voltage for the $R-L$ load: (a) the spectrum of the inverter input current and (b) the spectrum of the inverter input voltage.

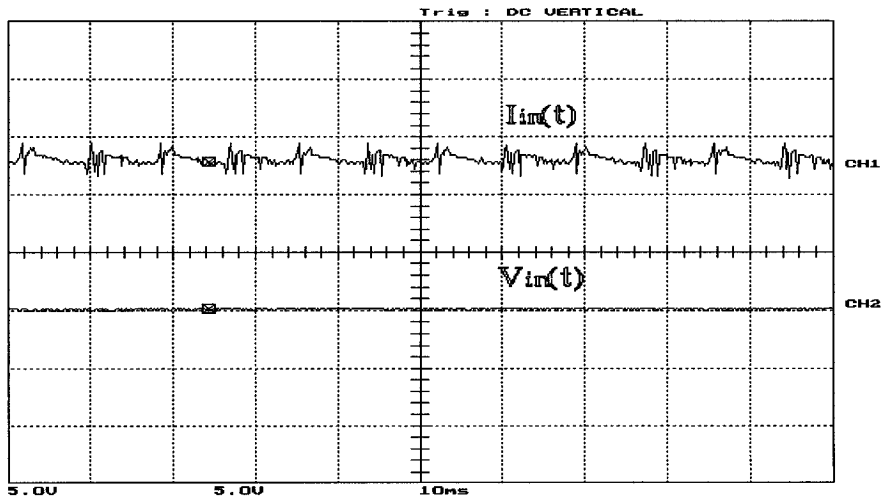

Figure A.18: Experimental waveforms of the tested 1ϕ WM inverter input dc current and voltage for the 1ϕ induction motor. The voltage scale is 50 V/Div and the current scale is 1 A/Div.

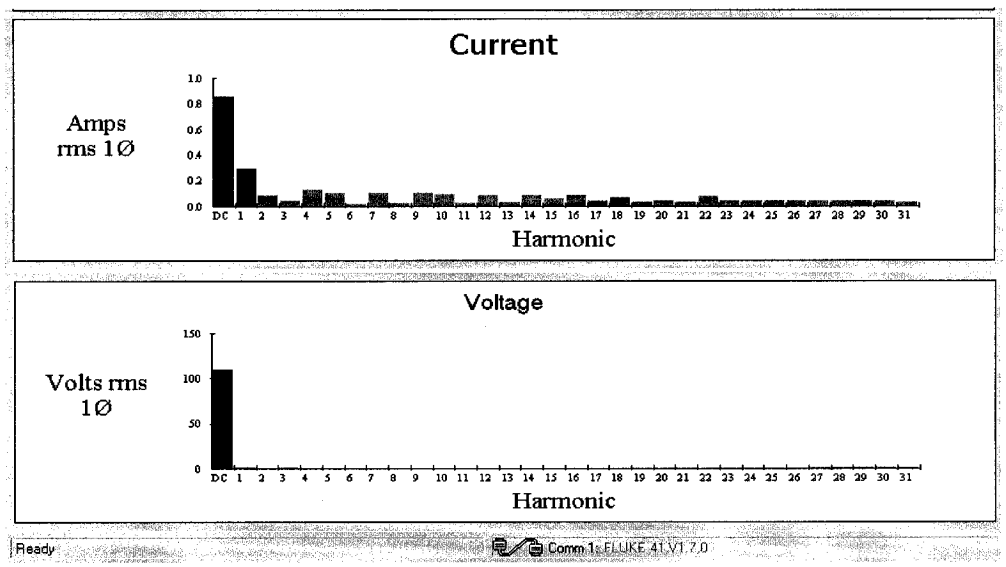

Figure A.19: Experimental spectra of the tested 1ϕ WM inverter input dc current and voltage for the 1ϕ induction motor: (a) the spectrum of the inverter input current and (b) the spectrum of the inverter input voltage. Current scale is 1:2.

Appendix B

1ϕ Resolution-Level Controlled WM Inverters

B.1 Static $R - L$ Load

B.1.1 $S'_M(t, \theta) = \cos(120\pi t)$

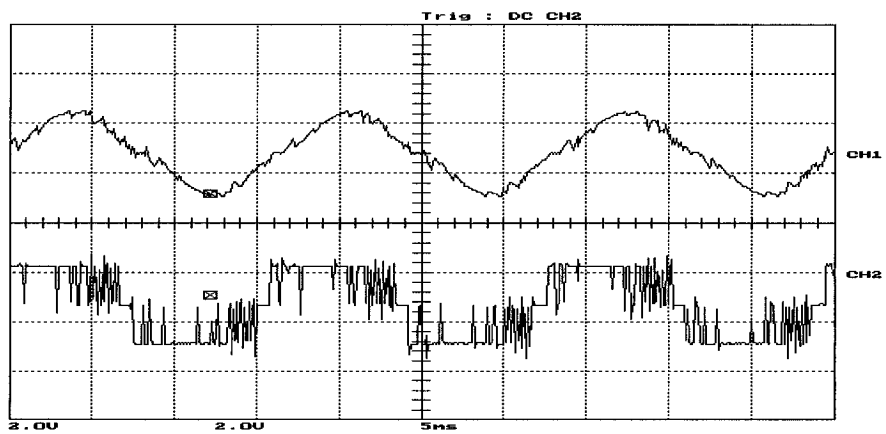

Figure B.1: The experimental inverter normal operation for $f_m = 60\ Hz$ and $\theta = 0$: the load current and the inverter output voltage. The voltage scale is 25 V/Div. and current scale is 1.5 A/Div.

B.1.2 $S'_M(t,\theta) = \cos\left(120\pi t - \frac{\pi}{12}\right)$

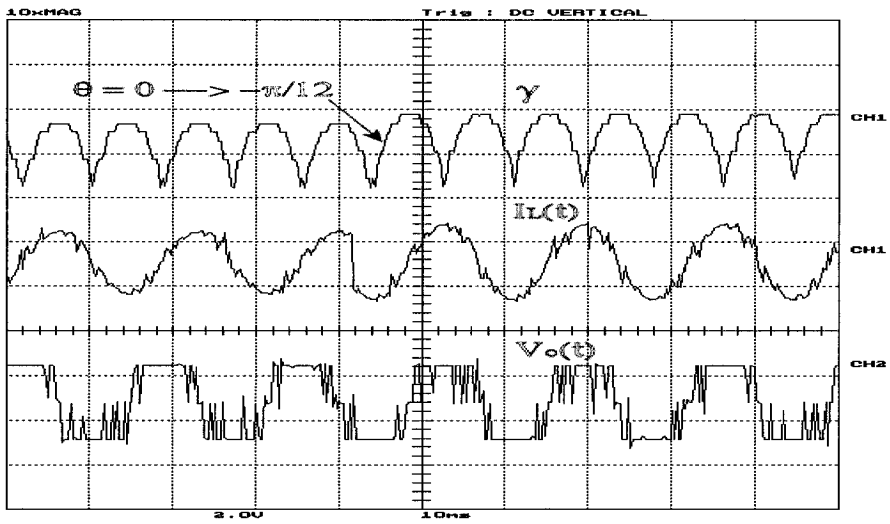

Figure B.2: Test results for shifting $S'_M(t)$ by $\theta = -\frac{\pi}{12}$: the scale-time interval factor γ, the load current and the inverter output voltage. The voltage scale is 25 V/Div. and current scale is 1.5 A/Div.

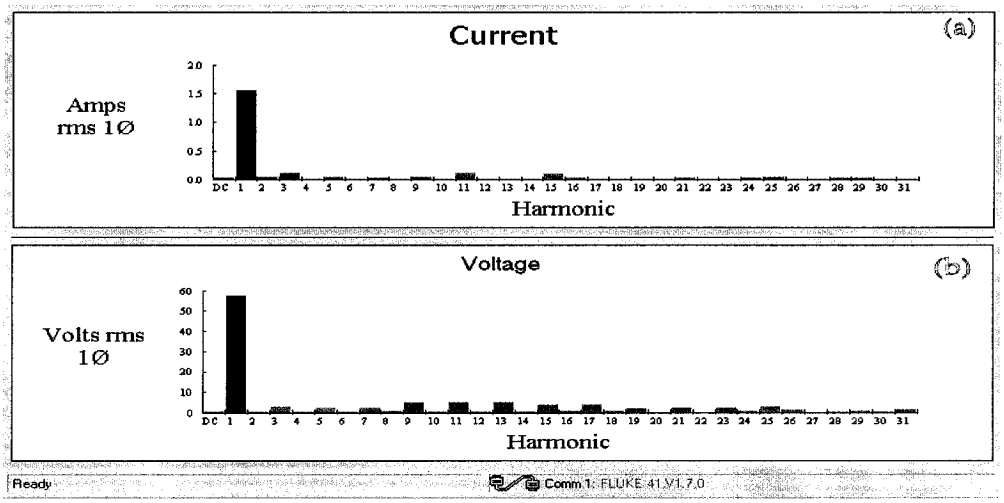

Figure B.3: Experimental test results for shifting $S'_M(t)$ by $\theta = -\frac{\pi}{12}$: (a) the spectrum of the load current and (b) the spectrum of the inverter output voltage. $|I_1| = 1.78\ A$ and $\text{THD}_I = 3.62\%$ $|V_1| = 58.34\ V$ and $\text{THD}_V = 18.46\%$.

B.1.3 $S'_M(t,\theta) = \cos(150\pi t)$

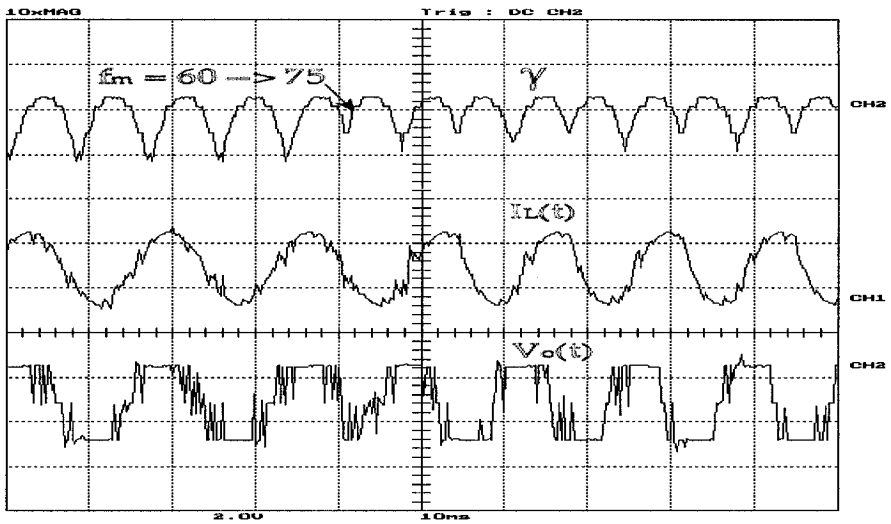

Figure B.4: Experimental test results for changing the output frequency f_m from 60 to 75 Hz: the scale-time interval factor γ, the load current and the inverter output voltage. The voltage scale is 25 V/Div. and current scale is 1.5 A/Div.

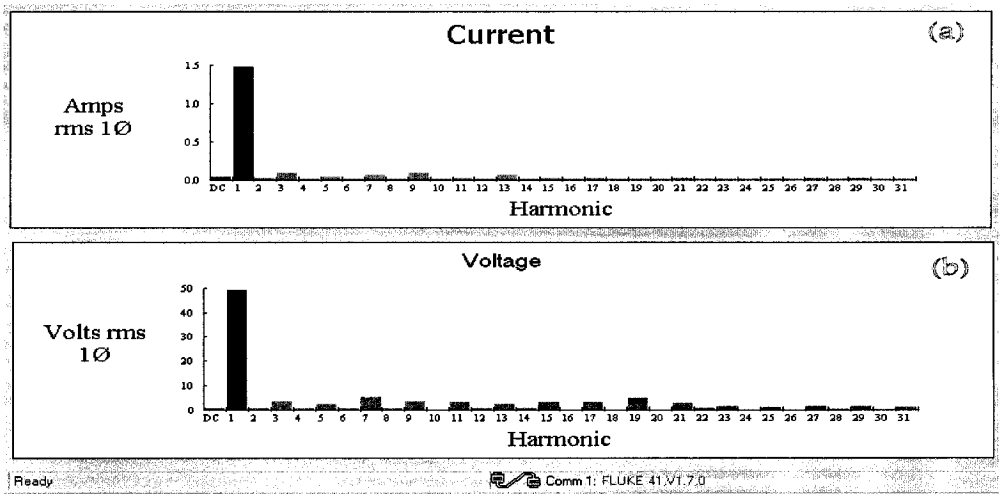

Figure B.5: Experimental test results for changing the output frequency f_m from 60 to 75 Hz: (a) the spectrum of the load current and (b) the spectrum of the inverter output voltage. $|I_1| = 1.48\ A$ and $\text{THD}_I = 2.87\%$ $|V_1| = 49.68\ V$ and $\text{THD}_V = 18.26\%$.

B.1.4 $S'_M(t,\theta) = \cos\left(100\pi t + \frac{\pi}{10}\right)$

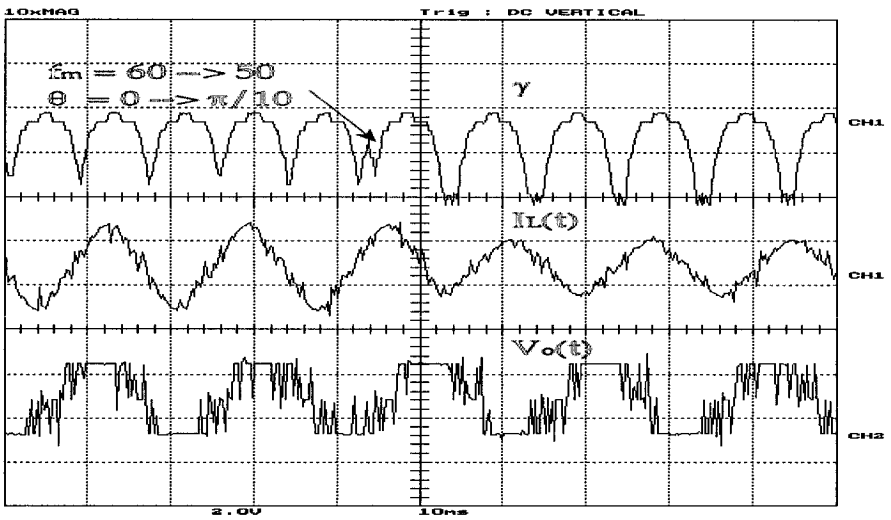

Figure B.6: Experimental test results for changing the output frequency f_m from 60 to 50 Hz with a phase-shift $\theta = \frac{\pi}{10}$: the scale-time interval factor γ, the load current and the inverter output voltage. The voltage scale is 60 V/Div. and current scale is 2 A/Div.

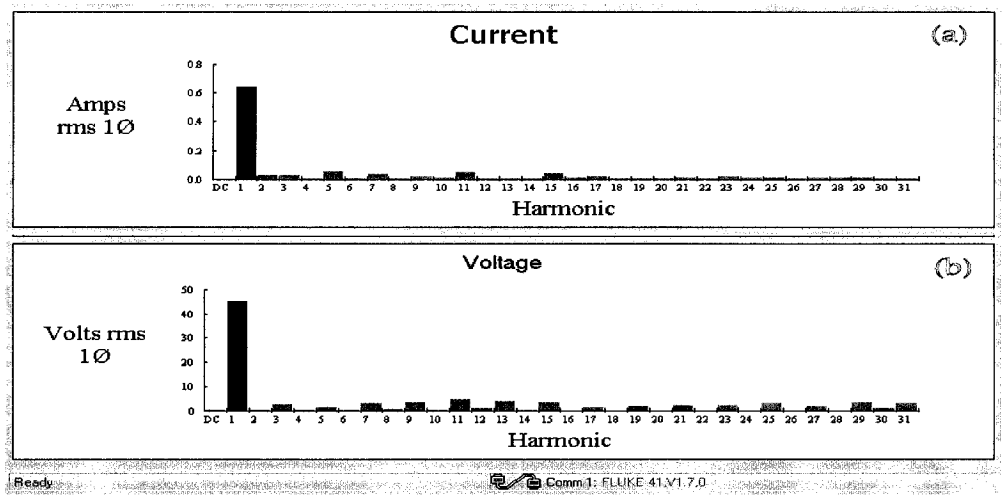

Figure B.7: The test results for changing the output frequency f_m from 60 to 50 Hz with $\theta = \frac{\pi}{10}$: (a) the spectrum of the load current and (b) the spectrum of the inverter output voltage. $|I_1| = 0.78\ A$ and $\text{THD}_I = 2.14\%$ $|V_1| = 44.12\ V$ and $\text{THD}_V = 19.74\%$.

B.2 Speed Responses of the 1ϕ Capacitor-Run Induction Motor

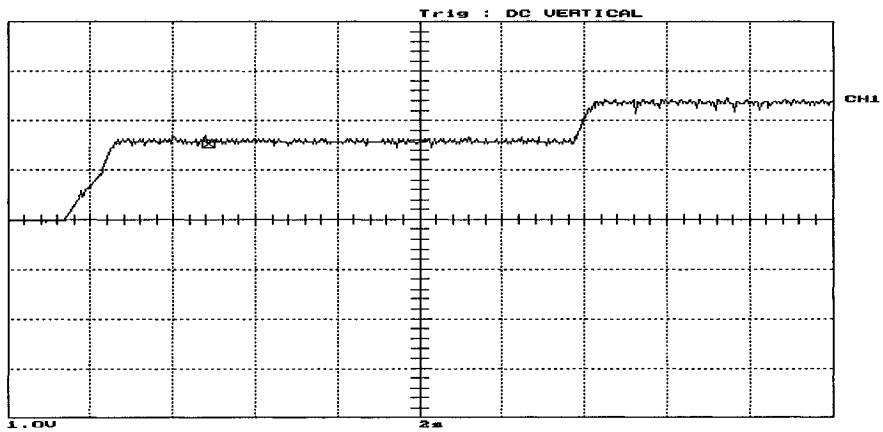

Figure B.8: Experimental testing of the resolution-level controlled WM inverter for $\theta = 0 \longrightarrow -\frac{\pi}{12}$: the capacitor-run 1ϕ induction motor speed response.

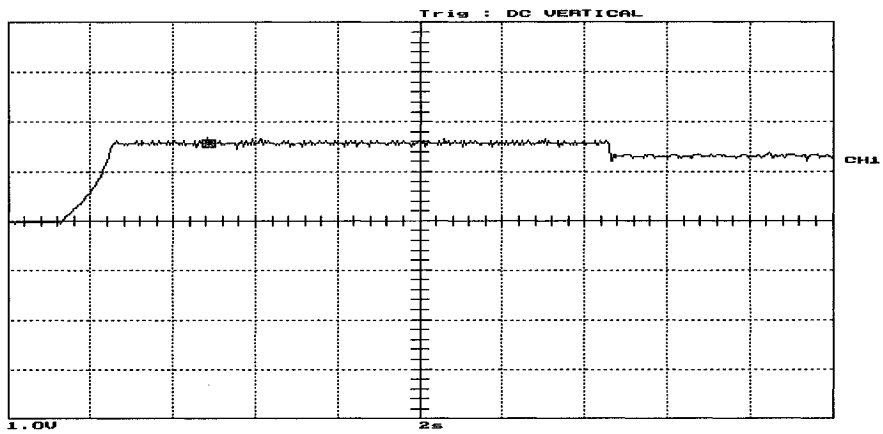

Figure B.9: Experimental testing of the resolution-level controlled WM inverter for $f_m = 60 \longrightarrow 50\ Hz$ and $\theta = 0 \longrightarrow \frac{\pi}{10}$: the capacitor-run 1ϕ induction motor speed response.

Appendix C

Snubber Circuits

Snubber circuits are $R-C$ circuits connected in parallel with power electronic switching elements to limit or reduce the rate of voltage change across them during ON-OFF operation. The rate of change of the voltage across a typical switching element becomes a critical issue when inductive loads are supplied. The fact that the current flowing through an inductor can not change instantly creates a longer OFF-switching time for a typical switching element. The function of a $R-C$ snubber circuit is simply to provide a path for the load current to decay and prevent high changes of the voltage across switching elements when supplying inductive loads. This can be stated as:

$$\frac{dv_{SE}(t)}{dt} < \infty \tag{C.1}$$

Typical resistances and capacitors that are used in snubber circuits are with the following values:

1. $R_s = 15\,\Omega$
2. $C_s = 0.1\,\mu F$

These values of R_s and C_s can limit the rate of change in the voltage across an IGBT switch to:

$$\frac{dv_{IGBT}(t)}{dt} \leq 300\ V/\mu\text{sec.} \tag{C.2}$$

Figure C.1 shows the schematic diagrams of the snubber circuits used for the experimental testing of both the 1ϕ and the 3ϕ WM inverters.

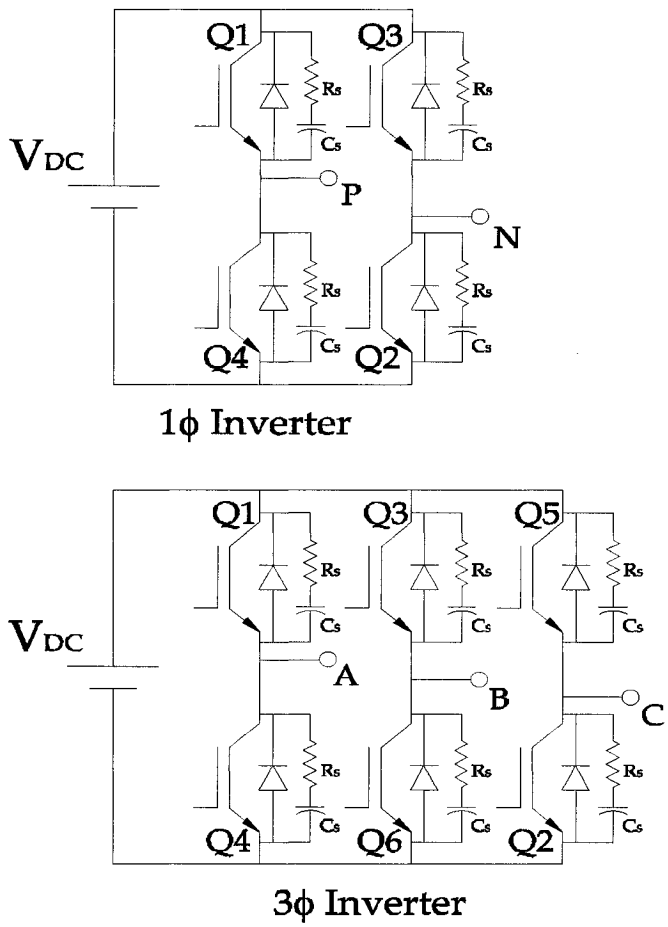

Figure C.1: The schematic diagram of the 1ϕ and the 3ϕ WM IGBT inverters with snubber circuits.